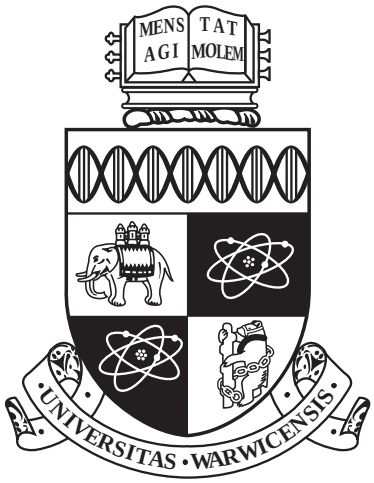

Aptamer-based Biosensors as a New Analytical Tool for Neuroscience

by

Martina Mengoni

Thesis

Submitted to the University of Warwick

for the degree of

Doctor of Philosophy in Biological Sciences

School of Life Sciences

September 2021

Contents

List of Tables

List of Figures

List of Abbreviations and Symbols

Table 1. *List of abbreviations and symbols*

Abbreviation	Meaning
1BS	1 binding site aptamer
1BSS	1 binding site aptamer short stem
2BS	2 binding site aptamer
5-HT	Serotonin
A	Area of active surface
AC	Associational commissural pathway
aCSF	Artificial celebrospinal fluid
ADP	Adenosine diphosphate
Ag/AgCl	Silver/silver chloride
AMP	Adenosine monophosphate
ANS	Autonomic nervous system
ATP	Adenosine triphosphate
Au	Gold
BSA	Bovine serum albumin
BWB	Beads washing buffer
C^0	Analyte bulk concentration
CAP-oligo	Capture oligo
CA1	Cornu Ammonis 1
CA3	Cornu Ammonis 3
CE	Counter electrode (Pt)
CE	Capillary electrophoresis

CNT	Concentrative nucleoside transporters
CNS	Central nervous system
CSF	Celebrospinal fluid
CV	Cyclic voltammetry
CY5	Cyanine-5 dye
D_0	Diffusion coeffiecient of the oxidised analyte
DG	Dentate gyrus
DNA	Deoxyribonucleic acid
dNTPs	Deoxynucleotide Triphosphates
dsDNA	Double-stranded DNA
e^-	Electron
e_a	Absolute error
E_0	Initial voltage
E_1	Final voltage
EC	Entorhinal cortex
ELISA	Enzyme-linked immunisorbent assay
ELONA	Enzyme-linked oligonucletide assay
ENT	Equilibrative nucleoside transporters
E-AB	Electrochemical aptamer-based
F	Faraday constan
F_0	Fluorescence without target
F_1	Fluorescence with target
Fc/Fc^+	Ferrocene/Ferrocenium
Fc	Ferricyanide
fEPSPs	Field excitatory post synaptic potentials
FET	Field-effect Transistors
FP	Forward primer
HOMO	Highest occupied molecular orbital
HPLC	High presssure liquid chromatography
HSA	Human serum albumin
i_p	Peak current

IR	Infra-red
ITC	Isothermal tritation calorimetry
IUPAC	International union of pure and applied chemistry
K_D	Dissociation constat
$K_3[Fe(CN)_6]$	Potassium Ferricyanide
KCl	Potassium Chloride
LED	Light-emitting diod
LOD	Limit of detection
LUMO	Lowest unoccupied molecular orbital
MB	Methylene blue
MCH	6-mercapto-1-hexanol
MCH_{11}	11-mercapto-1-hexanol
MEMS	micro electromechanical systems
MF	Mossy fibres
MFE	Minimum free energy
MIP	Molecularly imprinted polymer
MST	Microscale thermophoresis
NA	Nucleic acid
NC	Negative control
NEMS	Nano electromechanical systems
NMR	Nuclear magnetic resonance
NP	No primer
Ox	Oxidated agent
PAGE	Polyacrilamide gel electrophoresis
PBS	Phosphate buffer saline
PBS-Mg	PBS with 1 mM Mg^{2+}
PC	Phosphatidylcholine
PC	Positive Control
PCR	Polymerase-chain reaction
PEG	Poly(ethylene glycol)
PP	Perforant Pathway

Q	Total charge
R	Gas constant
Re	Reduced agent
RE	Reference electrode
RNA	Ribonucleic acid
RP	Reverse primer
RT	Room temperature
SAM	Self-assembling monolayer
Sb	Subiculim
SC	Schaffer collaterals
SD	Standard deviation
SELEX	Systematic evolution of ligands by exponential enrichment
SG	SYBRGreen I dye
SPR	Surface plasmon resonance
ssDNA	Single-stranded DNA
SWV	Square wave voltammetry
T	Temperature
TCEP	Tris(2-carboxyethyl)phosphine
UDP	Uridine disphosphate
UDP-galactose	Uridine disphospho-galactose
UDPg	Uridine disphospho-glucose
UDP-glucose	Uridine disphospho-glucose
UTP	Uridine trisphosphate
UV	Ultra-violet
WE	Working electrode
Γ^*	Surface density of the absorbed analyte
Δ_E	Peak-to-peak potential difference
ν	Scan rate

Acknowledgments

"The best way to explain it is to do it."– Dodo

Lewis Carroll - Alice's Adventures in Wonderland

I first would like to thank my supervisor Prof. Richard Napier for his constructive comments and discussions, his help inside and outside the lab, for showing me the good in my results when I could not find it and for his amazing cakes.

I would like to thank my examiners for agreeing to spend their time to read and evaluate my work.

I would like to thank the MSCA Curie Action and the PurinesDX training network for selecting me for this project and funding my work. I would also like to thank the network for the possibility to work with and form my self in multiple excellent institutes around Europe. I would also like to thank the University of Warwick School of Life Sciences for providing me with the funds for the extension after the bankruptcy of my previous employer.

Special thanks go to Dr. Emily Hill for the marvellous hippocampal slices provided and for having a look at my chapters; Dr. Mark Wall for help in troubleshooting the extracellular recordings; and to Dr, Caitlin Hatton and Dr. Karla Banjak for going through my chapters.

To Dr. Sireethorn Tungsirisurp for being my SELEX-pedia, my MST-expert, my go-to person, for the endless calls, for the incredible support. There aren't enough cappuccinos in the world to thank you.

I would like to thank my colleagues of the neuroscience lab (*Dr. Hill lab:* Pippa, Emily, Dan, Gabri, Jess, Aditi, Reno, Jenny, Circe and C116: Sarb, JC, Joe, Greta, Erick

and Will) and and from plant lab (Siree, Cat, Xinghao, Chitra, Susan, John and Sarah) for the days and evenings spent inside and outside the lab together sharing nonsense, laughs, successes and defeats, and for the inspiring discussions, scientific and not. Other special colleagues from SLS need mentioning: To Patrick and Caitlin, I could not have made it through these last months without you. Thank you for being such good friends. To the C30 people, the party people, you made so many days so much fun and reminded me there is more to life than lab drama. Best of luck with your PhDs, I swear it doesn't look like it, but this nonsense does end.

I would like to thank my fellow ESRs from the PurinesDX for being an amazing group to spend workshops and weekends around Europe with. You are so many kinds of amazing and I am so glad I got to share this with you.

I would like to thank my family for supporting my academic career. I would like to thank my mum for always believing in me and pushing me to strive for more. You are an amazing woman and I could not be prouder to be your daughter. I would like to thank my dad for teaching me to always believe there is good in people and that grit is the key to success. I would also like to thank my niece and nephew for the purity of their hearts, an gulp of fresh air every time my faith in humanity about to break.

I would like to thank my friends, all scattered around the world: the Piovono Mama's, the - Roberto + Agatha, Le donne di Agatha, the Muffins, the EMM Nano, the Leuven crew, the Dresden crew, the All the pretty girls, the Lockdown team, the Midlands having fun and my HOT CUNELLI. Some of you have been there my all life, some of you for way less. You are all such different people, but all so inspiring, kind and loving. Thank you for grounding me and reminding me of what matters. You are the roots to my tree, you are my chosen family. I am so lucky to have you my life and to get to see you all blossom in the best human beings the world has ever seen.

Special thanks go to Alessandra for being my rock, through thick and thin and for being the best friend one person could ask for. The last special thanks goes to my family in England: Nelli and Marta , Betty, Fra, Chiara, Fabrizio and Andrea. There are no words for you guys. There will always be a part of my heart with your names written on.

Finally, I would like to thank all the people who have wronged me. You got me to better appreciate all the people who love me and treat me fairly, and you gave me the chance to prove again and again, that I can rise against the odds because "I've got the Juice" (cit. Janelle Monae).

Declarations

I, Martina Mengoni, declare to be the only author of this thesis and that the work presented in it is original and was it was produced solely by me, unless otherwise stated in the reference or akwnowledgment. I declare I understand university policy on plagiarism, and that concepts from published work was properly referenced and cited. I certify that the work here presented has not been previously submitted, in whole or in part, for another degree or professional qualification.

Abstract

Electrochemical sensors have the capability to sensitively and reliably detect target molecules in complex media. Aptamers are single stranded nucleotide sequences capable of specifically and selectively bind a large variety of target molecules. The purpose of this project, comprising three main parts, was to establish an aptamer-based electrochemical platform as a new analytical method for the real-time continuous monitoring of small molecules released in the brain.

In the first part, the protocol for the production of an aptamer-based electrochemical sensing platform capable of continuous monitoring was established and optimised using the ATP/adenosine aptamer as a model. The redox-decorated aptamer was immobilised on a gold surface and the signal generated by the displacement of the electron donor upon binding of the target molecule with the DNA strand. The fabrication and its properties were assessed via cyclic voltammetry (CV) and the sensor response recorded via square wave voltammetry (SWV). Three aptamers for ATP/Adenosine were employed and their performance on the platform was evaluated both against the target and the downstream molecules.

In the second part, the characterised platform was employed to record a biological event: the *in vitro* release of adenosine from a hypoxic brain slice. Prior to performing the measurement that required tissue, all the control measurements were performed to evaluate influence of different environmental factors *e.g.* pH, temperature, buffer composition. Another preliminary measurement aimed to verify whether the sensor could be inserted in the tissue, by recording the sensor response whilst inserted in an agar block. Lastly the recording of adenosine release from hypoxic brain tissue was performed simultaneously with electrophysiology recordings.

In the third and last part capture-SELEX was employed to select two novel structure-switching aptamers against UTP and UDP-glucose, two neurochemicals connected to pathological conditions such as epilepsy, dry eye disease and metastatic cancer. The sequenced libraries were then analysed and the emerged candidates were at first screened with SYBRGreen assay, a high throughput fluorescence assay, and the results confirmed via microscale thermophoresis (MST). The final selected aptamer, for each target molecule, underwent the first truncation round. Finally, the binding affinity of the two obtained sequences were characterised via MST.

Chapter 1

Introduction

1.1 Biosensors

With a world population that gets older, cheaper and faster diagnostics are necessary for governments to contain the costs of healthcare. Biosensors with their fast response and low cost are emerging as an alternative to clinical analysis methods. In his 30th anniversary of biotechnology issue, Anthony Turner, one of the developers of the first glucose sensor, reflected on the fast progression that the biosensor field has experienced in the last three decades. In terms of publication statistics the number of published papers on biosensors went from a yearly average of just above 300 papers, to almost 5500 publications in the last decade [18]. At the same time commercial market share for biosensors went from nil to 25 billions USD [267, 19]. This exponential growth was made possible by advent of advanced miniaturisation technologies and nanomaterials, which improved the sensitivity and the response times of the sensors, whilst the discovery of novel biorecognition molecules broadened the spectrum of detectable analytes [16].

Biosensors are devices which make use of a biomolecular recognition layer to capture a specific target molecule from a sample and transform that detection event into an easy-to-interpret signal (Figure 1.1.a). The molecule detected is often called a biomarker, a chemical which is correlated to the occurrence of an event, *e.g.* pathological condition, and, as such, can be used as an indicator to diagnose a condition or

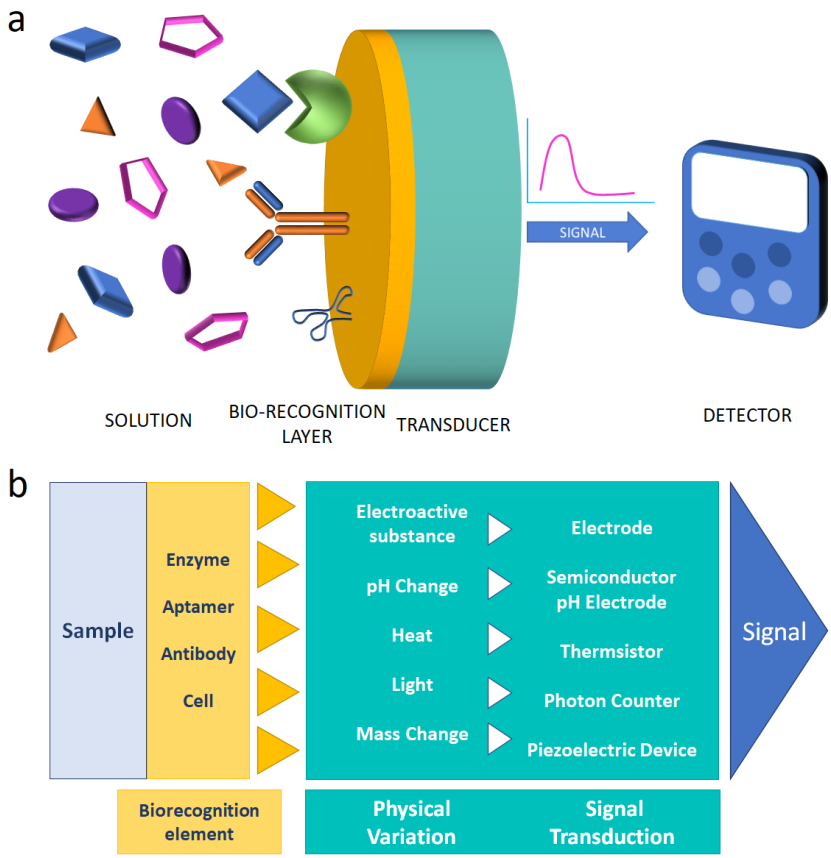

Figure 1.1. Structural elements of a biosensor. a) Illustration of the different components of the sensor. b) Illustration of the possible biorecognition elements and transduction mechanism.

monitor its progression. Thanks to their capability to deliver real-time qualitative and quantitative information from minimally processed samples, and the vast design possibilities, biosensors are transforming disease diagnosis and monitoring [243]. However, their applications are not limited to the medical field, as also the food industry, environmental monitoring, biodefence, and academic research, have invested in biosensor development to reduce production costs, speed up production processes, create new analytical tools and safeguard people's and the environment's health and safety [166].

1.1.1 Structure and Categorisation

Biosensor designs consist of three fundamental elements: a recognition element, to collect the analyte from the sample; a physical/chemical variation that takes place upon the capture of the target molecule; and a transduction system, to convert the variation into an electrical signal, which is then interpreted to generate a read out (Figure 1.1.a) [39, 104]. As illustrated by Figure 1.1.b, many combinations of biorecognition layer and transducer mechanism are possible, all of which can be used to classify the sensor itself.

For the biorecognition element the options are many: enzymes, antibodies and nanobodies, DNA and RNA aptamers, cells and molecularly imprinted polymers (MIP) to name a few [198]. Despite the different characteristics and properties, all biorecognition elements are characterised by a binding affinity and an equilibrium dissociation constant (K_D). The former describes the propensity of the recognition element to bind its target molecule and it is independent of the target concentration; whilst the latter is the concentration of the target molecule for which 50 % of the binding sites of the recognition elements are occupied. The higher is the affinity between ligand and target, the lower will be concentration needed to achieve 50 % of occupied sites, thus the K_D [262]. Interaction between ligand and target occur following two mechanisms: catalytic, where the analyte is converted into product by the substrate (Figure 1.2, top); and affinity, where the interaction between target molecule and the biorecognition layer is completely reversible (Figure 1.2, bottom). One example of the first is the glucose monitoring sensor that exploits the enzymatic reaction of glucose oxidase to produce hydrogen peroxide (H_2O_2), whilst for the latter the lateral flow Covid-19 test has become the most renowned commercial example. The choice of the biorecognition element should be made carefully as it determines how selective the platform will be and the stability of the signal. The sensitivity is also affected by the ligand of choice; but the transduction system, the design of the platforms can play a fundamental role too.

The transduction is the component of the sensor that turns the target binding event into a measurable signal. Given the many transduction systems available, one

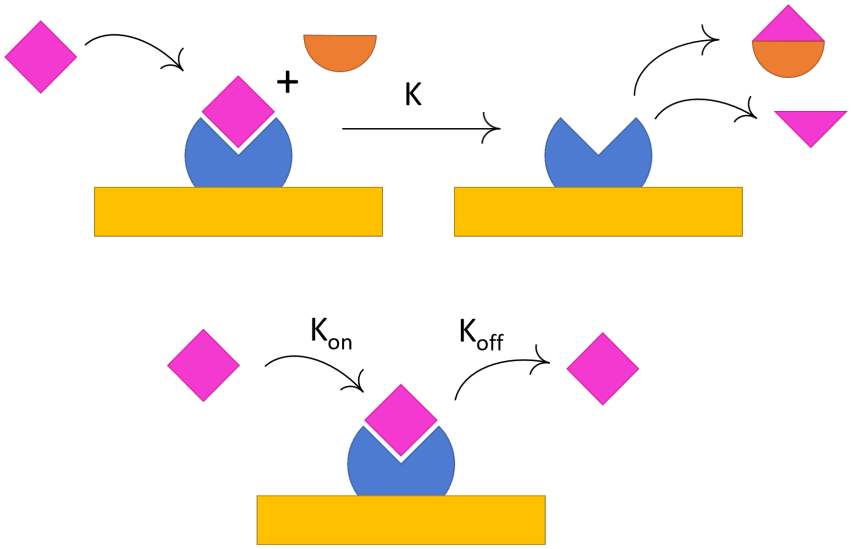

Figure 1.2. Illustration of the principles behind catalytic (top) vs. affinity (bottom) detection. *For catalytic biosensors, the target transformed via an irreversible reaction which proceeds at a rate K. On the other hand, affinity sensors bind and release the target following on and off rates, K_{on} and K_{off} respectively, but the target remains unchanged, thus it can bind again.*

way of categorising them is based on the type of variation exploited to generate a signal. The categories are: mass variation, physical variation and chemical variation. Amongst the techniques which detect change in mass are surface plasmon resonance (SPR), quartz crystal microbalance, oscillating nanorods, and micro or nanoelectrocmechanical systems (MEMS and NEMS). Chemical changes are exploited in pH sensors and colorimetric sensors; whilst variation in physical properties like charged state and conductivity properties, generate signals in electrochemical sensors, field-effect transistors (FETs) and piezoelectric sensors amongst others.

Some techniques have clear advantages over the others: electrochemical and optical transduction are the most popular, owing to the large number of techniques employable to both characterise the sensor and record the signal; and the design flexibility of the assay. Electrochemical transduction is inexpensive, fast and relatively simple. However, electrochemically active molecule present in the environment can generate false positive signals. Maintaining a small potential window can help reduce this fouling, but the sensor is still quite vulnerable to their presence and additional screening is necessary. Optical platforms, on the other hand, present higher average cost per device and the technique is more prone to fouling [211].

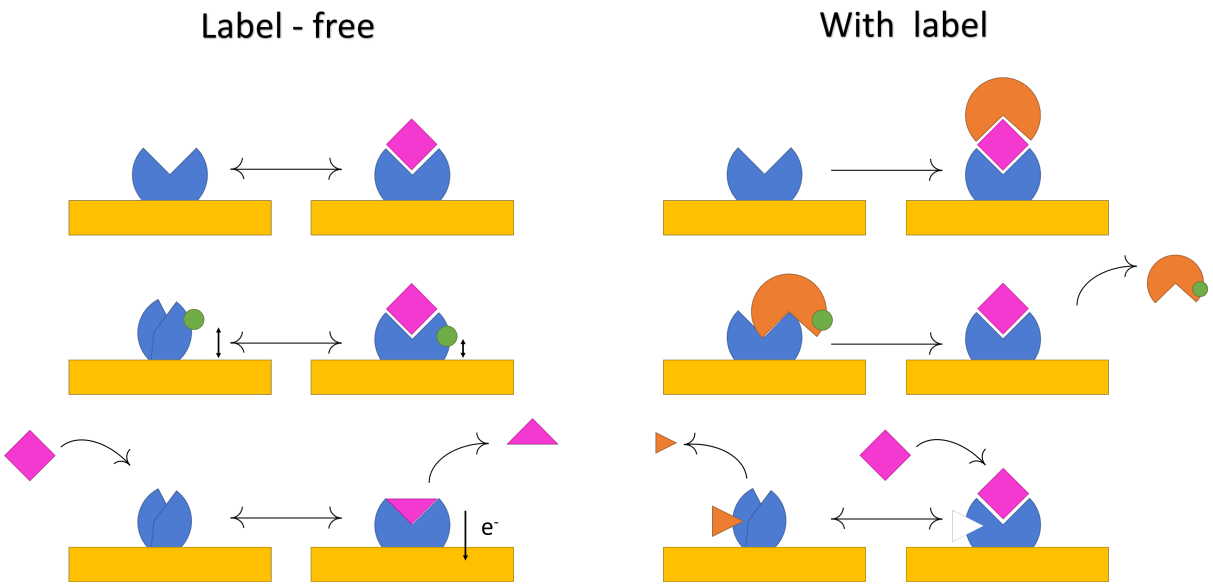

Figure 1.3. Examples of signal generation mechanisms label-free (left) and with label (right, orange). *The top panel shows an example of physical variation, where the sensor detects a change in mass at the surface. The middle panel illustrates an example of signal generated via reporter displacement (green). The bottom panel displays a biorecognition element undergoing conformational change, induced by the target (left) or an allosteric inhibitor (right).*

1.1.2 Designs Options

Dependent on the applications for which the biosensor is designed, its components need to fit different requirements. Selecting a sample, the biorecognition layer and a transduction system is not sufficient to unilaterally describe the sensor design. Sensors can be developed for continuous monitoring or single time point measurement, disposable or reusable, single step/reagentless or multi-step. In general, whether the biosensors belongs to the first or the second category depends on whether it presents a molecular label or not.

Label-free sensors exploit the ligand-substrate interaction to generate a signal (Figure 1.3, left). The signal can originate from displacement of a reporter or a change in the molecular or of the physical properties at the sensor interface itself. The labelled sensor make use of a second recognition element, to generate/amplify the variation which is transformed into a signal by the transduction system (Figure 1.3, right).

The main advantages of the label-free design is the possibility to continuously monitor the analyte concentration in the sample, without the need of regeneration

steps. Additionally, label-free sensors are easier to optimise and linearise, given the simpler design. However, sensors with molecular labels often present higher specificity, given that not one but two ligands have to interact with the target molecule to produce a signal *e.g.* sandwich assay such as ELISA or ELONA. The presence of a molecular label can also improve the sensitivity of the sensor as it can amplify the signal generated. For example, in an SPR assay, the mass change generated by a small molecule alone binding to its antibody is significantly smaller than the signal generated by a molecule and a secondary antibody (sandwich assay). The lack of signal amplification in the label-free sensor often results in a smaller signal variation recorded upon binding. Therefore, label-free sensors require their noise contribution to be minimised to achieve a sufficient signal-to-noise ratio.

1.1.3 Characteristics and Parameters

Biosensors are quantitative devices. Some sensors provide a binary answer upon detection: positive or negative. There are many commercial examples, *e.g* the Covid-19 lateral flow test or the pregnancy test. These devices are usually characterised by an easy-to-interpret visual response which indicates whether the sought analyte was present or not. The assay can also be tuned to provide a positive or negative response when the amount detected surpasses a defined threshold. In other sensors, the signal value is correlated to the concentration of the analyte detected in the sample. Some examples of such sensors are the glucose sensor, used diabetic patients, and the haemoglobin optical sensors.

The signal is correlated to the concentration of the analyte by the laws of kinetic which determine the equilibrium of the reaction between analyte (A) and ligand (L). An equilibrium constant is defined for each reaction by the ratio of the concentrations of the free forms and the complex

$$A + L \rightleftharpoons AL \tag{1.1}$$

$$K_D = \frac{[A][L]}{[AL]} \tag{1.2}$$

The fraction of bound ligand (f_a) is defined as a function of the analyte concentration is given by:

$$f_a = \frac{[A]}{K_D + [A]} \tag{1.3}$$

The plot is a rectangular hyperbola with asymptote at 1 (saturation). The K_D can be found at the concentration which produces f_a=0.5 Figure 1.4.a [262]. If the same function is plotted on a semi-logaritmic scale, the outputted curve is a sigmoidal curve. As the fraction of bound ligand is the one generating the signal, then the signal response is proportional to it, and thus to the bulk analyte concentration [263]. The proportionality factor depends on the transduction system chosen and on the presence/absence of a signal amplifier.

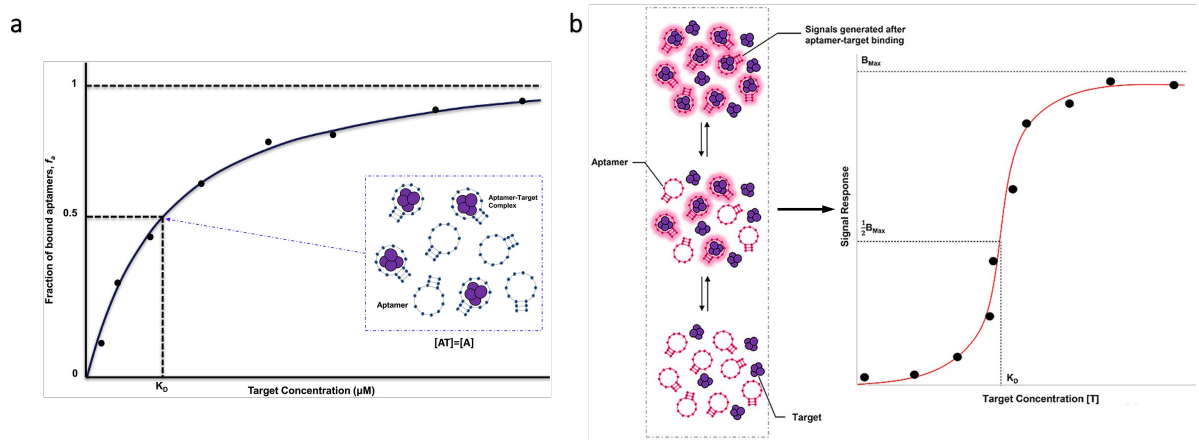

***Figure 1.4. Relationship between target concentration and sensor signal**. a) Plot of the bound ligand (fa_a) against the target concentration. Reprinted from Thevendran R., Navien T.N., Meng X., Wen K., Lin Q. , Shigdar S., Tang T-H, Citartan M. (2020). Mathematical approaches in estimating aptamer-target binding affinity. Analytical Biochemistry, 600, 113742, with permission from Elsevier ©(2022) [262]*

From these binding plots a lot of parameters can be extracted. The sensor sensitivity is the relationship between the signal variation (output) and the target concentration (input) that generated it. The latter can be further specified via the liner range, which is the concentration range for which the sensor response can be approximated to a line, and the limit of detection (LOD), which is the minimum concentration which causes a significant signal variation in the sensor and by convention is set at three times the standard deviation of the background signal, or the extrapolated y-intercept of the calibration working curve [263]. When designing a sensor for a specific applica-

tion, a lot of the effort is put into optimising the linear range around the biologically relevant analyte concentration and improving the signal-to-noise ratio to maximise the sensitivity

Other important parameters are the response time and the recovery time, which both determine the time resolution of measurements [203].

1.1.4 Continuous Monitoring Real-time Sensors: Challenges and Impacts.

Continuous monitoring sensors are a high interest application for both industry and academia. Given their promise to deliver *in situ*, sensitive, real-time detection in portable devices and at low costs, continuous monitoring biosensor have been envisioned as true game changers for a variety of fields. From biomarker and drug monitoring for health devices, to quality and safety for the food processing industries; from environmental safety with monitoring of water sources and toxin levels, to academic research to gather time resolved data [206, 76, 274, 173, 273, 269, 154, 68, 226].

However, despite the vast research and economic effort, continuous monitoring sensors have found limited application as some obstacles are still in the way. A design which supports reagentless detection is not sufficient to guarantee continuous monitoring. A sensor should not depend on exogenous reagents, it should resist fouling, be calibration-free, be able to correct the drift (change of sensitivity overtime) and have a sufficiently long lifetime in complex samples [30, 203].

One of the main obstacles, which affects all of the above mentioned characteristics is sensor fouling. Fouling is defined by the IUPAC Compendium of Chemical Terminology as the *"Process resulting in loss of performance"* of a sensor *"due to the deposition of suspended or dissolved substances on its external surfaces"* [165]. When performing measurements in complex samples, the fouling agents can bind the surface via multiple mechanisms *e.g.* adsorption, interaction, oxidation; but they produce similar outcomes: lowering the sensitivity and/or producing undesired signal. Biofouling is complex and still poorly understood. Past research has underlined a relationship with the physicochemical properties of the sensor interface, with the materials and

the topography employed. Therefore, a conscious design should be employed to minimise these contributions [203]. Additional resistance to fouling can be achieved with surface modifications. Many are the chemistries available and they have been summarised in Table 1.1 and multiple reviews (see [143, 268, 82, 29, 144, 158]). However, the explanations of an anti-fouling layer are not unanimous. This inconsistency in the results can be justified by the broad range of sensor designs and fouling agents studied.

The challenges above described are amongst the reasons why there still is a large disparity between the number of published designs and the number of commercially employed sensors for continuous monitoring. As pointed out by Ruckh and Clark [213] a lot of these designs fail their test in analytically complex samples, which indicates that more design effort needs to go into reducing fouling to allow a larger number of devices to reach commercialisation.

Table 1.1. *Summary table of surface chemistries available to reduce biofouling [143, 268, 82, 29, 144, 158]*

Antibiofuling chemistry	Pro	Cons
Polymer coatings		
poly(ethylene glycol) (PEG)	Gold Standard Hydration layer Steric hindrance repulsion	Oxidative damage Poor water solubility Low Protein resistance to temperature variations High impedance layer
pH-sensitive	Resistant to denaturing Good long-term stability ($\geq$ 6 hour)	Poor time resolution ($\geq$2 h)
pH-sensitive polymer coating	Resistant to denaturing Good long-term stability ($\geq$ 6 hour)	Poor time resolution ($\geq$2 h)
Thiolated monolyars		
- MCH	Simple Length dependent	Poor stability (storage) Low resistance Low electron transfer Non reproducible
- Ternary	Multiple chemistries Higher signal-to-noise ratio (up to 100x) Higher resistance Improved storage stability	Low water solubility
- Thioaromatic	Structural stiffnes High electrical conductivity (π) Packing efficiency	Hydrophobicity
Protein-based additives (BSA, HSA, etc)	Blocks defects 2 h resistance in whole blood	40 % signal reduction Need for engineered version (congenital diseases)
Cell membrane-mimicking - phosphatidylcholine (PC)-terminated monolayers	Hydration layer Long Lifetime ($\geq$ 12 h in whole blood) Improved signal gain Reduced drift	

Table 1.1 Continued

Antibiofuling chemistry	Pro	Cons
Hydrogels	Biocompatible Water swelling Variety of chemistries known Electroconductive options	Not compatible with structure switching designs
Peptide & Zwiterrionic		
Peptides	Biocompatible Tunable charges Simple structure and synthesis	Complex immobilisation chemistries
Zwitterionic	Strong hydration layer Less prone to oxidative damage Low immunogenicity	Complex immobilisation chemistries Low reproducibility of film formation
Peptoids	Biocompatible Tunable charge Backbone Chemistry	Further characterisation needed
Polysaccharide-based Materials	Hydrophillic	

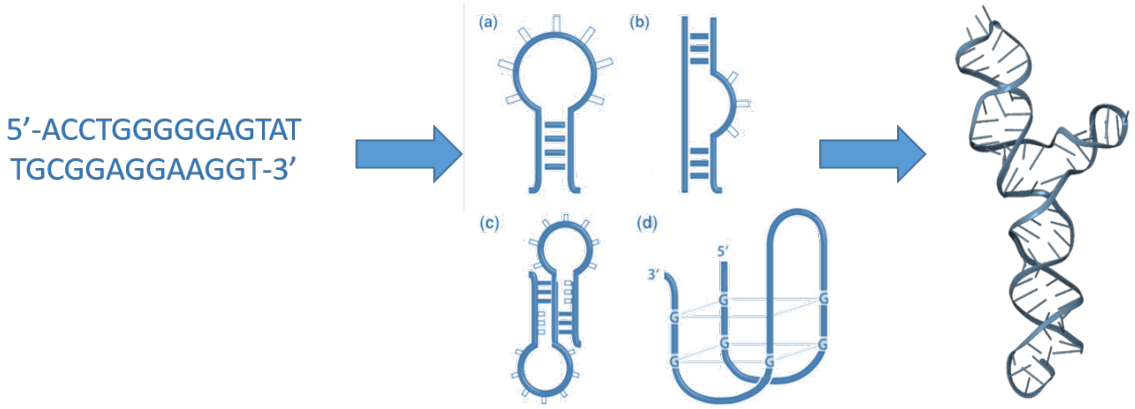

Figure 1.5. Linear (left), two-dimensional (centre) and full folding of an aptamer (right). *The central panel illustrates some of the possible secondary structures assumed by an aptamer: stem loop (a), K-turn (b), pseudo-knot (c) and G-quadruplex (d). Adapted with permission from Springer, Berlin, Heidelberg: Aptamer-Modified Nanoparticles as Biosensors by by Lönne M., Zhu G., Stahl F., Walter JG. In: Gu M., Kim HS. (eds) Biosensors Based on Aptamers and Enzymes ©(2013). Available at* `https://doi.org/10.1007/10_2013_231`.

1.2 Aptamers

Aptamers are single stranded DNA or RNA sequences, between fifteen and eighty bases, capable of selectively binding a target molecule with high affinity. Aptamers were isolated for the first time via systematic evolution of ligands by exponential enrichment (SELEX) protocols simultaneously by Ellington and Szostak [58] and Tuerk and Gold [266].

Aptamer binding and selectivity originate from the Watson-Crick interactions, which generate a three-dimensional disposition of hydrogen bonds, electrostatic interactions, π-πinteractions and Van der Waals interactions. These forces form a binding pocket for the target molecule (Figure 1.5, centre) [244]. However, in some cases the nucleic acid strand remains unfolded and it is the interaction with the ligand that triggers the aptamer to fold into its final, active structure [90, 223].

Since the first isolation, aptamers have been the topic of more than six thousand publications, with more than one-third of the papers published in the last three years. The designs find application mainly in the fields of diagnostics, imaging and drug delivery, developed by both academic and industrial interests [305, 139, 137, 233]. Up to today, aptamers have been designed to detect more than 200 organic and inorganic targets, which includes analytes as small as metal ions, organic dyes and amino acids,

molecules like drugs and antibiotics, up to cells and viruses [78].

1.2.1 Comparing Aptamers with other biorecognition molecules.

Enzymes were the first biomolecules to be integrated onto biosensing surfaces. They are the go to technology for catalytic sensors as they provide high target affinity and specificity, developed through evolution. Antibodies, are the current golden standard biorecognition element for affinity assays. Their pico- to nano-molar affinities, together with their standardised evaluation protocol and agency approval for a variety of applications, makes them the most viable option in terms of commercialisation as well. Nanobodies are antibody-fragments composed of a single domain that binds the antigen molecule. Given their smalll dimension (ca. 4 nm), they are easier to synthesise, with respect to the full antibody and some studies have shown improvement in affinities via *in vitro* maturation[15].

Both enzymes and antibodies have limitations. For enzymes, those commercially available can present batch differences in terms of kinetic properties, whilst for the others, in house isolation is necessary and the process can be long and complex, and further evaluation of the activity is required. Additionally, a few hundreds of naturally occurring enzymes exist, but many are the molecules which lack an associated redox-active enzyme. Some research has been done into engineering the binding pocket of existing enzymes into binding a different target and into the production of *de novo* enzymes. However, the effort has so far produced limited results [73, 124, 204]. Finally, enzymes can require co-factors to work, which introduces a design challenge: when integrated in a sensor, the co-factor concentration needs to be sufficient to maintain the enzyme active.

The most limiting factor in the employement of antibodies is the trasduction of the binding event between antibody and target in a design that allows for continuous monitoring. A few attempts to employ antibodies with electrochemical platforms have been made by the Plaxco and the Ricci groups, by mounting the antibody on a dsDNA, and relying on the latter to transduce the binding event [33, 190, 102]. Additionally, Antibodies can only be raised against targets which produce a strong immunogenicity,

whilst for molecules with low immunogenicity or even toxins, the process can become quite laborious and expensive, especially if the intended antigens are poorly soluble and tend to aggregate. Additionally, the impossibility to alter their affinity, often poor affinity to small molecules and the possibility of cross-talk limits their application [97].

Both antibodies and enzymes are protein and as such they can irreversibly denature if stored incorrectly or if exposed to temperature or pH variations. This is a limiting feature when incorporated on a sensor as it affects its storage capability. The matter is worsened by the short shelf life-time: months for enzymes and antibodies vs. years for aptamers [178]. Integration onto a sensing platform poses an additional challenge, as immobilisation on the surface via chemical modification can result in a improper folding of the protein or loss of activity. Also absorption can be a problematic technique, as the receptors could assume incorrect orientations, thus precluding the analyte from accessing the binding site, or the adsorption itself may cause the protein to denature, even partially, and cause loss of activity [21, 202]. A final drawback is their relatively large size, when compared to aptamers or nanobodies (Figure 1.6), which limits the number that can be bound to the surface, offering a limited dynamic range for the sensor.

Nanobodies, like antibodies, are proteins thus they present similar drawbacks: sensitivity to pH and temperature shifts, active only in physiological conditions [49]. Compared to aptamers however, their synthesis and chemical modifications are still challenging.

Aptamers posses some advantages over the above described biorecognition elements. Given their smaller size they have been widely employed to detect small molecules. The comparable size between aptamer and ligand is an important parameter in affinity sensors, as it improves the ligand specificity and results in a higher signal variation upon binding. Through SELEX, high affinity aptamers for a variety of target molecules has been produced. Once selected, aptamers synthesis is also done *in vitro*, which guarantees higher batch uniformity, maintains low costs and renders introducing modifications easy. Many chemistries and protocols have been developed to improve aptamer resistance in complex environments, to introduce structural properties, tune the affinity window and to label or immobilise the aptamer. Improving aptamer

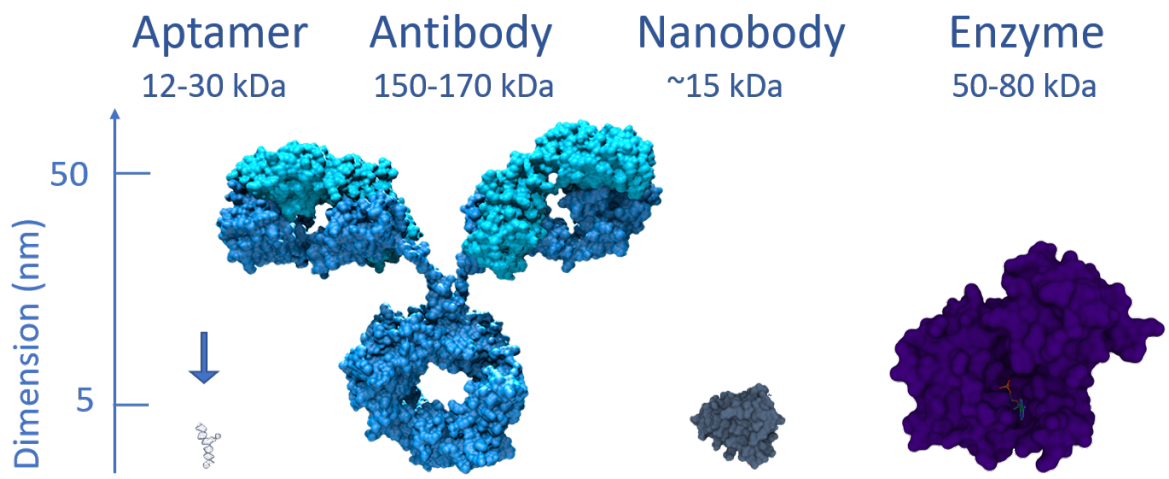

Figure 1.6. Size comparison between aptamers, antibodies, nanobodies and enzymes. *The mass of each category in kilo Dalton (kDa) is shown under each category. PDB ID: 4S11 (nanobody) 3UQ6 (enzyme). Image created using Mol* [229, 230]*

stability to prevent degradation by nucleases achieved, among others, by chemical modification of the 2'-site of the sugar ring or by substitution of the 4'-oxygen with a sulfur, by modification of the phosphodiester bond or by replacing the phosphate-sugar backbone entirely, *e.g* peptide nucleic acid (PNA) [120, 159, 182]. Mutagenesis is often employed to induce or increase the stability of a structure, which results in higher affinity of the aptamer, as seen in the work by Biniuri, Albada, and Willner [17]. An improvement in affinity can also been obtained by truncation: by removing the unnecessary bases, other folded structure are eliminated and the equilibrium is pushed toward the one that binds to the target [70]. Further tuning can be obtained through *in silico* sequence recombination, but extensive knowledge on the aptamer structure and its binding pocket are necessary [85]. Aptamer immobilisation can be obtained by a variety of methods and chemistries: physical adsorption and chemisorption, covalent bonding, hybridisation and affinity coupling. Dependent on the requirement of the assay one Finally, aptamers are more robust as they can fully recover their functionality after denaturation, once brought back to their working conditions (pH or temperature), which guarantees good storage stability.

1.2.2 Adenosine and ATP aptamer

The adenosine and ATP aptamer was first identified by Huizenga in 1995 (Figure 1.7)[95]. The aptamer is a single-stranded DNA sequence 27 bases long and has proven affinity to adenosine, ATP and AMP in the 1-10 µM range. The similar affinities for the molecule, lead Huizenga *et al.* to believe that the aptamer interacted with the adenosine and that the phosphate group/s do not play a part in the interaction. The structure hypothesised by Huizenga contained only one binding site: a stacked G-quartet. However, a later study Lin and Patel [141], in which the aptamer structure bound to AMP was resolved via NMR, proved that the aptamer presented two binding pockets formed by a double-stacked G-quadruplex (Figure 1.7).

Zhang, Oni, and Liu [307] performed a study on the cooperativity of the two binding sites using isothermal tritation calorimetry (ITC). The wild type, containing two binding sites, and the mutated versions, with one or three binding sites, presented low/no cooperativity between the binding sites. According to the work by Ortega et al. [184], cooperativity between binding sites, especially when strong, can reduce the affinity of the aptamer, which becomes less sensitive at low target concentration. On the other hand, in absence of cooperativity, that the affinity of the aptamer is not determined by the number of binding sites, which explains the relatively small improvement obtained by the authors after removing one binding site.

Zhang and Liu [306] went on to study the effect of the double-stranded portion of the aptamer. By truncating one or more base pairs (1-27 to 4-24), they verified which nucleotides where necessary for the binding and studied the effects of a shorter stem on the aptamer affinity. The results show that removing more than three base pairs from the stem, resulted in a significant reduction in binding affinity (from 7 µM to $>$ 250 µM). However, no difference in affinity was found between the version with 3 to 8 base pairs long stem.

Xie, Eriksson, and Zhang [295] applied molecular dynamics to verify the hypothesis previously made on the binding dynamics of the aptamer. Their results confirmed that the aptamer is already in its final folding state in absence of the analyte. From the simulation emerges that the binding nature of the two binding sites

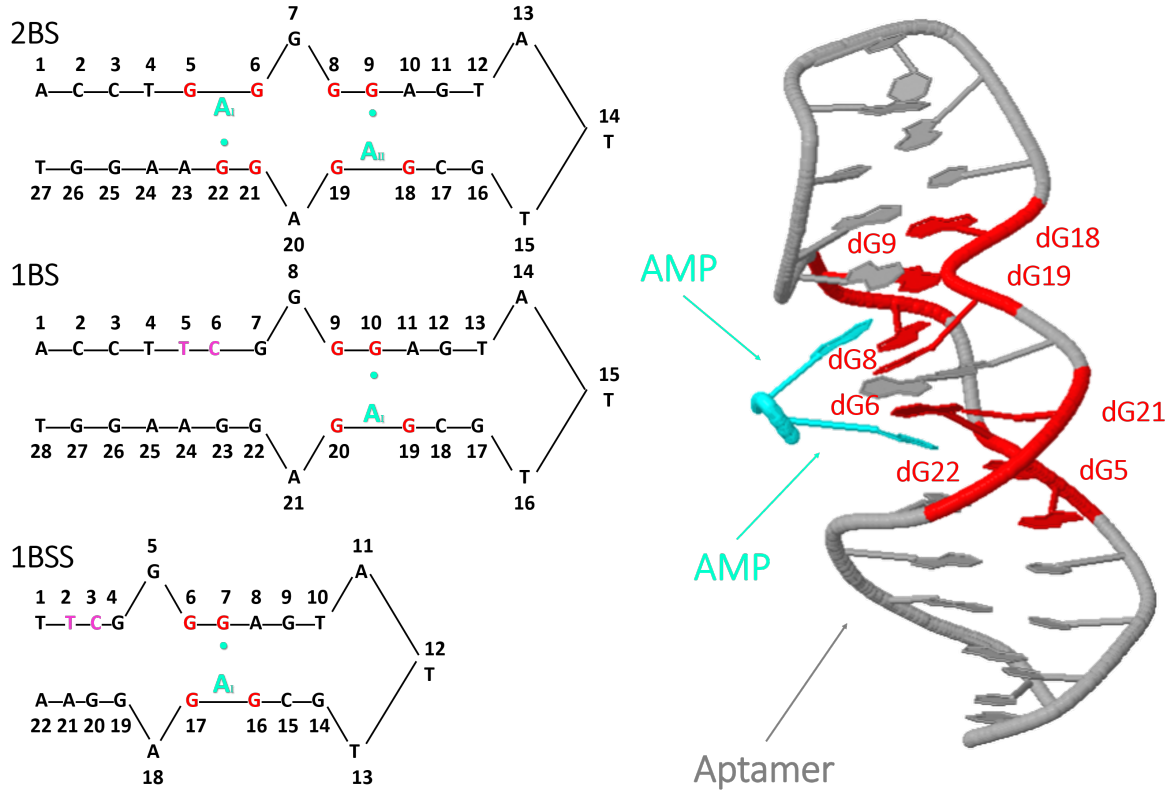

Figure 1.7. Secondary structure of the ATP/adenosine biding aptamers (left) and crystal structure of the Huizenga aptamer (right). *The target molecules are represented in cyan, the guanosine bases taking part to the G-quadruplex are highlighted in red, whilst the modified nucleotide to close the first binding site are highlighted in magenta. Left panel: secondary structures of the original aptamer by Huizenga (2BS, top [95]), and the engineered versions with one binding site (1BS, middle [307]) and one binding site with shorter stem (1BSS, bottom [306]). Right panel: crystal structure of the 2BS aptamer with detail of the two target molecules (cyan). Secondary structure adapted from [307] with permission. 3D structure from Lin and Patel [141], available at DOI: 10.2210/pdb1AW4/pdb. PDB ID: IAW4*

are different: whilst the interaction between G22 and adenine in the target molecule is driven by hydrogen bonding and catalysed by surrounding water molecules, the second binding site, containing G6 and A23, is based π-πinteraction stacking between these bases and the adenine.

1.2.3 Aptamer Isolation via SELEX

Despite some non-SELEX isolation methods being published [14], SELEX remains the main technique for the isolation of new aptamers. The process starts with a pool of 10^{15} random nucleic acid (NA) sequences and through consecutive incubation and amplification rounds, the pool evolves favouring high affinity sequences. The NA library design usually consists of a random region flanked by the primer sites on each side, used for the PCR amplification. The random region length should be a trade-off between structural complexity and coverage of the sequence space. Little research has been done to figure out the correlation between random region length and resulting affinity, namely the study by Legiewicz et al. [133], not even mathematical studies have focused on it [270, 134, 232]. McKeague et al. [162] overview more than 400 aptamer selections and found no correlation between random region length and dissociation constant (K_D) of the selected aptamer.

The SELEX process consists in mainly of: affinity incubation, partition, elution and amplification and they are represented in Figure 1.8. In the affinity incubation step, the library is incubated with the target molecule at a specific concentration and for a determined incubation time. The concentration and incubation time is reduced through the cycles, making the binding conditions more stringent to promote the enrichment of the strands that present higher affinities. Once the aptamer-target complexes have formed, the NA strands that interacted need to be separated from the rest of the library - partition step. Depending on the type of SELEX employed, this step is performed in a variety of ways: elution, magnetic beads separation etc. Mathematical modelling studies of SELEX have shown that partition is the most critical step in the SELEX process as it determines whether the library will produce some valid candidates [270, 281]. If the binding candidates are not efficiently separated from the

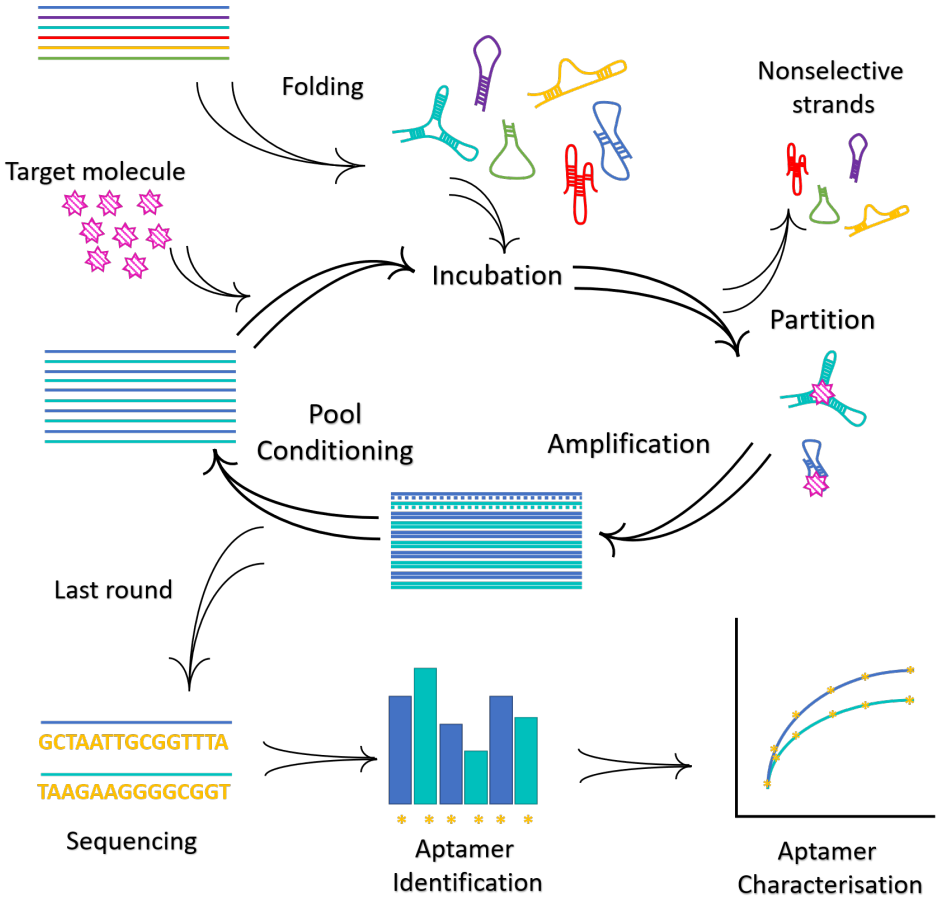

Figure 1.8. The SELEX process. *Image adapted from from Komarova and Kuznetsov [119].*

non-binding library, the latter will be amplified as well. This can prevent the library convergence, thus failing to produce some strong binding candidates.

The binding candidates are then amplified via PCR and then the pool conditioned in order to produce the new single stranded DNA [155], or RNA library and start the next round. In this pool the binding sequences compose a larger portion of the library. Usually 10-15 cycles of SELEX are necessary to achieve pool enrichment. Then the pool is sequenced and the candidates isolated and their binding affinity and selectivity characterised. To improve the enrichment and eliminate cross binders negative selection rounds can be performed to remove strands that could bind a second target molecule present in the sample.

Ever since the first aptamer isolation, many variation of the original SELEX protocol have been published to provide a suitable approach to select aptamers for all applications. A review of the different SELEX procedures was published by Kong and

Byun [120], Ozer, Pagano, and Lis [186], Zhuo et al. [309] and more recently by Yan et al. [297]. The latest methods developed were mainly focused on the automation of the selection process [292] and integration of high/throughput sequencing, to better control the evolution process [118]. There are reviews on the impact of the multiple parameters on the selection process based on mathematical modelling of the SELEX process [270, 134, 232, 281, 245] and by comparison of the aptamer selections [162, 275, 119].

Isolating Structure-switching Aptamers via Capture-SELEX

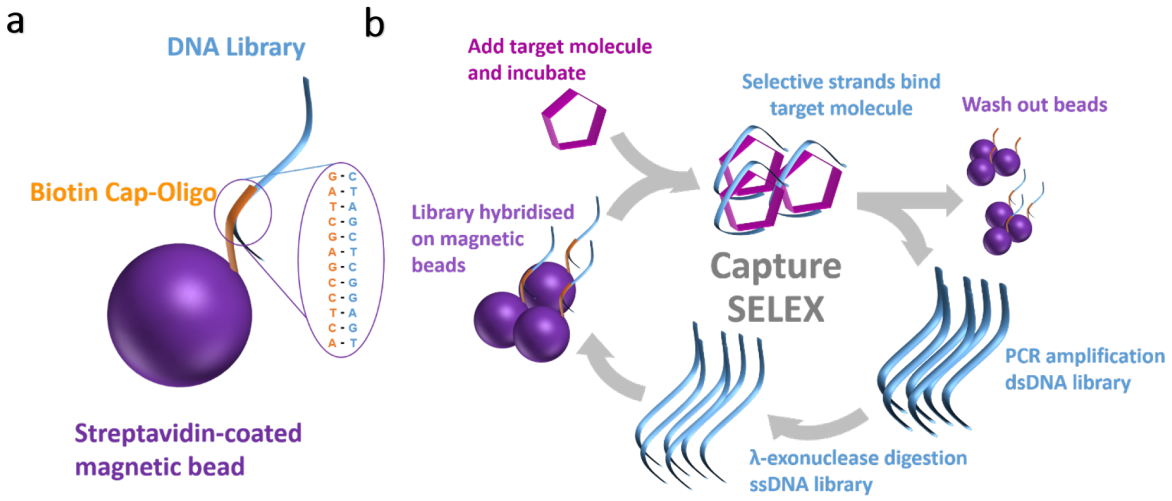

Figure 1.9. The Capture-SELEX work flow. *a) Schematic of the immobilisation of the DNA library on the beads. The streptavidin-coated magnetic beads (purple) are functionalised with biotin-tagged DNA strands, the capture oligo (orange). The DNA library (blue) hybridises onto the beads thanks to the 12 bases-complementary sequence. b) Schematic representation of Capture-SELEX protocol for each cycle. As for traditional SELEX, the protocol starts with a randomised library. The Capture-SELEX library presents an additional known sequence in the middle of the randomised region, and complementary to the cap-Oligo one, which anchors the library (blue strand) to beads. Upon addition of the target molecule (magenta pentagon) and after an incubation time, the strands that interact with the target will detach from the beads, perhaps undergoing a conformational change as they bind to the target molecule. After collecting these released strands from the beads, the selective library is amplified via PCR reaction and returned to single stranded DNA by means of λ-exonuclease digestion, where nuclease binds the negative strand thanks to the phosphate functionalisation of the reverse primer. The sub-library is ready to be re-complexed with the beads and for another Capture-SELEX round.*

The conventional SELEX protocol is designed to work with analytes immobilised on a surface and the DNA library free in solution. Having to immobilise the

target is a limiting requirement for the technique: some binding sites may be prevented from interacting with the oligonucleotides, and small-molecule targets cannot be easily anchored to a surface without changing their characteristics. To improve matters, Stoltenburg, Nikolaus, and Strehlitz [250] developed Capture-SELEX. As shown in Figure 1.9, Capture-SELEX immobilises the DNA library on magnetic beads leaving the target molecule free in solution. The library presents an anchoring sequence, placed inside the random region, which hybridises with its complementary strand, capture oligo (Cap-Oligo), attached to the beads via biotin-streptavidin interaction (Figure 1.9.a). The library immobilised on the beads is then incubated with the analyte, and only the strands binding the analytes will come off of the beads. The release of the library from the beads is promoted by the conformational change underwent by the aptamer upon binding the target molecule, which ensures the structure switching capability of the sequence. The strands that were not released from the beads are washed out with the beads, whilst the eluted aptamers are amplified and regenerated into single-stranded DNA to make up the pool for the successive round (Figure 1.9.b). Lyu, Khan, and Wang [150] described in detail the Capture-SELEX protocol, the variations developed over time and reviewed the aptamers selected via Capture-SELEX for both food safety and environmental monitoring.

1.2.4 Aptamer Characterisation techniques

Aptamer selection does not end with the sequencing of the library of the final round, as it can be heterogeneous and still return a large number of candidates, which need to be evaluated. Multiple techniques are available and each technique has its own characteristics in terms of sensitivity, sample volume, assay running time and costs (Figure 1.10) [258, 163]. Nevertheless, not all techniques are suitable for characterising aptamers against small molecules. Many techniques can not be employed due to technical limitations, *e.g.* the impossibility to separate the aptamer from a much smaller molecule via size excluding membrane; impossibility to label or immobilise the target molecule or the lack of significant signal generated by the small molecule in mass sensitive techniques to name a few. A review of the available techniques and their em-

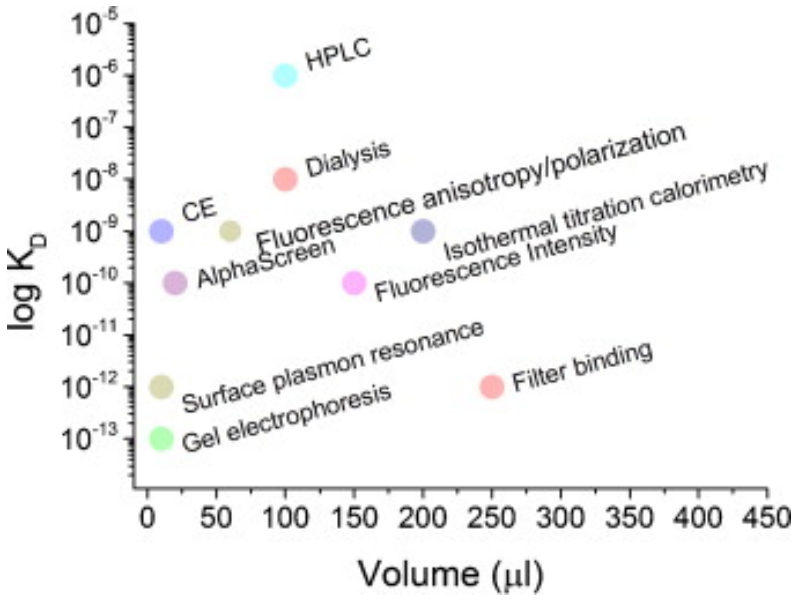

Figure 1.10. Comparison of the different characterisation techniques in terms of sensitivity achievable and amount of sample necessary to run the assay. *CE stands for capillary electrophoresis. Reprinted from Szeitner, Z., András, J., Gyurcsányi, R. and Mészáros, T., 2014. Is less more? Lessons from aptamer selection strategies. Journal of Pharmaceutical and Biomedical Analysis, 101, pp.58-65., with permission from Elsevier ©(2021)*

ployability for small molecule aptamer characterisation was published by McKeague and DeRosa [161].

The requirements of the employed technique also change through the phases of aptamer characterisation. In the first stages with a high number of candidates, the technique needs to be cost-effective and high-throughput. In the later stages, when the candidate number is low and the K_D is evaluated, the technique has to provide more quantitative and precise information on the aptamer-target interaction with the oligonucleotide both in solution and immobilised on a surface [163].

A thorough characterisation process in necessary to evaluate the K_D of the same aptamer on multiple assays. The final value obtained might differ dependently on the technique employed; whether it requires for the aptamer or the target to be labelled, whether the length of the oligonucleotide influences the outcome. Therefore, by testing the aptamer affinities in multiple assays with different set up it is possible to achieve an complete knowledge of the kinetic properties of the oligonucleotide.

SYBRgreen Assay

The SYBRGreen assay is a fluorescence technique for the characterisation of the aptamer-target interaction in solution. It employs SYBRGreen I (SG), a nucleic acid stain which intercalates double stranded DNA. SG interaction with DNA is multifaceted as it intercalates base-pairs, establishes both coulombic and macromolecular interaction with the grooves [51].

The DNA/SG complex excitation and emission peak are placed at 497 nM and 520 nM,in the blue and green light portion of the spectrum, respectively .The dye fluorescence is quenched in its free state but displays a 1000-fold enhancement when complexed with the oligonucleotide [51]. This property is exploited in the SG assay. As illustrated in Figure 1.11, by incubating the aptamer and the SG dye, the complex formed by the two will produce a strong fluorescence signal (panel b, blue). Adding the target molecule to the solution will dislodge some of the SG molecules if the aptamer is selective. The now free SG molecules are quenched, which results in a smaller fluorescence peak (panel b, magenta) [164].

The SG assay can sensitively detect DNA-target interactions in solution and without the need for any labelling or surface immobilisation. The employment of a fluorescence plate reader, a commonly available tool, renders the technique high throughput and quantitative. With the correct design, the assay can also provide structural information to help reduce the target to its minimum binding sequence. Overall, the technique is inexpensive, easy to optimise, high throughput and does not require specific equipment, and thus is an ideal candidate for the first stages of aptamer screening and characterisation.

Microscale Thermophoresis

Microscale thermophoresis is novel technique in which the interaction between aptamer and binding molecule is detected by measuring the change in the migration properties of the labelled ligand and ligand/target complex down a localised temperature gradient. The migration properties of a molecule depend on the hydration shell, charge and dimension. Binding to a target changes at least one these properties *e.g.*

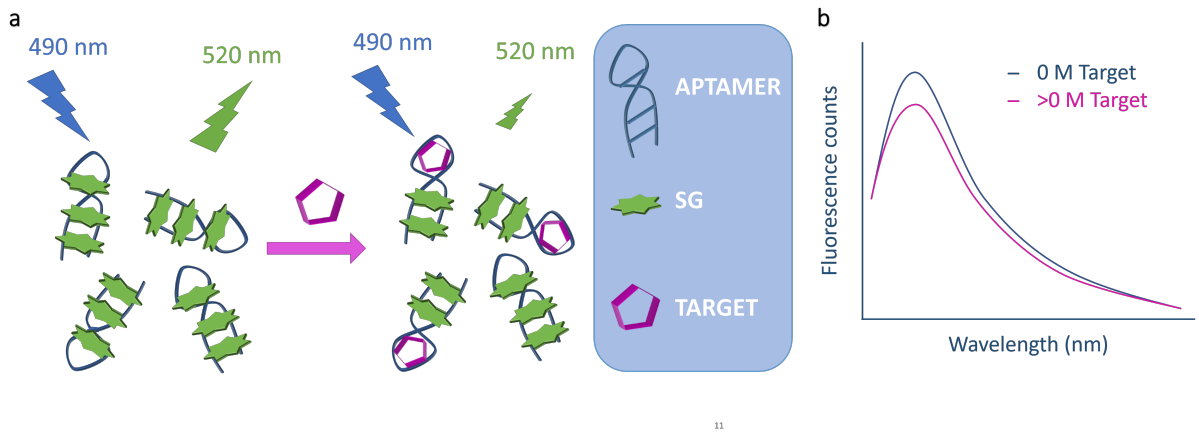

Figure 1.11. SYBRGreen assay working principle (a) and output curves (b). *Adapted from McKeague et al. [164]*

in the case of an aptamer, binding with the target molecule can reduce the number of uncoupled base pairs, which in turn increases the size of the aptamer hydration shell. Consequently, the ligand-target complex presents a different migration profile with respect to the ligand alone [54, 207].

In the assay, ligand (fluorescent-labelled) and target are mixed together and placed in capillaries. For each, an MST trace is recorded by scanning the capillary along the transverse direction (Figure 1.12.a), thus only the fluorescence in a single spot of the capillary is recorded. Two lasers are employed: an infra-red (IR) laser, to generate the heat spot, and a LED laser, to record the fluorescence signal and of wavelength matching the one of the fluorophore employed. The measurement starts in ”cold” conditions (IR laser off) for the first 5 s , then the IR laser is turned on for 30 s, to generate the temperature gradient, and then off again. The fluorescent signal is recorded throughout the stages (Figure 1.12.B). The IR laser generates a localised heat spot. The fluorescent-labelled molecules start migrating down the temperature gradient, thus generating changes in the localised fluorescence intensity. The plot of the localised fluorescence intensity over-time is the migration profile. The migration profiles of the ligand and the target-ligand complex will differ and by extracting the normalised fluorescence value, the binding event can be verified (Figure 1.12.c).

MST is a highly sensitive technique that provides quantitative information on the ligand-target interactions and can be used to determine K_D and structural infor-

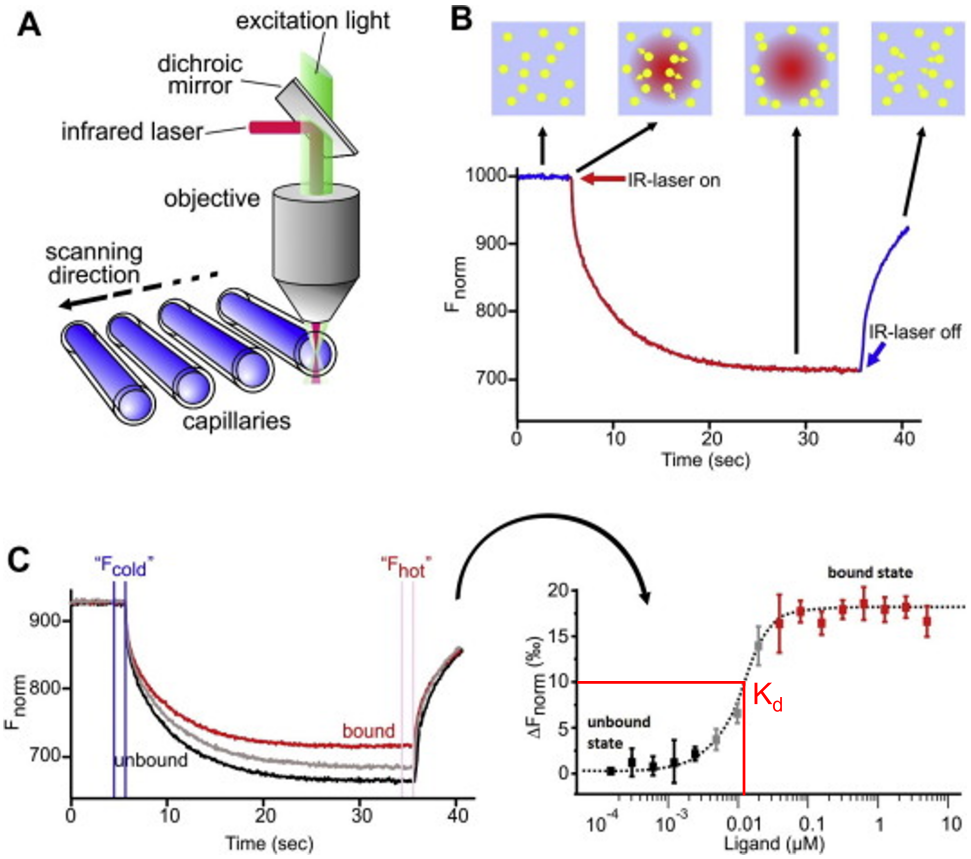

Figure 1.12. MicroScale Thermophoresis (MST). *A) Technical setup of the MST, with the optics recording at the centre of the capillary. B) MST time trace. Correlation between the fluorescence signal recorded (bottom) and the fluorophore distribution before, during and after the IR laser pulse (top). C) Illustration of exemplary experimental results assessing the binding affinity of a ligand with its target over a concentration range. In the left panel the MST traces are superimposed to each other with the traces of the unbound and complex state being significantly different. The right panel illustrated the normalised fluorescence value measured for each trace plotted against the target concentration. A fitting algorithm is then used to determine the binding affinity parameters. Reprinted from Entzian, C. and Schubert, T., 2016. Studying small molecule–aptamer interactions using MicroScale Thermophoresis (MST). Methods, 97, pp.27-34., with permission from Elsevier ©(2021)*

mation. The K_D can be obtained by recording the migration profile for a concentration range of the target molecule, mixed with a constant concentration of the ligand. The fluorescence value can be extracted and plotted against the target concentration. The points are then fitted and the binding curve with its K_D are determined. Structural information, on the other hand, can be obtained by testing different version of the aptamers in which specific sequences have been removed. By evaluating the loss/gain in signal variation, the role of the specific sequence can be determined.

In the assay, both elements are free in solution, but the labelling requirement is a limitation, especially for small molecules, where modifications can significantly affect its chemical properties. For aptamer-target screening with small molecules target, a possible solution is to label the aptamer instead of the target. However, given the large aptamer/target size ratio in initial stages of the aptamer maturation, the change in the migration profile caused by the binding event is smaller, thus reducing the assay sensitivity. A study from Reineck, Wienken, and Braun [207] found that the ratio the diffusion coefficient between the bound and unbound state is linearly dependent to ca. the cube root of the oligonucleotide length. Despite that, the technique has successfully been employed to characterise the small molecule-aptamer interaction for the thrombin aptamer [9, 22] and characterise and gather structural information on the ATP aptamer [9, 59]

1.3 Electrochemistry

The electron transfer reactions taking place at the electrode-electrolyte interface follow the laws of electrochemistry and are described by the reaction

$$Ox + ne^- \rightleftharpoons Re. \tag{1.4}$$

where Ox and Re are the oxidised and reduced species, respectively. The electrode-electrolyte interface presents a net neutral double layer, composed of two charged phases. On the solution side, the double layer is followed by a depletion area called diffusion layer, where the concentration gradients of reactants and products are present

(Figure 1.13, light blue line for the reactant, and navy for the product). Further away from the interface, is the solution bulk, where the solution is homogeneous. Likewise, the electrode bulk is homogeneous and the surface is charged, positively or negatively, dependent on the material employed. The electron transfer between the two phases is driven by the potential applied to the electrode and therefore it is considered an heterogeneous process [63]. One example of an heterogeneous electron transfer between surface and electrolyte is illustrated in Figure 1.14, using ferrocene as redox couple. The electrode can reduce the ferrocenium (Fc^+) molecule when its Fermi level, energy of the excess charges, is higher than the standard potential (E_0) of the Fc^+ molecule, which is the energy of its highest occupied molecular orbital (HOMO) (Figure 1.14, left).

By applying a potential the Fermi level can be raised until it exceeds the value of E_0 (Figure 1.14, centre). At this point the electrons at the Fermi level posses higher energy than E_0 and the Fc_+ molecule is reduced Figure 1.14 into ferrocene (Fc), right). The reverse process, oxidation, is obtained by changing the sign of the applied potential [57].

When the redox couple is formed by an electrode surface and a surface-confined redox reporter, the dynamics of the reaction change, dependent on the characteristics of the molecules anchored on the sensor surface. A conductive layer, for example a polythiophene coating, can reduce the potential necessary to drive the redox reaction. The opposite effect is achieved by coating the surface with an insulating layer, such as alkanethiol mat. This difference is exploited by many electrochemical techniques to characterise the properties of the functionalised surface and study its functionalisation [37, 52, 45, 177].

1.3.1 Cyclic Voltammetry (CV)

Cyclic voltammetry is a simple and yet powerful electrochemical technique employed for the characterisation of surface functionalisation and dynamics.

In a cyclic voltammetry scan a potential triangular wave is applied for each cycle (Figure 1.15, left). The ramp starts at E_0 and ends at E_1 and then returns to E_0. For each

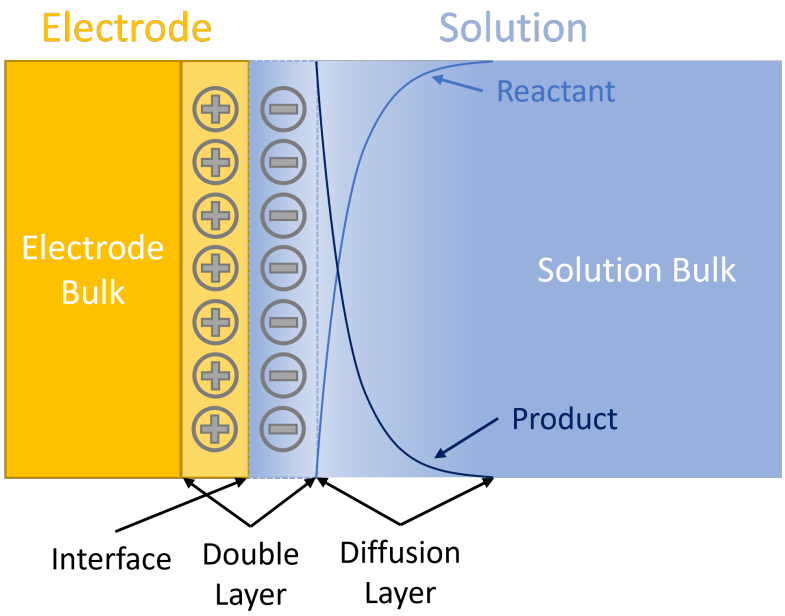

Figure 1.13. Structure of the electrode/electrolyte interface. *Adapted from Faulkner [63] (https://doi.org/10.1021/ed060p262)*

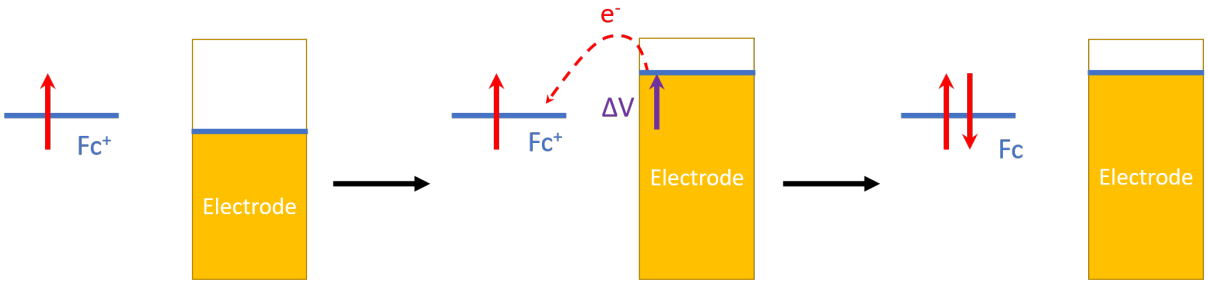

Figure 1.14. Heterogeneous electron transfer between a redox active molecule e.g ferrocene/ferrocenium (Fc/Fc^+) and the electrode surface. *If the surface potential is not sufficient to reduce the Fc^+ molecule (left), by controlling the Fermi level of the electrode potential with the potentiostat, it is possible to increase the potential at the electrode surface (centre) and reduce the Fc^+ molecule (right). The same process can be reversed by inverting the sign of the applied potential. Adapted from Elgrishi et al. [57], (https://doi.org/10.1021/acs.jchemed.7b00361), with permission from ACS*

ramp the redox couple undergoes once either oxidation or reaction. The right panel of Figure 1.15 illustrates the resulting curve from a CV scan of a reversible redox couple, recorded on macroelectrode. The shape of the curve is determined by the equilibrium between the oxidised and the reduced species, described by the Nernst equation

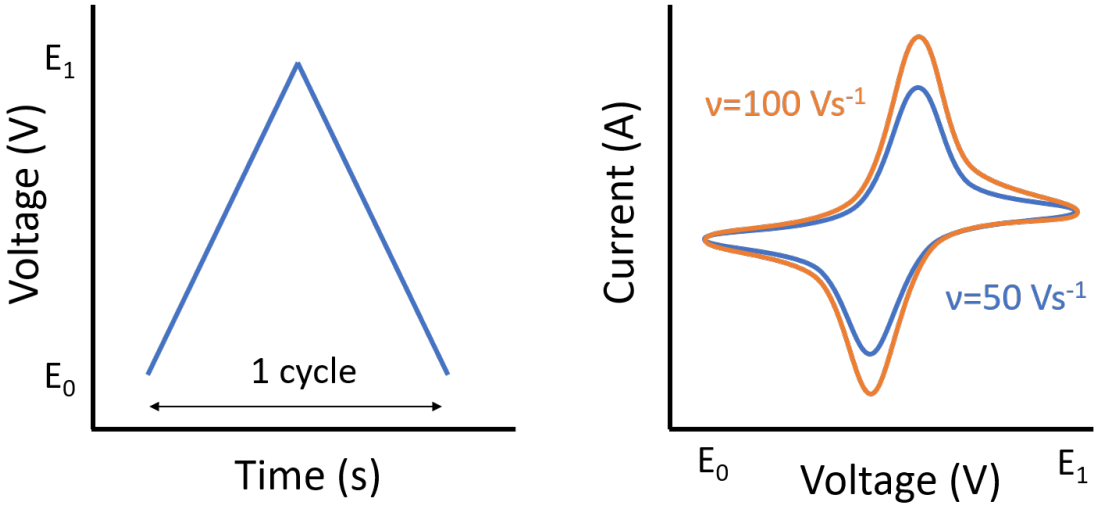

Figure 1.15. Potential applied, parameters and output curves of square wave voltammetry

$$E = E^0 - \frac{RT}{nF} \ln [Q] = E^0 - 2.303 \frac{RT}{nF} \log [Q] \tag{1.5}$$

where E is the potential of the cell, E^0 the standard potential of the redox couple, R the gas constant, T the temperature, n the number of electrons exchanged in the transfer, F the Faraday constant, and Q the ratio between the products and the reactants of the reaction studied [227].

The Nernst equation is also affected by pH variations. The equation for hydrogen evolution reaction

$$2H^+ + 2e^- = 2H^+ + 2e^- H_2 \qquad E^0 = 0V \tag{1.6}$$

The Nernst equation for this reaction at 25 °C and 1 atm :

$$\begin{aligned} E_{H^+/H_2} &= E^o_{H^+/H_2} - \frac{RT}{nF} \ln \left[H^+\right]^2 \\ &= 0 - 2.303 \frac{RT}{nF} \times 2 \log \left[H^+\right] \\ &= -0.059 \times pH \end{aligned} \tag{1.7}$$

thus the Nernst slope would be of -59 mV per pH unit [227].

The size of the current is linearly dependent on the square root of scan rate (ν

Figure 1.15) as described by the Randal-Sevcik for a reversible electron transfer:

$$i_p = 0.446\, n\, F\, A\, C^0 \left(\frac{n\, F\, \nu\, D_0}{R\, T}\right)^{1/2} \tag{1.8}$$

where i_p is the peak current, A the area of the active surface, C^0 is the bulk concentration of the analyte, D_0 is the diffusion coefficient of the oxidised analyte, for a reduction reaction.

If the analyte is adsorbed on the surface, Equation 1.8 becomes

$$i_p = \frac{n^2\, F^2}{4\, R\, T}\, \nu\, A\Gamma^* \tag{1.9}$$

where Γ^* the surface density of the adsorbed analyte. From the equation, two main differences can be extrapolated, first the diffusion constant does not play a role, second the peak current is now linearly dependent on the scan rate and no longer to its square [57].

1.3.2 Square Wave Voltammetry (SWV)

SWV voltammetry is an powerful electrochemical technique that allows to repetitively and quickly interrogate the sensor with high sensitivity.

In SWV the potential applied to the electrode is the superimposition of staircase with a square wave potential. The imposition of equally sized pulses for each voltage step (cathodic and anodic half-cycles) produces two currents, the forward and the reverse current. Both currents are sampled at the second half of each cycle to minimise the contribution of the double layer charging current (I_C). In fact, I_C decays following an exponential behaviour, $\propto e^{-t/RC}$, whilst the Faradaic current I_F is proportional to $t^{-1/2}$, thus the former decays much more rapidly and can be considered negligible. The difference of the forward and reverse currents is a final current with a higher signal-to-noise ratio and reduced drift contribution, as the latter affects both forward and reverse current equally [205].

The height of the final current peak depends on both the amplitude and the frequency used to record the voltammogram as explained in the models by Mirčeski

and Lovrić [46].

1.4 Hippocampus and Hypoxia

1.4.1 Hippocampus: structure and neuronal network

All the physiological measurements in this work were performed in the hippocampus. The hippocampus is the brain region encompassed in the hippocampal formation and it sits below the temporal lobe of the brain. The hippocampal formation contains the hippocampus, the dentate gyrus (DG) and the para-hippocampal gyrus (Figure 1.16). The latter can be subdivided into enthorinal cortex (EC) and subiculum (Sb).

The hippocampus is mainly known for playing a role in memory formation and retrieval, but it carries out also other functions [172]. The hippocampus can be described as a C shaped structure which has been subdivided in 3 regions (CA1-CA3).

A simplified version of the wiring of the different parts of the hippocampal formation is illustrated in detail in Figure 1.16. The input information reaches the hippocampus in a monodirectional network that starts in the EC. The perforant pathway (PP), which originates in the EC, projects the input into the dentate gyrus (DG). The mossy fibre (MF) travel from the DG and project into neurons in CA3 region. The neurons of the CA3 and CA1 regions are connected via the axon of the Schaffer collateral pathway (SC). To close the loop, CA1 neurons project into the subiculum, the main output of the hippocampal formation, which connects the hippocampus with the other parts of the cerebrum.

Secondary linking is also present: the EC projects into the CA3 and CA1 region; the collaterals of the axons of the CA3 region form synapses with CA3 neurons, the CA3 feeds back into the DG via the excitatory mossy fibres. Additional transverse connections are present, creating complex network in the hippocampal structure [113, 64].

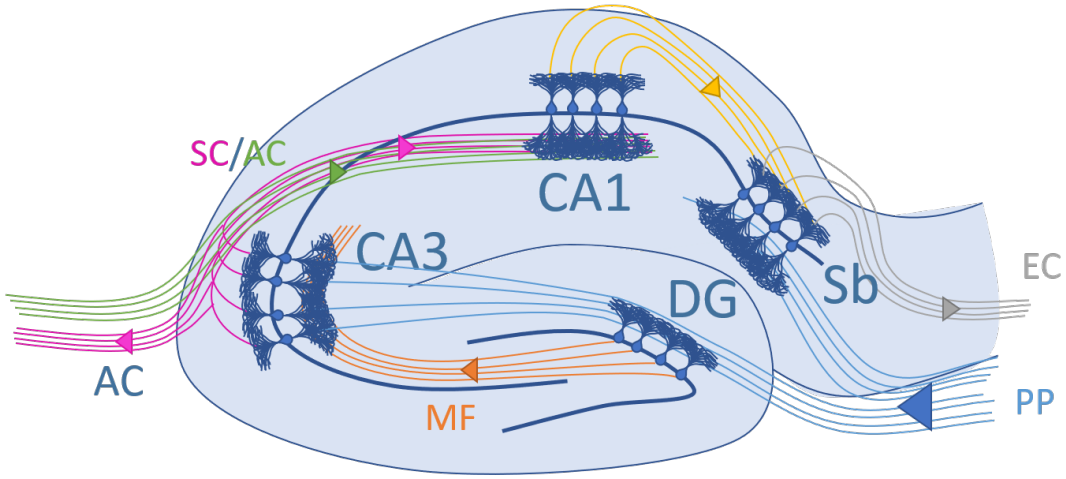

Figure 1.16. Hippocampus structure and network. *The main circuitry is composed by the trisynaptic loop: the entorhinal cortex (EC) projects into to the dentate gyrus (DG) via the perforant pathway (PP). The mossy fibres (MF) connect the DG to the CA3 region .The CA3 neurons project into the CA1 via the Schaffer collateral pathway (SC). The CA1 region then projects into the subiculum (Sb), closing the loop. Output fibres also leave the hippocampus via associational commissural pathway (AC).*

1.4.2 Hypoxia in the brain

Hypoxia is the pathological condition which occurs when the oxygen supply is interrupted or strongly reduced. The brain is especially sensitive to hypoxia because its tissue is unable to regenerate and the brain does require a relatively high amount of energy and oxygen to function [201]. In humans, despite accounting for only 3 % of body weight, the brain is responsible for around 20 % of the total body energy and the oxygen consumption [287, 92]. Since the brain does not store oxygen, in the occurrence of an hypoxic event, it has to rely on anaerobic breakdown pathways to retrieve energy. These processes are inefficient and only allow the brain to survive for a few minutes [201].

In normoxic condition, oxygen is used to produce adenosine triphosphate (ATP) from adenosine diphosphate (ADP), through a process called oxidative phsphorylation. ATP is produced and consumed at the same rate, maintaining the [ATP]-[ADP] ratio constant (Figure 1.17, left-blue) [47]. This equilibrium is broken by the absence of oxygen, which stops the ATP synthesis but not its catabolism. The levels of ADP increase, initiating adenylate kinase acitvity, which employs ADP as substrate to produce ATP and AMP [88]. The latter is hydrolysed into adenosine, which is then re-

leased into the extracellular space [38, 43, 69, 189, 236, 191]. In the extracellular space adenosine is able to interact with its receptors: A_1, A_{2A}, A_{2B}, A_3 (reviewed in [252, 196, 236]). Adenosine binding to its receptor at the postsynaptic cell, inhibits Ca^{2+} influx via the voltage-gated calcium channel [107, 98, 138]. The latter inhibits glutamate release and results in the repression of the synaptic transmission (Figure 1.17, right-red) [66, 157, 86]. The protective role of adenosine release in the extracellular space in correlation with the A_1 receptor (A_1R) was further characterised by [100, 109], which have seen that A_1R knock out (KO) mice show a a delayed and reduced sysnaptic repression and a longer recovery time.

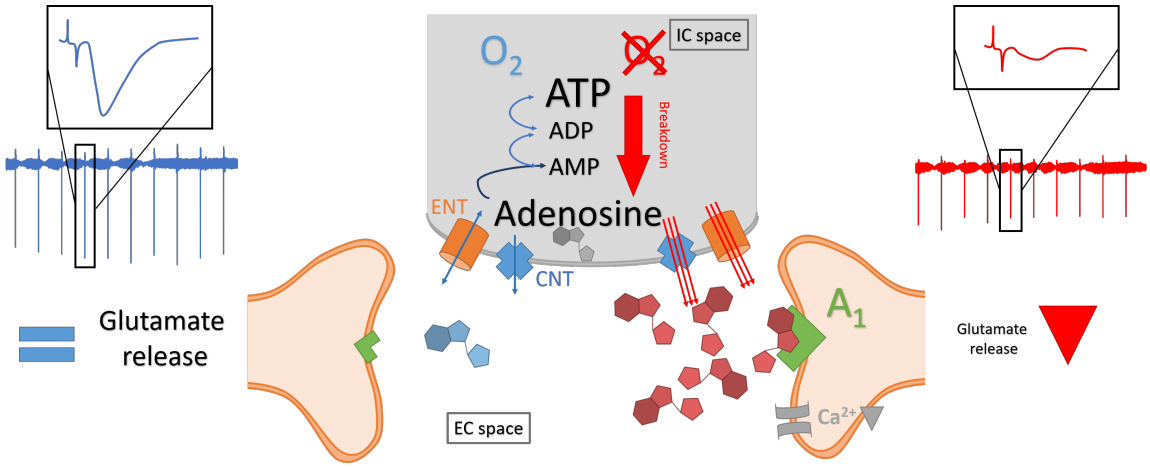

Figure 1.17. Adenosine pathways in normoxia (O_2, left side) and hypoxia (CO_2, right side, red). *In normoxic conditions (95% O_2 / 5% CO_2) ATP and ADP are in equilibrium and all the savage pathways to produce ATP starting from as low as adenosine as a building block are active. Synaptic activity is normal (left panel, blue). In the absence of oxygen (95% N_2 / 5% CO_2), the phosphorylation of ADP into ATP no longer takes place, thus starting the breakdown cascade that results in an overall increase in concentration of intracellular adenosine. The excess adenosine is released in the extracellular space via transporters (CNTs and ENTs). There it binds the A_1 receptor and inhibit glutamate release. The voltage-gated calcium channels are blocked, thus the synaptic transmission is repressed and the field excitatory post synaptic potentials are smaller in amplitude*

.

Multiple studies were made to determine both directly and indirectly the amount of adenosine and downstream metabolites released in the extracellular space [291, 81, 199, 196, 65, 13]. These techniques allowed, in combination with extracellular recordings, to unveil the pathway. With the advent of microelectrode sensors, Dale, Pearson, and Frenguelli [43] and Pearson et al. [194] recorded in real-time and simultaneously

adenosine release and synaptic repression from rat hippocampal slices undergoing 5 min hypoxic episodes. The recording confirmed that adenosine release preceded the repression of the synaptic transmission and achieved a recorded release of 5.6 $\pm$ 1.2 µM of adenosine, compared to $\backsim$ 4-200 nM for resting conditions [115]. With an improved sensor design and performance, the recording was repeated uncovering "novel aspects of adenosine release during hypoxia" [67]: the discovery of post hypoxia-purine efflux and the timescales of both adenosine release and synaptic transmission repression and recovery. The same sensor design was applied to measure extracellular release of ATP following hypoxic insult, but no evidence of its release was found, within the sensitivity parameters of the sensor [69].

1.5 Current analytical methods for neurochemical monitoring

Neurons and glia communicate with each other via small molecules released via controlled mechanisms and that act on specific receptors to provide chemical signalling. The first real-time measurements of neurochemical release was reported by Stamford, Kruk, and Millar [247]. Following the pioneer work by Adams [2], they recorded the release of dopamine and ascorbate in different brain regions via fast scan cyclic voltammetry [247, 248]. Ever since, with the optimisation of carbon fibre microelectrode and by applying different potential steps, many neurochemicals have been detected with increasing sensitivity and selectivity, among which dopamine, serotonin (5-HT), adenosine, (3,4-dihydroxyphenyl) acetic acid and ascorbic acid [271, 96, 193, 212, 237]

The advent of enzymatic microelectrode biosensors constituted a further step in neurophysiological measurements, as it allowed researchers to measure the release of small non-electroactive molecules Patel et al. [192]. Multiple chemistries are available to form the biolayer coating, which make the technique versatile for a variety of applications [276, 112, 277]. Dale, Pearson, and Frenguelli [43] employed a microelectrode sensor to record for the time the real-time release of adenosine from hypoxic hip-

pocampal slices. The sensor exploited an enzyme-based cascade which started with adenosine, and its downstream purines, and returned uric acid and hydrogen peroxide as final product. The latter was reduced to generate the amperometric current.

Other methods such as luciferase and sniffing, have also been employed. However, these techniques despite providing high spatial resolution presents poor sensitivity and temporal resolution [42]. More recently, the focus has shifted on FRET-based and single-Wavelength sensors. The former is sensitive but presents low signal-to-noise ratio, whilst for the second the characteristics are inverted [293].

Many are the challenges to overcome as many are the requirements: the device should be small, to acquire space-resolved measurements; fast, to record neurochemicals release in the extracellular space before they are degraded; it should acquire continuous measurements to monitor the event evolution and dynamics; and present a linear behaviour in the high pico-molar to the low millimolar range [11, 123]. No technique can possibly satisfy all requirements, and the most appropriate one should be chosen based on the characteristic of biological event recorded. In the case of hypoxia, the linear range requirements are in the hundreds of picomolar to hundreds of micromolar, covering four orders of magnitude, the time resolution should be in the second range.

Many neurochemicals are involved in signalling; being able record release could facilitate understanding of their function and help to create new tools for both diagnostics and therapeutics [239, 261, 241].

1.5.1 Uridine triphospate (UTP) and UDP-glucose (UDPg) and their role as extracellular signalling molecules.

The purinergic system describes the group of chemicals, associated receptors families and regulating enzymes. The adenine and uracil nucleotides (ATP, ADP, adenosine, UTP, UDP) and nucleotide-sugars (UDP-glucose and UDP-galactose) agonise/antagosine their respective receptors. The main families are the adenine-associated P0 and adenosine-binding P1 (A1, $A2_A$), $A2_B$ and A3); follows the P2 family, containing both the ligand-gated ion channels P2X, and the G-protein coupled P2Y sub-families Fig-

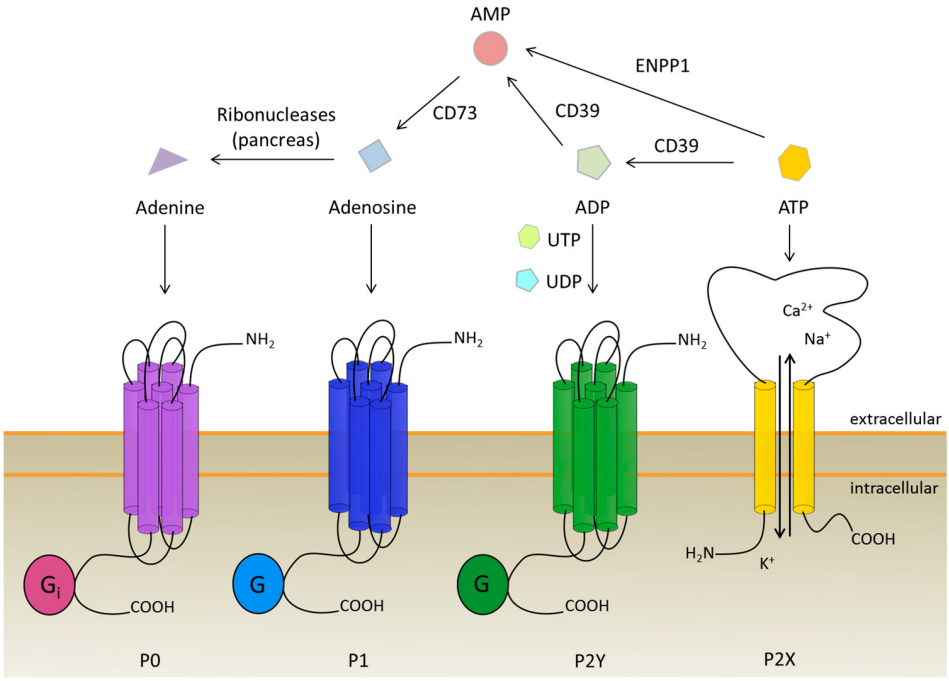

Figure 1.18. Schematic representation of the purinergic system. *P0 receptors are activated by adenine, whereas P1 receptors are stimulated via adenosine binding. The P2 receptors are divided into ATP-dependent P2X ion channels and G protein-coupled P2Y receptors which are stimulated by ATP, ADP, UTP, UDP, and UDP-glucose. Degradation of ATP to adenosine is done by ectonucleotidases, namely CD39, CD73, and NPP1. Adenine is produced during the nucleotide recovery in the pancreas. Reprinted from Ottensmeyer et al. [185]*

ure 1.18.

The purinergic system is ubiquitous and its influence extends across multiple physiological processes, which renders its characterisation complex. Ever since purinergic signalling was first theorised by Burnstock [25], a considerable effort has been put into the characterisation of the function of purines and pyrimidines as extracellular signalling molecules and verify whether the system could be used as a potential drug target [61]. However, most of the effort went into characterising the ATP and ADP regulated events and release mechanisms [1, 26, 50], whilst the uracil nucleotides and uracil sugar side of the system is still quite poorly understood [3], not least due to the lack of assays available that can sensitively detect their release [84]. Wu and Li [293] reviewed the current probing techniques for monitoring the dynamics of purinergic signalling and from their work it emerges that none of them could be employed to detect uracil-based nucleosides.

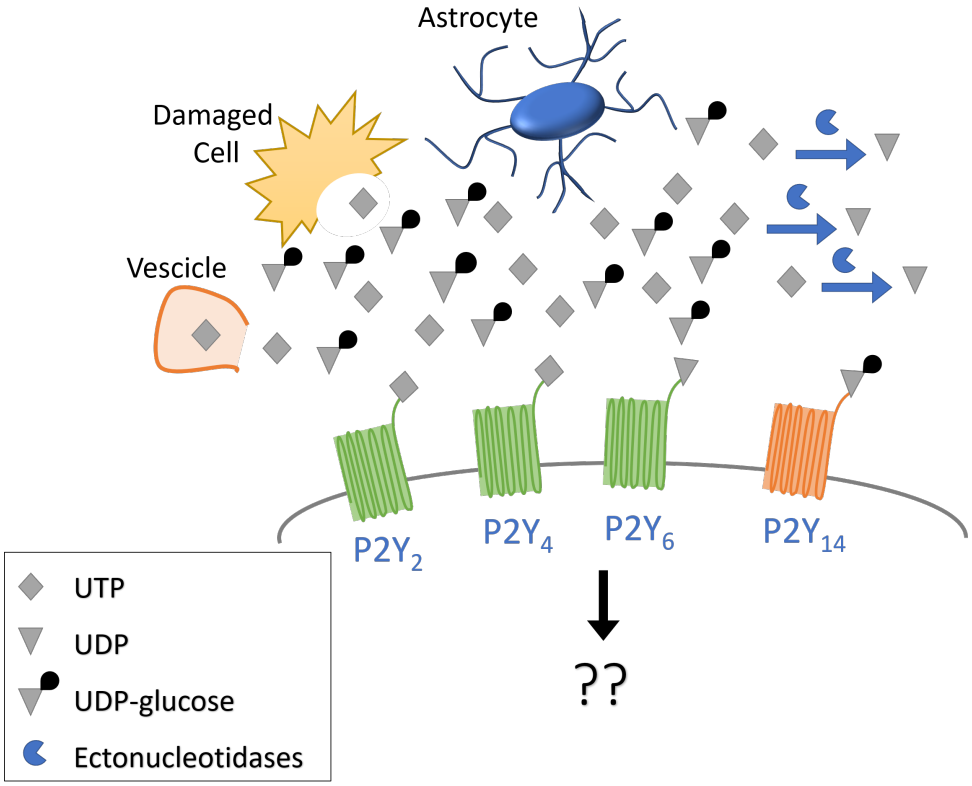

Figure 1.19. Hypothesised release mechanisms for uracil based nucleosides and respective receptors. *UTP binds the $P2Y_2$ and $P2Y_4$, and only weakly the $P2Y_6$ which interacts mainly with UDP. UDP-glucose binds the $P2Y_{14}$ receptor. The hypothesis sees UTP and UDP-glucose mainly released through vesicles, leaky or damaged cells and astrocytes, whilst UDP is thought to mainly originate from the break down of UTP by ectonucleotidases. The impact of these molecules and their associated receptor varies dependently on the studied system and new tools are needed to understand the roles plaid by each molecule in these pathways.*

The uracil nucleotides and sugars bind the receptors of the P2Y family, which can be found in many organs they play a role in central nervous system (CNS) and in the autunomic nervous system (ANS). More specifically UTP activates with the $P2Y_2$, $P2Y_4$, and less effectively the $P2Y_6$ receptor, whilst UDP-glucose is an agonist of the $P2Y_{14}$ receptor, first identified by Chambers et al. [34], thirty years after the first publication on purinergic signalling. The mechanism of release of these nucleoside is still uncertain and the hypothesis mainly rely on vesicle-mediated, maxi anion channels mediated release and outflow from leaking membrane of damaged cells [127]. It has also been shown that in astrocytes, the release of these nucleoside was not only accompanied, but also promoted by the release of ATP (Figure 1.19) [84, 126].

Due to the widespread expression of its receptors, UTP and UDP glucose have

found to play a role in a variety of pathological conditions, such as diabetes [187], cancer [283], pulmonary disease, cystic fibrosis [28], dry eye disease, hypertension, immune response and inflammation [61, 129].

Like their adenine counterparts, uracil nucleotides can regulate the autonomic nervous system (ANS) [75]. Kauffenstein et al. [108] have shown in NTPDase1 deficient mice that UTP mediated vasoconstriction in blood vessels via $P2Y_2$ and $P2Y_4$ receptors. UDP-glucose activated $P2Y_{14}$ induced vasoconstriction in pancreatic cerebral and coronary arteries in a $P2Y_2$ knock out and wild type mice [80].

Finally, UTP and UDP-glucose also play a role in regulating the central nervous system. Koizumi et al. [117] have shown UTP release in mice where *status epilepticus* was induced with Kainic acid intraperitoneal injections. Status epilepticus also induced upregulation of expression of the $P2Y_6$ receptors in the CA1 and CA3 regions of the hippocampus. A similar result was published by Alves et al. [4], where they have shown that status epilepticus induced mice showed upregulation of the uracil sensitive P2Y receptor and downregulation of the adenine-sensitive counterpart. In the thalamus and in the cortex, spontaneously epilectic rats treated with UTP showed a decrease of firing rate [121]. Similarly, the same treatment employed on mice with induced status epilepticus in resulted in reduction in both epileptic seizure severity and cell damage in [4]. Also patients with epileptic encephalopathy treated with UTP metabolites have shown a reduction in epileptic seizures [114]

These results stress the need for sensitive and selective tools for measuring the release of uracil-based nucleotides, if we are to progress with understanding a wide set of neurological conditions.

1.6 Problem statement

Small molecules play multiple roles as signalling molecule and receptors ligands [146]. Given their small size, they can travel through membranes throughout the body and can be found in a variety of interstitial fluids, which makes them ideal diagnostic targets [89]. Real-time, continuous biosensors would provide time resolved information of the molecule/drug levels thus providing novel physiological information.

The brain employs hundreds of signalling molecules and many lack an analytical technique that allows measurement of their release with sufficient selectivity, sensitivity and time resolution. For smaller molecules, such as hormones and nucleosides, e.g. orexin, UTP, MCH, achieving detection is even more arduous due to the lack of specificity in antibodies and limited number of available oxidases. Therefore, there is a need for a universal platform that could be adapted and employed to detect in real-time the dynamics involving these poorly characterised neurochemicals.Baker et al. [10] proposed the combination of electrochemical platforms with aptamers as solution for continuous monitoring of small molecules in crude sample/physiological conditions.

Electrochemical transduction has high sensitivity, a wide variety of techniques and it is inexpensive and easy to miniaturise [211]. However, fouling is still an issue when using the sensor in cerebrospinal fluid (CSF), or any crude sample, due to the presence of electrochemically active molecules, genetic, protein and polymer fragments and oxidised materials. Therefore, great effort in designing biosensing platforms needs to go into screen the sensors against such interferences in physiological applications [44]

Aptamer with their reduced dimension, high selectivity and *in vitro* selection are the ideal candidates for detecting small molecules and can be selected for a great variety of target molecules, thus providing an almost universal biorecognition template.

The platform has to be label-free to support reagentless continuous monitoring. The platform first published by Xiao et al. [294] exploits aptamers undergoing conformation changes upon binding of it target molecule. This folding property has been exploited in electrochemical assays by conjugating the aptamer to redox-active molecule and using its displacement from the surface proximity as the signal generating mechanism (Figure 1.20) [223]. Many redox moieties have been characterised in the literature: ruthenium purple [265], prussian blue, ferrocene, nile blue. Kang et al. [103] studied their stability for use over time and in complex media and showed that methylene blue is the most stable both over time and in complex media. Arroyo-Currás et al. [7], combining the structure switching capability of aptamers and electrochemical de-

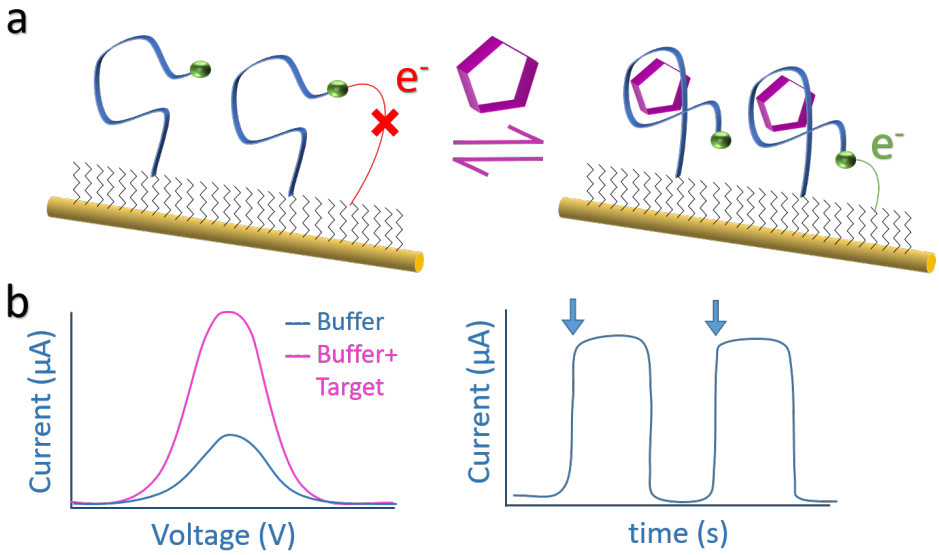

Figure 1.20. Schematic of the working principle of the sensor adapted from Arroyo-Currás et al. [7]. *a) The gold electrode probe is functionalised, via thiol chemistry, with a uniform mat of 6-mercapto-1-hexanol and aptamers-methylene-blue complex. In the absence of adenosine, the aptamer strand is unfolded and the methylene blue (MB) molecule is far from the surface. The distance impairs the electron transfer rate, resulting in a low signal (blue curve, b). Upon adenosine binding, the aptamer folds, carrying the MB closer to the surface and rearranging the solution electrical layer, thus its conductivity. The electron transfer rate increases, thus generating a higher signal (pink curve, b). Taking each peak value as a time point and plotting it as a time vs current curve, the obtained curve should look like a step function, as illustrated in the second graph. The function should look like a step function. The arrows point at the response to the target molecule*

tection, showed the successful detection of small molecules from unprocessed blood samples in awake animals.

Building on these results, my project aims to establish a protocol for the production of electrochemical aptamer-based (E-AB) biosensors to be used as a new tool for detecting chemical signalling molecules released in the brain. However, for aptamer-based biosensors to take a more prominent role in the field of biosensors, more aptamers for relevant target molecules need to be selected and and published. Therefore, after establishing a platform fabrication protocol using a well characterised target, adenosine, to compare the performance of the sensor with previously published work, I will undertake a selection process to isolate structure switching aptamers for UTP and UDP-glucose. These two signalling molecules whose dynamics are poorly characterised, but whose relevance is becoming evident both as possible therapeu-

tic agents and as biomarkers. The final goal is to employ then the selected aptamers on the previously established platform to achieve detection of biologically relevant events, thus gathering novel data on the dynamics of their release.

1.7 Project aims

1. Establish an characterise and aptamer based electrochemical platform to be employed for continuous detection of small molecules in the brain, starting from adenosine.

2. Achieve a recording of adenosine release from a biological event to asses the platform fouling resistance in a complex environment and the possibility to employ it in parallel with other platforms.

3. Identify and characterise new aptamer strands for UTP and UDP glucose; two signalling molecules for which no analytical technique is yet available to detect their release in real time.

Chapter 2

Materials & Methods

2.1 Electrochemical aptamer-based biosensor for adenosine and ATP

2.1.1 Materials

Buffers were produced in house and chemicals other than those specified were from Fisher Scientific (Thermofisher Scientific, Paisley, UK). For the sensor fabrication and response recording, gold disk electrodes (2 mm and 1.6mm), reference electrodes, alumina slurries and polishing pads were purchased from IJ Cambria Scientific Ltd (Llwynhendy, UK), whilst the wire sensors (probes) were fabricated in house. All aptamers strands were purchased already HPLC purified from LGC Biosearch Technology (Riskov, Denmark), methylene blue 1% W/V in H_2O from Scientific Laboratory Supplies Ltd (Nottingham, UK), potassium hexacyanoferrate (III), adenosine, inosine, hypoxanthine and adenosine triphosphate were purchased from Merck (Poole, UK). Recordings were performed with an IJ Cambria CH630B potentiostat, IJ Cambria Scientific Ltd (Llwynhendy, UK) using a three electrode system with Ag/AgCl reference electrode stored in 3.5 M KCl, IJ Cambria Scientific Ltd (Llwynhendy, UK) and an in house fabricate Pt counter electrode, made of a 99% Pt square of 0.25 cm^2 soldered onto a copper wire via a 1 cm 99% Pt wire, using a lead-free solder.

2.1.2 Adenosine/ATP aptamers

Three adenosine and/or ATP-binding aptamer strands employed in this project are reported in Table 2.1

Table 2.1. Adenosine/ATP aptamer sequences employed in the project. Aptamer sequences, characteristics and first publication

Type	Sequence (5′ - 3′)	# binding site	Tail	K_D	Author
2BS	ACCTGGGGGAGTATTGCGGAGGAAGGT	2	Long	16.4 µM	Huizenga and Szostak [95]
1BS	ACCTTCGGGGAGTATTGCGGAGGAAGGT	1	Long	12 µM	Zhang, Oni, and Liu [307]
1BSS	TTCGGGGAGTATTGCGGAGGAA	1	Short	12 µM	Zhang and Liu [306]

Figure 2.1. Chemical modifications at 5′ and 3′ end of the aptamers. *Each aptamer sequence presented on the 5′ end a thiol group (SH), used to anchor the aptamer on the gold surface, and a carbon chain ($(CH_2)_6$) acting as a spacer between the aptamer and the surface. On the 3′ end a seven carbon chain spacer ($(CH_2)_7$), an amide group (NH) and the redox molecule, methylene blue (MB).*

All sequences present common 5′ and 3′ modifications (Figure 2.1). At the 5′ end, the aptamers were attached to a six-carbon chain, to act as a spacer as reports have suggested that direct constrain of the aptamer to the surface can affect the aptamer secondary structure, thus its K_D [71]. The spacer was followed by a thiol, employed to anchor the aptamer on the gold surface. The thiol linkage to the surface was chosen despite being less stable than a covalent bond and more expensive, because fabrication through self-assembled monolayer, allowed the freedom of testing multiple protocols which allowed better control over the orientation of the bound species. On the 3′ end, the oligonucleotides present a seven-carbon chain spacer, an amine group and a methylene blue (MB) molecule that constitutes the redox moiety used for signal detection. The 5′ to 3′ direction is indifferent in this case as the structure formed by the folded aptamer is symmetrical. The MB molecule was placed at the distal end of the aptamer as it has been shown to produce the highest and more reproducible signal [160].

2.1.3 Sensor fabrication

Electrodes employed

Two sensors designs were employed in this project and they are represented in Figure 2.2. The 2 mm and 1.6 mm gold disks were made of poli-crystalline gold which was surrounded by a sealed insulating polymer layer, which delimited the surface active area (Figure 2.2, left and centre). The probes, were made by threading a 50 µm 99 % Au wire into a glass capillary and sealing the sensor end with a silicon paste, which also helped delimiting the surface area (Figure 2.2, right).

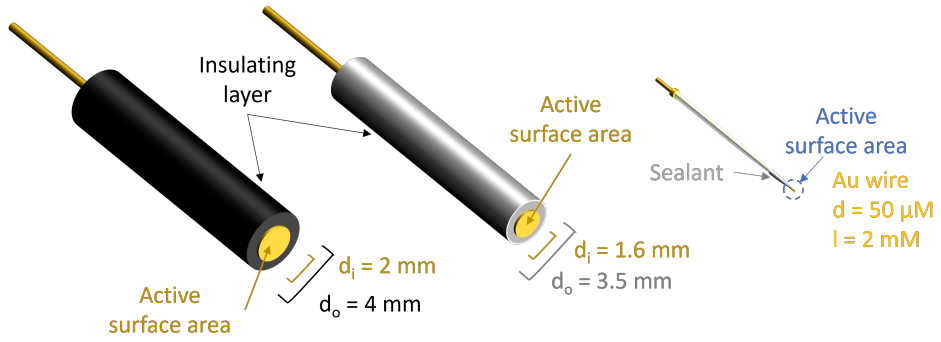

Figure 2.2. Sensors designs employed in the project.

Activation of the gold surface

The fabrication of the biosensor starts with the activation of the gold (Au) surface. **For the 2** mm **and 1.6** mm **diameter disk electrodes** the pre-treatment consist of two steps. First, polishing of the electrodes to a mirror-like surface by performing figure-8 motions on a polishing pad wetted with 1.0, 0.3 and 0.05 µ-acqueous-alumina slurries. After thorough rinsing with nanopure water, immersion in pure acetone for 30 s and another rinsing step, the surface was characterised via cyclic voltammetry in a potassium ferricyanide solution (0.5 mM $K_3[Fe(CN)_6]$ and 0.2 M KCl). **For the probe electrodes**, the surface activation consists in cleaning an electrochemical roughening. First cleaning of the surface with a 10 s immersion in nitric acid (HNO_3) and rinsing in nanopure water. Next 10000 voltage pulses ranging from 0 V to 2 V, 2 ms in width at 100 Hz were applied to the sensor whilst immerse in 0.5 M sulfuric acid (H_2SO_4). It was paramount to continue immediately with the surface fictionalisation to prevent

oxidation and contamination of the surface (adapted from [7]. The electrochemical roughening was performed to improve the sensor signal-to-noise ratio as seen in the work by Arroyo-Currás et al. [6].

Self-assembling monolayer (SAM) protocol

The self-assembling monolayer protocol starts with thawing the aptamer aliquot (500 nM, final concentration) at room temperature (RT). The thiol-protective cap was removed by incubation with 100x excess tris(2-carboxyethyl)phosphine hydrochloride (TCEP) for 2 h. **For the melting protocol**, the aptamer aliquot was first thawed at room temperature, then heated at 95 °C for 5 min, and snap cooling it in ice for 10 min. The 2 h incubation step with 100x excess TCEP was also performed in ice.

Two self-assembling monolayer (SAM) protocols were tested: backfilling and insertion protocols. **For the backfilling protocol**, a freshly polished/roughened sensor was incubated first with the aptamer-TCEP mix for 1.5 h at RT, followed by incubation with 5 mM 6-mercapto-1-hexanol (MCH) for 18 h at 4 °C. **For the insertion protocol**, a freshly polished/roughened sensor was incubated first with 5 mM 6-mercapto-1-hexanol (MCH) for 18 h at 4 °C, followed by the incubation with a newly prepared aptamer-TCEP mix for 1.5 h at RT.

For the fabrication with MC_{11} backfilling a freshly polished/roughened sensor was incubated first with the aptamer-TCEP mix for 1.5 h at RT, followed by incubation with 5 mM MCH_{11} for 18 h at 4 °C.

2.1.4 Electrochemical measurements

All recordings were performed with a three-electrode system using platinum foil as the counter electrode (CE) and an Ag/AgCl electrode as the reference electrode (RE) in a chamber open to atmosphere Figure 2.3. All solutions were bubbled for 15 min with N_2. For all measurements 1 mM $MgCl_2$ was added to PBS (PBS-Mg).All recordings where performed in an open chamber. The chamber was created using a 35 mm Petri dish bottom and a 1 ml tip cut to a length of 2 cm and sealed at both sides to obtain a

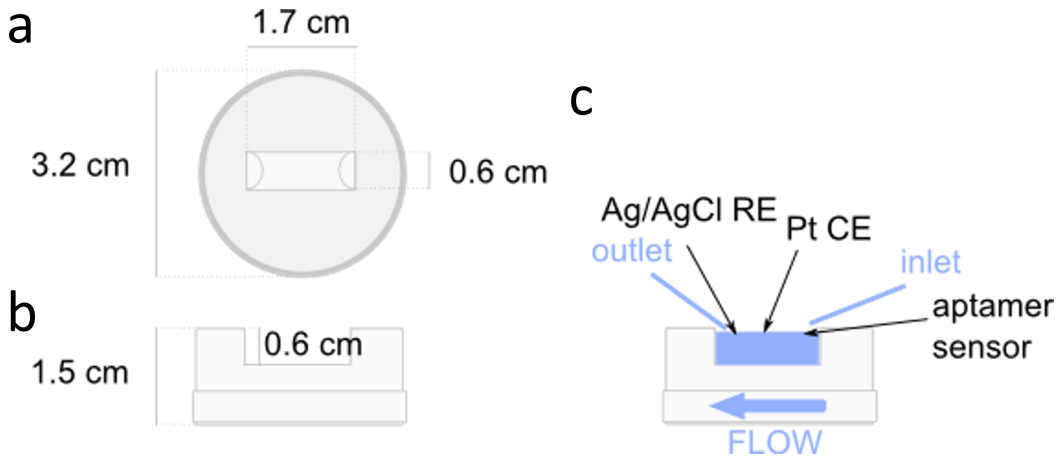

Figure 2.3. Representation of the chamber used for performing sensor characterisation and interrogation and placement of elements. *All recordings were performed with the chamber open to atmosphere. a) Top view of the recording chamber with measures. The container is a 3* cm *petri-dish bottom. The chamber was created by means of a cylindrical mold (1.7* cm *x 0.6* cm*) filling the rest with a silicon resin. b) Side view of the chamber with dimensions. c) Side view of chamber with indication of the position of the different elements used during the recording with respect to the inlet and outlet of the flow. From left to right: inlet, aptamer sensor, platinum counter electrode (Pt CE), Ag/AgCl reference electrode (RE) and outlet.*

cylindrical mould for the chamber. The chamber was filled with

Sensor characterisation

All sensor fabrications were characterised via cyclic voltammetry (CV) in ferricyanide solution (0.5 mM $K_3[Fe(CN)_6]$ and 0.2 M KCl) by applying -0.5 V to 0.5 V with a scan rate of 50 mV s^{-1} for 10 cycles and the recordings for cycle 3-10 averaged. These measurements were used to check that the SAM layer deposition had occurred by noting the variation in the Δ_E.

The presence of the methylene-blue-functionalised aptamer on the surface was verified via CV in PBS, by applying voltages ranging from -0.4 V to -0.1 V for 10 cycles and the recordings averaged. The molecule surface density was calculated by adapting the method published by Yu et al. [300], using the equation

$$Q = nFA\Gamma_{DNA} \tag{2.1}$$

where Q is the total charge, calculated as the area under the redox peaks, n is

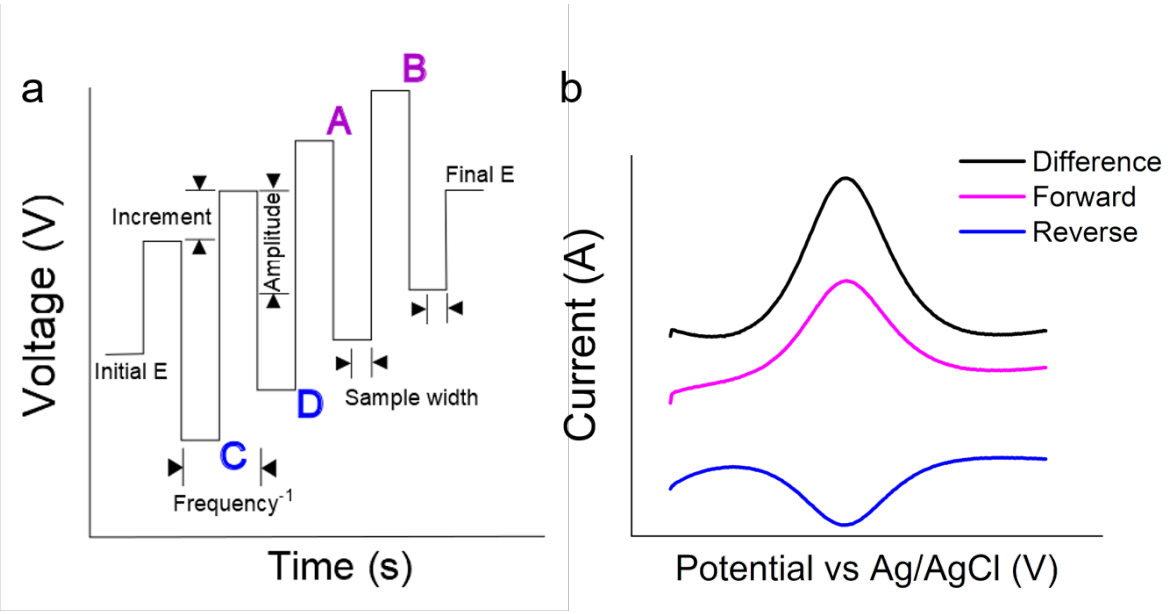

Figure 2.4. Schematic of square wave voltammetry (SWV) measurements. *a) Representation of the voltage curve applied over time with definition of each parameter. A and B (magenta), and C and D (blue), indicate the sampling points for the forward and reverse current curves respectively. b) Voltage vs. current plot resulting from SWV measurement. In magenta the forward current of the reduction process, in blue the reverse current of the oxidation process. In black, the difference between the two currents, increases the signal and cancels out background currents.*

the number of exchanged electrons, A the electrochemically active surface area and Γ_{DNA} the concentration of DNA on the surface.

Sensor interrogation

The sensor response is recorded via square wave voltammetry (SWV) using the following parameters: initial voltage -0.4 V, final voltage -0.1 V vs. Ag/AgCl, amplitude 25 mV, voltage step 1 mV and frequency 60 Hz (parameters physical meaning in Figure 2.4). The voltage range of -0.4 V - 0.1 V was chosen to have the peak at the centre of the graph, sufficient baseline and a shorter recording time for each SWV scan. The protocol was adapted from Arroyo-Currás et al. [7].

Initially, the response was measured by averaging five recordings taken at each incubation step (PBS with 1 mM $MgCl_2$ (PBS-Mg) (1), 2. adenosine in PBS-Mg at 0 min (2) and 5 min (3), and in PBS-Mg again (4)). Later on, over-time measurement were achieved by acquiring 120 SWV recordings (40 in PBS-Mg, 40 with the indicated

concentration of target molecule in PBS-Mg and 40 in PBS-Mg again to check the recovery). The response was calculated as the difference between the peak current with target molecule and with buffer. In order compare the performance of the sensors they had to be normalised. This result can be obtained in two ways, which produce the same result: by either normalising the signal against the baseline value or by averaging the signal against the geometrical surface area of the sensor (cm^2). In this work the second option was employed. The surface area was calculated using the theoretical formulas and the diameter provided by the supplier (for the 2 mm and 1.6 mm), whilst for the probe sensors the length was measured using a ruled objective with $\pm$ 0.2 mm accuracy and using the supplier provided diameter (50 µM).

For each condition, three sensors were fabricated and tested to assess the reproducibility of the fabrication and sensor performance. The data are reported as average value $\pm$ absolute error ($\bar{x} \pm e_a$, average value $\pm$ absolute error.). Since the low n number for the measurements (n=3), the absolute error of the repeated measurements was calculated as the semi-dispersion with the formula:

$$e_a = \frac{x_{max} - x_{min}}{2} \tag{2.2}$$

For the sensor response over a concentration range, for each sensor at each concentration, 40 recordings were averaged to generate a response, and then the 3 responses averaged to obtain the final reported value ($\bar{x}$)

2.2 Hypoxia recordings

2.2.1 Materials

Buffers were produced in house and chemicals other than those specified were from Fisher Scientific (Thermofisher Scientific, Paisley, UK). Agar for analytical grade was purchased from Merck.

For the temperature measurements a temperature controller with feedback probe was employed.

For the extracellular recordings the measurements were performed in a in house

made chamber containing three different wells: an in-flow well, the main chamber and an out-flow well. The wells were glued together and connected to allow for constant level in the main chamber, important to reduce noise during the recordings (for dimensions Figure 2.7. The current steps for the field recordings were induced via DS3 Isolated Current Stimulator from Digitimer Ltd (Letchworth Garden City, UK), the signal recorded by the recording electrode passed through AC/DC differential amplifier from A-M Systems Inc. (Sequim, WA, USA) and a data acquisition unit Micro 1401 from CED (Cambridge, UK). The set up was controlled and the data recorded via Spike2 from CED (Cambridge, UK).

2.2.2 Measurments in 0.5% agar slice

0.5% agar block was made up using 0.5 g in 100 ml 1x Tris-acetate-EDTA buffer (TAE, pH 7.5). A slice of 6 mm^3 was cut out and pre-incubated with 1 mM adenosine in aCSF (127 mM NaCl, 1.9 mM KCl, 1 mM $MgCl_2$, 2 mM $CaCl_2$, 1.2 mM KH_2PO_4, 26 mM $NaHCO_3$) for 30 min (Figure 2.5.a) . The measurement started with a CV in aCSF to check that the sensor fabrication was successful. Then the sensor was calibrated with 1 mM adenosine in aCSF (120 SWV). Then a CV was performed in 1 mM adenosine in aCSF, followed by 50 SWV measurements in 1 mM adenosine in aCSF (Figure 2.5.b). The sensor was then inserted in the agar slice and allowed to rest and stabilise for 20 min. A CV and 50 SWV were recorded in the slice with continuous flow of 1 mM adenosine in aCSF in the chamber (Figure 2.5.c). Then, the sensor was extracted from the slice, placed again in the chamber and after 20 min of rest, a CV and 50 SWV recordings were taken (Figure 2.5.d).

2.2.3 Measurement in 0.5% agar slice to simulate the tissue diffusion layer

A newly fabricated sensor was placed in the chamber and a baseline recorded in aCSF (Figure 2.6.a) for 40 SWV measurements. Then the solution was switched to 1 mM adenosine in aCSF for 40 SWV (Figure 2.6.b). The same protocol was then repeated with the sensor was placed in a 8 mm^3 0.5% agar slice, to test the delay that the dif-

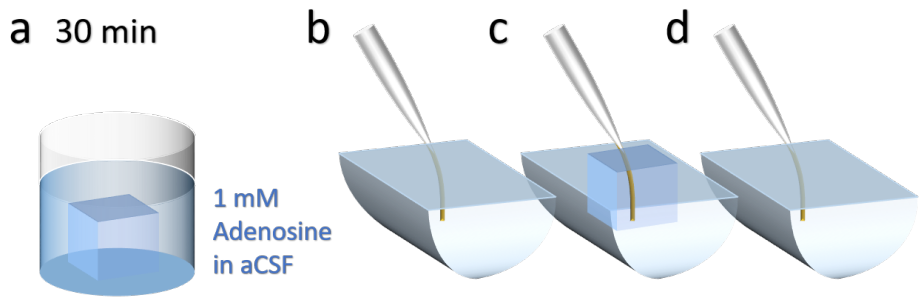

Figure 2.5. Set up for measurements in the agar slice. *The 8* mm^3 *0.5% agar slice was pre-incubated with 1* mM *adenosine in aCSF for 30* min *(a). Cyclic voltammetry and square wave voltammetry measurements were recorded with the sensor in the chamber (b), with the sensor inside the 0.5% agar slice (c) and again back in the chamber (d).*

fusion layer introduced by the agar slice would induce on the sensor response. After insertion in the slice, a rest time of 20 min was observed. Then the recording started in aCSF (40 SWV, Figure 2.6.c) and then switched to aCSF spiked with 1 mM adenosine and recorded for 20 min (Figure 2.6.d).

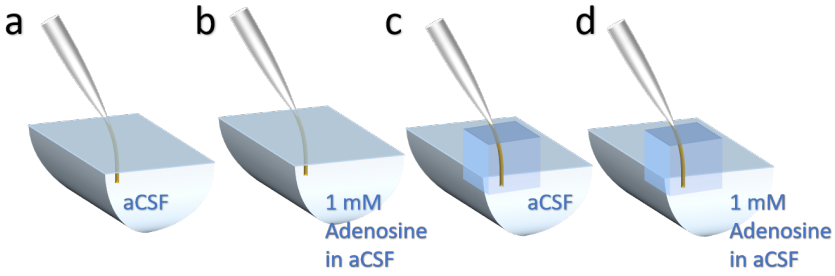

Figure 2.6. Set up for measurements in the agar slice to simulation tissue diffusion layer. *The response of a newly fabricated sensor was tested in aCSF (40 SWV, panel a) and in 1* mM *adenosine in aCSF (40 SWV, panel b). The same protocol was repeated with the sensor inserted in a 0.5% agar slice. After 20* min *recovery time with 120 SWV recordings in 1* mM *adenosine in aCSF*

2.2.4 Extracellular recordings in hypoxic brain slices

Brain slices preparation

Male BL6 mice (P15-P18) were killed via cervical dislocation and decapitated in compliance with the United Kingdom Animals (Scientific Procedures) Act (1986). Parasagittal brain hippocampal slices, 400 µm in thickness, were cut with a Microm HM 650V

microslicer in cold (2–4 °C) high Mg^{2+}, low Ca^{2+} aCSF containing: 127 mM NaCl, 1.9 mM KCl, 8 mM $MgCl_2$, 0.5 mM $CaCl_2$, 1.2 mM KH_2PO_4, 26 mM $NaHCO_3$, and 10 mM D-glucose (pH 7.4 when bubbled with 95% O_2 and 5% CO_2, 300 mOsm) (performed by Dr. Emily Hill, University of Warwick, protocol from [91]). Slices were stored at 34°C in 1x aCSF (1 mM Mg^{2+} and 2 mM Ca^{2+}, pH 7.4) for up to 8 hours, and precooled to 21°C in aCSF 30 min prior to the measurements.

Simultaneous Extracellular and Sensor recording set up

For field-EPSPs recordings, a single brain slice was placed in an immersion chamber,on an elevated net, and submerged in continuously circulating aCSF equilibrated with 95 % O_2/ 5 % CO_2. The stimulator was positioned in the CA3 region of the hippocampus to stimulate the Schaffer collaterals, and the recording electrode, aCSF-filled glass microelectrode, in CA1 region. Stimulation was applied via current steps of approximately 80 µA in amplitude and 220 µs in duration approximately every 8 s. The amplitude of the current step was determined by performing an input output curve, which correlates the step amplitude with the fEPSP amplitude. Current steps ranging from 20 to 200 µA (increments of 20 µampere were appplied [303]. The aptamer biosensor was placed parallel to the brain slice surface in between the stimulator and the recording electrode (Figure 2.7.d) and it recorded one value every duty cycle (approximately 8 s).

Induction of Hypoxia

In all the experiments, the recording started in aCSF bubbled with 95% O_2/5% CO_2. After 100 s,the solution was switched to identical aCSF bubbled with 95% N_2/5% CO_2 for 550 s, then switched back to aCSF bubbled with 95% O_2/5% CO_2 for 450 s. The fEPSPs amplitude was normalised to the baseline (first 100 s of recording).

The syanptic depresiion started when normalised fEPSPs varied by more than 3 times the standard deviation of the baseline signal. The recovery started when the normalised fEPSP amplitude increased by 3 times the standard deviation of the averaged depressed signal. Alternatively, the start of recovery can be indicated as the

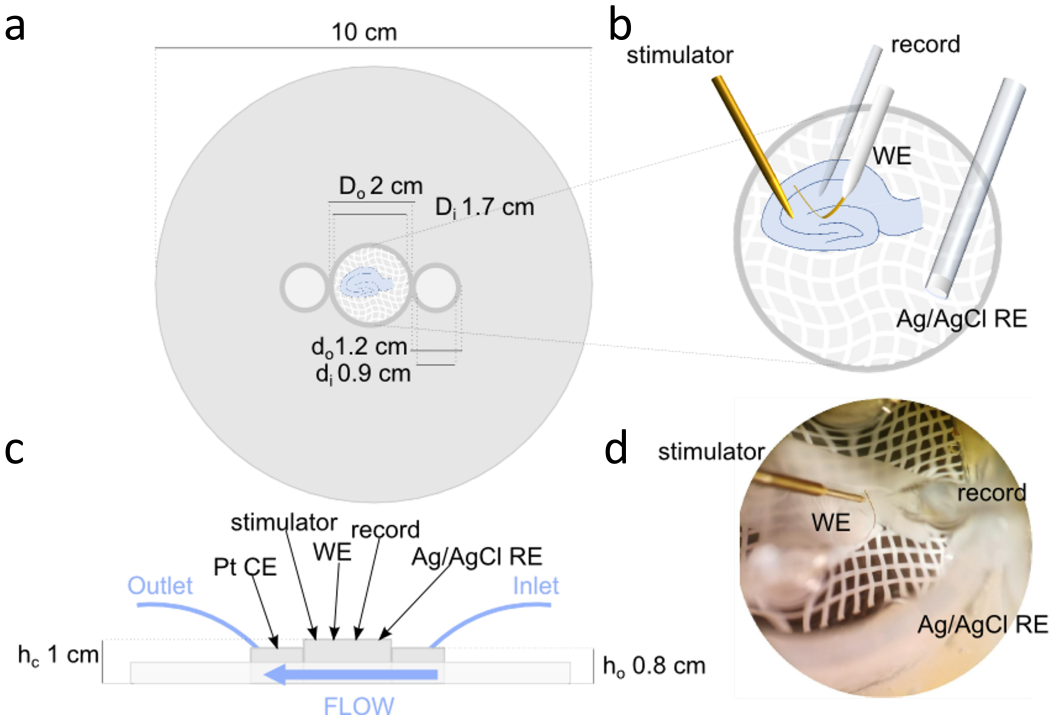

Figure 2.7. Representation of the chamber used for performing extracellular recordings with dimensions and placement of elements. *All recordings were performed with the chamber open to atmosphere. a) Top view of the recording chamber with measures. The container is a 10* cm *petri-dish lid. The main chamber is cylinder cut out of a 5* mm *syringe. A suspension bridge (C shaped) and a net are place at the bottom of the chamber to ensure oxygen perfused the slice in all directions. The inlet and outlet flow are a 0.8* mm *cylinder cut out from a 2* mm *syringe. The three cylinders are glued together, connected via a channel. b) Schematic of the positioning of the aptamer biosensor, recording electrode and stimulator on the slice. c) Side view of chamber with indication of the position of the different elements used during the recording with respect to the inlet and outlet of the flow. From right to left in order: inlet, Ag/AgCl reference electrode (RE), recording electrode (record), aptamer sensor (WE), stimulator, platinum counter electrode (CE) and outlet. d) Photo of the chamber with all the elements are positioned on the slice.*

point where the tangent of the normalised fEPSP curve becomes positive.

2.3 Selection and characterisation of new structure switching aptamers for UTP and UDP-glucose

2.3.1 Materials

All buffers were made in-house and all salts and chemicals were purchased from Fisher unless otherwise specified.

For capture SELEX: UTP was purchased from Alpha Aesar (Heysham, UK), UDP-glucose and primers from Merck (Poole, UK), the DNA library and the capture oligos from Microsynth AG (Balgach, Switzerland), Taq polymerase kit from KAPA Biosystem (Wilmington, MA, USA), the DNA ladder, λ-exonuclease, λ-exonuclease buffer, Taq-polymerase and Taq-polymerase buffer from New England Biolabs (NEB) (Ipswich, MA, USA). The streptavidin-coated magnetic beads M-270 and the Dynal MPC-S magnetic stand from Invitrogen (Thermofisher Scientific, Paisley, UK). The agarose gels were stained using RedSafeTM (20,000x) from Bulldog Bio (Portsmouth, NH, USA), and imaged using BioDoc-It®2 Imaging system, Analytik Jena (Jena, Germany) mounting a GelCam 315 (5.0 MP; 8-48mm, f/1.2 manual zoom lens) wand equipped with the VisionWorks® Analysis Software.

For SYBRgreen assay: SYBR Green I Nucleic Acid Gel Stain 10,000X concentrate in DMSO was purchased from Invitrogen (Thermofisher Scientific, Paisley, UK), UTP was purchased from Alpha Aesar (Heysham, UK), UDP-glucose and Corning® 96 well microplates (black, flat bottom) from Merck (Poole, UK). The unlabelled aptamer sequences were synthesised by Merck (Poole, UK). The fluorescence spectra was recorded with CLARIOstar® Plus Microplate reader by BMG Labtech (Aylesbury, UK)

For CY5-labelling of full-length aptamers: Q5®high-fidelity polymerase and 5x buffer were purchased from New England Biolabs (NEB, Ipswich, MA, USA), GelRed®was purchased from Biotium (Fremont, CA, USA), CY5-labelled and dT25-modified primers were purchased from Integrated DNA Technologies (Coralville, IA USA), Whatman®glass

microfiber filters (thickness 0.26 mm, pore size 1.6 µm) and dNTP were purchased from Merck (Poole, UK). The gels were imaged with the Typhoon FLA 9500, from GE Healthcare (Chicago, IL, USA). Sample concentrations were measured using the Nanophotometer NP80 from Implen (Munich, Germany)

For Microscale Thermophoresis (MST) assay: Buffers (MST and PBS) were made in house. CY5-tagged DNA and primers were purchased from Integrated DNA Technologies (Coralville, IA USA). standard capillaries (MK-022) were purchased from NanoTemper Technologies GmbH (Munich, Germany). The Monolith station and the software for data acquisition (MO. COntrol) and data analysis (MO. Affinity Analysis) were all purchased from NanoTemper Technologies GmbH (Munich, Germany).

2.3.2 Capture SELEX

The Capture-SELEX protocol was adapted from Stoltenburg, Nikolaus, and Strehlitz [250]. The capture-oligo (CAP-oligo) was a 12 base DNA strand functionalised with a biotin molecule to anchor it to the beads (Table 2.2). The library, 108 bases long, was composed of two primer-binding sites, two random regions of 10 (R10) and 40 bases (R40) separated by a 12 base sequence used to bind the library to the CAP-oligo, hence to the beads (Figure 2.8, Table 2.2). Capture-SELEX was performed in rounds according to the following protocol: after re-suspending the beads, the appropriate amount (2 ml in the first round), was transferred to 1.5 ml Eppendorf tubes (500 µl max each) each washed with 1 ml of beads washing buffer (BWB, 5mM Tris-HCl, 0.5 mM EDTA, 1 M NaCl, pH 7.2) (3x) followed by washing with 1 ml PBS (2x). The beads were resuspended in 2 µM CAP-oligo in PBS and incubated with gentle shaking at room temperature (RT) for 20 min to allow biotin- streptavidin complex formation. Then, the beads were washed with 500 µl PBS (3x), followed by the Capture-SELEX DNA library and incubated overnight with gentle shaking at RT. The unbound library was collected, the beads washed with 500 µl PBS (5x). A temperature (28 °C, 20 min, gentle shaking) and a background incubations steps were performed (RT,45 min, gentle shaking). The beads were washed again with 500 µl PBS (5x), resuspended in 500 µl of 100 µM (first round) of target molecule in PBS and incubated for 1 h with gentle shaking at

Table 2.2. Sequences of the different DNA components used to perform Capture-SELEX. *N represents any nucleotide randomly allocated. The capture oligo was used to bind the library to the beads, and it was anchored via the coupling of a biotin-streptavidin bond. The starting library was a randomised pool of DNA sequences that will be tested for affinity to the target molecule. The reverse primer presents a phosphate modification to allow the λ-exonuclease to digest the 5′ phosphorylated strand of dsDNA produced during the PCR amplification and return the library to a single strand DNA library from solution*

Name	Sequence (5′→3′)
Capture Oligo	[Biotin]GTC [Hexaethylene-glycol] **GATCGAGCCTCA**
Library	TAGGGAAGAGAAGGACATATGAT - R10 - **TGAGGCTCGATC** - R40 - TTGACTAGTACATGACCACTTGA
Forward Primer	TAGGGAAGAGAAGGACATATGAT
Reverse Primer	Phosphate-TCAAGTGGTCATGTACTAGTCAA

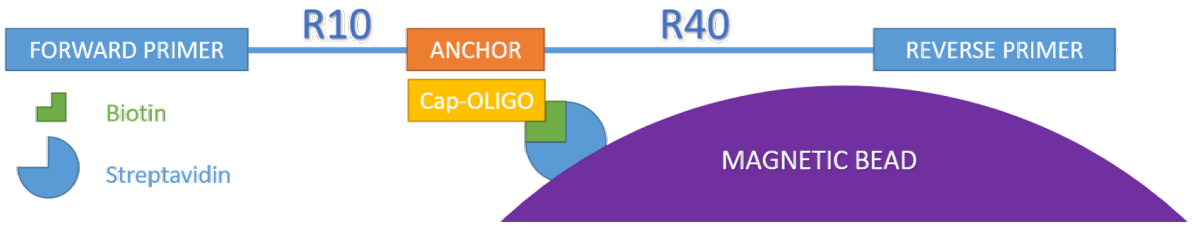

Figure 2.8. Graphical representation of the structure Capture-SELEX library and its anchoring to the magnetic beads. *The library is composed of a 23 base forward primer, followed by a random region of 10 bases (R10). Next comes the anchoring sequence of 12 bases; then another random region of 40 bases (R40). Finally a 23 base reverse primer. The anchoring of the library on the magnetic beads is achieved by hybridisation of the anchor sequence with its complementary strand (Cap-Oligo). The latter is functionalised with biotin, which binds to the streptavidin coated magnetic beads.*

RT. The supernatant containing the sub-library eluted by the target was collected and amplified via polymerase chain reaction (PCR) and the amplification verified via electrophoresis in a 2% w/v agarose gel. Then, the negative strand digestion, performed by incubation with λ-exonuclease in two temperature steps (37 °C for 20 min, 75 °C for 10 min), was followed by ethanol precipitation and resuspension in PBS of each successive sub-library, now ready to undergo the next round.

2.3.3 Sequencing of the SELEX library

To sequence the library the strands needes to be isolated first, and then amplified, as the only way to perform sequencing of a mix pool is through next genearation se-

quencing (NGS), which is too expensive to justify the sequencing of a single round. Therefore, to isolate the single sequences, the aptamers were purified from the PCR product using the PCR clean-up kit, ligated using the TOPO vector kit protocol and transformed into One shot TOP10 F' E.coli competent cells using the standardise protocol. Successful insertion of the aptamer was verified with a colony PCR was performed using M13 primers and the product run on a 2% agarose gel. The colonies were then picked and stroked on an LBA plate and inoculated in 5 ml LB broth and 10 $\mu g\,ml^{-1}$ ampicillin and incubated overnight at 37 °C and 180 rpm. The culture was pelleted (8000 rpm, 3 min) and miniprepped according to the provided protocol. The samples were prepared and sent for GATC Sanger sequencing.

2.3.4 Bioinformatic tools

Jalview2 was employed for visualisation, sequence alignment and calculation of the phylogenetic tree [285, 151].

APTANI2 [32] was employed for calculating the 2D folds (through the embedded viennaRNA package [148] and the motif discovery based on the protocol of AptaMotif [93].

Matlab scripts were generated to analyse the sequencing results, to calculate averages and standard deviations for the SYBRGreen assays.

2.3.5 SYBRgreen (SG) Assay

The following protocol was adapted from the work of McKeague et al. [164]. Aptamer and SYBRgreen dilutions were prepared in sterile water. UTP and UDP-glucose dilution were prepared in 1x PBS-Mg. The aptamer was diluted down to 10 µM incubated for 10 min at 95 °C and snap-cooled in ice for 10 min. Then 3.75 µl of the aptamer (10 µM) and 3.75 µl of SG (1x) were mixed and then added to the indicated concentration of UTP or UDP-glucose to make up a volume of 125 µl. The mix was left to incubate for 10 min and then transferred 115 µl a the black polystyrene plate. Each condition was performed in triplicate. The fluorescence spectra was recorded from 512 nm to 600 nm (1 nm step) with an excitation wavelength of 490 ($\pm$8, laser working window) nm. The

maximum value (525 nm) used to calculate the aptamer response using Equation 2.3, with F_0 being the fluorescence intensity recorded in absence of target molecule at 525 nm and F_0 were the fluorescence intensities recorded in absence and presence of the target molecule respectively

$$\Delta_F = \frac{F_0 - F_1}{F_0} \tag{2.3}$$

Hybridisation control SG assay

For the hybridisation control the complementary sequences to each primer were used and they are listed in Table 2.3

Table 2.3. Primer complimentary sequences for hybridisation control

Name	**Sequence (5′→3′)**
Complimentary Forward Primer	ATCATATGTCCTTCTCTTCCCTA
Reverse Primer	TCAAGTGGTCATGTACTAGTCAA

The aptamer sequence and the reverse/complimentary primer were mixed to a final concentration of 1 µM and 1.25 µM, respectively. The mix was then incubated at 95 °C for 5 min, followed by 10 min at 50 °C and then cooled at room temperature for 20 min. The mix was then employed following the protocol of the SG assay.

2.3.6 CY5-tagging of full-length aptamers

CY5-labelling of the full-length aptamers was achieved via PCR amplification using the primer in the Table 2.4.

Table 2.4. Table of the primers used for the modification of the full-length aptamer with CY5 dye.

Name	Sequence (5′ → 3′)
CY5-Forward Primer	CY5-TAGGGAAGAGAAGGACATATGAT
Reverse Primer	TTTTTTTTTTTTTTTTTTTTTTTT-iSp18- TCAAGTGGTCATGTACTAGTCAA

Table 2.5. Incubation steps times and temperature for the Q5 high fidelity polymerase amplification

Step	Temperature	Time
Initial Denaturation	98°C	30 s
15 Cycles	98°C	10 s
	58 °C	30 s
	72°C	30 s
Final Extension	72 °C	2 min
Hold	4 °C	∞

The 50 µl PCR reactions were prepared (10 µl 5x reaction buffer, 1 µl of 10 mM dNTPs, 1 µl of 10 µM CY5-Forward Primer, 1 µl of 10 µM dT25-Reverse Primer, 0.5 µl of Q5 High-Fidelity polymerase, 0.5 µl of template DNA and dH_2O up to 50 µl). The parameters used for the amplifications are reported in Table 2.5

The PCR product was then run on an 2% agarose gel at 90 V for 50 min and post stained with RedSafe and imaged on a UV lamp to verify the correct size of the product. The remaining sample was then loaded onto a 12% urea PAGE gel and run at 180 V for 2 h. After post-staining the gel was imaged using the Typhoon FLA 9500 Image Analyser both at the wavelength of 520 nm (250 W) and 635 nm (300 W). Once located, the band of interest it was cut out using a UV lamp, and the DNA purification started using a modified version of the crush and soak method [77]. Gel slices were placed at -80 °C for 30 min, followed by 90 °C for 5 min. The slices were then each placed into a 1 ml pipette tip with sealed end and filled with a glass microfibre filter of 2 mm in diameter. Using a 200 µl pipette tip, the slice was finely crushed against the tip wall. 20 µl of elution buffer (2 mM EDTA, 300 mM sodium acetate, pH 7.8) were added and the sealed tips incubated overnight at 37 °C with mild shaking. The bottom of the sealed tip was then cut out and the tips placed into a 0.5 ml eppendorf and centrifuged at 13 krpm for 10 min. The flowthrough was collected as well as any liquid left on the pipette and on the microfibre using a pipette, being mindful not to pick up any crushed gel. The sample was then centrifuged again at 13 krpm for 10 min and the supernatant collected.

2.3.7 Microscale Thermophoresis

Sample preparation

The sample were prepared in PCR tubes and in a minimum of 20 µl volume per reaction to minimise the surface adhesion and evaporation of the sample. The stock solutions were all centrifuged for 5 min at 13 rpm to eliminate any aggregate from the supernatant. Only the supernatant was used to prepare reactions. The sample were mixed by pipetting the volume 5-10 times. Dilutions of the aptamers were incubated at 90 °C for 2 min and then placed in ice until used in the assay [60] All the stock solutions were made in deionised water. Dilutions were done in PBS-Mg with 0.0 % TWEEN 20 for UDP-glucose and in MST buffer (50 mM Tris-HCl pH 7.5, 150 mM NaCl, 10 mM $MgCl_2$, 0.05% TWEEN 20) for UTP. In all final reactions, the buffer concentration was kept constant.

Calibration

Calibration of the amount of necessary aptamer (CY5) to produce a viable signal were performed by preparing an aptamer dilution series staring from 200 nM to 1.56 nM. The capillary scan was performed at 21 °C, with the LED power set to 50% and the infra-red (IR) set to medium. For the MST on-time measurements the standard settings were employed (IR off: 1 s, MST on-time: 20 s, MST off: 3 s). The capillary scan illustrates the fluorescence profile over the capillary diameter. Optimal conditions are achieved when the capillary shape presents a single peak with no widening and with a fluorescence count comprised between 200 and 2000. In the experiment described the count was kept between 300 and 600.

Binding Checks

Binding checks experiments were prepared in 16 PCR tubes: 1-4 for the buffer autofluorescence check; 5-8 is the 0 M check which contains the aptamer in its final optimised concentration and buffer; 9-12 is the complex sample contains both the aptamer and the target molecule at the specified concentration; and 13-16 is the target autofluorescence check, containing target molecule at the specified concentration and buffer. In all

tests, a capillary scan was performed to exclude target induced fluorescence changes. The target and buffer autofluorescence was performed only the first time a new caombination was tested. The LED power was optimised for each test using the "auto" settings in the software, which automatically determined the optimal condition. IR power was set to medium, the temperature set to 21 °C and MST on-time parameters to standard. The response amplitude was calculated by taking the averaging the value of the normalised MST trace (Fnorm) between the chosen time point and the second before, *e.g.* MST on-time 5 s: 4 s - 5 s. Table 2.6 reports the minimum value of the response amplitude to conclude binding.

Table 2.6. MST on-time minimum response ampliture for IR power set to medium

MST on-time (s)	Response Amplitude
1.5	≥ 1.5
2.5	≥ 2.5
5	≥ 3.5
10	≥ 5
>10	≥ 7

The signal-to-noise ratio (S/N) was calculated according to the following formula

$$S/N = \frac{Response\ Amplitude}{\sqrt{\frac{\sum_i (r_i - \bar{r})}{n-1}}} \tag{2.4}$$

The software concludes significant binding when S/N ≥ 5.

Binding Affinity

Binding affinity measurements were prepared on 16 PCR tubes. A target molecule dilution series was prepared starting from 1 mM to 30.5 nM for a volume of 10 µl per reaction. The 10 µl of aptamer stock were added (final concentration: 2.5 nM or 5 nM). The LED power was set at 50% (5 nM aptamer) or to auto (100%, 2.5 nM aptamer) The IR power was set to medium, the temperature set to 21 °C and the standard settings were kept for the MST on-time measurement.

Chapter 3

Optimisation of an aptamer-based electrochemical biosensor platform for real-time continuous detection of small molecules

3.1 Introduction

This chapter describes the processes undertaken to establish, optimise and characterise an electrochemical aptamer-based platform for the continuous monitoring of the release of small molecules. Aptamers, small in size, robust, with high sensitivity and a convenient *in vitro* selection process, provide an universal solution for detection of small molecules, where antibodies may lack selectivity and enzymes do not exist.

Building on these results, my project aims to establish a protocol for the production of aptamer-based electrochemical biosensors as a novel tool for detecting purine release in the brain. The devices are composed of self-assembled monolayer of methylene-blue-decorated aptamer and backfilling molecule on a gold surface. The device exploits the conformational change in the aptamer structure to generate a displacement of the methylene blue molecule. The movement alters the contact probability with the gold surface, which results in a signal variation. The signal plotted over time

should presents a step-like increase where the target is added. The backfilling with 6-mercapto-1-hexanol (MCH) acts as a compact layer passivating the sensor surface. The design allows for continuous real-time monitoring of molecule release.

The process started with the adenosine and adenosine triphosphate (ATP) aptamer with two binding sites published by Huizenga and Szostak [95], and proceeded with the characterisation of the modified sequences published by Zhang, Oni, and Liu [307] and Zhang and Liu [306]. These presented a chance for higher sensitivity as both contain one binding site, and the latter has been destabilised to induce structure-switching properties [289]. The sensor should ideally present a limit of detection in the high picomolar/low micromolar range for adenosine but not for its downstream purines and a time resolution possibly millisecond-second range.

With the intent to improve the sensor performance, different SAM fabrication protocols, characterisations, measuring techniques and device geometry were assessed. Finally the selectivity of the biorecognition element was assessed by testing the response to downstream purines and ATP.

I set out with the hypothesis that methylene blue conjugates of an aptamer could be developed into a sensitive electrochemical biosensor for purines. Extensive development and testing of the hypothesis is described.

3.2 Results

3.2.1 Sensor fabrication

The first experiments aimed to verify whether the protocol produced aptamer sensors successfully. To do so, I recorded a cyclic voltammogram (CV) in ferricyanide solution after each incubation step. For an ideal gold surface, the distance separating the oxidation and the reduction peaks (ΔE_p) in the cyclic voltammogram is c.a. 59 mV as described by the Nernst Equation [57]. After the incubation steps, the molecule density on the surface of the electrode increases. The newly formed molecular layer hinders the electron transfer from the ferricyanide in the solution to the electron surface and vice-versa, thus requiring more extreme voltages to achieve both oxidation and reduction. Consequently, the ΔE_p increases. The cyclic voltammograms recorded after each incubation step confirmed the expected results, with a ΔE_p of 68 mV for the bare surface (after polishing), which increased to 160 mV following the 1.5 hour incubation with 500 nM aptamer solution, and to 243 mV after 18 h incubation with 5 mM MCH. This shows that the fabrication protocol was effective (Figure 3.1.a). However, these observations are not sufficient to characterise the surface functionalisation, as it does not provide confirmation for the surface entrapment of DNA aptamers.

To verify the presence of aptamers on the surface, I recorded a CV in PBS to identify the redox peaks characteristic of methylene blue (Figure 3.1.c). The resulting CV was compared to the one obtained by scanning the same potential range with a gold surface functionalised with only with MCH, *i.e.* lacking the aptamer, as working electrode and using 10 µM methylene blue in PBS as electrolyte (Figure 3.b). The redox peaks for the free methylene blue appear at slightly less negative voltages compared to the ones of the DNA-methylene blue complex anchored on the sensor.

This difference in behaviour could originate in the surface localisation of the redox moieties [74] or from the conjugation of the dye to the oligonucleotide. The ΔE_p of the two cyclic voltammograms was also different, with 29 mV for the free methylene blue and 16 mV for the DNA-methylene blue complex. For the free MB, the value matches expected ΔE_p derived from the nerst equation for a 2 electron transfer. For reversible species adsorbed on the surface, the peak-to-peak separation should be

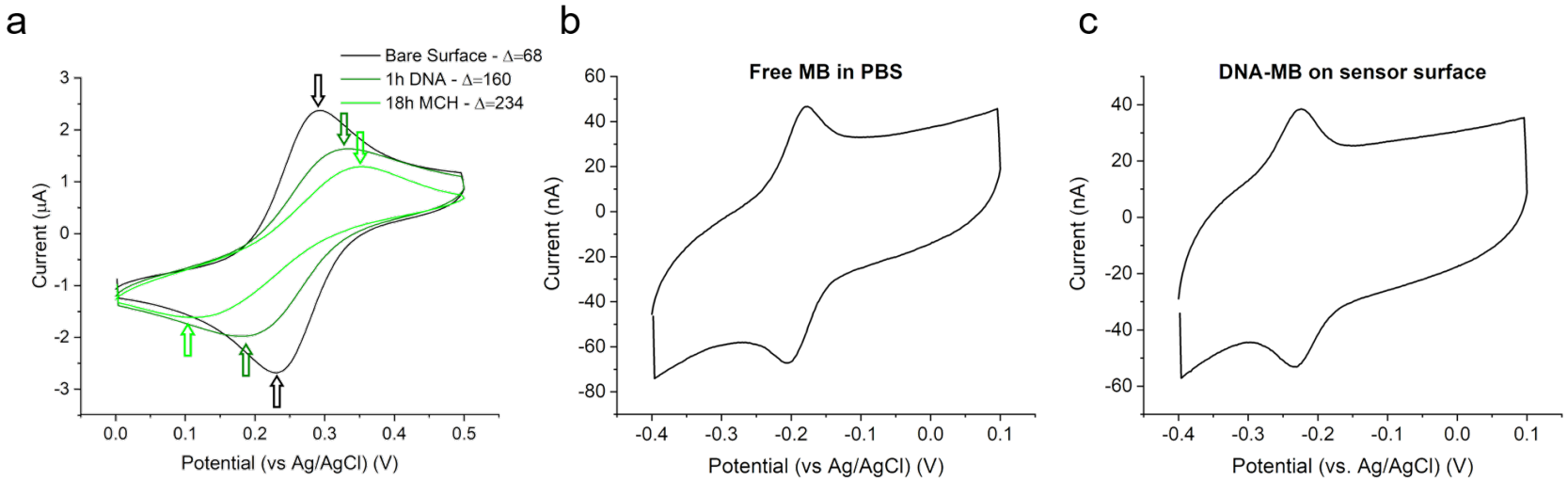

Figure 3.1. Cyclic voltammetry scan of the sensor fabrication. *a) Cyclic voltammograms recorded in ferricyanide (0.5* mM*) sparged with* N_2 *for 10* min *from 0* V *to 0.5* V *vs Ag/AgCl and scan rate of 50* $\mathrm{mV\,s^{-1}}$*. The scan were recorded after each incubation step of backfilling protocol used in the sensor fabrication. As expected, the binding of DNA (*ΔE_p*=160* mV*) and 6-mercapto-1-hexanol (MCH) (*ΔE_p*=234* mV*) to the surface impairs the electron transfer between the ferricyanide and the gold surface, thus increasing the value of the* ΔE_p *(legend). The arrows indicate the oxidation and reduction peaks used to evaluate the delta (*$\Delta E_p = E_{red}\text{-}E_{ox}$*) for each curve. b)-c) Cyclic voltammetry scan on the range -0.4* V *- -0.1* V *vs. Ag/AgCl covered in MCH in PBS with 10* µM *free methylene blue (MB) in PBS (redox peaks at -0.198* V *and -0.175* V *vs. Ag/AgCl, panel b) or with DNA-MB anchored on the surface (redox peaks at – 0.254* V *and – 0.238* V *vs. Ag/AgCl, panel c). All recordings were performed in solution sparged with* N_2

zero [57]. However, the methylene blue was adsorbed onto the surface via a DNA and carbon chains, thus the ΔE_p value larger than zero would suggests that the MB anchored to the surface via the oligonucleotide experiences a restive component to the electron transfer.

Therefore, it can be concluded that the fabrication successfully produced a MCH and MB-aptamer mixed layer on the gold surface.

3.2.2 Self-assembling monolayer (SAM) protocol optimisation

Having demonstrated successful fabrication of the sensor, I next sought to optimise each step. I started by comparing the two main protocols employed to form self-assembling monolayers (SAM) found in literature: the backfilling and the insertion protocols. According to the backfilling protocol, adapted from Arroyo-Currás et al. [6], fabrication starts with the incubation of the sensor surface with the oligonucleotides for 1.5 h, followed by incubation with the passivisation layer, 6-mercapto-1-hexanol (MCH), overnight. Instead, in the insertion protocol adapted from Jia et al. [99] the order is inverted with the sensor undergoing first overnight incubation with MCH and then 1.5 h incubation with the aptamers.

Each protocol has its own advantages. The backfilling protocol generates higher aptamer density on the surface, given that they have access to the full surface. However, given the diffusional nature of the thiol bond [23, 253, 254, 242, 231], the surface-bound oligonucleotides can migrate and aggregate, driven by hydrophobic interaction. The clustering generates both steric hindrance and repulsive coulombic interactions which can reduce the sensor capability to detect the target molecule [286]. Additionally, the DNA-strands, based on their orientation with respect to the surface, can prevent access to the gold binding site which can result into an incomplete passivation by the MCH and leaves the surface free for oxygen reduction and fouling by molecules [101, 298]. On the other hand, the insertion protocol produces a uniform and complete passivation layer, as the MCH is incubated first with the freshly activated gold surface, with homogeneously distributed probes [298]. The drawback of this method is that the only sites left for the DNA to bind are the unstable binding sites, either crystal

defects or boundary sites between different crystal structures. This results both in low signal and low stability of the bonds [101].

Once fabricated three sensors with each protocol, a CV in PBS was recorded to characterise signal generated by each sensor. The comparison of the resulting voltammograms demonstrates that the backfilling protocol produced a higher signal, thus aptamer density, with respect to the insertion protocol(Figure 3.2), in agreement with the previously published work. Given that the higher signal, means higher signal-to-noise raitio, fundamental in achieving detection at lower concentration, the backfilling protocol was employed from this point onward to fabricate the sensors.

Next, denaturing and snap cooling of the aptamer was tested as an initial step with the aim to improve aptamer immobilisation on the sensor surface. The aptamer aliquot was thawed at room temperature, incubated at 95 °C for 8 min and snap cooled in ice for 10 min. Heat denaturation destroys the secondary structure and converts the aptamer to a linear form. Rapid (snap) cooling prevents refolding and H-bond formation once the temperature is again below the melting temperature. To ensure aptamers stay in linear form, the next incubation step with TCEP was also performed at 4 °C.

Once fabricated the sensors following each protocol (3x backfilling and 3x melting+backfilling) a CV was recorded in PBS to characterise the sensor functionalisation. The sensor produced with the melting+backfilling protocol (black) resulted in a methylene peak that is 1.7-fold larger with respect to the backfilling protocol only (orange, Figure 3.3), further improving the sensor signal. Looking at the aptamer densities, the melting+backfilling protocol proved to best the backfilling only protocol with an aptamer density of 2.2 fmol cm^{-2} compared to 1.5 fmol cm^{-2}, with an increase of factor 1.44x. As a result, all subsequent fabrications followed the melting and backfilling protocol. However, this result is not absolute, as the optimal concentration may vary depending on multiple parameters such as: aptamer length, the target molecule size and the detection technique.

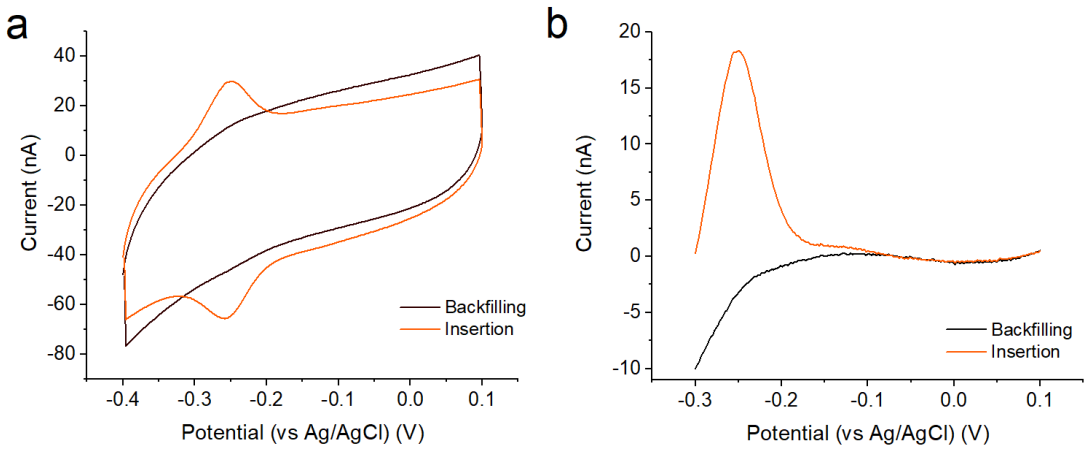

Figure 3.2. ***Cyclic voltammogram of two sensors fabricated using the backfilling (black) and insertion (orange) protocol (a) and detail of the methylene blue (MB) peaks with background current subtracted.***

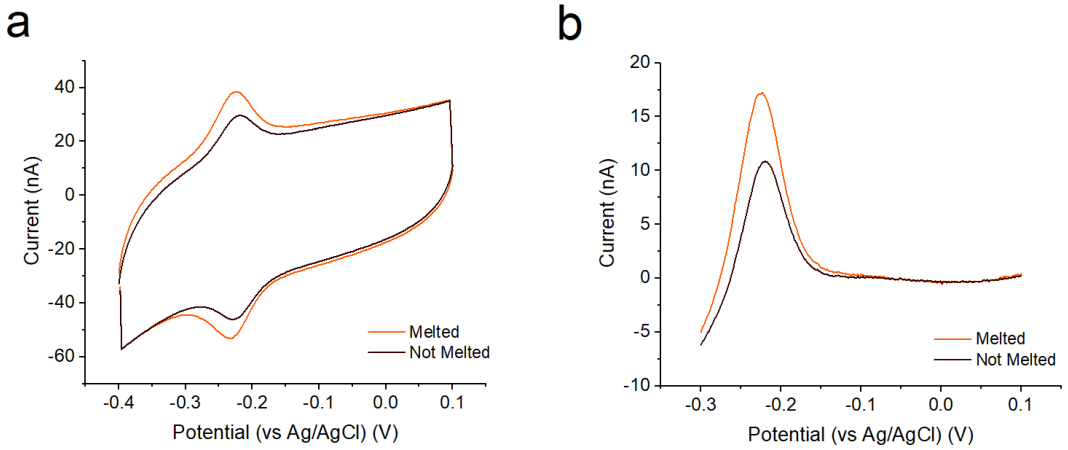

Figure 3.3. *Cyclic voltammogram of two sensors fabricated with backfilling protocol (black) and backfilling+melting of the aptamer (orange) (panel a) and detail of the peak with background current subtracted (panel b). The higher peak (1.7 fold increase) indicates a higher aptamer density on the surface.*

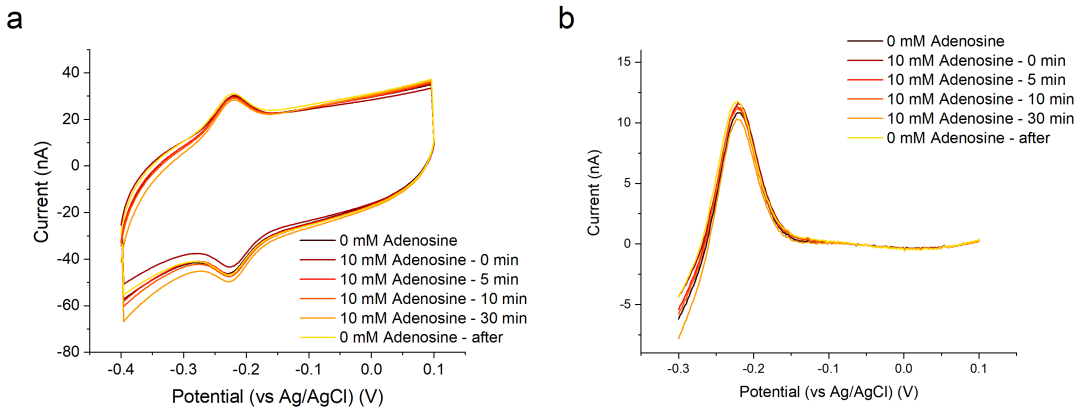

Figure 3.4. Response to 10 mM ***adenosine recorded from recorded from the a sensor produced with melting+backfilling protocol.*** *a) CVs recorded in presence and absence of the target molecule at different time points (legend) and detail of the peak (b)*

3.2.3 Square Wave Voltammetry

With each optimisation step, I made an attempt to record the sensor response to the presence of adenosine at different time points with CV. Despite the 10 milliM concentration of adenosine, well above the aptamer K_D and the long incubation time tested (up to 30 minute), none of the recording presented a response. I hypothesised that since the 2BS aptamer was already in a stem-loop conformation in absence of the target molecule [307], the conformational change caused by the binding was not sufficient to generate a measurable signal.

Since cyclic voltammetry showed insufficient sensitivity to detect signal variation in the presence and absence of the target, a different technique was employed. Square wave voltammetry (SWV) is an electrochemical technique in which the potential applied is the superimposition of a staircase with a square wave potential. The current is sampled in the second half of the potential step (positive and negative) resulting in a forward and the reverse current and the difference between the two is used as the final curve. By applying a staircase potential with small increments and a high enough frequency, the non-faradaic contribution to the current (charge and discharge of the double layer) is eliminated which results in a lower background current. Furthermore, by evaluating the difference between the forward and the reverse process,

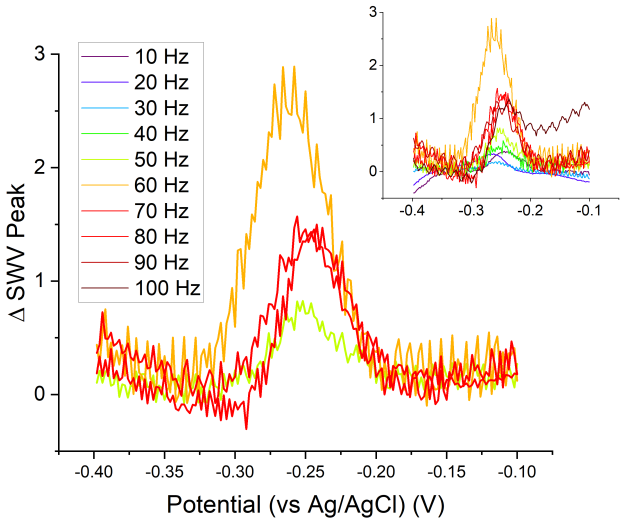

Figure 3.5. Evaluation of the optimal frequency for square wave voltammetry (SWV). *The image overlays the difference between the curves recorded in PBS spiked with 1* mM *for each frequency in presence and absence of 1* mM *adenosine. The insert shows the plot of all curves.*

also any drift contribution is cancelled, as both reactions would be equally affected by it [122]. Therefore, SWV was employed to characterise the sensor response to the presence of adenosine.

I started by investigating the optimal frequency by testing the range spanning from 10 Hz to 100 Hz. A SWV peak was recorded for each frequency at 0 mM and 1 mM adenosine in PBS spiked with 1 mM $MgCl_2$ (PBS-Mg), keeping the rest of the parameters constant. The two recordings were subtracted from each other and the result plotted in Figure 3.5. 60 Hz was selected, as it presented the highest signal-to-noise ratio.

Once established the optimal frequency, the sensor response was recorded in PBS-Mg, 10 mM adenosine and PBS again, to monitor the target release. The measurements were performed in the indicated solution, in absence of flow, and the value obtained from 5 successive recordings plotted. Figure 3.6.a illustrates the averaged raw traces recorded in presence and absence of the target molecule, whilst Figure 3.6.b shows the analysed response. The plot show that the sensor responded to the presence of the target molecule with an average increase in peak current of 58.4 $\pm$ 4.0 nA ($\bar{x} \pm e_a$, n=5). The response remained stable after 5 min and recovered to the baseline

after washing out. Having successfully recorded a signal variation, I proceeded with studying the concentration-response curve of the sensor over a range of concentrations spanning from 100 nM to 10 mM. As demonstrated by Figure 3.6.c, the sensors exhibited reproducible performance as all the devices presented a response above the concentration of 100 µM. However, the observed limit of detection was an order of magnitude greater than the aptamer K_D which was reported to be 14 µM [95]. This result suggested that the design of the sensor needed further improvement.

In the attempt to improve the sensor response a longer backfilling molecule, 11-mercapto-1-undecanol (MCH_{11}), replaced MCH in the protocol to reduce the background noise. Six electrodes are fabricated with only the backfilling layer (18 h in 5 mM MCH (3x) or MCH_{11} (3x) at 4 °C). The CV scan in PBS solution presented no significant difference in the background measured between the surfaces fabricated with MCH and MCH_{11} and the methylene blue peak is smaller (Figure 3.7). Given that the aptamer was functionalised with a six-carbon chain on the 5' end, it can be hypothesised that the presence of a compact mat of an eleven-carbons chain reduced the electron transfer rate or hindered the aptamer folding into its secondary structure, thus resulting in a lower signal. Additionally, the shorter aptamer disrupting the mat could promote aptamer clustering and reduce their binding capability due to Coulombic interactions. Schoukroun-Barnes et al. [223] published similar results when looking at the optimal protocol for the fabrication of their electrochemical biosensor. However, in their study they used spacer with matched length for both the passivation mat and the aptamer spacer and still found that the MB signal was reduced compared to the signal of the 6-carbon spacer.

Next, the three adenosine and ATP aptamer strands Table 2.1 are compared by fabricating three sensors on the 1.6 mm Au disk and their response to adenosine was measured over time for concentrations spanning from 100 nM - 10 mM. The purpose of this experiment was to evaluate whether the single binding site aptamers could provide a higher sensitivity to the sensor, especially for the 1BSS aptamer as in the work by White, Rowe, and Plaxco [289] truncating the aptamer stem of the 2BS aptamer resulted in a significant improvement of the signal recorded. Figure 3.8 reveals that both 1BSS and 2BS aptamers present a higher response to target binding, 3.92 ± 0.38

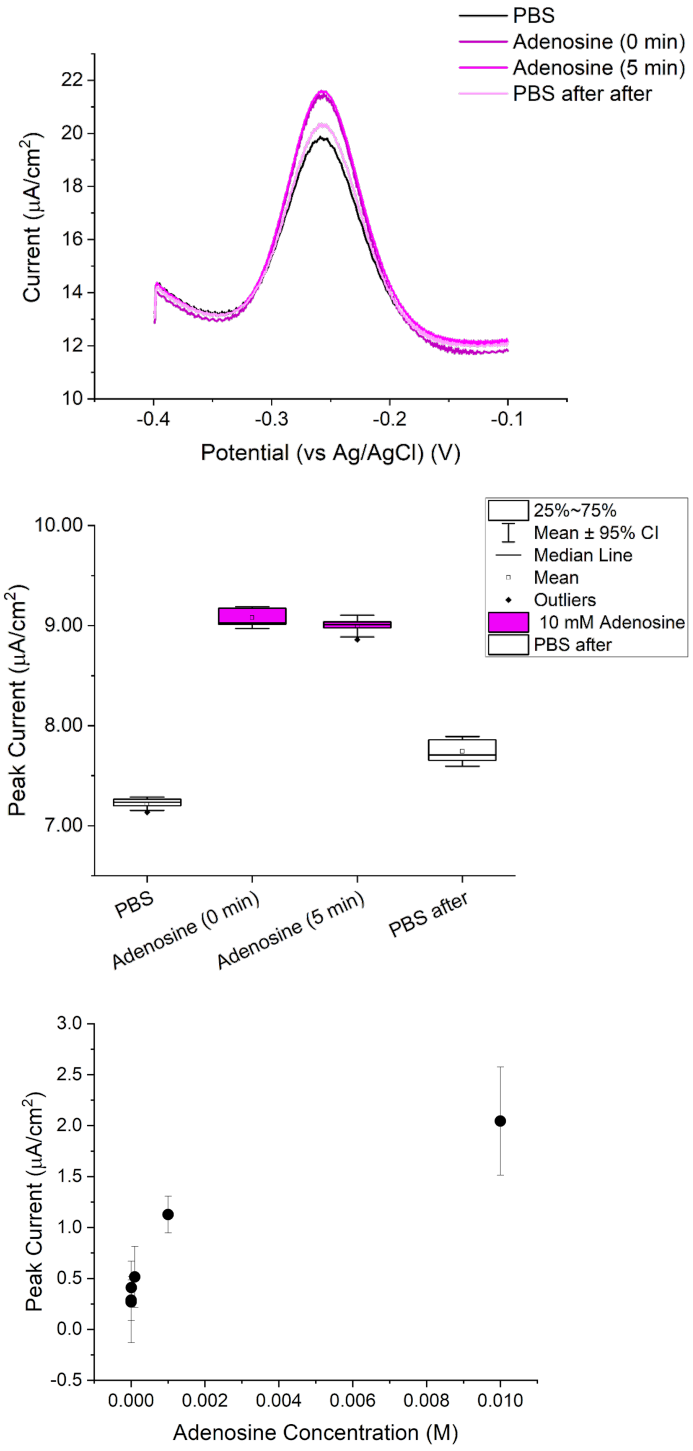

Figure 3.6. Sensor response characterisation with square wave voltammetry (SWV). *a) Raw trace of the SWV voltammetry measurements and the sensor response to 10* mM *adenosine. The SWV acquired in PBS (before and after) are in black, and the graph demonstrates that the sensor does recover its baseline once in buffer, whilst the response to 10* mM *Adenosine at both 0* min *and 5* min *time points are represented in magenta. b) Response of one sensor fabricated using the melting and backfilling protocol to 10* mM *adenosine. Five consecutive SWV measurements are performed for each solution. The sensor presents no delay in responding to the target molecule with an average increase of 1.86* $\mu A\,cm^{-2}$ *in its peak current. c) Measurements from three sensors fabricated with melting and backfilling protocol are displayed comparing their responses to a range of adenosine concentrations (100* nM *to 10* mM*) in PBS-Mg. The response is calculated as the difference between current density for the response and baseline. Data: mean ±* e_a*, n=3.*

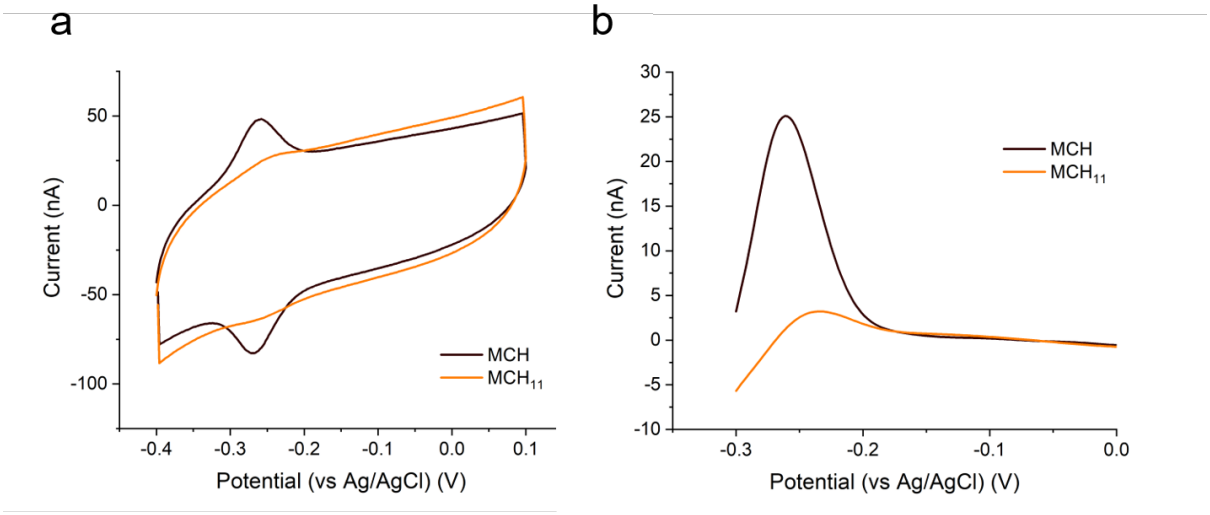

***Figure 3.7. Cyclic voltammogram of two sensors fabricated using different length backfilling molecules**: 6-mercapto-1-hexanol (MCH, black) and 11-mercapto-1-undecanol (MCH11, orange) (panel a) and detail of the two peaks with background current subtracted (panel b).*

µm cm^{-2} respectively for 10 mM adenosine in PBS, compared to the 1BS aptamer 1.06 ± 0.35 µm cm^{-2} ($\bar{x} \pm e_a$, n=3). Furthermore, the 1BSS and 2BS aptamers responded to lower concentrations down to 100 µM, whilst the 1BS exhibited no signal increase except for the highest concentrations (millimolar range). This result is in contrast with the reported K_D for the three aptamers as they all were in the range of 14-16 µM. I hypothesised that the much lower response presented by the 1BS aptamer was due to the 7 bp-long double-stranded DNA stem at the base, which reduces significantly the variation in the position of the redox probe upon binding. This hypothesis is also supported by the response measured for the 1BSS aptamer, where the long stem has been reduced by 4 bp, and the signal strength was recovered and was comparable to the one of the original aptamer. Since neither of the modified strands significantly improved the sensor response, later experiments were carried out with the 2BS aptamer.

Table 3.1. Au sensor surfaces employed in the project with respective geometries and surface areas.

Device	Diameter	Geometry	Surface area
2 mm Au disk	0.2 cm	Disk	0.0314 cm^2
1.6 mm Au disk	0.16 cm	Disk	0.0201 cm^2
50 µm Au wire	0.005 cm	Wire, 2 mm long	0.0031 cm^2

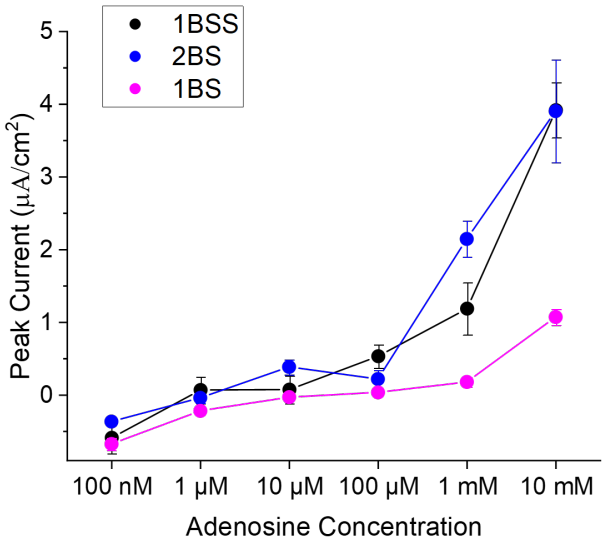

Figure 3.8. Evaluation of the biosensor response produced on the 1.6 mm ***Au disk with the three adenosine and ATP aptamers****: the one binding site with shorter stem from Zhang and Liu [306] (1BSS, black), the two-binding site from Huizenga and Szostak [95] (2BS, blue) and the one-binding site with full-length stem from Zhang, Oni, and Liu [307] (1BS, magenta). The response is evaluated in a concentration range spanning from 100* nM *to 10* mM*. The response is calculated as the difference between response and baseline, averaged by the surface area (*cm^2*). The data reveal that the 1BS aptamer is the worst performing with a response of 1., aft06±0.35* $\mu A\,cm^{-2}$ *at the maximum concentration tested, whilst the 2BS and 1BSS performed above 3.90±2.20* $\mu A\,cm^{-2}$ *and 3.92±0.38* $\mu A\,cm^{-2}$ *respectively. Data: mean ± e_a, n=3.*

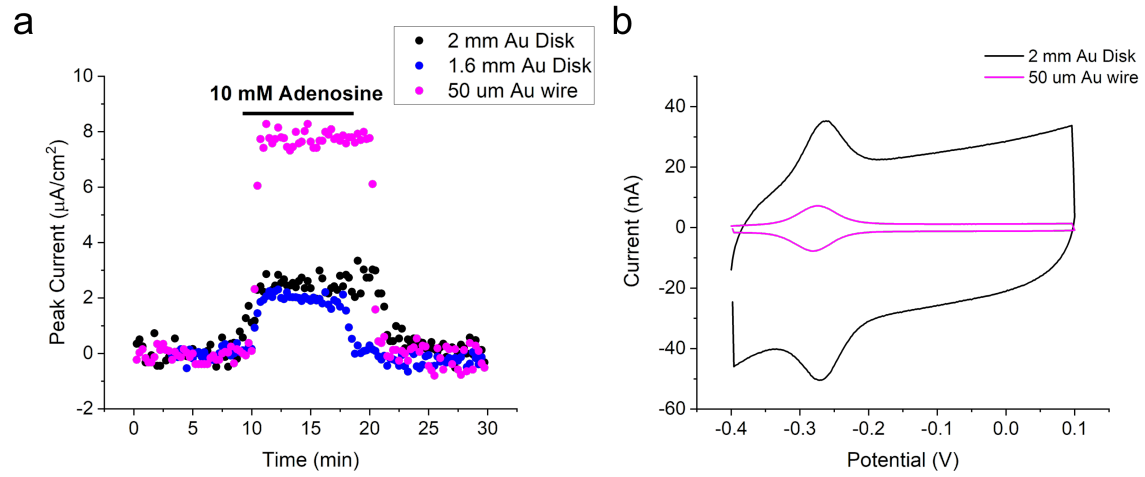

Figure 3.9. Analysis of the relationship between surface dimensions and signal to noise ratio. *a) The three sensors are fabricated with the melting+backfilling protocol using the 2BS aptamer on 2* mm *Au disk (black), 1.6* mm *Au disk (blue) and 50* µm *diameter, 2* mm *long Au wire (magenta). The response to buffer containing 10* mM *adenosine is measured via repeated SWV measurements. The signal measured over-time is normalised by the surface area of each sensor. As displayed, the 50* µm *Au wire improved the signal registered by roughly three-fold with respect to the 2* mm *Au Disk. b) Cyclic voltammogram of the fabricated 2* mm *Au disk and 50* µm *(2* mm*) Au wire sensors. The cyclic voltammogram demonstrates that the wire design presents higher signal to noise ratio (S/N) with respect to the disk design.*

Finally, different sensor design were tested to improve the sensor response. Two sizes of disk sensors, 2 mm and 1.6 mm Au disk; and a wire sensor, 50 µm diameter and 2 mm long Au wire (dimensions in Table 3.1); were employed to fabricate the biosensors following the melting and backfilling protocol and their response to 10 mM adenosine recorded via repeated SWV measurements. Figure 3.9 illustrates the response registered for the 2 mm Au disk (black), 1.6 mm Au disk (blue) and the 50 µm Au wire (magenta) to 10 mM adenosine in PBS-Mg. The average responses are 2.51 $\pm$ 0.32 µA cm^{-2}, 1.92 $\pm$ 0.26 µA cm^{-2} and 7.67 $\pm$ 0.43 µA cm^{-2} for the 2 mm, 1.6 mm and 50 µm probe respectively ($\bar{x} \pm e_a$, n=3). The probe design displays a three-fold increase in the current-per-square-centimetres with respect to the disk counterparts, thus suggesting that the new wire geometry effectively improved the signal-to-noise ratio.

Figure 3.9.b illustrates two exemplary CV recordings done on a disk sensor (black) and on a wire sensor (magenta). By extracting the moles of electrons exchanged

between the surface and the solution and averaging them by the geometrical surface area of the sensor, the wire sensor proved to exchange four-times the moles of the electrons exchanged by the disk sensor (16 ± 8 nmol e cm^{-2} vs 3.8 ± 0.4 nmol e cm^{-2}, for the wire and the disk sensor respectively. Data: $\bar{x} \pm e_a$, n=3). This result could justify the higher signal-to-noise ratio recorded. However, the geometrical area is an underestimation of the two areas since both the disk sensor underwent an etching preparation step, physical for the disk and chemical for the wire), so the evaluation is not exact. Additionally, another factors could have contributed to the improvement in sensor performance is the geometry itself. In the wire sensor, a higher surface packing density can be reached before incurring into steric hindrance and crowding effects amongst the oligonucleotide strands [210], thus resulting in a higher signal. Finally a difference in the flow in the electrochemical cell could have contributed to the difference in sensor performance.

To verify the impact of the new design on the sensor response and the dynamic range I fabricated three probe sensors using the melting+backfilling protocol and the 2BS aptamer. Each sensor was interrogated with square wave voltammetry using the same range of adenosine concentrations (100 nM - 10 mM) and its response was recorded as the difference between the current peak with and without target. The responses of the three sensors are plotted in Figure 3.10.

The data illustrated shows overall a significantly higher response to the presence of the target molecule with a significant response that start now at 10 µM, one order of magnitude smaller than what reported for the disk sensor. Additionally, by paying closer attention to the single concentration, it emerges that the highest concentration shows a response almost 5-times the one of the disk sensor (2 µA cm^{-2}) and that the same variation in peak current was registered by the probe design for 100 µM adenosine, an improvement of 3 order of magnitude in sensitivity.

After having established the fabrication protocol, improved the aptamer concentration on the surface, tested different techniques and changed the design from micro to mini-electrode, the sensor detection range matched the physiologically interesting one. Therefore, I decided to move on from the optimisation process and

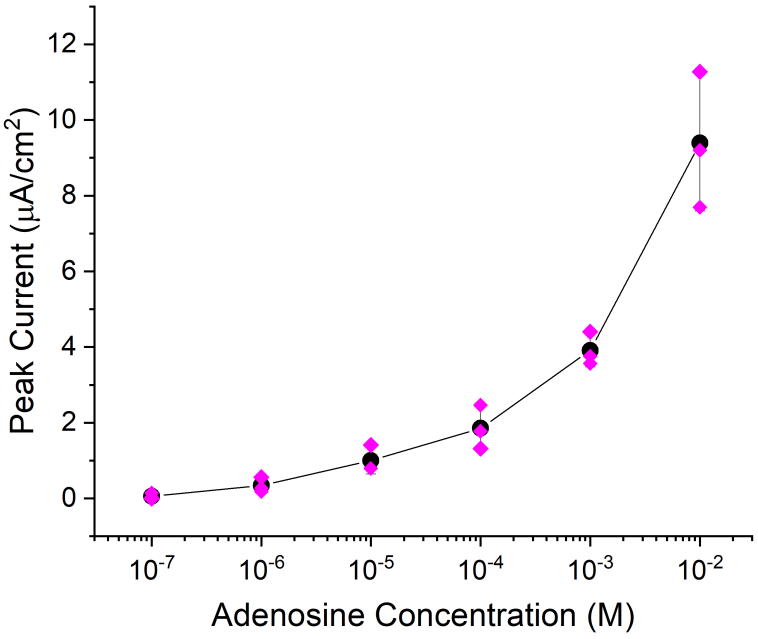

Figure 3.10. Evaluation of the probe sensor response to test the dynamic range of the sensor response. *Measurements from three sensors fabricated with melting and backfilling protocol are displayed comparing their responses to a range of adenosine concentrations (100* nM *to 10* mM*) in PBS-Mg. The response is calculated as the difference between current densities of the response and baseline. The sensors present response to the presence of adenosine from 10* μM *on, one order of magnitude lower than the LOD for the disk sensor (Figure 3.6.c). Data: mean* ± e_a*, n=3.*

continue by evaluating the selectivity of the platform so far described.

3.2.4 Evaluation of sensor response to downstream purines

To verify whether the platform was sufficiently selective, I proceeded with characterising the response of the sensor to downstream purines. In the brain, adenosine is present in the high nanomolar range (10 to 100 nM), as the product of the breakdown of adenosine triphosphate (ATP) and its di- and mono-phosphate form. Adenosine can also be produced further broken down in its downstream purines: inosine and hypoxanthine [189]. Consequently, both inosine and hypoxanthine will be present when recording from biological samples and it is important that the sensor shows no or a low enough sensitivity for the relevant concentrations. Multiple studies employing different protocols and measuring techniques were performed to evaluate the amounts of adenosine, inosine and hypoxanthine released upon an hypoxic event [13, 81, 43] have reported that in rat brain slices undergoing ischemia and hyp[oxia of variuous duration, the extracellular concentration of adenosine, inosine and hypoxanthine were in the ranges of 3-30 µM, 1-10 µM and 1-5 µM respectively. For the sensor to be considered selective for adenosine, it should not be responsive to 100 µM of either inosine and hypoxanthine.

Therefore, the 2BS aptamer was evaluated against ATP, Hypoxanthine and Inosine, using recordings over the 10 µM - 10 mM concentration range. I made many attempts to measure a response to ATP in disodium salt, but none of the recordings showed any response from the sensor, even at the highest concentrations tested (10 mM). Since in biological systems, ATP exists as a chelated complex with Mg^{2+}, I examined whether ATP as a magnesium salt could be detected, and both aptamers responded. Figure 3.11 illustrates the response to 1 mM ATP disodium (black) and magnesium (magenta) for the 2BS aptamer.

To test whether the difference in response recorded by the aptamer was due to the sensing platform or the aptamer itself, the SYBRGreen (SG) assay [164] was performed using the same concentration ranges used for the electrochemical platform (100 nM - 10 mM). Figure 3.12 displays the fluorescence spectra of SG intercalated with the 2BS aptamer. The spectra intensity shows a decreasing signal in response to higher concentrations of ATP magnesium (panel a) and disodium (panel b). By comparing the

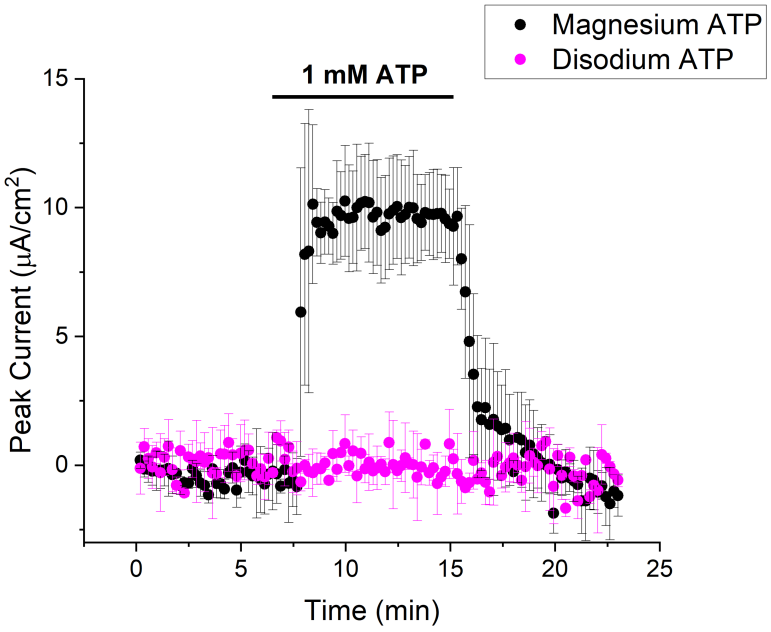

Figure 3.11. Response to disodium and magnesium adenosine-triphosphate (ATP). *The graph shows the average response of sensors fabricates using the two binding site aptamer [95] to 1* mM *magnesium ATP (black) and disodium ATP (magenta). The illustration proves that the aptamer on the platform is not sensitive to disodium ATP even at high concentrations, where a significant response is expected. Data: mean ± e_a, n=3.*

two responses normalised against the 0 mM concentration (PBS) (Figure 3.12, c) it was possible to conclude that the aptamer showed an increasing response to both forms of ATP from 10 µM onward. An additional test was made using the Thioflavin-T assay published by Renaud de la Faverie et al. [209]. The results confirmed the one obtained with the SG assay (data not shown). Therefore, it was deduced that the reason behind the lack of response from the sensor is an issue inherent to the platform itself.

Therefore, I proceeded to characterise the dose response of the sensor to ATP-Mg and adenosine. Figure 3.13.a demonstrates that the sensor is more responsive to ATP (orange) than to adenosine (black), with a signal on average 4.7-times larger. However, the standard deviation for the response for ATP are significantly larger relative to the response *e.g.*, 19.5% for adenosine and 26.3% for the 10 mM concentration, the smallest of the error bars for ATP. Figure 3.13.b displays the dose response of adenosine (black) against its metabolites: inosine (blue) and hypoxanthine (magenta). The traces prove an overall higher affinity of the aptamer towards adenosine, when compared to the downstream purines.

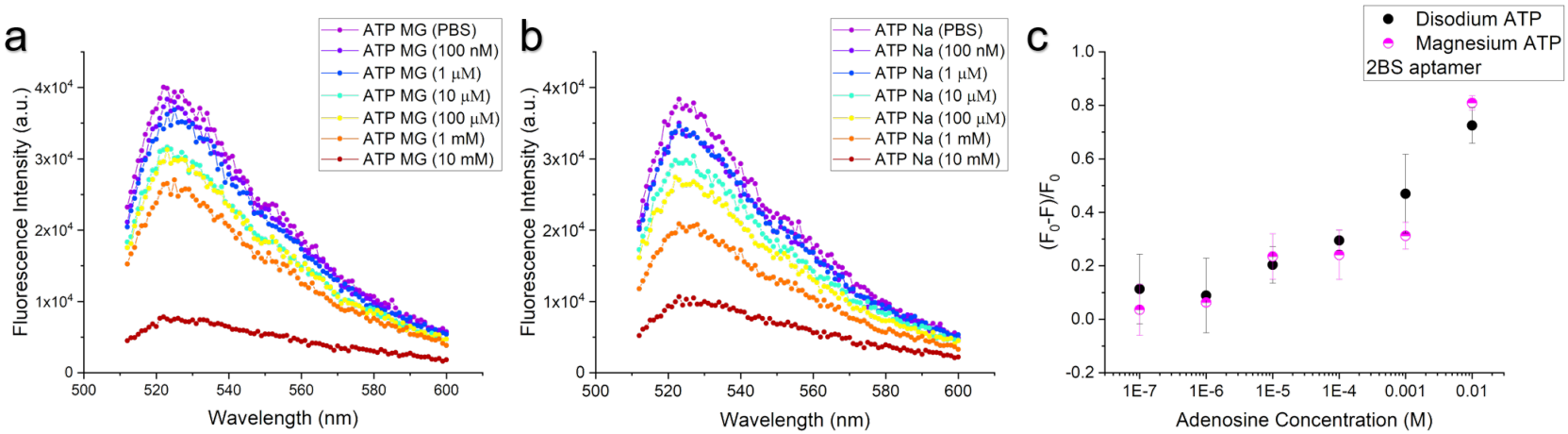

Figure 3.12. Evaluation of the Huizenga and Szostak [95] aptamer response to adenosine triphosphate in disodium and magnesium salt using the SYBRGreen assay. *Spectral curves of the fluorescence intensity signal recorded for the aptamer to ATP magnesium (panel a) and ATP disodium (panel b). c) Comparison of the sensor response to the ATP in the two salts. Data: mean ± e_a, n=3.*

Remarkably, the sensor does not to appear to present any response to the downstream purines below the millimolar range: 0.5 mM and 1 mM for hypoxanthine and inosine respectively. This lack of response matches the requirement for the sensor selectivity for performing extracellular recordings.

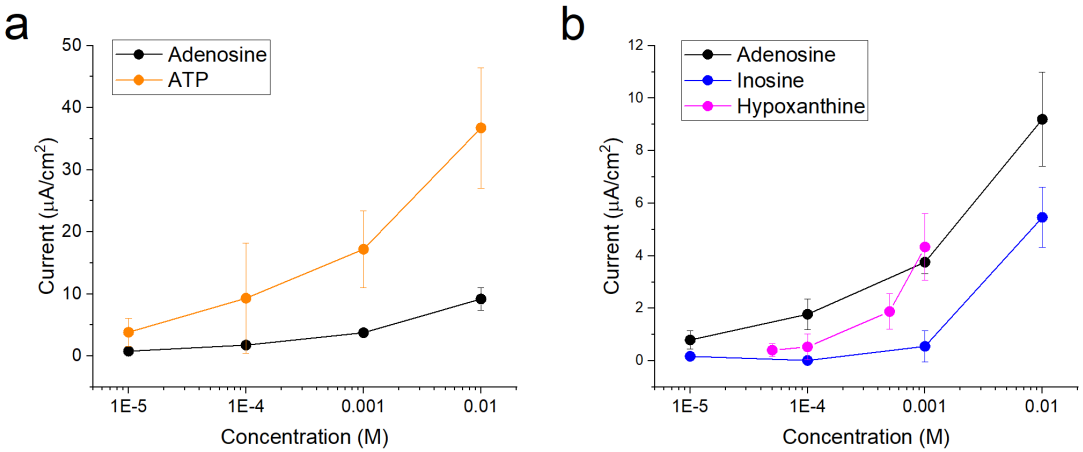

Figure 3.13. Characterisation of the sensor response to ATP, adenosine, inosine and hypoxanthine. *The sensors are fabricated with melting+backfilling protocol with the 2BS aptamer on a probe device. The sensor is interrogated over a concentration range spanning from 10* µM *to 10 10* mM *of ATP (orange, panel a), adenosine (black, panel a and b) and inosine (blue, panel b). For hypoxanthine (magenta, panel b) the range spans from 50* µM *to 1* mM *due to the low solubility of the molecule. The response is calculated as the difference between peak current density in presence and absence of targets. The average of three sensors is plotted for each condition. The graph illustrates the averaged response over the concentration range. Three sensors are used to test each condition. Data: mean* $\pm$ e_a, n=3.

3.3 Discussion

The aim of the first part of this chapter was to establish the optimal protocol for the fabrication of an aptamer-based biosensors for the continuous detection of adenosine and ATP in real-time. The initial step consisted in producing the biorecognition layer via self-assembling monolayer protocol (SAM) and its characterisation via cyclic voltammetry in ferricyanide and in phosphate buffer saline (PBS) with methylene blue. The results demonstrated that the gold surface was successfully coated with both the backfilling mat of thiolated carbon chains and the presence of methylene blue-labelled aptamers.

The SAM fabrication was then optimised by testing two protocols: the insertion and the backfilling protocol. The results confirmed what found in literature, with the sensor produced following the backfilling protocol showing a significantly lager signal with respect to the insertion one. Given that the sensor was still not showing any significant difference in signal generated in presence and absence of target molecule, I chose the backfilling protocol to continue the optimisation. The higher MB signal provided the best chance for achieving a response, backed by the many previous publications reporting successful sensor fabrication with controlled surface densities using this protocol *e.g.* Zhang et al. [302], Arroyo-Currás et al. [7], Yan, Wang, and Chen [296], and Steel, Herne, and Tarlov [249]. However, the comparison between backfilling and insertion will need to be repeated, possibly with optimised aptamer concentration and MCH incubation for the insertion protocol, once the measurements are performed with in a complex environment.

The aptamer surface density was increased by melting and snap cooling the aptamers, which destroyed the secondary structure and reduced the aptamers to linear form. The sensors fabricated using this method presented a 1.5 fold increment in aptamer density on the surface with respect to the previous protocol. The aptamer surface density of the melting protocol better mimics the optimal concentrations found in literature. Cheng, Ge, and Yu [36] and Simon, Bognár, and Gyurcsányi [240] found that the optimal aptamer concentration is of approximately 2.7 $\mathrm{fM\,cm^{-2}}$ for respectively their electrochemical biosensor and SPR assay to detect IgE. However, despite hav-

ing employed the same protocol the probe densities obtained dis not match the ones published in previous works employing the same protocol, which display protocol densities of 2-20 pM for detection of thrombin and cocaine [294, 257], target molecules of comparable size scale to ATP and adenosine.

Before undergoing another optimisation of the protocol, I characterised the response to adenosine in a concentration range spanning from 100 nM to 10 mM to verify the quality achieved so far by the sensor and its optimisation process. In previous attempts at recording a response cyclic voltammetry and amperometric current-vs-time curves were employed, but neither showed sufficient sensitivity to record the signal variation. Consequently, the sensor was interrogated using square wave voltammetry, a technique that, by sampling the current values at voltage pulses, removes the double layer contribution to the current. This results in a lower background current. Furthermore, since the oxidation and reduction current are subtracted to each other, the overall signal is higher and the drift contribution is automatically eliminated, as it affects both currents equally. The sensor dose response presented a linear behaviour starting from 100 µM. This result matches what previously achieved by White, Rowe, and Plaxco [289]. However, since the K_D of the aptamers reported by Huizenga and Szostak [95] and Zhang, Oni, and Liu [307] is of 14 µM, the result indicated that platform needed further improving. The lowest detected quantity being almost one order of magnitude larger than the published K_D indicated that the optimisation needed by the platform was more structural than tuning in nature. Finally, for the platform to be used for its intended application, to detect extracellular adenosine from brain tissue, the sensors needed to work in the physiologically relevant concentration range, which is in the low micromolar range [125].

To further improve the sensor performance, the relationship between sensor geometry and response was investigated by testing two disk and one wire sensor. The wire sensor presented the highest signal-to-noise ratio. A possible explanation is that the difference in design and exploiting the different mass transport properties of planar and cylindrical sensors could have improved the sensor response [222]. The advantages of wire geometry versus disk geometry were previously reported by Wang et al. [279] by comparing the two geometries at the nanoscale. If this hypothesis was to

be true, then adenosine diffusion would be the rate determining step in the response.

Additionally, the wire design could have reduced the steric hindrance among the oligonucleotides, with respect to the disk sensor, thus generating a higher signal for the same surface density.

The adenosine and ATP aptamer by Huizenga and Szostak [95] is quite an old and popular one amongst researchers. Many platforms with radically different designs have been created using this aptamer, thus providing a very rich library for a comparison of the different sensor characteristics.

The limit of detection (LOD) of the electrochemical sensor here described is almost always outperformed by other platforms employing the same aptamers. Amongst electrochemical biosensors, many of the works previously published display LOD in the picomolar and micro-molar range (Table 3.2). However, the two thirds of these designs can not achieve real time detection as the sensor requires incubation with the target molecules for a minimum time of 30 min, 1 h or 1.5 h. Amongst the devices that can detect in real time with a few minutes time resolution [143, 105, 302, 289, 217], only the designs published by Sanghavi et al. [217], White, Rowe, and Plaxco [289], and Liu et al. [143] are able to continuously monitor the target concentration in the sample, without the need of regeneration or additional incubation steps.

Table 3.2. Overview of Adenosine/ATP aptamer-based sensors and their characteristics

Surface	Range	Transduction / Technique ‘	Regeneration / Incubation time	Label-free	Real-time / Continuous	pH	Pubblication
2 mm Au Disk, 2 mm Au Wire (d=50µm)	10 µM - 10 mM	Electrochemical / SWV	No / No	Yes	Yes / Yes	7.3	This work
2 mm Au Disk	10 nM - 1 µM	Electrochemical / DPV	1.5 h / 1 h	No	No / No	7.6	[296]
2 mm Au Disk	0.1 nM - 10 µM	Electrochemical / ACV	2 h / 1 h	No	No / No	7.4	[41]
2 mm Au Disk	100 nM - 2 µM	Electrochemical / ACV	16 h / 1 h	No	No / No	6.2	[53]
4 mm Au Disk	5 nM - 1 µM	Electrochemical / SWV	3 h / 1.5 h	No	No / No	7.4	[99]
Au Disk	100 nM - 3 mM	Electrochemical / DPV	No / No	No	Yes / No	5.5	[105]
2 mm Au Disk + AuNP	0.1 pM - 5 nM	Electrochemical / EIS	No / 1.5 h	No	No / No	7.4	[280]
AuDisk - AuNP	0.5 nM - 4 nM	Electrochemical / CV	0.5 h / 1.5 h	No	No / No	7.4	[304]
25 µM Au Disk	50 µM - 2.5 mM	Electrochemical / SWV	1.5 h / 1.5 h	No	Yes / Yes	7.3	[142]
C-paste Electrode + Graphene + AuNP	tunable	Electrochemical / SWV	1.5 h / 1.5 h	No	Yes / Yes	7.3	[217]
2 mm Au Disk	0.1 mM - 250 mM	Electrochemical / SWV	No / No	Yes	Yes / Yes	7.4	[289]
AuNW	1 pM - 500 nM	Electrochemical / SWV	2 h / 0.5 h	No	No / No	7.3	[279]
Paper	0.3 µM - 450 µM	Electrochemical / DPV	NA / No	No	Yes / No	4.7	[282]
Gox + AuNC 1 mM	0.1 nM - 1 mM	Electrochemical / DPV	Yes / 2 min	No	Yes / No	7.3	[301]
2 mm Au Disk	5 nM - 2 µM	Electrochemical / DPV	NA / 1 h	Yes	No / No	7.4	[256]
AuDisk, PEDOT Source and drain	100 nM - 50 µM	FET / Electrochemical	No / 0.5 h	Yes	No / Yes	7.4	[140]
Graphene on PDMS silver Source and Drain	10 pM - 100 µM	FET / Liquid Gated	No / No	Yes	Yes / Yes	7.3	[174]
Suspended	5 µM - 120 µM	Fluorescence / FRET	NA / 1 h	No	No / No	7.4	[149]
Gox, 3mM AuDisk-AuNP	10 pM - 10 µM	Electrochemistry / EIS, ECL Luminescence	No / 2 h	No	No / No	7.4	[94]
Gox	200 µM - 900 µM	Fluorescence / ITC	No / No	Yes	Yes / Yes	7.6	[306]
CdS/Ppy/g-C_3N_4	0.3 nM - 200 nM	Photoelectrical / i-t curve	No / 1 h	No	No / Yes	7.4	[145]

All the others designs involve the use of a label or a complimentary DNA strand, a design choice that efficiently and neatly improves the sensor working range and can bring the LOD down to the pico- or nano-molar range, despite the poor aptamer affinity, but that prevents it from acquiring data with a significant time resolution. This sensor was developed to record dynamics data from brain tissue and the time resolution required is in the seconds to minute range.

Examining in further detail the two platforms that posses the same detection characteristics as the sensor presented in this chapter, it emerges that the work published by Liu et al. [143] very closely resembles the design employed by my platform, as the both rely on structure switching decorated aptamers immobilised on gold surfaces. The main difference between the two works is that the sensor surface for Liu et al. [143] is an in-house fabricated 25 µm Au disk with electrodeposited dendritic nanostructures, whilst the one described in this work is a 50 µm 2 mm long wire.

Some further improvement could be achieved by engineering the aptamer to produce a higher structure switching variation, like the one reported in [289] where the double stranded part of the adenosine aptamer [95] was truncated to destabilise the secondary structure and induce its folding only in the presence of the target molecule.

Additionally, Liu et al. [143] incubated its sensor with 30 mg ml^{-1} for 2 h to passivate the sensor surface and layer defect from oxygen interferences. The additional antifouling layer allowed the sensor to record its response in 100 % Bovine Serum, as opposed to just PBS-Mg in this work. This passivation technique could be employed to improve the sensor stability against fouling of the response in a biologically complex sample.

On the other side, the work published by Sanghavi et al. [217] employed a more complex design, in which the target recognition and the signal transduction are produced by separate reactions. The sensor consists of gold nanoparticles (AuNP) decorated with ATP aptamers-FAD complex. In the presence of ATP, the aptamer releases FAD which is reduced at the graphene coated carbon-paste electrode thus producing a signal. This method presents some clear benefits *e.g.* tunable linear range, an enhance sensitivity given by the graphene-decorated electrode, single step reaction and continuous monitoring. However, since not all the sensor components are confined on

a surface, it can not be employed in systems with a constant flow as the AuNP would disappear. Additionally the time resolution of the measurement is above 30 s, whilst the sensor in this work can be repeatedly interrogated every 8 s.

Finally, the sensor selectivity was evaluated against the downstream purines: inosine and hypoxanthine. The response was measured over the 10 µM - 10 mM range and the sensor did not show any response for either of the adenosine metabolites in the physiologically relevant concentration range (low micromolar). This result is important for the final application, guaranteeing that the signal generated can be attributed to adenosine only, despite the presence of the other metabolites in the extracellular environment. The selectivity against other nucleotides was not tested as multiple publications have already shown that the aptamer response to ATP is significantly higher than to any other nucleotide based on measurements using electrochemical, fluorescence, luminescence platforms [209, 256, 217, 149, 170, 145, 94, 106, 260, 306].

Regarding the affinity to ATP, the electrochemical sensor has shown to be responsive to ATP magnesium salt but not to ATP disodium salt. A possible explanation is that the ATP aptamer published by Huizenga and Szostak [95] is selective to the Mg-ATP complex but not to ATP itself, as the selection was performed in buffer containing 3mM $MgCl^{2+}$. The same stands for the sequences published by Zhang, Oni, and Liu [307] and Zhang and Liu [306] , as they are derived from the previous ATP aptamer. Still, there is no explanation for the lack of detection of ATP disodium salt as the Mg-ATP complex could still have formed, as the PBS buffer had been spiked with 1 mM Mg^{2+} to better mimic the cerebrospinal fluid (CSF). To further investigate the issue, the aptamer affinity to both ATP salts was assessed independently of the electrochemical platform using the SYBRGreen assay published by McKeague et al. [164]. The results of this test demonstrated the aptamer to be responsive to both ATP salts. The result was confirmed with another fluorescence assay employing a G-quadruplex intercalating dye: thioflavin T [209]. The results lead to the conclusion that the lack of response must be inherent to the platform itself.

In conclusion, the sensor has proven to be selective and sensitive enough in the required concentration range. However despite presenting a linear range of three orders of magnitude, it offers relatively small responses in the physiological range of interest. Therefore, it would be interesting to test whether it is possible to engineer the platform to produce a higher response at lower adenosine concentrations, maybe at the cost of reducing the saturation concentration by a few orders of magnitudes. This could be achieved either by working on the aptamer itself and increasing its sensitivity or by increasing its concentration on the surface. Additionally, the sensor has so far been tested in PBS-Mg but further work will be necessary to optimise its use in physiological measurements.

It is worth noting that no further optimisation process of the sensor signal and probe packing density was undertaken in this project as they are mainly determined by the aptamer [290]. The aim in establishing this platform was not to create an adenosine sensor, as many techniques already exist which greatly outperform this *e.g.* fast scan voltammetry, enzyme-based biosensors [188, 42]. The aim was to evaluate the platform as tool to detect small molecules released in the extracellular space that can not be detected in any other way *i.e.* are not electrochemically active or do not have an enzyme.

Chapter 4

Towards achieving quantitative detection of adenosine released by hypoxic brain slices

4.1 Introduction

This chapter describes the use of the electrochemical aptamer-based (E-AB) sensors developed in the previous chapter, to record adenosine release in a biologically complex environment.

The model I have chosen to characterise the sensor with is hypoxia-induced adenosine release from a mouse brain slice. Brain hypoxia and its pathways have been thoroughly characterised in multiple publications using a variety of techniques including extracellular recordings, whole cell patch clamp and microdialysis [199, 197, 125, 259, 291, 194, 69, 109]. In brain slices, hypoxia shows two defining features, illustrated in Figure 4.1. The first is the release of adenosine in the extracellular space, quantified in the range of 10-50 µM [81, 224, 125], dependent on the duration of the insult. The second feature is the decrease in amplitude of the field excitatory post synaptic potentials (fEPSPs) [66], which is the result of the neuroprotective action of adenosine. Once released in the extracellular space, adenosine binds to the A_1 receptors, which decreases glutamate release via the voltage gated calcium channels, causing a depres-

sion of the fEPSP. [109, 189].

Further knowledge on the kinetics of adenosine release in hypoxia was collected with the advent of enzyme-based electrochemical biosensors first published by the Dale group [43], with a limit of detection of 12 nM and a rise time of 75 s [278]. This work revealed that the adenosine release preceded and accompanied the repression of synaptic transmission.

Given the properties of the my aptasensor (Range 10 µM - 1 mM, time resolution of 8 s and low sensitivity to inosine), the device should be able to reproduce the results published by Dale, Pearson, and Frenguelli [43]. However, since the fouling resistance of the sensor has yet to be assessed, some preliminary measurements are necessary. The initial trial runs aimed to evaluate possible interference from the different environmental conditions *e.g.* pH, oxygen and temperature. The possibility of testing the detection from within the slice, as published by Frenguelli, Llaudet, and Dale [67], was verified by using a 0.5 % agar block to mimic the diffusion layer of the tissue [179]. Finally, the sensor was employed in parallel with extracellular recordings to detect in real-time adenosine release from an hypoxic brain.

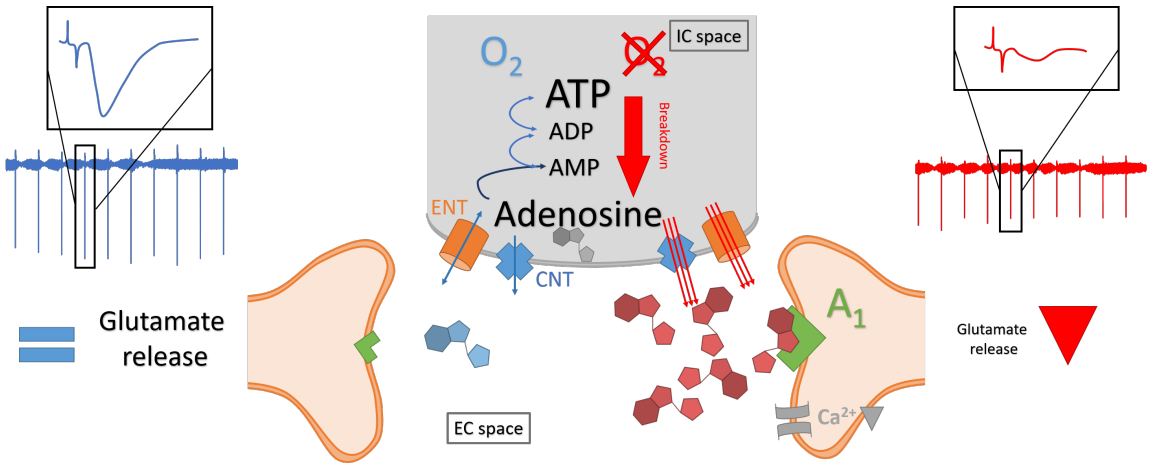

Figure 4.1. Adenosine pathways in normoxia (O_2, left side) and hypoxia (CO_2, right side, red). *In normoxic conditions (95% O_2 / 5% CO_2) ATP and ADP are in equilibrium and all the savage pathways to produce ATP starting from as low as adenosine as a building block are active. Synaptic activity is normal (left panel, blue). In the absence of oxygen (95% N_2 / 5% CO_2), the phosphorylation of ADP into ATP no longer takes place, thus starting the breakdown cascade that results in an overall increase in concentration of intracellular adenosine. The excess adenosine is released in the extracellular space via transporters. There it binds the A_1 receptor on the pre-synaptic neuron and its activation results in the inhibition of voltage gated calcium channels. The reduced influx of Ca^{2+} ions causes the suppression of glutamate release, thus the synaptic transmission is repressed and the field excitatory post synaptic potentials are smaller in amplitude*

.

4.2 Results

4.2.1 Preliminary measurements in hypoxia-mimic conditions

The process of creating a new analytical platform does not end with the optimisation of the technique in a controlled environment and a clean sample. To make the technique useful and applicable, it has to fulfil its function in a complex environment, surrounded by fouling agents, and be able to record a biological event. Considering the characteristics of the sensor I have developed so far, the second-range response time and the lowest detected concentration being 10 µM; I decided to verify whether the my E-AB could detect an hypoxia-induced adenosine release in brain slices.

Some preliminary measurements were necessary to evaluate the impact of the new environmental conditions on the sensor response. These preliminary tests also provided the chance to identify and correct any interference. The adenosine aptamer

Table 4.1. Table with buffer composition of aCSF and PBS containing 1 mM *$MgCl_2$*

Component	**aCSF**	**PBS+1** mM **$MgCl_2$**
NaCl	127 mM	137 mM
KCl	1.9 mM	2.7 mM
$MgCl_2$	1 mM	1 mM
$CaCl_2$	**2** mM	**0** mM
KH_2PO_4	1.2 mM	1.8 mM
Na_2HPO_4	0 mM	10 mM
$NaHCO_3$	26 mM	0 mM
D/glucose	**10** mM	**0** mM

sensor was placed in the main chamber together with the Ag/AgCl reference, whilst the Pt counter was positioned in the out-flow chamber. This set up was chosen after testing all possible arrangements as it emerged to be the one that minimised both noise and overcrowding of the main chamber. The hypoxia conditions were mimicked in absence of tissue, to verify the capability of the sensor to detect a response despite the new conditions (chamber geometry and the presence of both oxygen and carbon dioxide).

The recording started in artificial-spinal fluid (aCSF) equilibrated in 95% oxygen/ 5% carbon dioxide (95% O_2). After 7 min, the solution was substituted with aCSF bubbled with 95% nitrogen /5% carbon dioxide (95% N_2) and containing 50 µM adenosine (mimic of hypoxia release), and then back to oxygenated aCSF. Throughout the entire recording the solution in the chamber was kept at 32 °C. Figure 4.2 displays the recorded sensor response for a representative data set. As illustrated, the sensor signal is decaying and shows no response to the presence of adenosine (magenta). There were two main results. The first was that the sensor failed to detect the adenosine in solution despite the concentration of target added being almost double of the maximum value expected for a hypoxia-induced release and more than ten times the average value of released adenosine (3 - 5 µM). The second is that a strong drift (signal decay) was present in the measurements which indicated that either the environmental conditions or some dirt in the chamber were affecting the sensor.

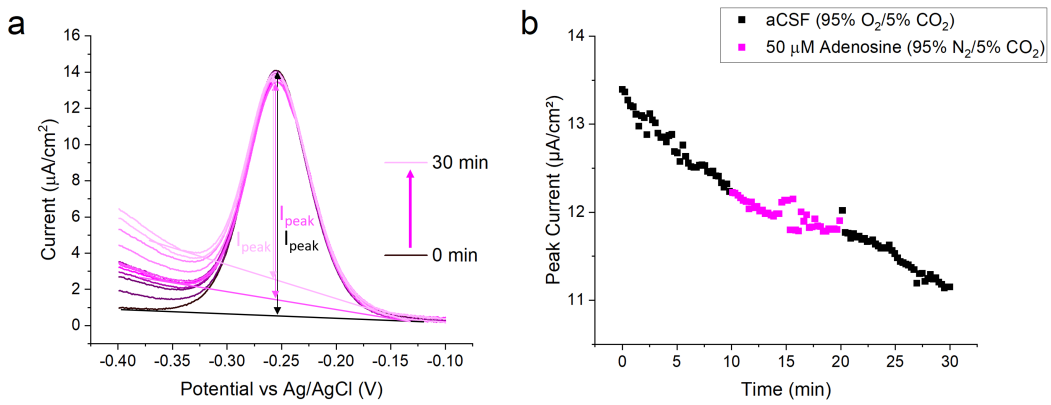

Figure 4.2. Sensor response to 50 µM ***Adenosine in aCSF with an hypoxia degassing.*** *The sensor was interrogated with square wave voltammetry (SWV) first in aCSF bubbled in 95% O_2 / 5% CO_2 (black), the in aCSF bubbled in 95% N_2 / 5% CO_2 and spiked with 50* µM *adenosine (magenta, hypoxia mimic) and then back to aCSF bubbled in 95%O_2 / 5% CO_2 (black) to mimic the recovery. The measurements were conducted at 32* °C *in absence of tissue. The sensor showed no response to the presence of adenosine.*

4.2.2 Evaluation of the sensor's dependence on buffer, degassing and temperature

Supported by the previously collected data on the sensitivity and limit of detection of the sensor, I decided to test first whether the different environmental conditions were liable for the lack of response. The two experimental set-ups, the one used to characterise the sensor and the one for the measurements in brain slices, presented four main differences: buffer composition, bubbling gas, temperature and chamber geometry. Extracellular recordings from brain slices are performed in aCSF, which contains 10 mM D-glucose and 2 mM calcium chloride in addition the components of PBS+1 mM $MgCl_2$ used in the previous measurements Table 4.1.

Hypoxia was induced using aCSF bubbled with 95% O_2 or 95% N_2 as opposed to the 100 % nitrogen (100 % N_2) used for assessing the sensor response in previous measurements. Regarding temperature, extracellular recordings in brain slices are conducted at 32 °C, to mimic physiological conditions, whereas sensor characterisation was carried out at room temperature. Finally, the chamber geometry changes from a single cylindrical chamber for, the characterisation, to three circular communicating chambers for the tissue measurements.

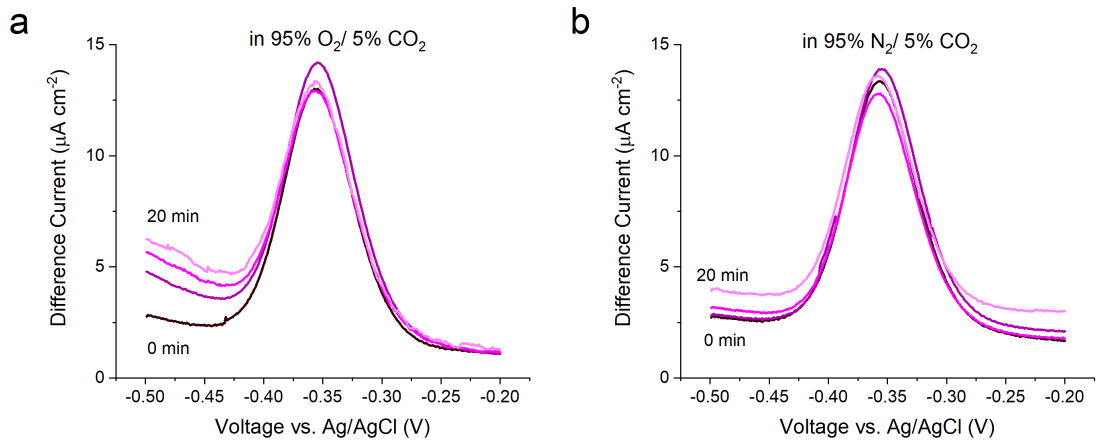

Figure 4.3. Effect of the oxygen reduction current on the sensor signal. *Square wave voltammetry recordings in oxygenated buffer show an increasing background current at the more negative potentials (panel a), compared to the stable baseline recorded in absence of oxygen (panel b). This variation caused the signal variance to increase for the oxygenated solution. However the increase was not significant (Levene test, $p>0.05$, $n=3$).*

Oxygenation The first condition tested was the effect of introducing oxygen in the system. Oxygen, due to its high electronegativity, favours the oxidation of the redox reporter, methylene blue and thus affects the sensor signal. Figure 4.3 illustrates square wave voltammetry (SWV) performed in oxygenated (panel a) and not oxygenated media (panel b). As at each time point the current peak is the distance between the baseline, generated with the non-faradaic portion of the SWV recording, and the maximum peak. An increase in the height of the base line at more negative potentials was registered for the oxygenated solution, which resulted in a reduction of the signal overtime. This signal variability did not produce a significant difference in 20 min (Levene test, $p>0.05$, $n=3$). However, the impact could be greater for a longer measurement.

pH Next, I tested the effect of the introduction of carbon dioxide in the system, as it affects the pH of the solution. The height and voltage of the peak of SWV curve were recorded in aCSF bubbled with 100% N_2 (40x), then with 95% N_2/ 5% CO_2 (40x) and back to 100% N_2 (40x). The peak current (black) and voltage curves (magenta) illustrated in Figure 4.4.a, both increase upon introduction of the PBS equilibrated with carbon dioxide. The current showed an average 10.5 $\pm$ 1.8 % increase, whilst the voltage shifted by 18 $\pm$ 3 mV (mean $\pm$ e_a, n=3). An almost identical result was

obtained when introducing 5% CO_2 to a fully oxygenated buffer (Figure 4.4.b), where an average variation of 11.8 $\pm$ 1.6 % in signal and 24.7 $\pm$ 2.7 mV (mean $\pm$ e_a, n=3) in the peak voltage was recorded (Figure 4.4.b). By introducing 5% CO_2, the pH lowered from 7.8 to 7.4, with a pH variation of 0.4. Since potential of the reaction varies at the rate of -59 mV per pH unit, the expected decrease is of 23 mV. Thus both results agree with the prediction by the Nernst equation.

Since the variation in the signal due to pH is always accompanied by a shift in the peak voltage, it is sufficient to monitor that the peak voltage does not vary to exclude a pH effect on the sensor response.

Buffer All measurements performed in the previous chapter to characterise the sensor response were conducted in PBS containing 1 mM $MgCl_2$ bubbled in 100% N_2. Therefore, I next sought to evaluate the response in aCFS bubbled with 100% N_2 which differed from the previous buffer for the presence of 2 mM $CaCl_2$ and 10 mM D-glucose. In both cases the sensor showed the expected step-like response, which indicated that the additional components in the buffer did not affect either the aptamer or the sensor capability detect adenosine (data not shown). I further proceeded to characterise the effect of the different buffer composition in hypoxia conditions and buffer spiked with 1 mM adenosine. The concentration of 1 mM adenosine was chosen, despite it being at least one order of magnitude larger than what was expected from the release, to ensure that if a signal was not recorded it would be due to the new environmental conditions and not just lack of sensitivity from the sensor. Therefore, 40 SWV measurements were recorded in 95% O_2 bubbled buffer to measure a baseline; followed by 40 SWV measurements in buffer spiked with 1 mM adenosine and equilibrated with 95% N_2, to mimic the hypoxia-induced adenosine release; and 40 SWV measurements back in oxygenated buffer, to mimic the recovery time. The same protocol was performed, first with PBS spiked with 1 mM $MgCl_2$ and then aCSF as buffer. Figure 4.4.c and Figure 4.4.d illustrate the sensor response (black) and peak voltage (magenta) recorded in aCSF and PBS respectively. Again, for both buffers the sensor response showed a steep increase in the response of 3.1 $\pm$ 1.2 $\mu A\,cm^{-2}$ for aCSF and 2.2 $\pm$ 0.5 % for PBS (mean $\pm$ e_a, n=3). However, in this case the peak voltage remained

stable on the same value, thus proving that the response recorded was not generated by a pH variation.

The hypoxia conditions were repeated without adenosine spiked buffer. Figure 4.4.e illustrates the peak current (black) and voltage (magenta) for both aCSF (full) and PBS (top-half filled). In both cases no variation was measured, thus further proving that the previously recorded response was only due to adenosine.

Temperature Finally, the effect of temperature on the sensor sensitivity was evaluated by measuring the variation in the sensor response with increasing temperature. The sensors were interrogated using a 1 mM adenosine solution in aCSF in hypoxia conditions, with bath temperatures ranging from 21 °C to 35°C. The temperature controller used to set the bath temperature was unable to maintain a constant temperature and continued cycling between the nominal value and $\pm$ 0.5 °C. The data illustrated in Figure 4.5.a displays response curves that present a strong temperature dependence, as the step response of the sensor disappears with increasingly higher temperature. This result agrees with the findings from Zhang, Oni, and Liu [307], which using found that the aptamer affinity increases by lowering the temperature from 16.4 $\pm$ 1.4 µM at 25 °C to 4.6 $\pm$ 0.4 µM at 10 °C. Notably, with increasing temperature, also a slight drift in the current appears (diagonal orientation of the response). Additionally, at higher temperatures, the noise generated by the controller becomes more dominant over the sensor signal(Figure 4.5.b). Finally, the temperature dependence on the voltage peak was evaluated. Nernst equation (Equation 1.5), predicts that the potential decreases by 0.2 mV $^{\circ}C^{-1}$. However, Figure 4.5.c shows peak voltage to become more negative by an average of 0.52 $\pm$ 0.02 mV $^{\circ}C^{-1}$, a variation 2.5-fold larger than the one predicted by theory.

Consequently, measurement in brain slices were performed at room temperature, as opposed to 32 °C to ensure the best working conditions for the sensor.

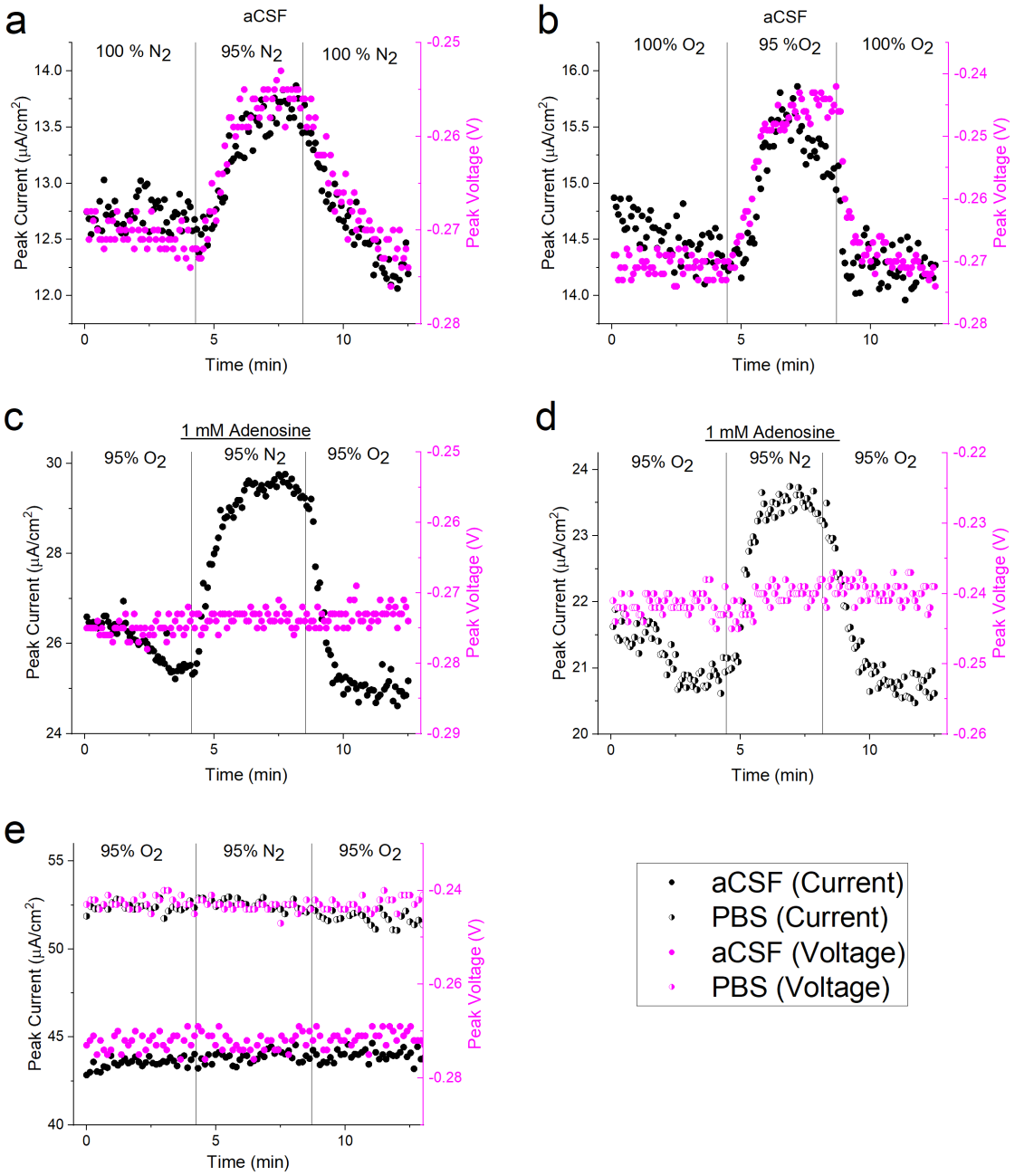

Figure 4.4. Effect of different degassing conditions on the sensor response. *a)-b) Effect of switching from aCSF equilibrated with 100% N_2 and 95% N_2 / 5% CO_2 (panel a) and with 100% O_2 and 95% O_2 / 5% CO_2 (panel b) on the sensor response (peak current-black) and on the voltage (peak voltage - magenta). b) Effect of switching from aCSF equilibrated with on the sensor response (peak current-black) and on the voltage (peak voltage - magenta). c)-d)-e) Sensor response and voltage recorded in hypoxia conditions (95% O_2 / 5% CO_2→95% N_2 / 5% CO_2→95% O_2 / 5% CO_2 at room temperature in aCSF (panel c) and PBS (panel d) spiked with 1* mM *adenosine and in absence of adenosine (panel e).*

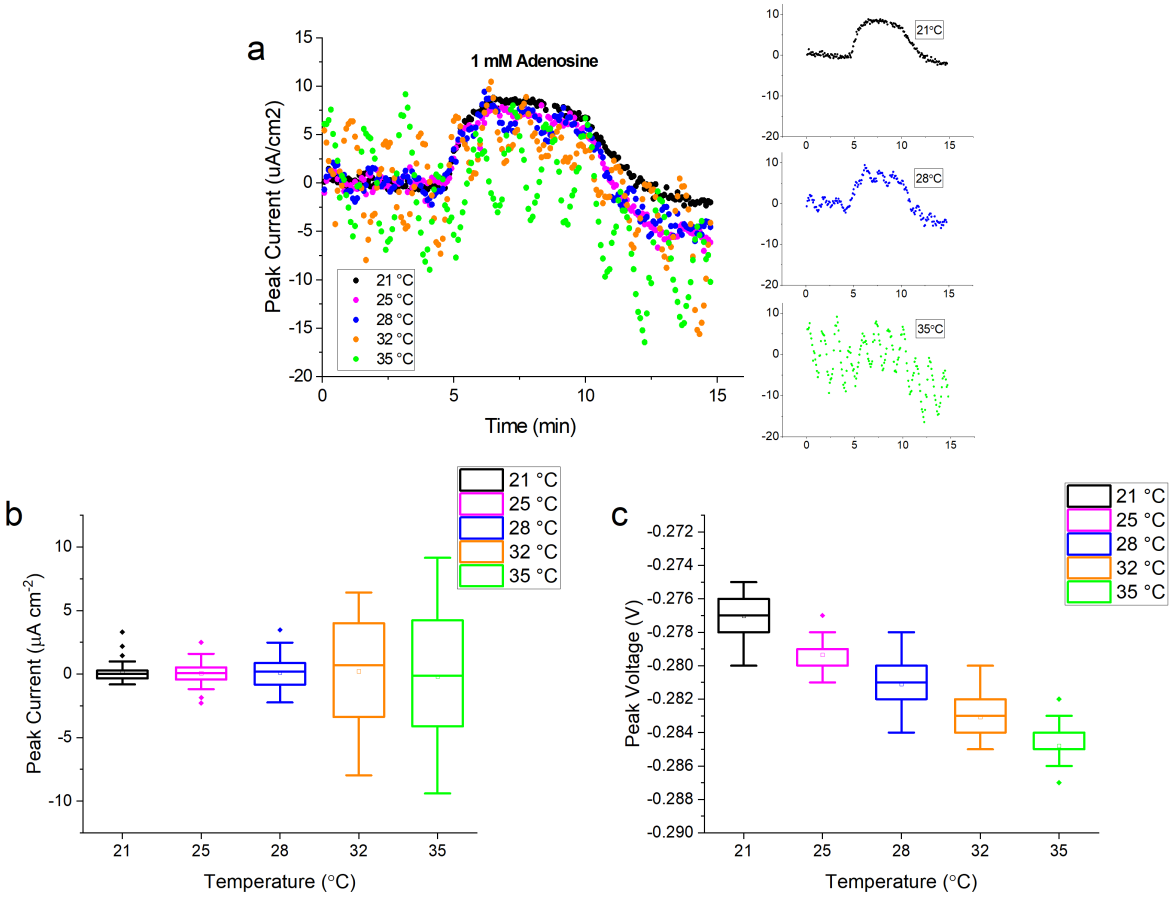

Figure 4.5. Temperature dependence of the sensing platform. *a) Sensor response to 1* mM *adenosine at different temperatures (21 - 35 °C). The data present a clear step response from 21 °C (insert, black), becomes less prominent at 28 °C (insert, blue) and almost completely disappears at 35 °C (insert, green). b) Evaluation of the average value and noise measured at the baseline for the different temperatures. As displayed, the average value remains constant, whilst the noise increases with increasing temperature. c) Plot of the peak voltage recorded at the different baths temperatures.*

4.2.3 Recording in agar block to mimic the effect of the tissiue diffusion layer

Before moving on to detecting release in a brain slice, I wanted to test whether it was possible to record the hypoxia-induced adenosine release from within the tissue as published in the work by Frenguelli, Llaudet, and Dale [67]. Insertion in the slice could affect the sensor in two possible ways: it could remove the aptamers from the surface, thus damaging it and hindering its detection capability; or the diffusion layer generated by the cells surrounding the sensors could delay the sensor response.

To test the first hypothesis, the effect of the slice was mimicked with a 0.5 % agar block, adapting the experiments published by [179]. Prior to the measurements, the slice was incubated with 1 mM adenosine in aCSF to ensure that the slice was saturated with adenosine and that the lack of response was not due to the delay caused by the diffusion layer of the slice. Each sensor was first calibrated in aCSF and 1 mM adenosine, then the response to 1 mM adenosine was recorded outside the agar block, inside and then outside again. In between each step a cyclic voltammetry (CV) measurement was recorded. The alternated CV and square wave voltammetry (SWV, 50 repeats) aimed to characterise the status of the aptamer coating and the sensor capability to measure a response, respectively. The effect of the agar block on the oxidation peak and on the sensor response are illustrated in Figure 4.6.a and b, respectively. From both graphs it can be deduced that the insertion in the agar block negatively affects the sensor: first the oxidation peak recorded in the agar and after removal from the agar was visibly smaller, with a total loss of approximately 2 $\mathrm{nM\,cm^{-2}}$ in aptamer density. This would indicate that the sensor was damaged upon insertion and removal from the agar block. This result is further supported by the difference between the two recordings in 1 mM adenosine before (Figure 2.5.b, magenta) and after the insertion in the agar block (green). Additionally, the significantly lower signal recorded in agar (Figure 4.6.b, blue) compared to the response recorded outside after removal (green) would suggest that the agar matrix significantly hinders the sensor response.

I started by performing a calibration with 1 mM adenosine inside and outside the agar block. In this case the slice was pre-incubated with aCSF only and the calibra-

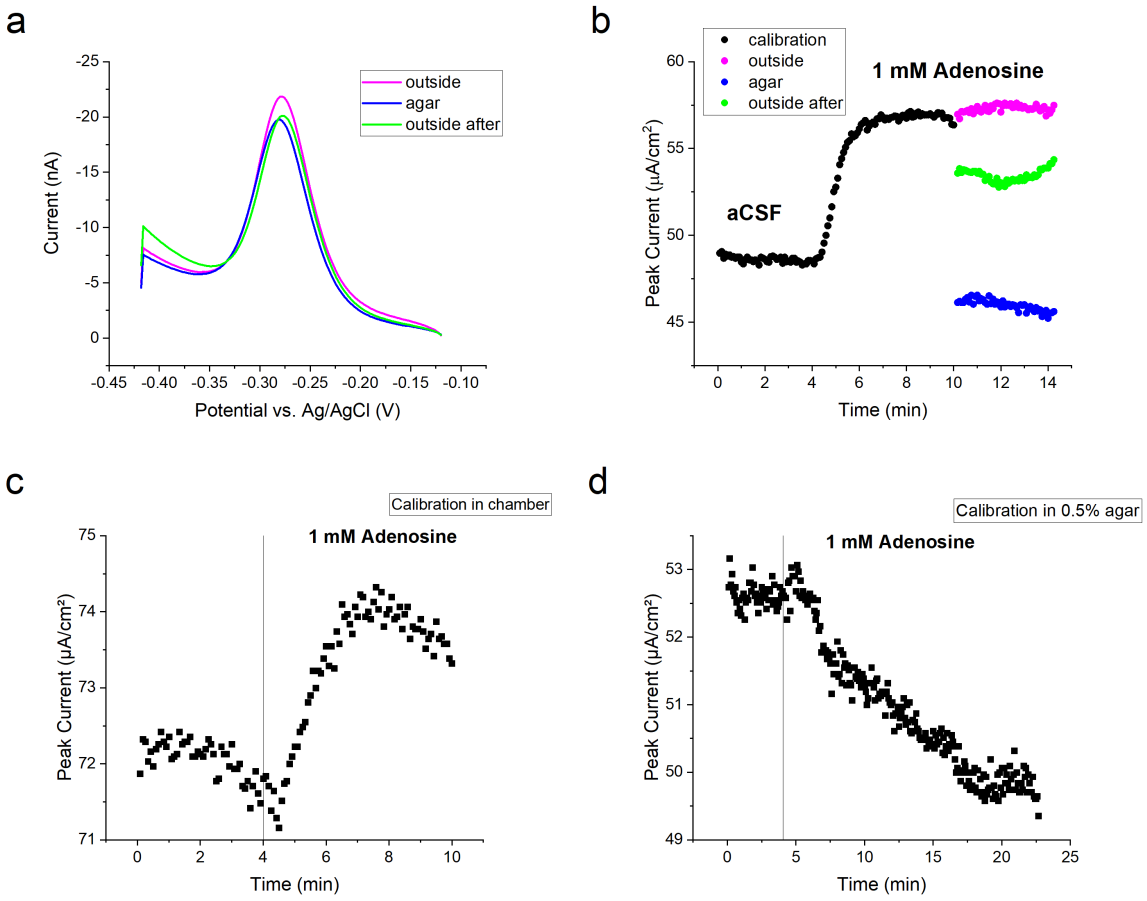

Figure 4.6. Effect of an 0.5 % agar block on the sensor response and coating. *a) The oxidation peak of the cyclic voltammetry (CV) measurements in PBS used for calculating the aptamer density on the sensor surface. The CV were recorded in 1* mM *Adenosine in aCSF, inside the 0.5 % agar block (pre-incubated in 1* mM *adenosine in aCSF for 30* min*), and outside after removal from the slice. The peak recorded inside the agar and again outside in solution is smaller than what recorded in 1* mM *adenosine prior to the insertion. This corresponds to a lower aptamer density on the sensor surface which reduces from 40.25* $\mathrm{nM\,cm^{-2}}$ *to 38.81* $\mathrm{nM\,cm^{-2}}$ *and 38.43* $\mathrm{nM\,cm^{-2}}$*, for inside the agar and after the agar respectively. b) Plot of the sensor response to a calibration with 1* mM *adenosine (black), and then the response of the same sensor to 1* mM *adenosine in the chamber (magenta, outside), in the adenosine pre-infused agar block (blue, agar) and in the chamber again once removed from the slice (green, outside after). c) calibration curve for a sensor with 1* mM *adenosine over 120 square wave voltammetry (SWV) measurements with an increment of 2* $\mathrm{\mu A\,cm^{-2}}$ *in the response, compared to the constant decay in the sensor signal when the calibration was performed with the same sensor in the 0.5 % agar block (panel d, 300 SWV).*

tion was performed first in the chamber with 80 SWV measurements, then in the agar block with 300 SWV measurements, to allow the adenosine detection with the delay caused by the diffusion layer. As it emerges from the comparison of the calibration curves in the chamber and in the slice (Figure 4.6.c and Figure 4.6.d respectively) the sensor in the slice did not produce step response to 1mM adenosine and the current exhibited an exacerbated drift.

Consequently, the release from brain slices was measured with the sensor laying on surface to avoid any damage.

4.2.4 Simultaneous recording of extracellular and adenosine sensor recordings in hypoxic slices

An initial attempt was made at measuring simultaneously the responses of both the E-AB sensor and the enzymatic sensor published by Frenguelli, Llaudet, and Dale [67]. However, given the shared circuitry and the potentials applied to record measurements (constant +0.5 V for the enzyme microelectrode sensor and a staircase from -0.4 V to -0.1 volt for the E-AB sensor) it was impossible to record any response on the aptamer sensor.

Therefore, to ensure that the hypoxia was occurring and that the adenosine release was detected as a result, the synaptic transmission and adenosine levels were simultaneously monitored with field excitatory post synaptic potentials (fEPSPs) and with the E-AB sensor respectively. This set up consisted of a stimulator and a recording electrode for the fEPSPs, and the aptamer sensor (2 mm Au wire, 1BSS aptamer). Since all the electrodes were present in the same bath, the two electronic circuits shared a branch. Therefore, whenever a SWV measurement was performed (Figure 4.7, blue), it would appear on the recording electrode track. Consequently, the fEPSP (green) could only be recorded at the end of the duty cycle (DC, magenta) as illustrated in Figure 4.7.

Having changed the recording temperature from the physiological (32 °C) to room temperature (21 °C), I performed an initial test run, recording fEPSPs only, to determine the timings for the fEPSP amplitude decay and recovery. As illustrated in

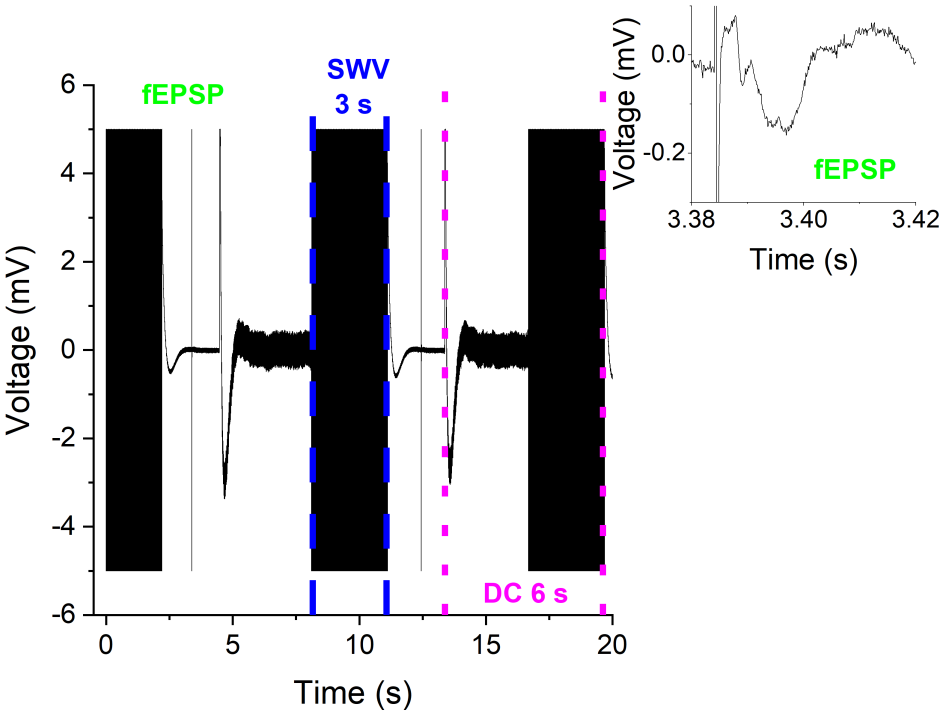

Figure 4.7. Example of a field recording with simultaneous extracellular and square wave voltammetry (SWV) recording. *Effect of Square wave voltammetry (SWV) potentiostat duty cycle (DC, magenta) on the recording electrodes measurements (black). The SWV measurement (blue) took 3* s *and generated too much noise or signal to allow the measurement of field excitatory-postsynaptic potentials (fEPSPs, green), which were therefore taken in the quiet time of the recording. Overall, both a SWV and a fEPSP were recorded approximately every 8.5* seconds. *The inset is a magnification of the fEPSP recorded between two SWV duty cycles*

Figure 4.8 the synaptic depression started with a 330 s (5.5 min) delay with respect to the beginning of the perfusion with 95% N_2 aCSF (Figure 4.8.a, magenta line). The 50 % inhibition (IC_{50}) was reached after 2 min. The fEPSP amplitude had shrunk by 67 % of the original signal when oxygen was reintroduced. Recovery started with a 100 s delay. Using these results, I decided to incubate the slice with aCSF 95% O_2 for 100 s to obtain a baseline, then switch to aCSF 95% N_2 and incubate for 550 s, then switch back to aCSF 95% O_2 for 450 s to measure the recovery.

These parameters were used to record adenosine release from hypoxic slices. Figure 4.9.a illustrated the raw data from the sensor response. The sensor successfully detected the adenosine released from the tissue, as proved by the step in the response placed around 200 s). However, the trace presented a strong drift throughout the mea-

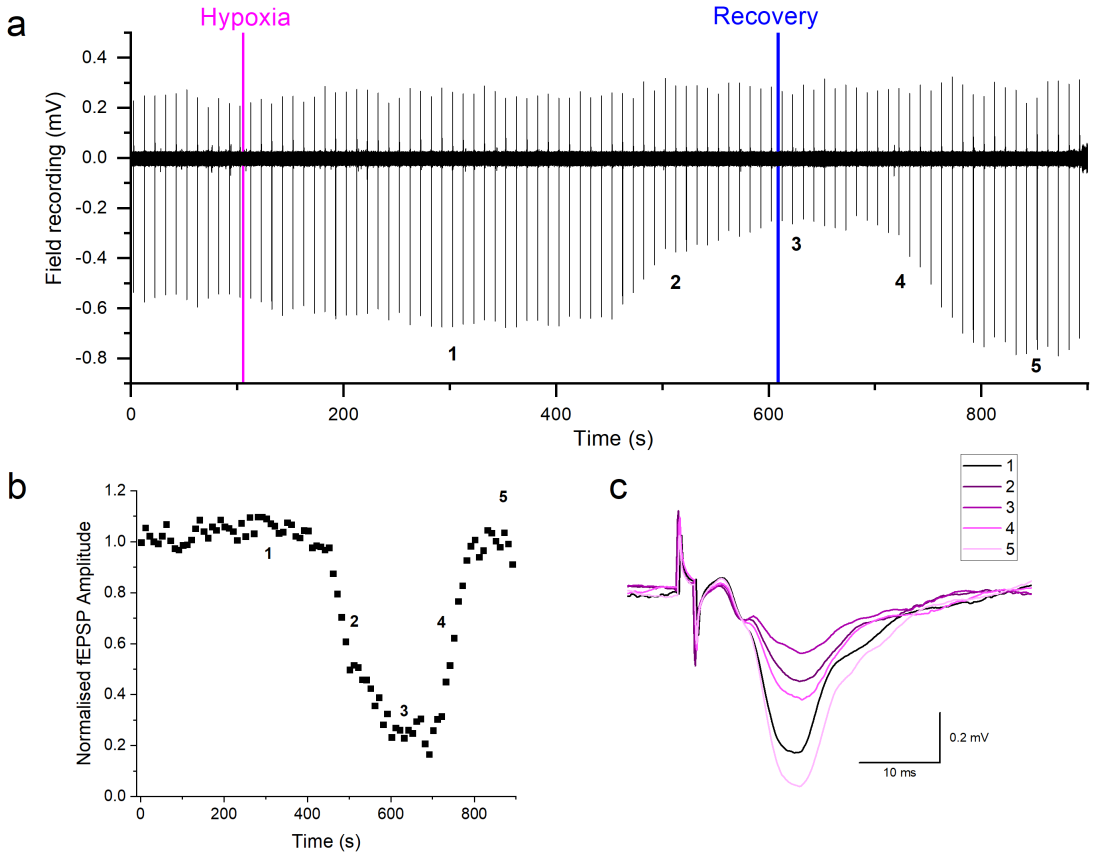

Figure 4.8. Extracellular recording of a hippocampal slice to determine timings for hypoxia induction at room temperature. *a) Plot of the extracellular recording over time recorded at room temperature. The magenta line titled hypoxia indicates the time when the solution was switched from aCSF bubbled with 95% O_2 / 5% CO_2 to aCSF bubbled 95% N_2 / 5% CO_2 bubbled aCSF. The blue line indicates the time when the solution was switched back to aCSF bubbled with 95% $0_2$5% CO_2 bubbled aCSF. b) Plot of the normalised fEPSP amplitudes. c) Plot of representative fEPSP from the hypoxia recording. The time of recordings is indicated by the number in plots* ***a*** *and* ***b****.*

surement. The continuous decay in the signal could indicate that the sensor surface was being damaged by contaminats present in the chamber. As a result, it was impossible to quantify the adenosine released, as neither a calibration before or after the measurement would provide a reliable comparison; and further work is necessary to improve the sensor resistance to fouling. Figure 4.9.b illustrates the plot of the normalised fEPSPs amplitudes (black) overlapped with the sensor measurements, with drift correction (magenta). The rise in the sensor signal, detecting adenosine release, occurred around 80 s after hypoxia was induced, and reached the maximum value 100 s earlier than decay in the slice fEPSP amplitude. In contrast, the signal decay and the fEPSP recovery happen almost simultaneously, around 80 s after switching back to oxygenated aCSF. The experiment was repeated using the same conditions for five times and similar results were found.

Simultaneously, extracellular recordings were employed to verify whether synaptic depression occurred together with adenosine release measured by the sensor. The amplitude of fEPSPs showed an average depression of 69.1 $\pm$ 7.0%. However, the depression in the amplitude started an average of 231.4 $\pm$ 25.8 s (mean $\pm$ e_a, n=5) after the sensor detection of adenosine release.

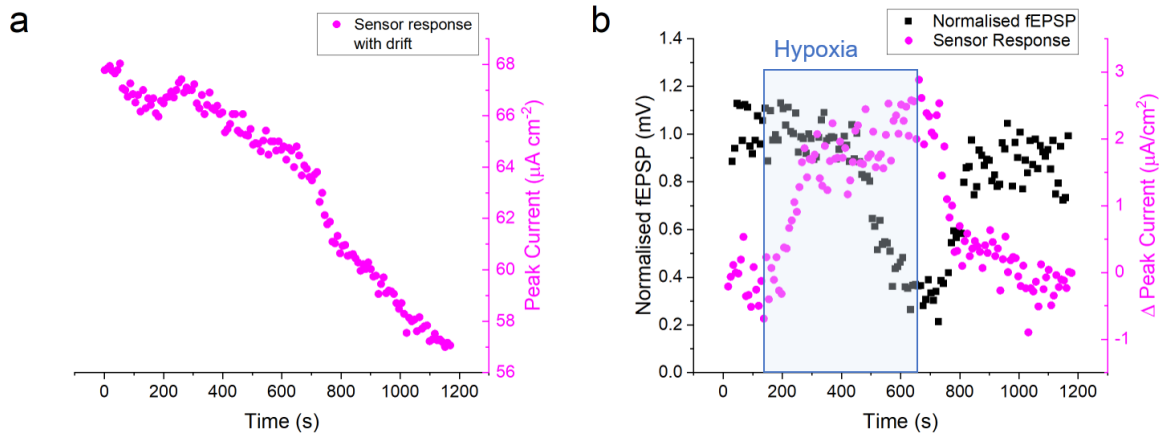

Figure 4.9. Recording of hypoxic-induced adenosine release in a mouse hippocampal slice. *a) Plot of the raw curve recorded by the aptamer electrochemical sensor. b) Plot of the sensor response (drift corrected, magenta), overlapped with the normalised fEPSPs amplitudes from the extracellular recordings (black). The blue box indicates the hypoxia-induction window. The graph illustrates the sensor detection of adenosine approximately 80 s post hypoxia induction and reaching maximum signal 100 s earlier than the decay of fEPSPs amplitude. However, the sensor signal decay and the fEPSP amplitude recovery occurred simultaneously*

4.3 Discussion

The aim of this chapter was to record adenosine release from a brain slice. Hypoxia was chosen as a model as the characteristics of the adenosine release fitted the characteristics of the device developed so far: release over a second-time window and adenosine release in micromolar concentration [189]. However, before employing the sensor in a complex environment a few preliminary tests were performed to ensure that no external factors (fouling, pH changes, oxygen) could affect the sensor response.

pH The first preliminary test aimed to evaluate the sensor response dependence on pH variations. The results showed that the introduction of 5% carbon dioxide induced a shift in both potential and peak current of the redox reaction. Since carbon dioxide is an acidic gas, bubbling aCSF with 95% O_2/5 % lowered the overall buffer pH from 7.8 to 7.4. As predicted by the Nernst equation (Equation 1.7), an increase in proton concentration (lower pH) causes the redox potentials to move toward more positive values by 2. This theoretical prediction was met by the data in Figure 4.4.a and b. In fact, the pH decreased by 0.4 units resulted in an increase in the peak current by ca. 10

% of the signal, when carbon dioxide added in the gas mix used to equilibrate aCSF, thus reducing the pH of the solution. A possible explanation for the change in signal is that the variation in proton concentration (ΔpH) affects the charge transfer rate between methylene blue and the surface, as the protonation/deprotonation conditions shift.

One would assume that the pH variation should also affect the capability of the aptamer to fold and form a secondary structure, given that the majority of interactions involve hydrogen bonds. However, a study by Pilch et al. [200] found that the target molecule is more affected by pH variations, especially when crossing the pK_a value of the ligand. The variation in pH changes the charged state of the target molecule, thus affecting its capability to interact with the aptamer. Additionally, a recent study published by Thompson et al. [264] showed that the K_m of the adenosine and ATP aptamer was independent of pH.

Temperature Another interesting result was the test on the effect of the temperature on the sensor signal and on the response. Figure 4.5 demonstrates that the sensor performance was strongly affected by temperature and that the optimal working conditions were at room temperature (21 °C). As expected, the optimal temperature matched the conditions under which the adenosine and ATP aptamer was selected [95]. As for increasing loss of responsiveness with increasing temperature, again it must be considered that the platform is complex, multiple interactions are taking place at the same time and that a macro parameter like temperature affects all the processes.

For the aptamer, a 27-bases long sequence, the evaluated average melting temperature (T_m) was 40 °C. This value was calculated by averaging the three most frequent secondary structures at room temperature and in the buffer conditions (137 mM Na^+, 1 mM Mg^{2+}) using the *UNAfold* platform [156]. This low T_m partially justifies the loss of sensitivity of the sensor with the increasing temperature. With higher temperature, hydrophobic interactions are continuously broken as water molecules move quickly. Similarly, hydrogen bonds have lower life time. This is not a surprising result as heat provides energy to a system. Overall, the temperature increase causes the secondary structure of the aptamer to destabilise, as predicted by the second law

of thermodynamics. The Van't Hoff equation describes how the equilibrium constant changes upon a change in temperature

$$\ln K_D = \frac{\Delta_r H}{RT} + \frac{\Delta_r S}{R} \tag{4.1}$$

Not many studies have empirically evaluated this relation between aptamer affinity and temperature [262]. On the same aptamer using isothermal tritation calorimetry (ITC), Zhang, Oni, and Liu [307] found that lowering the temperature from 25 °C to 10 °C improved the aptamer K_D by three-fold. The work from Reining et al. [208] proved that with increasing temperature the K_D also increases, thus indicating an increasing loss of affinity.

Similar results were previously published for the same aptamer by Du et al. [53], which found 30 °C to be the cut-off temperature over which the background signal increased due to aptamer destabilisation. Goda and Miyahara [72] also did not record any response for the Huizenga aptamer on their electrochemical platform for any temperature ranging 25-55 °C, supporting that the lack of response was due to the lack of structure-switching of the aptamer. Additionally, Goda and Miyahara [72], have shown that the stabilised version of the aptamer, with a 7-bases longer hairpin stem and a melting temperature of 49 °C, showed responsiveness at 37 °C. Increasing stem length is a common technique to improve aptamer stability against increasing temperature [238, 72].

Regarding the temperature dependence of the peak voltage, the Nerst equation predicts the peak voltage to increase by 0.2 $\mathrm{mV\,°C^{-1}}$ per degree celsius. The result obtained displayed a dependance that is 2.5-folds larger than what described in the Nernst equation (Equation 1.5).

Diffusion layer mimic Last of the preliminary measurements aimed to test whether the E-AB sensor could detect target release from within the tissue. The experiment aimed to evaluate whether insertion in tissue would damage the sensor surface and whether the diffusion layer caused a delay in the sensor response. The aptamer density on the sensor surface showed a 3.6 % reduction upon the insertion of the sensor on the agar block, and an additional 1 % loss upon removal (total reduction 4.6 %).

As stated by Newton, Wall, and Richardson [179], it is the structure and the detection mechanism of the enzyme-based biosensors which creates a depletion of the area surrounding it. This problem does not apply to the sensor here developed as the aptamer binds and releases the target molecule without breaking it down. However, similarly to the enzyme-based sensor, a reduction in the current was measured upon insertion into the agar block. Newton, Wall, and Richardson [179] saw a signal reduction of 70 % for the enzymatic sensor, whilst the E-AB biosensor presented a reduction in response of 130 %. This result indicates that the insertion in the agar block did not only damage the biosensor surface, but also affected the device working capability. The sensor signal recovered to 55 % of its initial value once removed from the block.

Temperature effect on adenosine release Hypoxia measurements on mouse brain slices were performed at room temperature (21 °C, as opposed to physiological temperature (32-34 °C) to overcome the sensor's poor signal-to-noise ratio at high temperature.

Performing a recording of brain activity at a temperature so different from the physiological one (ΔT = 11 °C) can affect the activity of the brain slice and the timings at which the events occur. For example, comparing the onset time of the hypoxia in measurements performed at physiological temperature *versus* the measurements here reported (Figure 4.8), it emerged that whilst at physiological temperature the depression of the synaptic transmission started around 150 s after the switching from the oxygenated to the non-oxygenated aCSF Fowler [66] and Pearson et al. [195], at room temperature started after ca. 350 s. An initial part of the delay is the time necessary for the solution to reach and completely perfuse the chamber, which was estimated to be around 80 s. Once subtracted, the difference between the delay in the two responses was still substantial (ca. 200 s). This lag in the depression in synaptic transmission can be attributed to the neuroprotective action of hypothermia. Multiple studies have shown preventive and therapeutic potential in inducing localised lower temperature both during and post the brain insult [152, 12, 56]. The mechanism behind the protection provided by lower temperature is complex and yet not fully understood [215, 299]. However, the main effect of reducing the temperature is reducing the oxygen

and the glucose consumption of the cell, its metabolism, thus allowing it to withstand oxygen- and glucose-deprivation conditions for longer [168].

***In vitro* recording of hypoxia-induced adenosine release using the electrochemical aptamer-based sensor.** The result in Figure 4.9 proved that the sensor was sufficiently sensitive to record adenosine release from tissue. However, the strong drift present in the recording indicates that more work needs to be done to improve the fouling-resistance of the sensor but also that no quantitative result can be extracted from the recording. Spike-and-recovery control could be used to quantify the signal, however in this case it was not performed as the sensor signal was too low. Therefore, one can only estimate the amount of adenosine that the sensor must have detected based on the previously published results. From literature, it is known that hypoxia-induced adenosine release at physiological conditions is in the range of tens of micromolar range [125, 43]. However, due to the lower temperature used in these recordings, the value must differ.

Using microdialysis and a microlectrode enzymatic sensor respectively, Masino et al. [157] and Frenguelli et al. [69] tested whether ATP was also released in the extracellular space post hypoxia . Neither author reported a difference in the value of extracellular ATP before and after insult. Therefore, despite the higher sensitivity of the aptamer for ATP with respect to adenosine it can be assumed that the response recorded was not caused by ATP.

Examining further the contribution of inosine and hypoxanthine to the signal, Moser, Schrader, and Deussen [171] showed that adenosine half-life in the extracellular space is in the order of seconds, and broken down into its metabolites, mainly inosine. The study from Takahashi et al. [259], reported inosine levels in normoxia to be ten times larger than adenosine. However, post hypoxia, inosine levels increased only by three-fold, mostly originated from adenosine breakdown [259]. Overall, this should make the final concentration of adenosine only 3 times smaller than the one of inosine. Still the amounts being considered belong to the low micromolar range, concentrations at which the sensor showed no response for inosine. Therefore, it can be concluded that the response recorded (Figure 4.9.b) can only be attributed to adeno-

sine released in the extracellular space post insult.

Regarding the dynamics of the adenosine release vs. the synaptic depression, in agreement with the results published by Dale, Pearson, and Frenguelli [43] and Frenguelli, Llaudet, and Dale [67] shows that the adenosine release precedes the synaptic depression. However, compared with the results from Frenguelli, Llaudet, and Dale [67], the time difference between the onset of the two events was significantly different. Whilst in the previous studies the two were separated by less than 100 s, the difference between the two onsets exceeds 200 seconds. This delay can be attributed to the combined effect of multiple factors. First, the lower temperature than the physiological one at which the measurements took place. The difference of 10 °C causes the metabolism of cells to slow down and therefore cause a delay in the oxygen depletion with respect to the adenosine release [259].

Additionally, the difference between the characteristics of the two recordings could play a role. The fEPSPs are local measurement of synaptic activity and take place on the tissue, whilst the sensor, which lays above the slice, better reflects a larger region of the hippocampus.

In conclusion, despite the need to improve some aspect of the sensor design and fouling resistance, the aptamer-based sensor (E-AB) achieved the detection of hypoxia-induced adenosine release from a mouse brain slice. To the author's knowledge this result joins another two publications which successfully employed E-AB sensor to detect neurochemicals in the brain [176, 218], thus proving as a promising platform for real-time continuous detection of small molecules released in the brain.

Chapter 5

Selection and characterisation of new DNA aptamers for potential biomarkers and neurotransmitters: Uridine-triphosphate and Uridine-diphosphate-glucose

5.1 Introduction

For aptamer-based biosensors to take a more prominent role in the diagnostic and monitoring fields, more aptamers for relevant target molecule and with a K_D in the physiologically relevant range (high picomolar - low micromolar), need to be selected and optimised. Uridine triphosphate (UTP) and uridine diphosphate glucose (UDPg) are neurochemicals which are released in pathological brain conditions, e.g. epilepsy [3], as a result of ischaemic events in organs [130, 62] and diseases like dry eye disease and metastatic cancer [283]. However, no knowledge is available on the dynamics of that release, as both molecules lack an analytical method to detect them with sufficient temporal and spatial resolution, *e.g.* an associated enzyme- or antibody-based biosensor. Being able to measure their release in real-time with a sensor could profoundly

increase our comprehension of the impact of such signalling molecules in the working of the brain and other organs, but also provide some new diagnostic tools.

In this chapter, the selection of two novel DNA aptamers via Capture-SELEX for UTP and UDP-glucose is described. The original SELEX design requires target molecules immobilisation, which is problematic for small-molecule targets as it can preclude the molecule from interacting with the aptamers. This obstacle was removed by Stoltenburg, Nikolaus, and Strehlitz [250] with the development of Capture-SELEX. As shown in Figure 5.1, Capture-SELEX immobilises the DNA library on magnetic beads leaving the target molecule free in solution. The beads are then incubated with the target molecule and the aptamers interacting with target will come off the beads. The eluted aptamers are then amplified and regenerated into single-stranded DNA to make up the pool for the successive selection round.

After sequencing of the selected Capture-SELEX pool, the sequences were analysed with the help of a bioinformatic software to reduce the number of candidates. The emerging sequences were further screened with a high throughput fluorescence assay using SYBRGreen I dye [164] and then characterised with microscale thermoelectrophoresis (MST) [207]. Further optimisation of the emerging sequence was continued with MST to reduce the aptamer length to the minimum binding sequence.

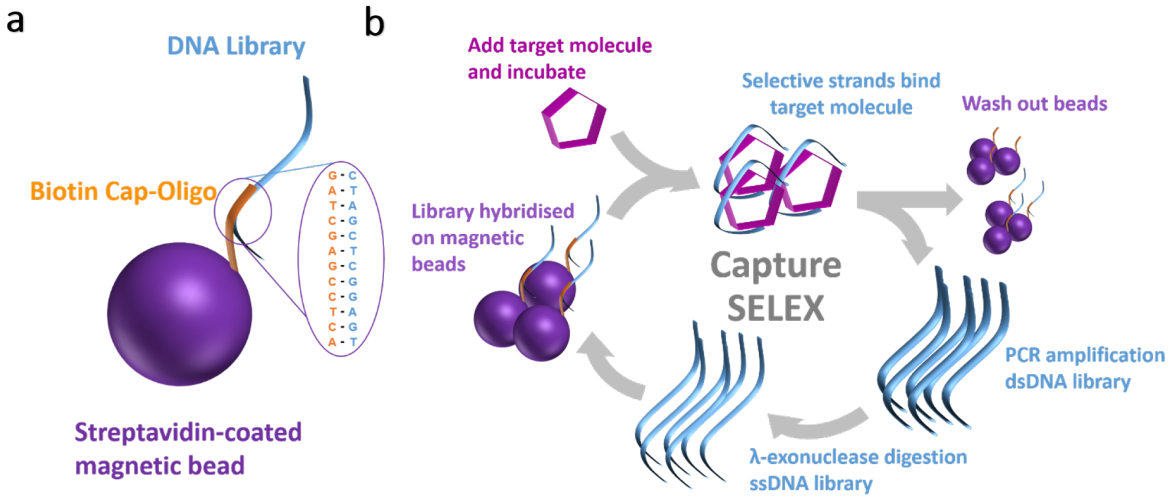

Figure 5.1. The Capture-SELEX work flow. *a) Schematic of the immobilisation of the DNA library on the beads. The streptavidin-coated magnetic beads (purple) are functionalised with biotin-tagged DNA strands, the capture oligo (orange). The DNA library (blue) hybridises onto the beads thanks to the 12 bases complementary sequence. b) Schematic representation of Capture-SELEX protocol for each cycle. As for traditional SELEX, the protocol starts with a randomised library. The Capture-SELEX library presents an additional known sequence in the middle of the randomised region, and complementary to the cap-Oligo one, which anchors the library (blue strand) to beads. Upon addition of the target molecule (magenta pentagon) and after an incubation time, the strands that interact with the target will detach from the beads, perhaps undergoing a conformational change as they bind to the target molecule. After collecting these released strands from the beads, the selective library is amplified via PCR reaction and returned to single stranded DNA by means of λ-exonuclease digestion, where nuclease binds the negative strand thanks to the phosphate functionalisation of the reverse primer. The sub-library is ready to be re-complexed with the beads and for another Capture-SELEX round.*

5.2 Results

After having established a new protocol to produce an aptamer-based electrochemical biosensor, the natural next step was to look for a small molecule for which an enzyme does not exist and that had been hypothesised to be involved in neuroinflammation and neurodegenerative diseases that could also be used as a biomarker for diagnostic applications. After evaluating multiple candidates, the choice fell on UTP and UDP-glucose (UDPg). The two uracil-based nucleotides, poorly studied part of the ubiquitous purinergic system, have been linked to multiple pathological conditions. For example, in epilepsy and status epilepticus UTP release has beer recorded via HPLC [117], and has been administered as a seizure inhibiting drug as illustrated in Figure 5.2.a [121, 3]. However, the lack of a technique to measure with sufficient temporal resolution the dynamics of the release hinders the understanding of the function the nucleotides in the activated circuitry. An hypothesis of the working circuitry was made by Alves, Beamer, and Engel [3] and is illustrated in Figure 5.2.c. As indicated in the figure the role of UDP-glucose and its associated receptor $P2Y_{14}$ in epilepsy is still poorly understood also due to the lack analytical tools are available to measure its release [84].

Due to the working principle of the developed electrochemical biosensor and after evaluating a variety of different SELEX protocols, Capture-SELEX was the best option to select an aptamer for a small molecule that presented structure switching properties.

5.2.1 Optimisation of pilot polymerase chain reactions (PCR)

Since SELEX consist in a series of nested PCR, a PCR optimisation process was conducted to determine the ideal amount of template DNA (SELEX library), primers, the optimal annealing temperature, number of cycles and possible target molecule interference into the amplification. First, the template DNA concentration was studied with the range 50 pM, 100 pM, 200 pM and 300 pM. For the other reagents, the final concentrations were: 5 µl of the 10x Taq buffer, 200 nM forward primer (FP), 200 nM reverse primer, 200 µM of dNTP-mix and sterile water to make up to 50 µl per reaction. For

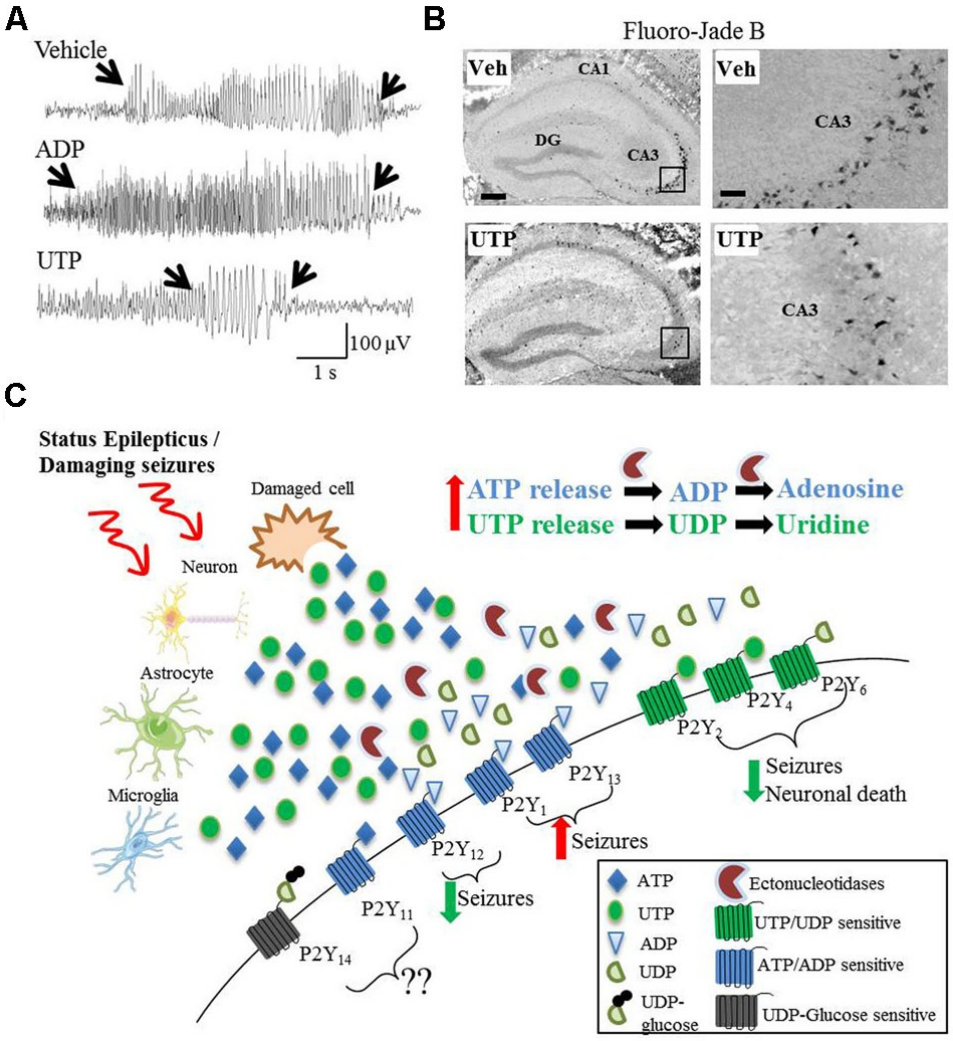

Figure 5.2. P2Y agonists and their effect on seizure. *A) EEG recording of the anti convulsive effect of UTP and the convulsive effect of ADP on status-epilepticus induced via kainic acid. B) Staining with Fluoro-Jade B of neuronal cell death which was reduced by UTP. C) Model of P2Y receptor and it its purines during and after epileptic insult and status epilepticus. Reprinted from Alves, Beamer, and Engel [3]*

the PCR, the samples underwent a 5 min denaturing step at 95 °C, then 25 PCR cycles (denaturing: 30 s at 95°C, annealing: 30 s at 56 °C, elongation: 30 s at 72 °C), followed by a 5 min extension step at 72 °C. The product was run on a 2% agarose gel at 90 V for 45 min and then imaged. The resulting Figure 5.3.a show that 200 and 300 pM concentrations present multiple bands. Out of 50 and 100 pM, the latter was chosen as the optimal condition and was therefore used in the next steps.

For the primer optimisation four concentrations were tested: 100 nM, 200 nM, 300 nM, 400 nM. All the other reagents were unchanged and 100 pM DNA template was added. The PCR cyclic conditions were the same as previously described. The gel showed the first band for 200 nM (magenta, Figure 5.3.b), which was therefore chosen as the optimal condition.

For the optimisation of the annealing temperature the range tested was from 55 - 65 °C. Therefore, 10 reactions were prepared using the optimised concentrations of template DNA and primers, 100 pM and 200 nM respectively. The cyclic conditions were maintained but at the annealing step, a gradient was set to allow testing for all the indicated conditions. The 2% agarose gel (Figure 5.3.d) displays the expected behaviour as the bands fade with increasing temperature. Multiple bands are present for 55 and 56 °C and dim product bands from 60 °C and above. The temperature chosen was 57 °C (magenta) as 58 °C is the melting temperature of the reverse primer.

The process continued with optimising the number of cycles and four conditions were tested: 15, 20, 25 and 30 cycles. During the PCR run, the samples were removed when the indicated cycle number was completed and were reinserted in the machine for the final extension step. Figure 5.3.c is the UV image of the 2% agarose gel. As shown for 15 cycles only a weak band is visible whilst the 30 cycles multiple bands are present. Both 20 and 25 cycles showed an ideal single band, but 25 (magenta) was preferred as brighter.

Summarising, the PCR optimisations resulted in the following parameters: 100 pM template DNA, 200 nM forward and reverse primers, 57 °C annealing temperature and 25 cycles. Such parameters will be used during the SELEX process to generate a positive control band, that together with the negative control, ensure that the SELEX product is being amplified correctly.

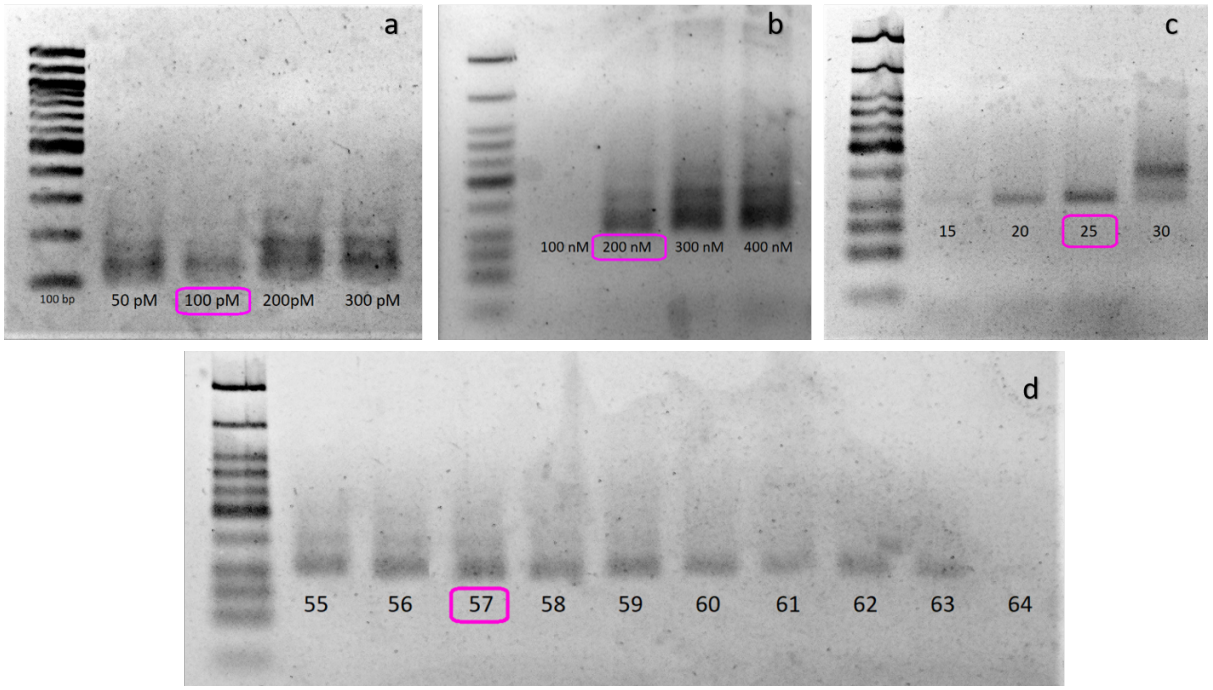

Figure 5.3. 2% agarose gels of the PCR products for the pilot studies. *a) PCR optimisation of template DNA concentration. The gel shows the DNA bands produced by amplifying with 50, 100, 200 and 300* pM *of template DNA. The expected profile of increasingly brighter DNA bands is visualised. The 200* pM *and 300* pM *however show multiple bands, indicating the formation of by-products. Therefore the condition chosen as optimal is 100* pM *(magenta). b) PCR optimisation of the primer concentration. As shown by the figure, four primer concentrations were tested: 100, 200, 300 and 400* nM*. Again the profile presented is of increasing number of bands and brightness. As 100* nM *showed no PCR product, 200* nM *(magenta) was chosen. c) Optimisation of the number of PCR cycles. The gel shows a very dim product band for 15 cycles and increasingly brighter single band around 100 bp for 20 and 25 cycles, whilst 30 cycles produce two bands (100 and 150 bp). 25 cycles (magenta) was chosen as the optimal condition. d) Optimisation of the annealing temperature. The figure shows the PCR product of annealing temperatures ranging from 55-64* °C*. The gel shows a decreasing number of bands and band brightness with the increase of the temperature. 55 and 56* °C *exhibit multiple bands and from 60* °C *up, the bands appear less bright. Therefore, 57-59* °C *is the optimal range; 57* °C *(magenta) was chosen.*

5.2.2 Selecting novel aptamers for the detection of UTP and UDP-glucose via Capture-SELEX

Table 5.1. Parameters of the Capture-SELEX rounds for UTP and UDP-glucose. *The parameters are the number of binding sites for the library for each target molecule, the concentration of the target molecule in solution and the incubation time of the library with the target molecule. In each round, only a single parameter was changed to avoid imposing too stringent conditions altogether and losing the library. In rounds 1 to 4 the library was selected using a mix of both molecules. From round 5 on, the two libraries were enriched separately. The stringency of the selection was raised gradually for concentration and incubation-time from the fifth round onward, either reducing the concentration or the incubation time from 60* minute *to 30* minute*. Whenever the concentration was reduced the incubation time was 60* minute*, to avoid imposing excessive stringency.*

Round #	Molecule	Concentration	Incubation time	# library immobilisation sites
1	UTP/UDPg	100 µM	60 min	4 nmol
2	UTP/UDPg	100 µM	60 min	3 nmol
3	UTP/UDPg	100 µM	60 min	2 nmol
4	UTP/UDPg	100 µM	60 min	1 nmol
5	UTP | UDPg	100 µM	60 min	0.5nmol
6	UTP | UDPg	50 µM	60 min	0.5nmol
7	UTP | UDPg	50 µM	30 min	0.5nmol
8	UTP | UDPg	10 µM	60 min	1 nmol
9	UTP | UDPg	10 µM	30 min	1 nmol
10	UTP | UDPg	5 µM	60 min	1 nmol
11	UTP | UDPg	5 µM	30 min	1 nmol

Table 5.1 shows the parameters used for each SELEX round. From round one to round four, the only parameter changed was the number of binding sites for the library on the beads. The beads are coated with streptavidin, to which biotin functionalised capture oligo was immobilised. The coating density suggested was 1 ml of beads for 2 nmol of the immobilised library. In round one, 2 ml of beads were used to immobilise the entire library (4 nmol). The beads functionalised with the library underwent an incubation at 28 °C for 20 min with mild shaking, to remove any loosely bound aptamer (temperature step) and a 45 min incubation at room temperature with mild shaking to remove any aptamer sensitive to any components of the buffer used for the selection (background step). Afterwards, the library-functionalised beads were incubated with 100 µM UTP/UDP-glucose mix for 1 h at room temperature with gen-

tle shaking. As the DNA concentration of the collected supernatant was unknown, a pilot polymerase chain reaction (PCR) was performed to evaluate the optimal DNA amount (Figure 5.4.b) to proceed with for the amplification of the entire library. Figure 5.4.b shows that no matter the amount of library used, the amplified library band appeared around the 150 bps size-marker, instead of around 100 bps, as it would be expected as the library is 108 bps long. One hypothesis is that the DNA assumes secondary structures while running in the gel, which prevented the DNA from running at the correct height. However, after running the PCR product on a denaturing gel which still produced the band at the wrong height, the hypothesis was discarded. Following this step, the entire round 1 library was bulk amplified, using 5 µl of DNA in each reaction, and the result imaged via agarose gel (Figure 5.4.c). As the PCR amplification produces double-stranded DNA (dsDNA), the negative strand was removed via λ-exonuclease digestion (Figure 5.4.d), thus returning to a single-stranded DNA library (ssDNA). Finally, the product was ethanol precipitated and resuspended in PBS-Mg, ready to be hybridised on to fresh beads to proceed with the next round. From the second to fourth round the volume of beads used halved in each round, thus reducing the amount of each sub-library available to interact with the target molecule, until reaching 500 pmol (Table 5.1, #library immobilisation sites). With each round the number of copies for each sequence increases exponentially, whilst the diversity of the pool decreases, thus a lower number of binding site on the beads would still suffice to bind the entire diversity of the library.

At the fourth round, a second band started to show on the PCR product gel as shown by Figure 5.4.e. A few attempts were made to continue the selection process but whenever amplifying the library, the 150 bps was disappearing, and more bands appeared on top of the 250 bps band. This phenomenon is a result of primer-product hybridisation and product-product hybridisation (by-products), as shown by Shao et al. (2011). Therefore, it was necessary to separate the library DNA from the by-products. Multiple approaches have been tested (gel extraction kit, gel electrophoresis from agarose gel slice, slice centrifugation, urea PAGE gel extraction) and the technique that produced the highest yield for this short DNA segment, and which proved to be the most reproducible was gel extraction via centrifugation. The DNA library

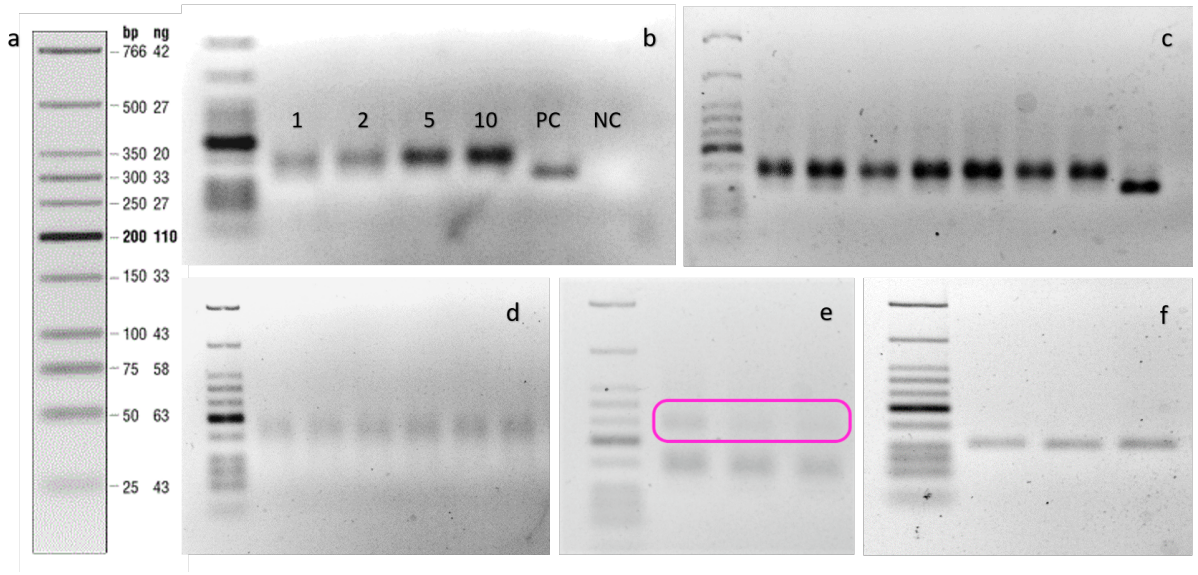

Figure 5.4. 2% agarose gel of the PCR product after different steps of the Capture-SELEX process. *a) Low molecular DNA ladder from NEB, band pattern and respective base length is shown. b) Pilot PCR product. The gel shows the DNA ladder, the PCR product using 1, 2, 5 and 10* µl *round 1 library, positive control (PC) and negative control (NC). A clear band was visible just above 150 bp for the amplified SELEX library despite the library being of 108 bases long. It can also be seen that for 1 and 2 µl products a faint band is appearing at the correct height. c) Bulk PCR amplification of the entire round 1 library (2 ml). 5 µl of the library was used in each reaction. Again the band of the amplified library lies above the 150 bp band, whilst a faint band can be seen above the 100 bp marker, at the same level as the positive control. d) λ-exonuclease digestion product. The DNA bands appeared at same sixe, but less intense. e) Bulk PCR amplification product of round 4. The magenta square highlights the second band at 250 bp which appeared after the bulk amplification, on top of the library band placed at 150 bp. f) PCR amplified DNA library after the gel extraction. The DNA band aligned with the correct original library length (above 100 bp)*

emerged from round 4 was concentrated and run on a 2% agarose gel. The bands containing the DNA with the correct length were cut out of the gel using a UV lamp and the slices placed in a perforated 0.5 ml tube, which was placed a 1.5 ml tube. The column was spun at 13 krpm for 20 min and the flow-through collected and pooled together to start the next round. To prevent further double bands, the PCR cycles were reduced to 20 at first, and to 15 afterwards. From the fifth round onward, the two target libraries were enriched separately. Once the library for round 5 was collected, a 2% agarose gel was performed to verify the length of the DNA product resulting from the extraction, which was confirmed to be in the expected range of 100 bps (Figure 5.4.f). After that, in each round, only the target molecule concentration or the incubation time were reduced, so as not to impose too stringent conditions (Table 5.1, Time and Concentration.).

5.2.3 Sequencing the UTP and UDP-glucose libraries

Once round 11 was completed, a portion of the library was amplified, and the template purified using a PCR clean-up kit (NEB). The template was ligated into a vector, using the TOPO vector Kit, and transformed into ONE-SHOT TOP10 F' E. coli competent cells and grown overnight at 37 °C. Ten white colonies for each library were amplified with colony PCR to verify the correct insertion of the aptamer in the plasmid. The incorrectly cloned colonies were discarded and the protocol continued by inoculating 96 different colonies for each library in 5 ml LB broth with 100 $\mu g\,\mu l^{-1}$ ampicillin left to grow overnight at 37 °C and 180 rpm. The cultures were pelleted and the plasmid extracted using the plasmid extraction mini-prep kit and suspended in 30 µl of TAE buffer. Ten tubes from each library were tested for their concentration and the result averaged. The UDP-glucose and UTP cloned libraries showed an average concentration of 710 $ng\,\mu l^{-1}$ and 620 $ng\,\mu l^{-1}$ respectively. The samples were prepared and sent for sequencing.

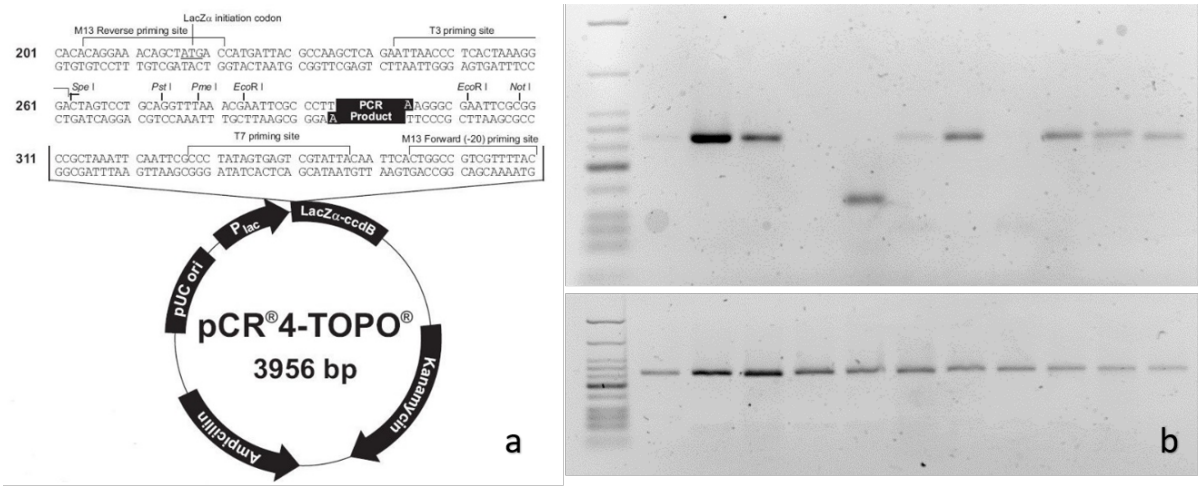

Figure 5.5. Cloning vector and 2% agarose gel of the colony PCR product for both UTP and UDP-glucose libraries. *a) Map of the TOPO vector used for the cloning of aptamer sequences. In black is indicated the location where the aptamer sequence is inserted, whilst the entire length of the segment run from the M13 forward primer site to the M13 reverse primer site. Overall, since the insert is of 108 bps, the total fragment length is expected around 270 bps. b) Colony PCR product for the UDP-glucose (top) and UTP (bottom) cloned libraries. As expected the DNA fragment band appeared between the 250 and the 300 bps bands, thus confirming the success of the cloning procedure. The bacteria cultures with no bands or smaller bands were not used for sequencing.*

5.2.4 Analysis of the sequencing data

The analysis of the sequencing data aims to verify the enrichment of selective aptamers as a result of the Capture-SELEX rounds and identify potential candidates. Enrichment can be detected by the repetition of certain nucleotide sequence motifs in multiple aptamers, as this supports the hypothesis that the motif is important for the binding of the target molecule. A motif can also represent a specific structure in which the aptamer folds upon binding to the target molecule.

In the specific case of Capture-SELEX enrichment can also be found in mutation of the anchoring sequence, which indicates a reduced hybridisation energy, thus facilitating the strand removal from the beads and its interaction with the target molecule [250].

For each library 96 strands were sent for sequencing. The resulting sequences were visualised in Jalview2 [285] and aligned via the embedded ClustalΩ algorithm [151]. For the UTP library, 10 sequences showed one or more duplicates, 1 a partial ligation, *i.e.* incorrect insertion in the vector, and 72 were present only once, whilst

Table 5.2. Summary table of duplicate sequences.

UTP			UDP-glucose		
Sequence	# Duplicates	Duplicate ID	Sequence	# Duplicates	Duplicate ID
A3	1	F5	A1	1	A2
A8	1	H10	A4	1	B7
A9	1	G11	A7	1	A8
A12	2	C1,C12	A9	2	F2,F3
B9	1	G4	B8	1	H7
C3	1	D3	B9	1	E9
C6	1	D4	C1	2	C2,C7
C8	4	C9,C10,D2,F4	C8	1	D6
D7	1	D8	C9	1	C10
E9	1	E10	C12	3	D2,D3,D7
			E1	2	F5,G6
			E6	1	G11
			E7	1	H5
			E12	1	G8
			H11	1	H12

for UDP-glucose library 15 sequences showed duplicates, 4 a partial insertion and 58 unique sequences. The presence of duplicates demonstrated that the library had undergone enrichment. Through the sequence alignment it was also possible to extract information regarding mutations or deletions in the anchor sequence. In their work, Stoltenburg, Nikolaus, and Strehlitz [250] hypothesised that the mutation on the anchor sequence are the result of the balance between selection pressure, favouring less stable docking sequences to promote conformational change, and a hybridisation sufficient to prevent unspecific elution. In the UTP and UDP-glucose libraries 8 and 2 sequences, respectively, were found to exhibit mutation on the anchoring sequence. All information duplicate sequences and mutations/deletions for both libraries are summarised in tables Table 5.2 and Table 5.3 respectively.

To try and extract more information, I calculated the phylogenetic tree using the neighbour joining algorithm coupled with the DNA weighting matrix, to group the sequences by similarity, calculate consensus sequences and extract some statistical information regarding conserved features among the sequences. The analysis produced inconclusive results. The sequences showed no significant motif conservation and no sequences could be grouped for the exception of the duplicates. This result is

Table 5.3. Summary table of mutations and deletions encountered in the anchor/hybridisation domain of sequenced candidates. *The table provides information for both libraries on the sequence, whether it presented a deletion and/or mutation, where the mutation is places, and which nucleotides were exchanged or how many were deleted*

Sequence	Variation	Position	Old→New or # bases deleted
		UTP	
A5	Mutation	# 12 Anchor	C → T
A6	Deletion	N40	1
A9-G11	Mutation	# 10 Anchor	A → G
C11	Deletion	N40	1
C2	Mutation	# 3 Anchor	A → T
D6	Mutation	# 2 Anchor	G → A
D7-D8	Deletion	N10	8
D9	Deletion	# 1-2 Anchor	2
E6	Deletion	N40	2
E9-E10	Mutation	# 8 Anchor	C → T
G6	Deletion	N40	1
G6	Mutation	# 6 Anchor	C → G
H2	Deletion	N40	4
		UDP-glucose	
C5	Mutation	# 1 Anchor	G → T
C11	Mutation	# 2 Anchor	T → A

not surprising: with 10 round of the SELEX the library diversity should have reduced from 10^{15} to 10^5 and only 10^2 sequences were identified.

To gather structural information on the sequences, I turned to the bioinformatics tools available. I employed the software APTANI2, developed by Caroli, Forcato, and Bicciato [32], to calculate secondary structures of the DNA sequences and their respective energy and identify structural motifs *e.g* hairpins, intra-strands or bulge loops. The analysis consisted in folding the sequences, via the viennaRNA package [148], and selecting only the final structure which had a minimum free energy (MFE) ≥ 3 kcal mol^{-1} (12.6 kJ mol^{-1} $\approx$ 5RT). Then the sequences are compared to a library of known binding motifs to find matches. 12 sequences in total (7 for UTP and 5 for UGP-glucose) showed binding motifs with sufficiently high energy and they are summarised in Table 5.4.

Table 5.4. Table of the sequences emerged from the analysis of APTANI2 [32]

Sequence	Target molecule	Sequence	Target molecule
A4	UTP	B11	UDPg
B1	UTP	D9	UDPg
B3	UTP	E3	UDPg
E1	UTP	E8	UDPg
E5	UTP	G11	UDPg
F12	UTP		
G2	UTP		

5.2.5 Aptamer candidates screening characterisation with high throughput SYBRgreen (SG) assay

The sequences emerged from the analysis with APTANI2, together with the ones presenting duplicates, mutations and deletions were taken further for additional characterisation. Given the high number of sequences to study, a high-throughout method was necessary in order to characterise them all in a relatively short turnaround-time. Considering also the high number of sequences involved, it was necessary for a label free method to contain the cost. After a literature review, a few methods emerged. Thioflavin assay, which exploits the presence of G-quadruplexes in the DNA structure could not be employed as from the 2D folding of the sequences it had emerged that only one sequence presented a G-quadruplex structure [209]. Another label-free assay exploits DNA intercalating dyes [219]. The Hoecst assay by Le et al. [131] and the SYBRgreen assay by Tan et al. [260] exploit two different DNA-intercalating dyes that upon binding present an enhanced fluorescence. The main difference is that the Hoechst 33258 dye binds the minor groove of AT-rich double-stranded DNA, whilst SYBRgreen I has multiple interaction modes [51]. Since Hoechst 33258 has shown a pH dependence on both fluorescent intensity and peak emission wavelength [79], SYBRgreen I (SG) was chosen.

To set up the assay, some control measurements were completed. The first aimed to evaluate whether the target molecules exhibited any auto-fluorescence in the spectrum of interest or whether they did in presence of SG. As illustrated in Figure 5.6.a and Figure 5.6.b, for both UTP and UDP-glucose the signal for the full assay and the highest concentration (target-DNA-SG, black) was respectively 7 and 4.5 times larger than the signal presented by the blanks (magenta, blue, orange), which allows for a high signal to noise ratio. However, looking more closely to the blanks, it appears that both UTP and UDP-glucose show some autofluorescence (5k a.u. for UTP, panel a, 10k a.u. for UDP-g lucose, panel b) which slightly increased in the presence of SG, especially for UTP (blue, panel a and b). A second assay was conducted to further investigate the autofluorescence of the target molecules and of the free SG. In this case PBS-Mg works as the blank to compare the authofluorescence of the target molecules

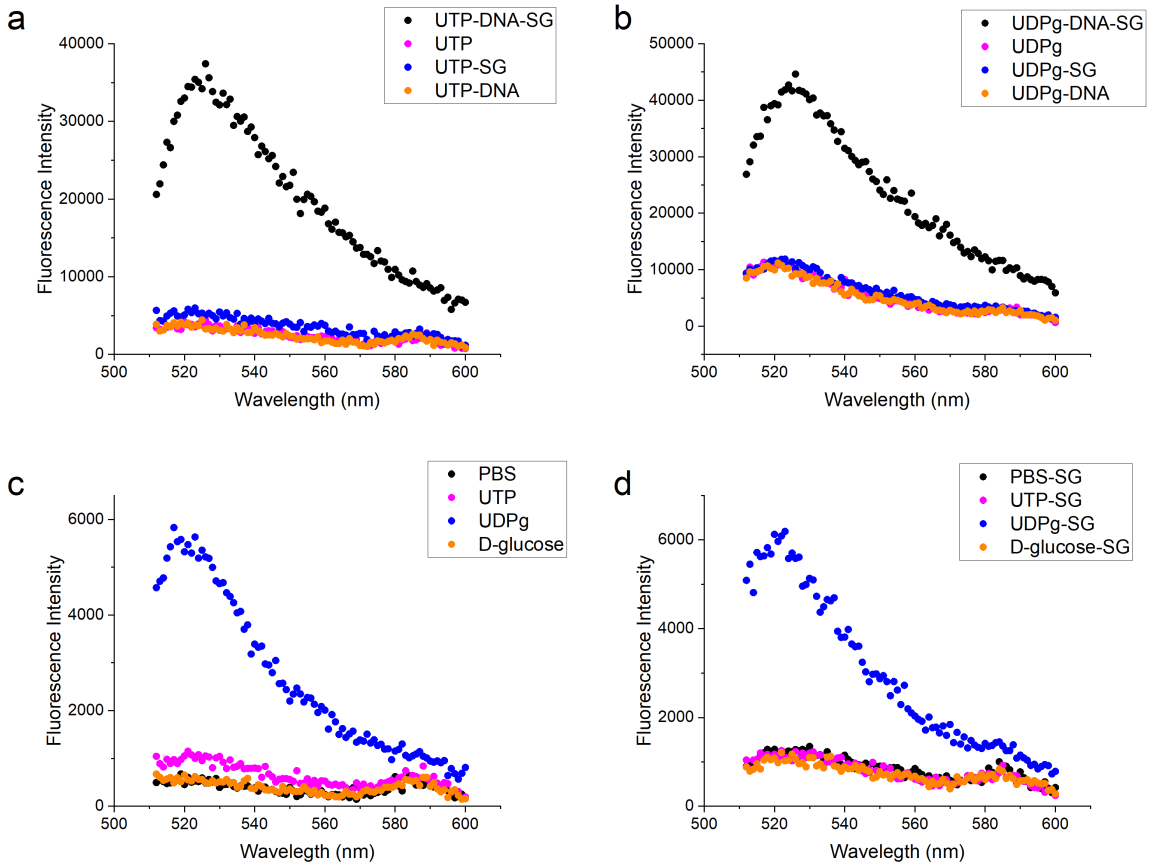

Figure 5.6. Autofluorescence control measurements for the SYBRgreen (SG) assay. *Autofluorescence control assay and blanks for UTP (a) and UDP-glucose (b). In black is the spectrum of the complete assay where the aptamer and the SG are intercalating producing the maximum fluorescence possible at this concentration of the target molecule. The emission spectra of the blanks: target molecule by itself (magenta), with SG (blue) or the aptamer (orange). c)-d) Assay on autofluorescence of the buffer (black) and buffer with target molecule both in absence and presence of SG. The fluorescence intensity increase normalised with the spectra of PBS-Mg (black, panel c) were 1.9 ± 0.3 for UTP (magenta), 9.8 ± 1.0 for UDP-glucose (blue), 1.1 ± 0.2 for D-glucose (orange, panel c); and 2.4 ± 0.4 for PBS-SG (black), 2.3 ± 0.4 for UTP-SG (magenta), 10.6 ± 1.3 for UDP-glucose-SG (blue) and 2.0 ± 0.4 for D-glucose-SG (orange, panel d). Each condition was tested in triplicate. Data: mean ± e_a, n=3.*

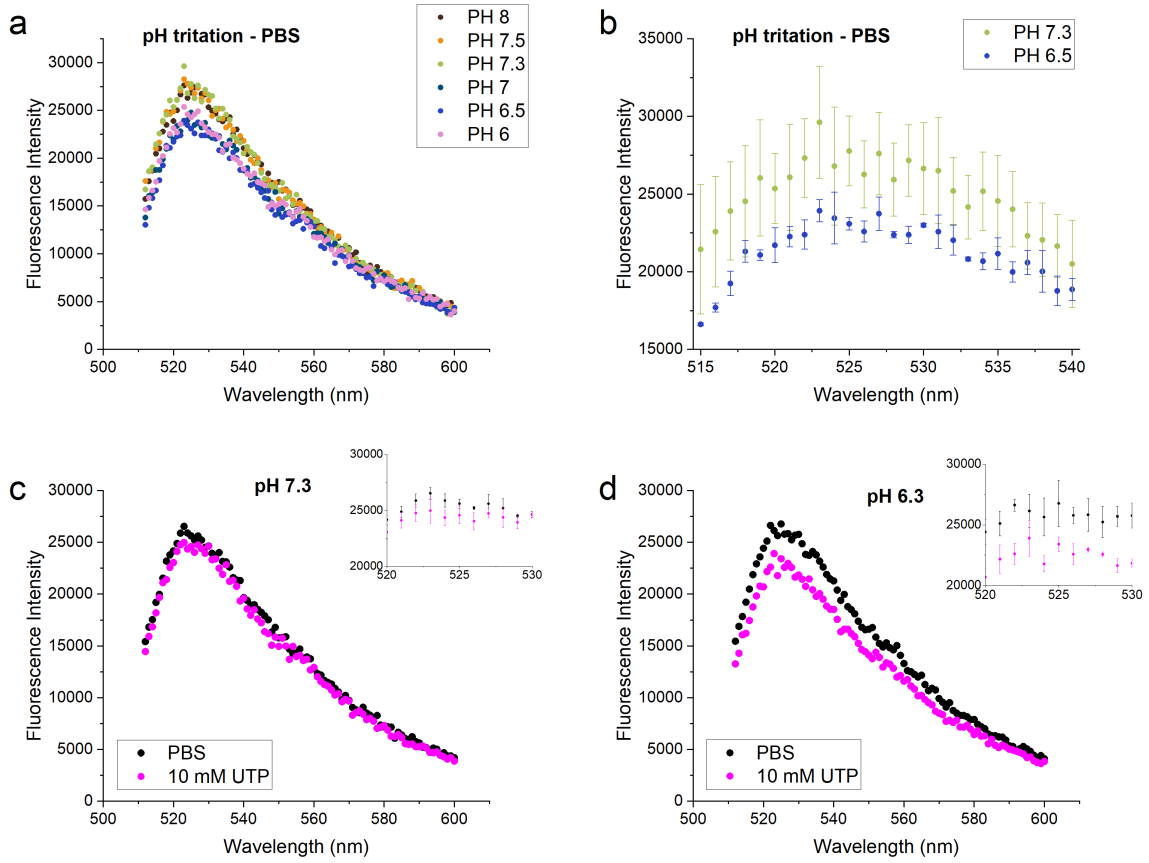

Figure 5.7. pH dependence of SYBRgreen (SG) fluorescence. a) Emission spectra of pH tritation of PBS with 1 mM ***$MgCl_2$ (PBS-Mg, buffer).*** *b) Detail of the peak of the emission spectra for pH of 7.3 (lime green) and 6.6 (blue) plotted as mean ± sd. c)-d) SG assay for an aptamer sequence selected for UTP. The SG signal was recorded in buffer and buffer spiked with 10* mM *UTP both at pH 7.3 (panel c) and 6.3 (panel d). The inset shows the detail of the peak of the emission spectra. Data: mean ± e_a, n=3.*

in the study. Figure 5.6.c shows the emission spectra for PBS-Mg (black), and PBS-Mg with 10 mM UTP (magenta), UDP-glucose (blue) or D-glucose (orange). UDP-glucose showed approximatively 10 times and UTP 2 times more autofluorescence than PBS-Mg, whilst D-glucose did not affect the emission spectra. When adding SG in solution the emission spectra of UDP-glucose and UTP did not significantly increase, but the fluorescence count for both D-glucose and PBS-Mg doubled (Figure 5.6.d). Considering that each assay will contain both the respective target molecule and the SG in each well, the fluorescence spectra of the target molecule with the SG, or PBS with SG was subtracted from all following measurements.

Next, I performed a second control measurement to evaluate the effect of the pH on the fluorescence intensity. This control was necessary as adding 10 mM UTP to PBS-Mg buffer changes the solution pH from 7.3 to 6.3. No difference in the pH of the solution was recorded for UDP-glucose in PBS-Mg (pH 7.3). Therefore, PBS-Mg was titrated with HCl and NaOH to achieve the pH of 8, 7.5, 7, 6.5 and 6. Then the SG assay was prepared according to protocol and the fluorescence emission spectrum recorded for each condition and plotted in Figure 5.7.a, entire fluorescence spectra and Figure 5.7.b the detail of the emission peak from to 515 nm to 540 nm. From the emission spectra it appears that the average value of the recorded fluorescence peaks around 28000 a.u. for pH ranging from 7.3 to 8, whilst the peak for pH 6 to 7 appears around 24000. From further examination of the data, by comparing the mean and standard deviation recorded for pH of 7.3 and 6.5 (Figure 5.7, panel b), it emerges that there is a significant difference in the fluorescence signal recorded for the two assay conditions. To gather further insight on whether different pH conditions affected the outcome of the assay, I tested the response of an aptamer candidate to the presence and the absence of the target molecule in two pH conditions: at pH 7.3 (Figure 5.7.c) and pH 6.3 (Figure 5.7.d), by matching respectively the pH of the 10 mM and 0 mM PBS-Mg solutions respectively. From the comparison of the two plots it can be deduced that the lower pH did affect both the aptamer folding and its affinity for the target molecule, as the same strand of DNA shows no response at physiological pH, but a significant decrease in fluorescence at pH 6.3 (Figure 5.7.d, inset). One could argue that the additional salts added into solution might also play a part, as sodium is known to play a part in DNA folding [8], but one can also argue that tertiary interactions *e.g.* H-bonds and electron-donor interactions, which are at the base of the aptamer-target affinity, are very much affected by the different amount of protonated and unprotonated molecules available. Consequently, for the assay containing UTP, the pH of the 10 mM solution was adjusted back to 7.3.

Once the necessary control measurements were completed , I went on to test the response of candidates from the previous analysis, 24 and 22 for UTP and UDP-glucose respectively, using 10 mM of the respective molecule in the SG assay. The choice to use a target concentration much higher than the biologically relevant one

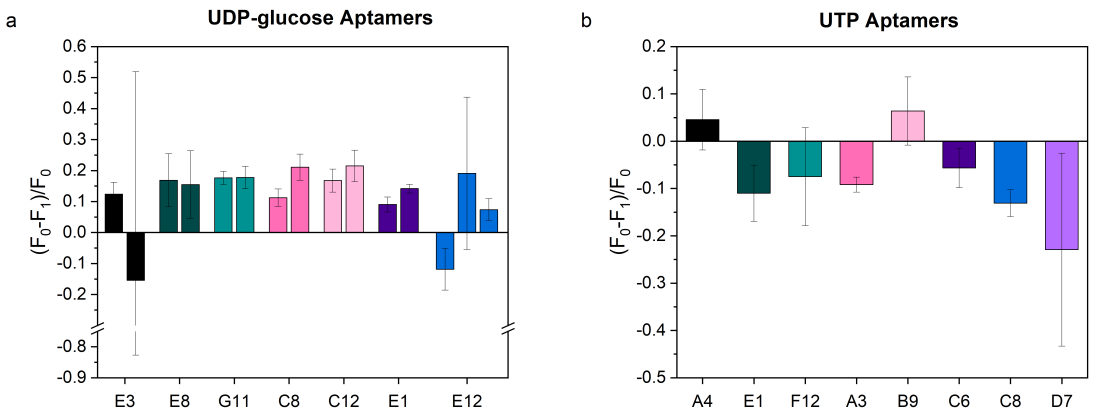

Figure 5.8. Plot of the response of UDP-glucose (a) and UTP aptamers (b) evaluated with the SYBRGreen assay. *The delta was calculated at 525* nm *using the formula* $\Delta = (F_0 - F_1)/F_0$*, where F0 and F1 are the fluorescence value measured in absence and presence of the target molecule respectively. Data: mean* $\pm$ e_a*, n=3.*

was due to the fact that the aptamers being tested are still full-length sequences (108 b) and that all the parts that do not belong to the binding site will contribute to the signal and make the signal variation, measured upon binding, smaller. Therefore, by adding a high concentration, the variation should still be meausrable. For the resulting spectra, average and standard deviation were calculated, and the background signal was subtracted to correct the contribution of the autofluorescence. For the strands that displayed a significant difference between the spectra recorded in absence and presence of the target, the Δ at 525 nm was calculated and the values are plotted in Figure 5.8.

I performed the SG assay with the aim to reduce the number of candidates from more than twenty to three, for each target molecule. From the results in Figure 5.8, it emerged that the assay can present both positive and negative Δ and that the same aptamer can showcase both responses. The comparison of the Δ and of the standard deviation, lead to the selection of the following candidates for continuing the strand characterisation and optimisation: C8, D7 and E1 for UTP and C12, E8 and G11 for UDP-glucose. The sequences are reported in Table 5.5.

The first step of the affinity maturation process consists in reducing the aptamer length. A bioinformatic study from Cowperthwaite and Ellington [40] has shown that the contribution of constant regions to the binding site of an aptamer is negligible. In

Table 5.5. Sequences of the selected candidates for each target molecule. *The forward primer region is in bold, the reverse primer binding region in bold and italic, the anchoring sequence is underlined and the random regions are in blue.*

UTP	
Name	Sequence
C8	TTGGGAAGAGAAGGACATATGATTACATGAGGATGAGGCTCGATCGGTATCTTTGGCATATCCTATCGTTCTATGTAACAGCCTG*TTGACTAGTACATGACCACTTGA*
D7	TAGGGAAGAGAAGGACATATGATGAAGAGGCTCGATCTAAGGATGTAATTATTCTTTTCGGTTAGTTATCTTCCTAG*TTGACTAGTACATGACCACTTGA*
E1	TAGGGAAGAGAAGGACATATGATTAGATCCGCATGAGGCTCGATCTGCATGTGGGCGACGCAGTGCCCGTGGGATTTACTTGCAC*TTGACATAGTACATGACCACTTGA*
UDP-glucose	
Name	Sequence
C12	TAGGGAAGAGAAGGACATATGATCCTTCCCTCATGAGGCTCGATCTGGTCTAATCATGCGATTAAACATATCGATAAAGTTTTTG*TTGACTAGTACATGACCACTTGA*
E8	TAGGGAAGAGAAGGACATATGATGTAATCCCTGTGAGGCTCGATCATGGCAGGTTGGTAACGGTGGCCTTCCGGCTATTTGTTCC*TTGACTAGTACATGACCACTTGA*
G11	TAGGGAAGAGAAGGACATATGATTACAAGATTGTGAGGCTCGATCTCCCCATATGTTTCGCATCAACGTGTTGGGACTGGGGTCA*TTGACTAGTACATGACCACTTGA*

Table 5.6. Summary table of the presence (YES) or inhibition (NO) of response by the aptamer candidates in the hybridisation test compared to the full length aptamer. *A lack of response in the hybridisation test could indicate a role for the primer in the binding site.*

UDP-glucose			
Aptamer	full	FP′	RP
C12	YES	YES	YES
E8	YES	NO	NO
G11	YES	NO	NO
UTP			
Aptamer	full	FP′	RP
C8	YES	YES	YES
D7	YES	NO	NO
E1	YES	NO	NO

the aptamer currently being evaluated, three random regions are present: the forward primer, the reverse primer and the anchor. The first two are used for the library amplification with PCR, whilst the third was used to anchor the strands to the magnetic beads. Since the primer sequences are each 23 bases long, I started by testing whether they could be removed without affecting the binding capability of the aptamer. To do so, I performed the hybridisation control SG assay following the protocol published by Le, Chumphukam, and Cass [132]. By adding the complimentary oligonucleotide to the primer strand, the interaction with those bases is impaired. If some nucleotides of the primer site are necessary for the binding of the target molecule, the SG assay should show no signal response. The summary of the results of the hybridisation test are reported in Table 5.6.

To get further insight into the role of the primer sequences in the binding, the 2D structures of the sequences of the candidates were calculated e in presence and absence of one or both primers, looking for folding patterns. The Vienna RNA package [148] was employed with the following settings: dangling ends at both ends of the helix, temperature set at 21 °C, DNA parameters and incorporating G-quadruplexes.

From the 2D analysis of the UTP sequences it emerged that: C8 presented a common core structure of 39 nucleotides for all sequences, with the exception of the full-length aptamer (Figure 5.9.a). D7 also showed an 18 bases common structure to the all sequences but the absence of the forward primer significantly affected the

random region structure (Figure 5.9.b). For E1, the presence of the forward primer defined the folding of the structure. A stem-loop of 16 bases placed in the longer random region was shared by all structures with the exception of the E1RP (Figure 5.9.c). For the UDP-glucose sequences: all C12 sequences presented a common structure 35 nucleotides-long, however the presence of the forward primer affected the folding of the rest of the aptamer (Figure 5.10.a). The E8 full-length aptamer and the sequence containing only the forward primer were predicted to present G-quadruplexes and 68 bases common structure , whilst the reverse and no primer sequences shared two stems of 23 and 25 bases (Figure 5.10.b). Finally, for G11 both the full-length and the sequence without forward primer have 42 bases-long structure in common, whilst there is less overlapping with the others (7 bases between full and RP and 10 bases between forward primer and no primer).

Combining the 2D analysis with the hybridisation test to check whether a common behavioural pattern existed, some conclusions could be dawn. Starting with the UTP candidates: for C8, the primers appeared to not play a fundamental role in both the SG hybridisation and the *in silico* folding, as their blocking/removal did not affect the aptamer activity. Therefore, the aptamer deprived of both primers (C8NP) was taken for further characterisation. For D7 the hybridisation SG assay showed that blocking the primer sites affected the response, which was confirmed by the 2D folding where the presence of the forward primer affected the calculated secondary structure. Consequently the sequence with no primers (D7NP) and the sequence containing the forward primer (D7FP) were carried on. No overlapping was seen for E1. Whilst for the UDP-glucose candidates: for C12 all the structures presented a core of 37 bases which folded in the same way and the SG assay confirmed no influence on from the primers, so the sequence deprived of both primers (C12NP) was carried on, whilst no conclusion could be made on the other two sequences E8 and G11.

5.2.6 Aptamer characterisation via Microscale thermophoresis (MST)

With a smaller list of candidates high throughput was no longer a requirement and the focus moved toward higher sensitivity. I chose to employ Microscale Thermopho-

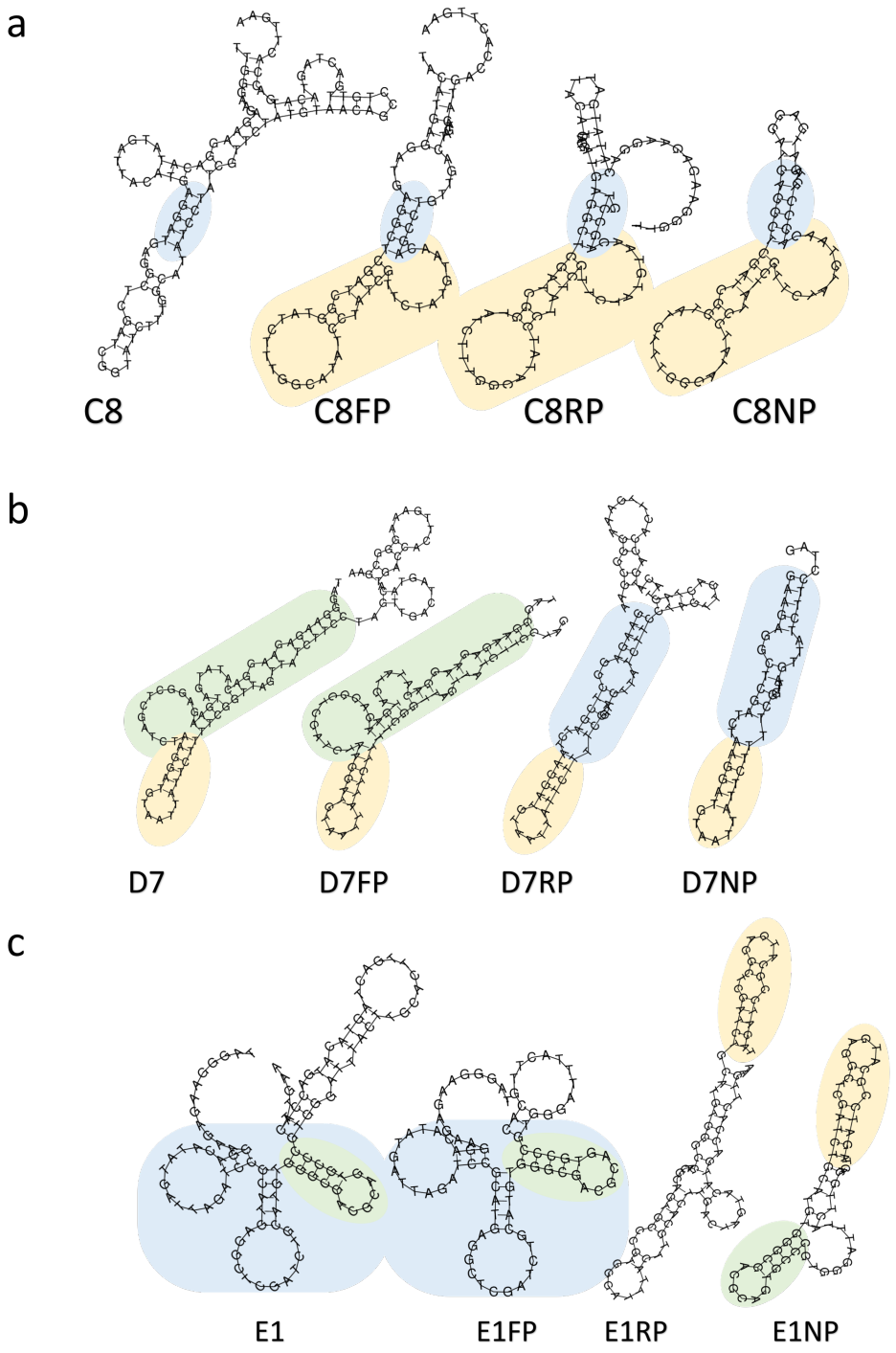

Figure 5.9. 2D folding of the three candidates for UTP (C8, D7 and E1) with and without the constant regions. *The image show the folding obtained for the full-length sequence, the aptamer containing only the forward primer (FP), only the reverse primer (RP), or no primers (NP). The coloured shape illustrate common structures. Folding performed with the ViennaRNA package [148]. The different colors correspond to foldings common to multiple sequences.*

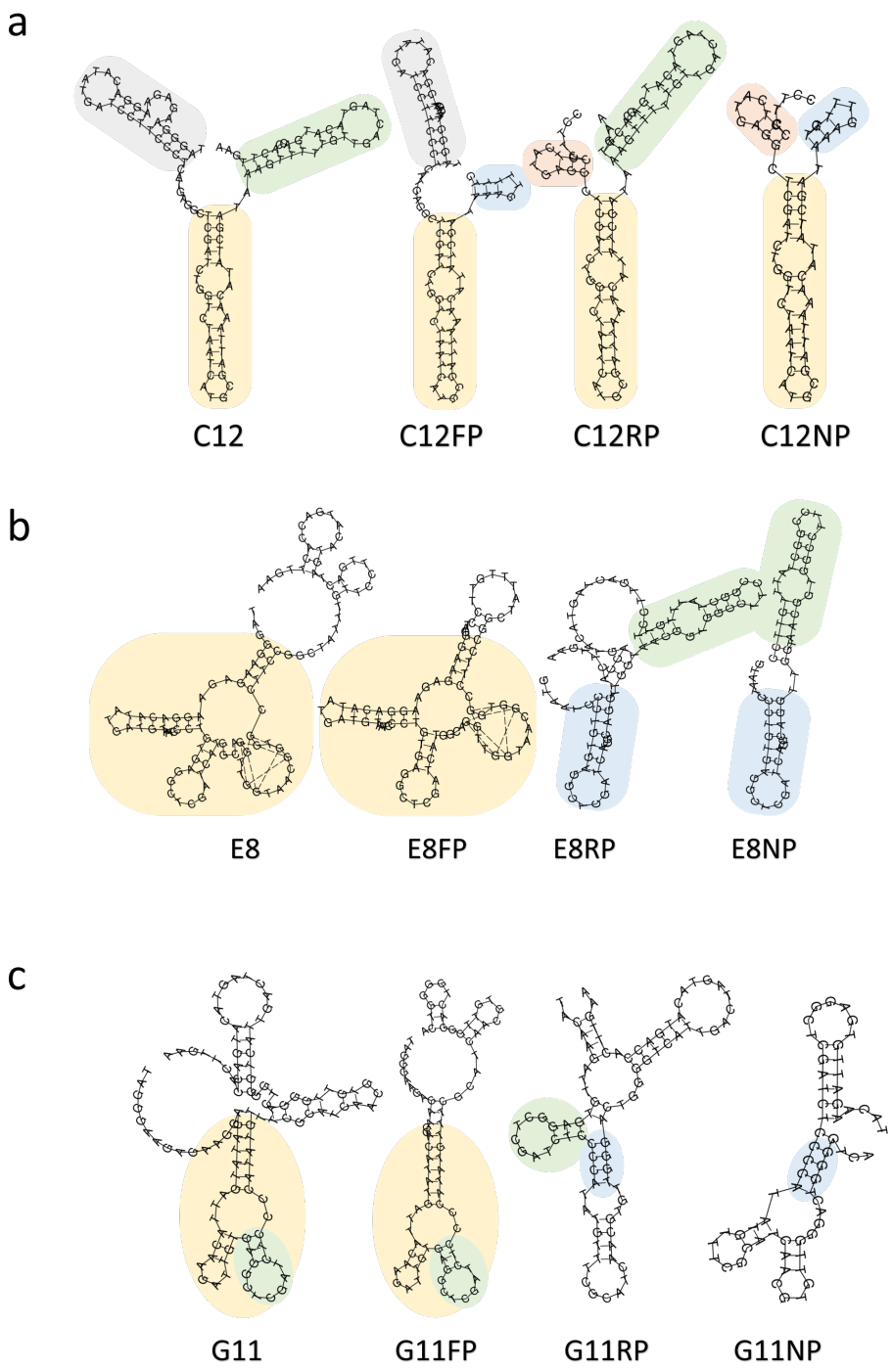

Figure 5.10. 2D folding of the three candidates for UDP-glucose (C12, E8 and G11) with and without the constant regions. *The image show the folding obtained for the full-length sequence, the aptamer containing only the forward primer (FP), only the reverse primer (RP), or no primers (NP). The coloured shape illustrate common structures. Folding performed with the ViennaRNA package [148]. The different colors correspond to foldings common to multiple sequences.*

risis (MST), a highly sensitive technique that exploits temperature gradient induced migration to verify whether a molecule is in the bound or unbound state. MST assays employs small sample size (µl), has a fast turnaround time time (c.a. 15 min) and it has been used to characterise challenging interactions like the one between aptamers and small-molecule targets [60]. For the assay, the candidates were purchased with a Cyanine-5 (CY5) modification on the 5' end. For the sequence where the combined hybridisation SG-*in silico* evaluation did not produce consistent result, the full-length aptamers were tagged with CY5 dye by PCR amplification. The forward primer contained the CY5 modification at the 5' end, whilst for the reverse primer an extra 25 T bases followed by and 18-atom hexa-ethyleneglycol spacer were added. The spacer and the 25 extra T were introduced to achieve size separation of the forward and the reverse strands once loaded on a urea PAGE denaturing gel. The gel was the imaged using both a 520 nm laser, to image the DNA content (Figure 5.11, a); and a 635 nm laser to image the bands labelled with CY5 dye (Figure 5.11, b). The dark band present on both sides was the forward strand as it presented a strong fluorescence at 635 nm, whilst the reverse strand, not labelled, was visible just above the forward strand, but with a much lower intensity only on the first gel (Figure 5.11). The band containing the forward strand was cut-out of the gel and the DNA extracted following the protocol described in the methods section. The extraction steps, however, caused some contamination of the sample, which made it harder in most cases to get a sufficient fluorescence for running a binding check assay using MST. To ramp up the final concentration, PCR amplification was performed in bulk (6x 50 µl reactions for each candidate).

Before commencing the affinity studies, I performed some preliminary tests to evaluate whether PBS-Mg was a suitable buffer for the assay by doing a capillary scan. Eight capillaries where filled with a dilution series (200 nM-1.56 nM) of CY5-labelled aptamer either in PBS-Mg or in PBS-Mg with 0.05% TWEEN 20. The control measurement verified that the aptamer in PBS-Mg experienced no adsorption on the capillaries walls as all the capillary scans within the fluorescence count range ($\leq$ 2500) showed no sign of adsorption (widening of the peak or multiple peaks, Figure 5.12,

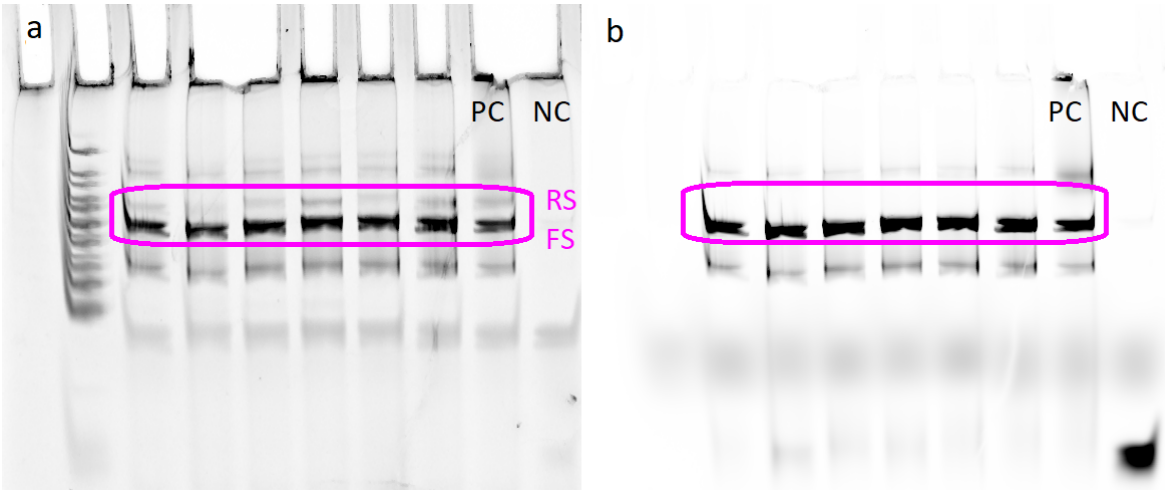

Figure 5.11. 12% urea-PAGE gel of CY5-labelled full-length aptamer imaged with 520 nm ***and 635*** nanom ***laser.*** *Inside the magenta boxes are the bands of the forward (FS, bottom) and reverse strands (RS, top) of the PCR product. The reverse strand is not visible on the right panel as it lacked the CY5 labelling.*

a and b). I continued by evaluating the effect on the fluorescence by characterising the concentration dependent fluorescence intensity. Figure 5.12.e illustrates the fluorescence intensity value for each capillary plotted against the concentration (legend). The signal intensity in PBS-Mg alone increase linearly from the concentration of 12.5 nM (Figure 5.12.c), whilst the addition of 0.05% TWEEN produced a linear behaviour throughout the entirety of the concentration range tested until the saturation value was reached (Figure 5.12.d). Therefore, PBS-Mg with 0.05% TWEEN20 was used as buffer for MST assays.

I then proceeded to characterise the response of the short versions of the aptamer candidates (C8NP, D7NP, D7FP for UTP and C12NP for UDP-glucose). For each candidate a first calibration was performed to determine the optimal aptamer-CY5 concentration. For all sequences, a concentration of 10 nM was sufficient to produce a viable signal with a 50 % LED power. Each aptamer was then tested against three concentrations of the respective target molecule: 500 nM, 50 µM and 500 µM, 100, 10 k and 100 k excess with respect to the aptamer concentration. None of the short aptamers showed variation large enough to conclude binding. Figure 5.14 shows two examples of the signal variations measured for the three target concentrations (C8NP for UTP and C12NP for UDP-glucose). Table 5.7 on the other hand summarises the

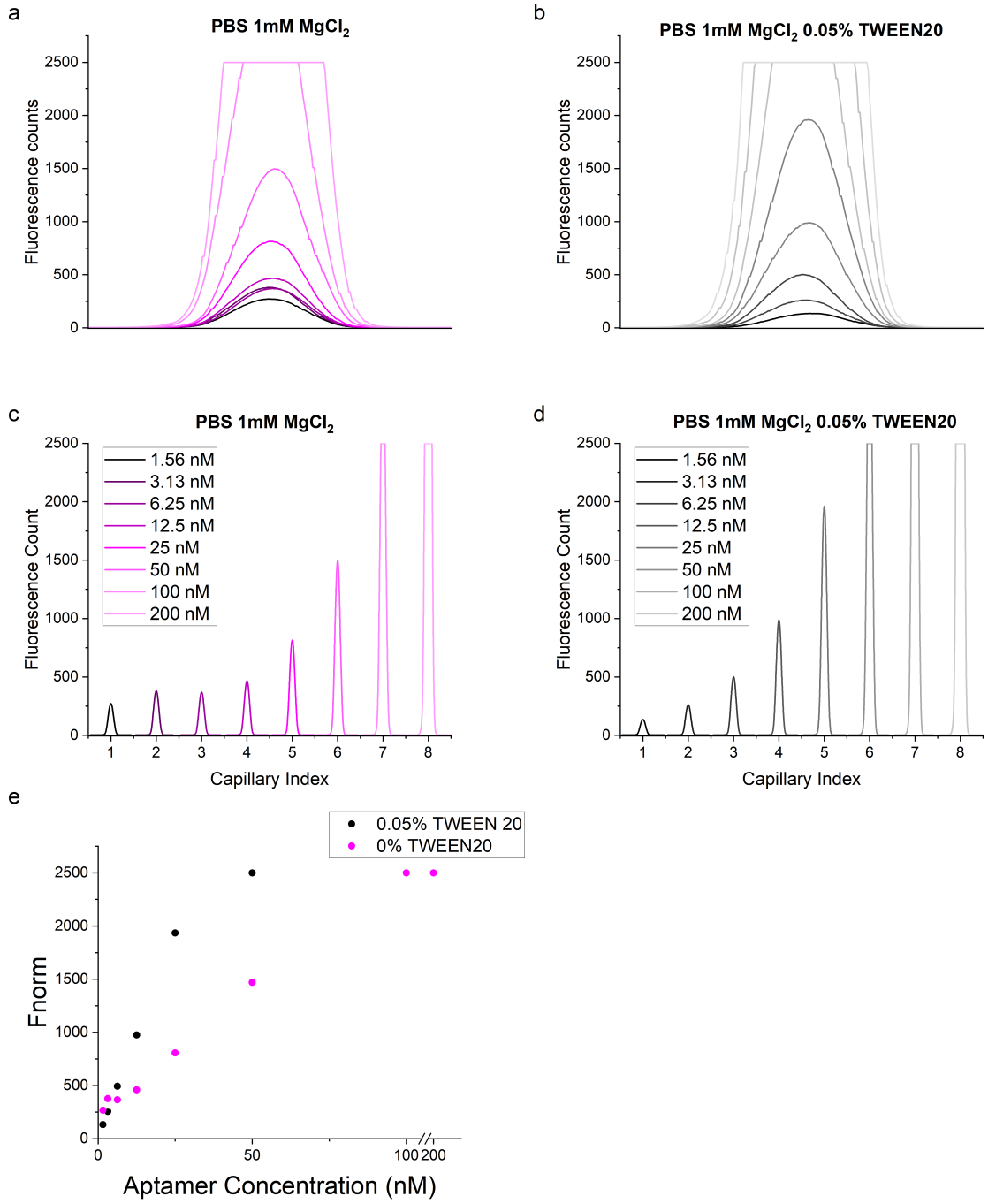

Figure 5.12. Evaluation of the effect of detergents on the fluorescence intensity recorded during the binding assay of microscale thermophoresis (MST). *Capillary fluorescence recorded at different concentrations of the CY5-labelled aptamer diluted in either PBS with 1* mM *$MgCl_2$ (magenta), or PBS with 1* mM *$MgCl_2$ and 0.05% TWEEN20 (black). a)-b) Display of the capillary of the fluorescence recorded for all capillaries below the saturation value ($\leq$2500). c)-d) Capillary scan recorded over the concentration range 1.56* nM *to 200* nM*. e) Fluorescence intensity recorded in PBS with 1*mM *$MgCl_2$ in presence (black) and absence of TWEEN20 (magenta).*

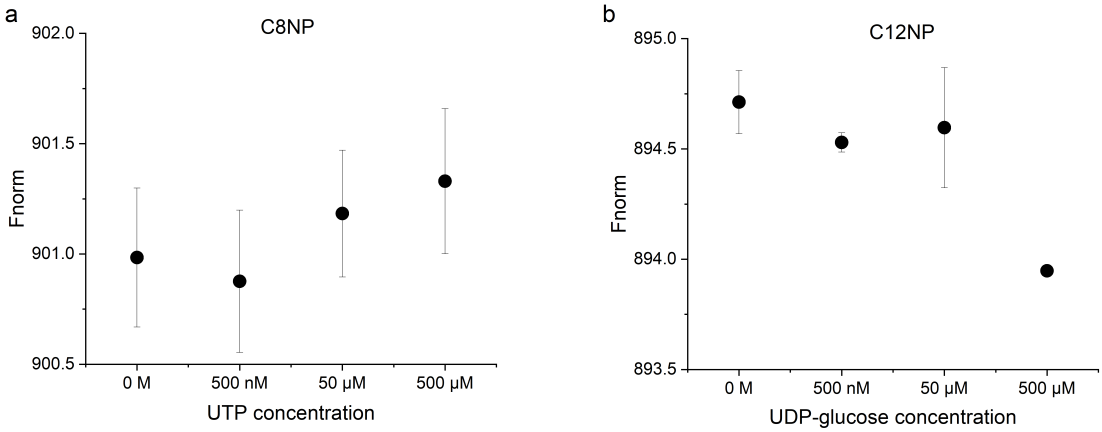

Figure 5.13. Examples of the responses recorded with the MST binding check assay to 500 nM***, 50*** µM ***and 500*** µM ***target for the optimised short candidates:*** *C8NP for UTP and C12NP for UDP-glucose. The responses were evaluated at MST On-Time of 2.5* s*. Data: mean* $\pm$ e_a*, n=3.*

response amplitude and signal-to-noise ratio recorded for each of the short candidates with 500 µM target MST on-time of 2.5 s.

Since none of the shorter aptamers successfully detected the target molecule, I decided to take a step back and test the full-length sequence for all the candidates that were carried through. Purification after bulk amplification of the full aptamer sequences still resulted in quite low yield and the sample presented some impurities due to glass microfiber filters. Therefore, the sample had to be centrifuged and only the supernatant collected. However, impurities were still present in the sample, which hampered the determination of the sample concentration via UV-spectrometry. Despite that, I attempted measuring a binding event with MST assay using the extracted aptamers and 100 µM of the respective target molecule. As illustrated in Figure 5.14, the attempt was unsuccessful and none of the aptamers showed a response large enough

Table 5.7. Response amplitude and Signal-to-noise ratio of the MST traces recorded by the strands for MST on-time of 2.5 s***.***

Sequence	Target Molecule	Response Amplitude	Signal-to-Noise
C8NP	UTP	0.4	1.1
D7NP	UTP	0.2	2.9
D7FP	UTP	0.2	8.1
C12NP	UDP-glucose	0.7	9.3

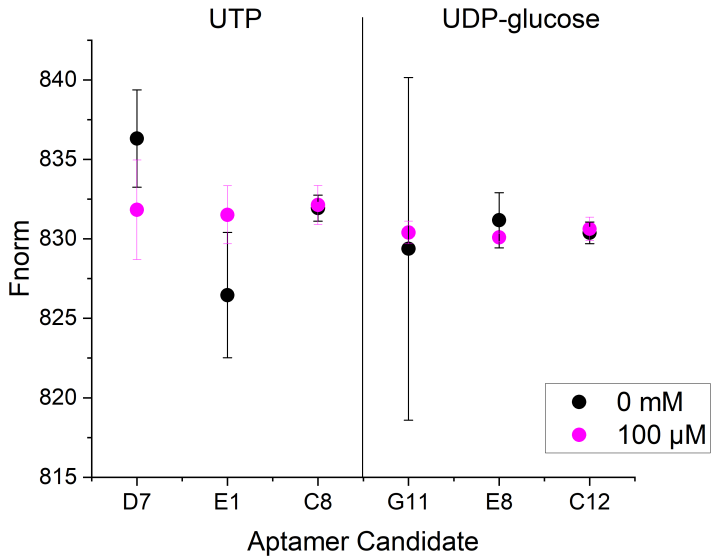

Figure 5.14. Responses recorded with the MST binding check assay for the full-length candidates (UTP left, UDP-glucose right). *The aptamer binding was tested against 100* µM *of the respective target molecule and the Fnorm value were evaluated at MST On-Time=2.5* s. *Data: mean* $\pm$ e_a, *n=3.*

to conclude any binding. The figure shows the data for MST on-time of 2.5 s, but the results were verified at a series of later time points (not shown).

5.2.7 Repeating SG assay to screen the aptamer candidates

Considering the negative results achieved with the MST assay, and since neither the UTP nor the UDP-glucose aptamer candidates showed any response to their respective target molecule, I assumed that the initial selection process must have been flawed. One possible reason was that the corrections applied to take into account the pH variation, for UTP, and autofluorescence for UDP-glucose, did not rectify the signal correctly. Therefore, I decided to start again from the SG assay and to change the conditions to minimise the corrections necessary. To avoid both the pH variation caused by UTP and reduce the impact of the autofluorescence of UDP-glucose, the concentration of the target molecule was reduced from 10 mM to 100 µM, whilst every other parameter was kept the same.

The pH of 100 µM UTP solution in was measured to verify that the pH had not changed. A negative control SG test was performed to confirm that the autofluorescence generated by 100 µM UDP-glucose was negligible with respect to the fluores-

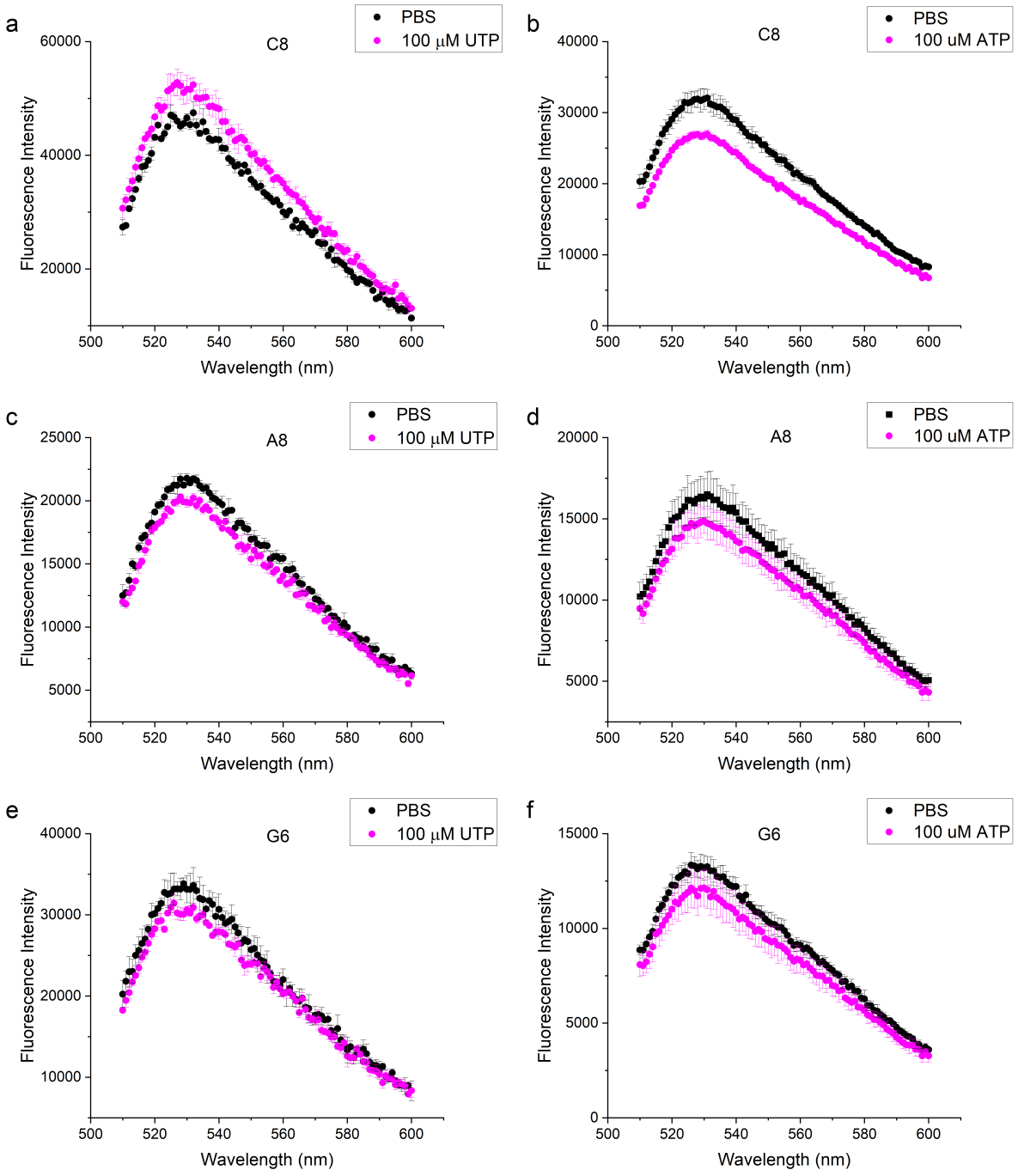

Figure 5.15. UTP candidates and their response to 100 μM UTP (panels a,c, e.) and with the negative control: ATP (panels b, d, f) using SG assay. *Data: mean ± e_a, n=3.*

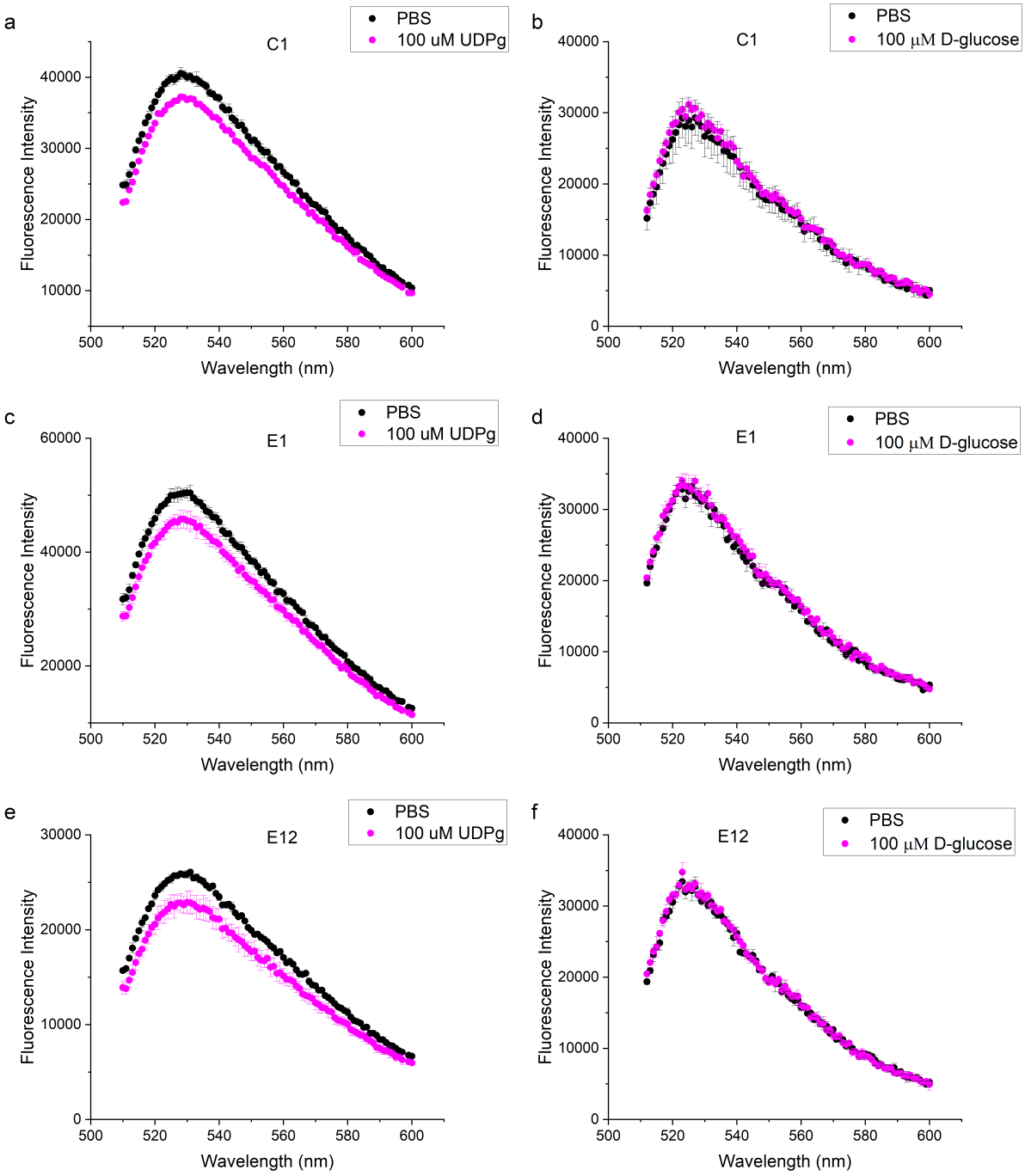

Figure 5.16. UDP-glucose candidates and their response to 100 μM UDP-glucose (panels a,c, e.) and with the negative control: D-glucose (panels b, d, f) using SG assay.. *Data: mean ± e_a, n=3.*

cence signals recorded for the assays.

Additionally, the sequences that emerged as binders were also tested against structurally similar molecules as a negative control: ATP for UTP, swapping a pyrimidine for a purine base, and D-glucose for UDP-glucose, to test whether the aptamer was selective for the full molecule or also for its parts.

The results of binding and the negative control assay are displayed side-by-side in Figure 5.15 and Figure 5.16. For each target molecule only three sequences showed significant signal variation. For UDP-glucose the selected candidates were C1, E1 and E12, whilst for UTP A8, C8 and G6 (Table 5.8).

Table 5.8. Sequences emerged from the second round of screening with the SYBRGreen assay. *The forward primer region is in bold, the reverse primer binding region in bold and italic, the anchoring sequence is underlined, the random regions are in blue and the mutations in magenta*

UTP	
Name	Sequence
A8	**TAGGGAAGAGAAGGACATATGAT** GCACGTTCA TGAGGCTCGAT C GTCAGTGGGTCGTCCCTCGAATCACATTGGGCACGGCTAA ***TTGAC TAGTACATGACCACTTGA***
C8	**TTGGGAAGAGAAGGACATATGAT** TACATGAGGA TGAGGCTCGAT C GGTATCTTTGGCATATCCTATCGTTCTATGTAACAGCCTG ***TTGACTA GTACATGACCACTTGA***
G6	**TAGGGAAGAGAAGGACATATGAT** ATAACCTGAC TGAGGGTCGAT C CGAAATTCAGCTGATTTTTTTTTGAACGAGGCTGTCGTGA ***TTGAC TAGTACATGACCACTTGA***
UDP-glucose	
Name	Sequence
C1	**TAGGGAAGAGAAGGACATATGAT** CTCCAAGCAC TGAGGCTCGAT C CAAACGGAGACATATGGAACTTTGTTATCTCTTCTTGATG ***TTGACT AGTACATGACCACTTGA***
E1	**TAGGGAAGAGAAGGACATATGAT** GGGATAAATA TGAGGCTCGAT C TTCTCTCTCGGGTGGCCGCTCTGACTTGGTCTGTGAGCCA ***TTGAC TAGTACATGACCACTTGA***
E12	**TAGGGAAGAGAAGGACATATGAT** CCTAGGGCGT TGAGGCTCGAT C TATTAAACGGACGGCGTAGGTATCTGTGGGGGTAATCCCA ***TTGAC TAGTACATGACCACTTGA***

In addition to being being selected for a second time against UTP, C8 exhibited a significant response to 100 µM ATP, with the two Δ going in opposite directions.

Since an aptamer for ATP does exist, I aligned, using clustalΩthe two sequences to verify whether there was an overlap. Figure 5.17 illustrates the sequences aligned with the detail of the first 40 bases of the C8 sequences. The sequences show identical sequences separated by some flank regions (12-18 and 22-28) in the C8 sequence and the rich conservation of Gs suggest a G-quadruplex motif as in the ATP aptamer. This overlap included the forward primer (5-11), the first random region (28-33) and part of the anchoring region (34-41). Despite this result, the candidate was not excluded since this binding site could be removed during the maturation of the strand and still produce a selective binder.

The other candidates, A8 and G5, did not produce significant variations for the negative control. On the other hand, UDP-glucose candidates displayed a larger variation in signal, with respect to UTP counter-part, and produced a null signal change in the presence of D-glucose, thus demonstrating some selectivity of the candidates toward the target molecule.

5.2.8 Confirming the screening results with MST

Before continuing with the process to optimise the aptamers and reduce them to the minimum binding sequence, I decided to confirm the results obtained with the SG assay using another technique. A few attempts were made to use another fluorescence assay based on the Hoechst 33342 dye, a DNA intercalating dye that binds preferentially to A-T base pairs [131]. Despite being another fluorescent assay with a similar

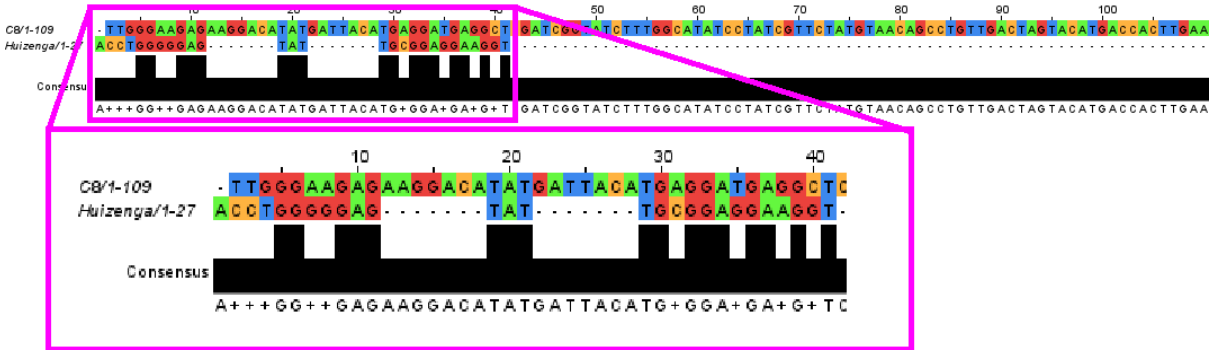

Figure 5.17. Alignment of the sequences of the C8 UTP aptamer and the ATP adenosine aptamer published by Huizenga and Szostak [95].

working principle, the Hoechst assay could have brought some new insight into the aptamer binding, since the oligonucleotide-dye interaction was much more specific that the one between DNA and SG. However the assay proved to be temperamental and not reproducible. The first controls showed equal fluorescence intensity for both samples containing ssDNA only or complexed with the dye. The same control was repeated with dsDNA, as the difference made by the dye complexed with the oligonucleotide should have produced a larger difference, which was not recorded.

Therefore, I went back to MST and optimised the assay to produce the best working condition for the aptamers. I started by increasing the target molecule concentration from 100 µM to 1 mM. However, increasing the UTP concentration to 1 mM generated a pH variation of the sample in PBS-Mg. This variation could affect the assay result bias it may affect the CY5 fluorescence and produce false-positive results. Therefore, to exclude such contributions all the measurements to characterise the UTP aptamers were conducted in MST buffer. Employing a different buffer, one in which the aptamer has not been optimised to perform in, could also affect the aptamer performance.

To characterise the differences between the two buffers, 5 nM of an IDT synthesised CY5-labelled aptamer was diluted in PBS TWEEN20 and MST buffers. Capillary scan and MST traces were recorded with 50 % LED power and the results are illustrated in Figure 5.18. For the capillary scan, the fluorescence intensities were not significantly different (420 $\pm$ 5 counts for PBS-Mg and 441 $\pm$ 4) as the values belong to the $\pm$ 20 % range (347-515 counts) of variability accepted by the assay (panel a), which indicates that the buffers do not affect the CY5 fluorescence and do not promote aptamer absorbance on the capillary walls (no double peaks). On the other hand the MST traces were significantly different (panel b). Since this control test was performed in absence of any target molecule, the difference in the MST curves indicates different migration properties of the aptamer strand in the two buffer, which is to be expected give that the two have different compositions (Table 5.9). Since, the migration properties will be different for each aptamer, this result was not sufficient to conclude that the MST buffer could not be successfully employed in the assay.

I proceeded with characterising the response from the full-length version of the

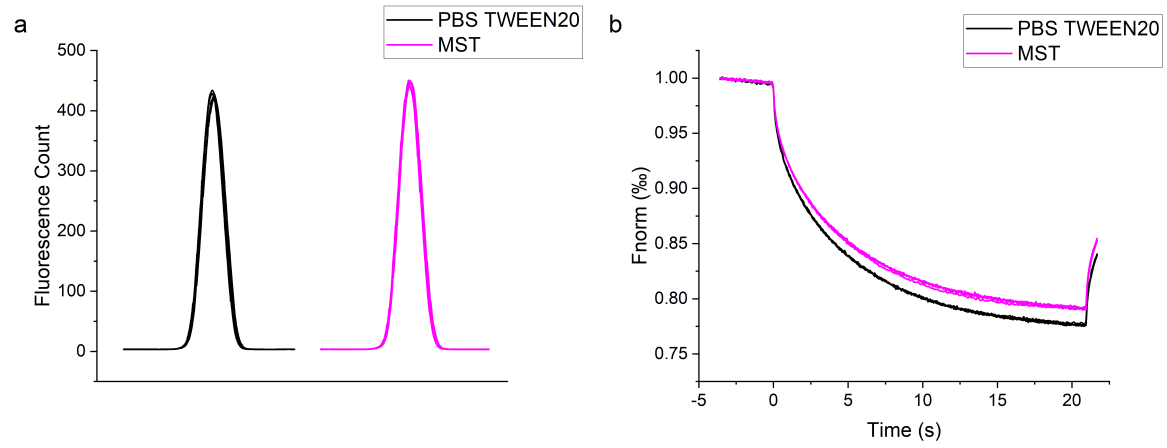

Figure 5.18. Evaluation of the difference in fluorescence intensity (a) and MST curve (b) between PBS-Mg TWEEN20 (black) and MST buffers (magenta).

Table 5.9. Composition of MST and PBS-Mg TWEEN20 buffers. *Both buffers have been adjusted to pH 7.4*

Component	**MST buffer**	**PBS-Mg TWEEN20**
NaCl	150 mM	137 mM
KCl		2.7 mM
$MgCl_2$	10 mM	1 mM
KH_2PO_4		1.8 mM
Na_2HPO_4		10 mM
Tris-HCL pH 7.5	50 mM	
TWEEN20	0.05 %	0.05 %

new candidates. The full-length sequences were labelled via PCR amplification with CY5-modified primer and extraction for the denaturing PAGE gel following the protocol previously described. All possible combinations of aptamer concentration, LED and IR laser power were tested to find the best working condition for the aptamers, but no pattern emerged, which indicated a sequence dependence of the assay and its response.

Out of six candidates that were carried through from the second round of SG assay only E12 for UDP-glucose and A8 for UTP showed a reproducible and significant response (Figure 5.19). The lack of response from the other aptamers was most likely due to two factors: the presence of impurities, which appeared to affect the signal by generating larger noise; and the significant size difference between the target molecule and the aptamer (1 base vs. 109 bases) which diluted the effect of the binding on the migration properties of the sequence. It is interesting to notice that the two strands display opposite behaviour in the response, the binding event was recorded at completely different MST on-times and the assay conditions were different: for E12 a low aptamer concentration and high LED power were employed, whilst for A8 the conditions were diametrically opposite. This supports again the high sequence dependency of the assay outcome.

5.2.9 Optimisation of the candidates sequenced by truncation of the constant primer regions

Left with one candidate per target molecule, I next sought to reduce the length of the sequence by evaluating the effect of removing the primer regions. Therefore, the CY5-labelled sequences deprived of the forward primer (A8 RP and E12 RP, 76 bases), of the reverse primer (A8 FP and E12 FP, 76 bases) and both primers (A8 NP and E12 NP, 53 bases) were purchased.

For all sequences, the assay set up was either 5 nM aptamer concentration and 50 % LED power or 2.5 nM concentration and AUTO setting for the LED power. These were found to be overall the best condition to run the assay.

Table 5.10 summarises the responses recorded at different MST on-times for

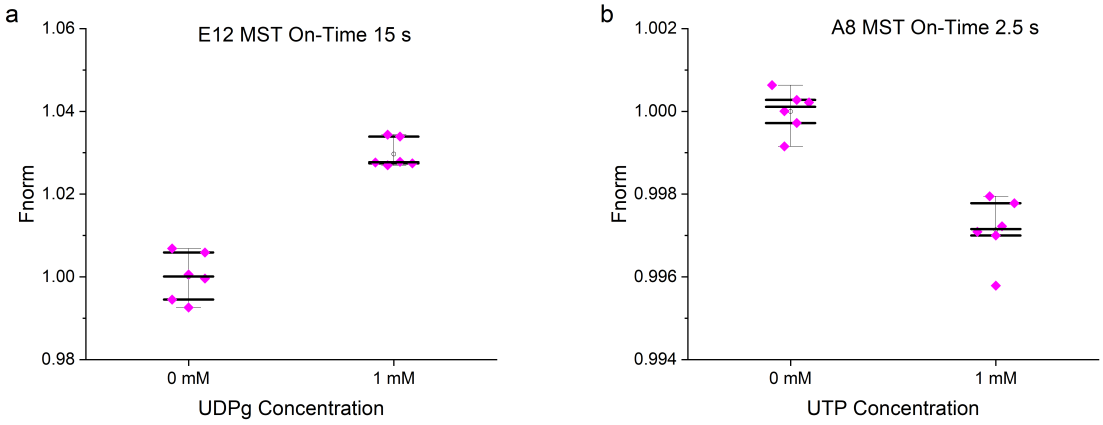

Figure 5.19. Result for the binding assay for the full-length aptamers. *a) MST response recorded at 15 s MST on-time with 1* mM *UDP-glucose in PBS-Mg TWEEN20 buffer (Reponse amplitude 22.3, S/N > 5). b) MST response recorded at 2.5 s MST On-Time with 1* mM *UTP in MST buffer (Reponse amplitude 2.5, S/N > 5). The Fnorm values were normalised to the 0* mM *value in order to pull together multiple sets of measurements. Raw data plotted over I-box, n=4.*

Table 5.10. Summary of the response amplitudes (RA) and signal-to-noise ratio (S/N) for each MST on-time for which binding events were recorded

MST On-Time	E12 FP		E12 RP		A8 RP		A8 NP	
(s)	RA	S/N	RA	S/N	RA	S/N	RA	S/N
1.5	1.4	6.9			1.1 6.2	1.7	8.3	
2.5	1.8	9.1	2.1	5.3	1.8 5.7	2.6	20	
5	2.7	7.7	2.7	5			4.1	14.2
10	3.8	6.8	3.8	5.1			6.3	14.2
15			5.1	7.9			8	11.4
20			5.7	5.3			8.8	8.9

which binding could be concluded. From the data it emerges that all aptamers that showed binding at MST on-time 2.5 s. Therefore, for all candidates tested the response at MST on/time 2.5 s was plotted in Figure 5.20. For UTP A8 RP and A8 NP showed binding, with the shortest version showing a very strong binding throughout the curve. whilst A8 FP showed no binding under any circumstance. For UDP-glucose, the sequence with no primers showed no binding under any condition, whilst both versions with primers, A8 FP and A8 RP, showed binding at MST on-time 2.5 s, 5 s and 10 s.

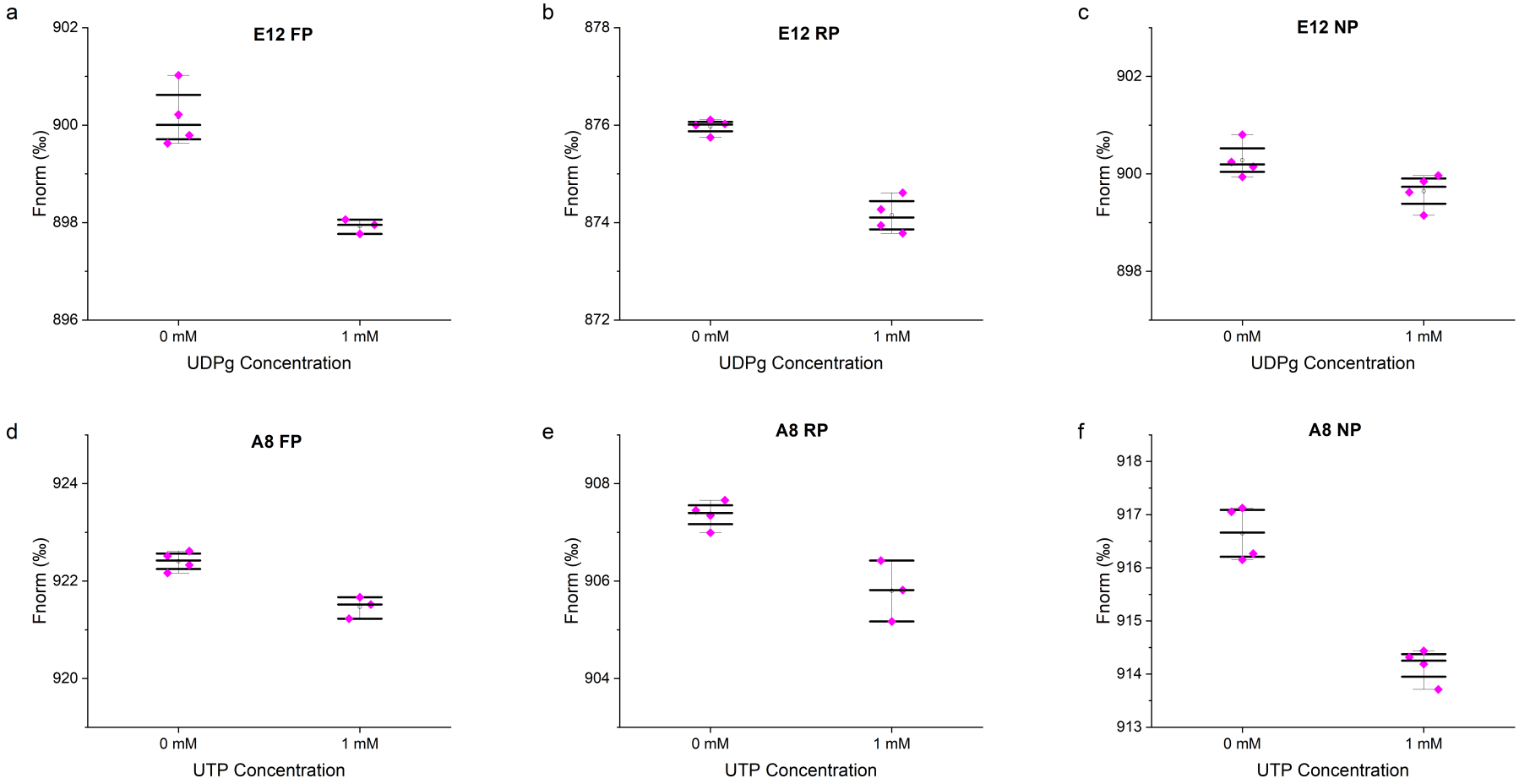

Figure 5.20. Results for the binding assay for the for the E12 (UDP-glucose, top) and A8 (UTP, bottom) aptamers containing one primer (FP or RP) or no primers. *Raw data plotted over I-box, n=4 for each measurement.*

Figure 5.21 illustrates some example MST traces. The top two traces show two binding sequences, A8 NP (panel a) and E12 FP (panel b) with the first being a very strong binder throughout and the second with a lower signal to noise ratio. With A8 NP being 23 bases shorter than E12 FP, the effect that the binding of the target molecule has on the molecular properties of the aptamer was much larger, thus allowing for a larger signal-to-noise ratio. The two bottom traces show the non binding sequences, with A8 FP being limited by a below threshold S/N ratio (≤ 5), whilst E12 NP clearly showed no response (RA ≤ 0.5 for all tested conditions).

Summarising, the results obtained from this aptamer optimisation, for UDP-glucose, E12 FP and E12 RP both produced binding events, whilst only A8 NP showed a reproducible and strong response to UTP. Therefore, these sequences were carried forward for the binding affinity characterisation.

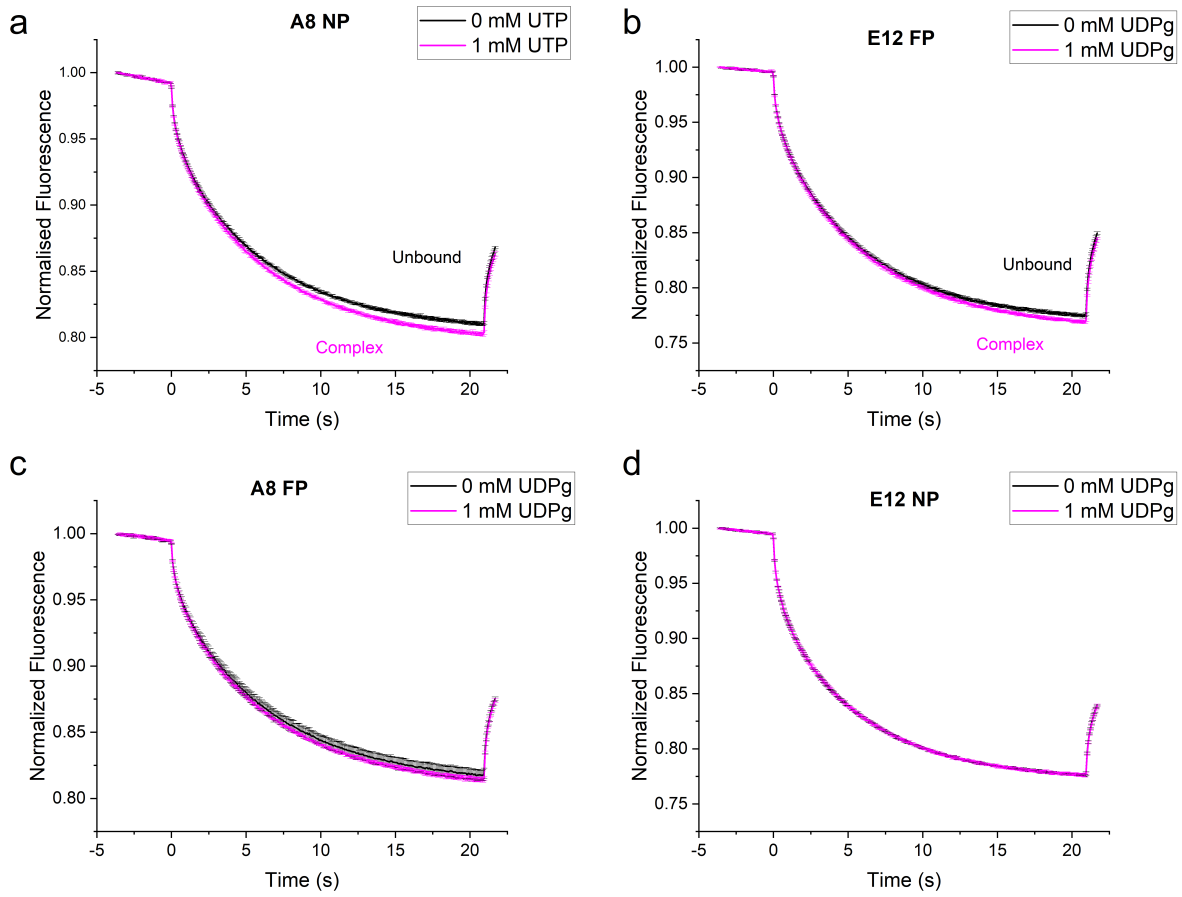

Figure 5.21. Exemplary MST traces of the binding (top) and not responsive sequences (bottom) for each target molecule, recorded at 5 nM ***concentration and 50 % LED power.***

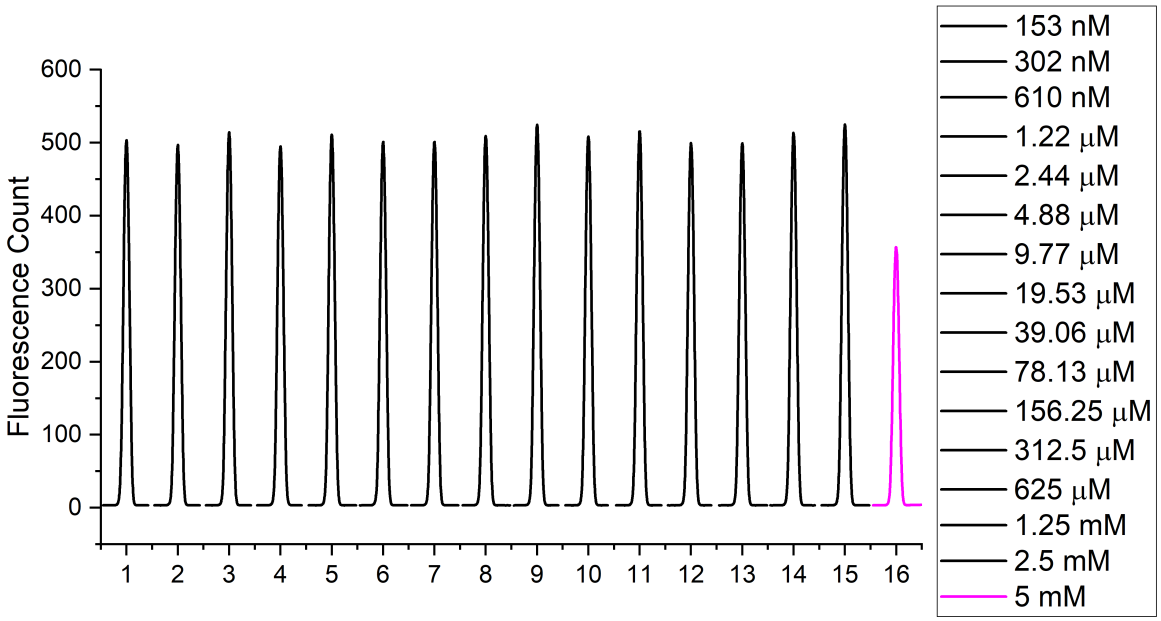

Figure 5.22. Example of target induced variation in the fluorescence signal of the capillary. *The fluorescence count of the capillary containing a high target molecule concentration (magenta) was significantly lower than the signal recorded for the other capillaries (black).*

5.2.10 Characterising the aptamer binding affinity

To gather further insight into the strength of the interactions between the selected aptamers and their respective target molecule, aptamers were incubated with a serial dilution of the target molecules. A binding affinity measurement was performed with the MO.Control software, which initiated a capillary scan to exclude binding induced variation in fluorescence. This was found to occur with a concentration larger than 2.5 mM as illustrated in Figure 5.22. The fluorescence count of the capillary containing a high target molecule concentration was significantly lower than the ones recorded for the other capillaries. One could assume that the high target concentration may have caused a shift int the physical properties of the buffer *e.g* pH. I tested such a high concentration because I was looking to get more data points on the saturation end of the dilution series. Therefore, the binding affinity measurements were carried out following a dilution series going from 30.5 nM to 1 mM.

From the data collected for E12 RP, the fitting of the dose response curve did not converge, and thus it was impossible to extract any kinetic information. I next characterised the E12 FP strand. Using 2.5 nM of the aptamer and LED power set to

auto and extracting the response at 2.5 s, the strand K_D was calculated to be 670 $\pm$ 230 µM (Figure 5.23.d). Figure 5.23.a and Figure 5.23.b illustrate the single data sets with fitting and the average binding curve, respectively. Finally, the merged overall signal variation generated by the binding by plotting the unbound and complex Fnorm values (Figure 5.23.c).

The same process was repeated for the UTP candidate A8 NP keeping all the experimental conditions the same (2.5 nM concentration, *auto* LED power and MST on-time 2.5 s). The plot of the data set (Figure 5.23.e) presents low variability in the signal at 2.5 s giving a K_D = 628 $\pm$ 24 µM

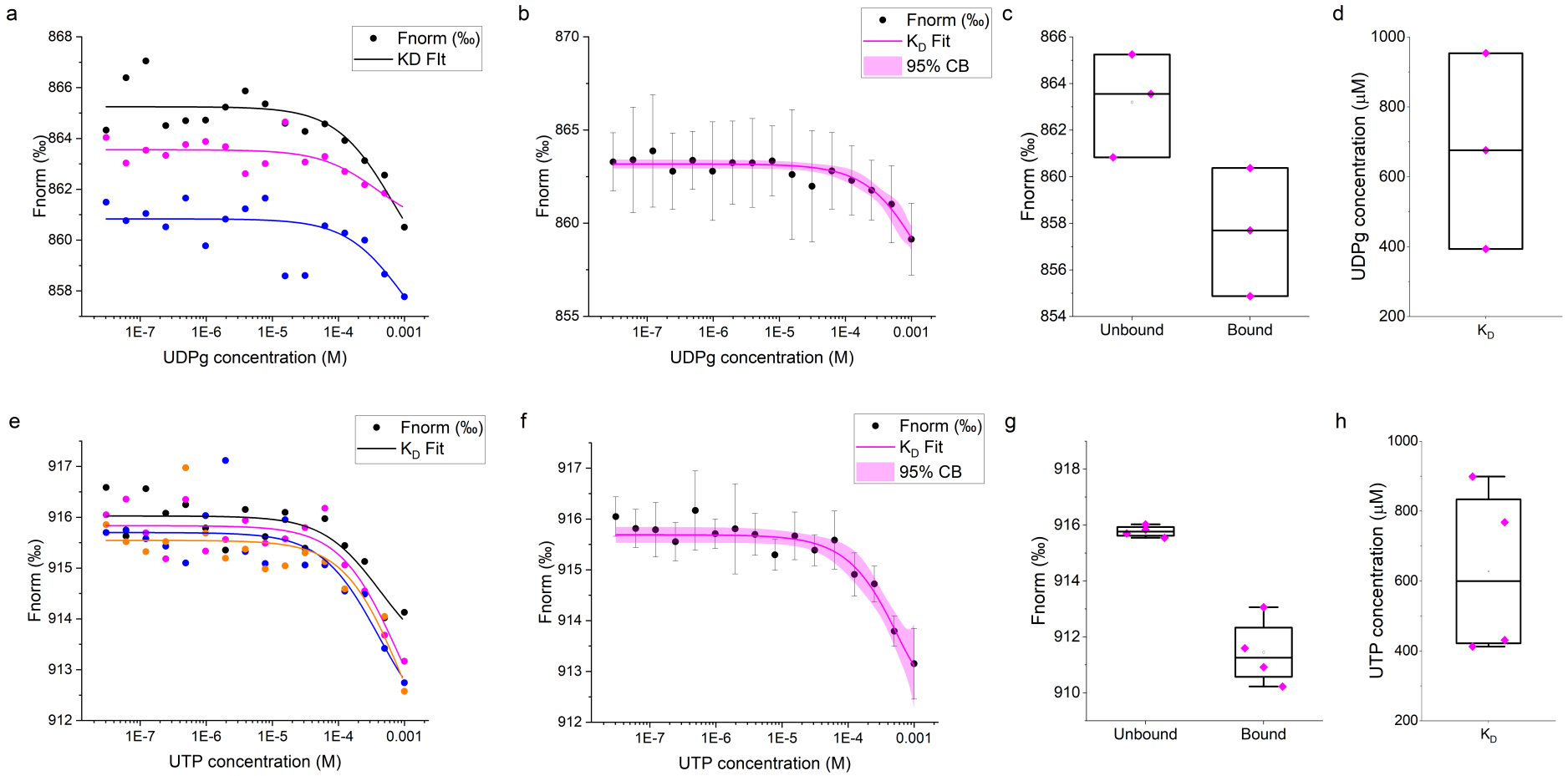

Figure 5.23. Binding affinity curves and K_D evaluation for E12 FP (top) and A8 NP (bottom) calculated at MST on/time 2.5 s. *a)-e) repeats data recorded forthe affinity valuation of each strand and fitting curves. b)-f) Final affinity curve calculated from the average of the three sets of data (R^2= 0.94 and R^2=0.93). Data: $\bar{z} \pm e_a$, n=3. c)-g) Box plot of the average signal variation recorded. d)-h) Box plot of the K_D. Data:*

5.3 Discussion

The aim of this chapter was to select, optimise and characterise aptamers for two neuro-chemicals: UTP and UDP-glucose. These two small molecules have been linked with several pathological conditions and they are known to be released in the brain. However, since no analytical method is available to measure their release directly, they were considered the perfect candidates for the sensor platform that was this project's aim to develop.

Selecting aptamers for small molecules: the challenges For the aptamer selection process Capture-SELEX [250] was chosen as the protocol was developed specifically for the selection of structure switching aptamers and for small target molecules. For the latter, immobilisation is an issue, both in terms of chemical modification and accessibility of the target molecule to the aptamer. However, selecting aptamers for small molecules is still challenging. Due to many technical difficulties, not only fewer aptamers have been selected for small molecules (25 %), but they also tend to have lower affinities than aptamers for larger target molecules (> 900 g mol^{-1}) [163]. The selection process started as a multiple-target SELEX (one library, two targets) and the libraries went through maturation separately from the fifth round onward. Despite the process requiring conditions to become more stringent over the rounds, the incubation time and target molecule concentrations were kept constant to avoid losing any candidates just because of the initial low frequencies [214], especially given the extra challenge posed by the presence of multiple targets and the separation of the two libraries on the fifth round.

The process experienced some initial issues. After the first selection round and pilot PCR, the DNA band of the library was migrating alongside with the 150 bps band of the ladder, instead of just above the 100 bp band, together with the positive control (PC). The issue persisted and worsened throughout the rounds with the appearance of the second DNA band on round four. The formation of longer DNA segments through SELEX was previously characterised by Musheev and Krylov [175] and it is mainly due to unspecific binding and dimer formation between the primer sequences and the

templates. Dimerisation occurs more frequently in SELEX because the presence of the random region, which makes it impossible to check for possible unwanted alignments and it is often impossible to avoid it by simply optimising the PCR process [119]. A possible solution to avoid this problem, other than just keeping the DNA material to the minimum, was published by Shao et al. [234] with a protocol called emulsion PCR, where the PCR reaction mix is resuspended into droplets giving amplification almost at a single-molecule level for each droplet. Dispersing the material into droplets reduced the overcrowding of the environment, thus lowering chances of the unspecific binding. Another way to avoid byproducts is to keep the PCR cycles number and the template concentration low [119]. However, the solution used in this work was to excise the DNA band with the correct size from gels and extract the library from it. Following the extraction, the library always migrated to the correct position.

SELEX stopped after eleven selection rounds, four with multiplexed targets and 7 rounds with the two libraries separated. The choice to stop after the seventh round was based on the average number of rounds being 10 for DNA SELEX [162] and by the results published by Schütze et al. [225], which found that the final motifs were already showing high frequencies as early as the forth round and reached the peak at the seventh. The same trend but with inverted direction was found for the background binders, which significantly reduced in number after the fifth round. Naturally the selection process is different for each target molecule and the conditions in which they are performed, but Vant-Hull et al. [270] have shown through mathematical simulation that the main obstacle toward the convergence of the SELEX process lies in the separation of the bound vs the unbound library, and not the dilution series or the random region length etc. Additionally, Schütze et al. [225] sustain that by reducing the number of rounds, one can minimise both the number of mutations introduced by Taq-polymerase, which can negatively affect the aptamer binding affinity, and the effect of PCR bias.

Analysis of the sequenced libraries for UTP and UDP-glucose Despite the literature, the sequencing of the library did not return highly enriched motifs. A possible

reason could lie in the parameters used. For example, the target concentration was halved every other round, whilst Vant-Hull et al. [270] found that diluting the target concentration by $1/n$, where n is the round number, with respect to the previous round, made the model converge faster. A further step where a lot of DNA material was lost and that could have affected the enrichment of the library was the library dimerisation and needed for consequent DNA extraction. Nevertheless the library did contain sequences that were present at over 1% from an initial diversity of 10^{15} or with mutations in the anchoring sequence, all sign of enrichment [250]. However, more than 70 unique sequences for each candidate could not have been experimentally evaluated as the work would have been both too time and cost expensive. Bioinformatic and computational software and servers have been developed and improved over the years to help the aptamer selection and help enhance aptamer performance. There is a large array of tools available which have been reviewed by Kinghorn et al. [111]. However, the majority of the bioinformatic tools deal with either very specific and detailed interactions which are very computationally expensive, *e.g* molecular dynamics or docking simulations, and therefore can not be used on such a long list of candidates, or they can work on very large datasets, *e.g.* NGS data analysis, which were not available in this study. The most useful tool at this point, in terms of trade off between computational cost, high throughput and final information gathered was the folding predicting algorithm and motif finder. The issue with the former was that the majority of the tools available for the folding prediction were coded for RNA only, which can not be as easily translated in DNA folding when the prediction encodes three-dimensional information. Despite these limitations and being conscious that the folding information for each aptamer was still incomplete since the aptamer, due to its structure switching nature, could undergo a target induced folding, the *in silico* analysis reduced the number of candidates by two thirds, leaving 22 and 24 candidates for UDP-glucose and UTP respectively.

Screening of the UTP and UDP-glucose candidates with SG The challenges of selecting an aptamer for small molecules do not end with the selection process. Aptamer characterisation is also challenging. The small molecular mass of the target molecules

is challenging to detect for a lot of analytical methods. Additionally, since the number of candidates was still high, the technique needed to be high throughput and require little aptamer modification to contain the costs. In the study, McKeague et al. [163] evaluated these techniques using published aptamers, which had already been reduced or partially reduced to the minimum binding sequence. Having undergone size reduction, the size gap between aptamer and molecule had already been reduced, which conferred the assay a higher sensitivity to the target molecule and can better detect the variation induced. Starting from a full-length aptamer sequence that was almost twice the average length of the aptamers used in the review, 108 bases and 60 bases respectively, meant developing an assay showing a much lower signal-to-noise ratio. Taking into consideration the structural information obtained from the *in silico* analysis and the technology available, the technique chosen was the SYBRGreen (SG) assay published by McKeague et al. [164]. The SG assay was fast, inexpensive and the SG interaction with the DNA was less sequence/motif specific [51], and as a plus it allowed aptamer interaction with its target molecule without the need to immobilise the strand on a surface, which could have affected the interaction and costs.

As expected, the results from the first rounds of candidate characterisations showed a small response especially when considering the large amount of target molecule present in solution and compared to the results obtained from the same assay performed with the ATP and adenosine aptamer [95] for concentrations five orders of magnitude smaller (Figure 3.12). Comparing the two sequences, 27 bases and 108 bases for the ATP aptamer and the Capture-SELEX libraries respectively, it is evident that the difference in size between the two aptamers contributed most to the low sensitivity shown by the aptamers. Diving further into the analysis of the Huizenga aptamer, the structure clearly shows that out of 27 bases only 3 are not involved in either a base-pair or part of the guanine-stack that interacts with the target molecule (bases 13-15: ATT). For the selected libraries no conclusion can be made but it can be expected that the ratio between bases that belong to the binding site and the total number of bases was much lower. One last consideration necessary for this comparison is that the ATP aptamer presents two binding sites, which amplifies the effect of the binding event by displacing more SG molecules, thus increasing the assay sensitivity.

Another point worthy of discussion was the corrections of the pH for UTP and of autofluorescence for UDP-glucose. Whilst for the latter very little could have been done in order to remove the autofluorescence, in the case of UTP a different buffer could have been employed. However, I decided to avoid changing buffer and to continue optimising the aptamer in the same buffer, or as close to the same buffer used for the final aptamer application, given that aptamer folding is known to be strongly dependent on the environmental conditions *e.g.* ion and anion concentration, pH etc. As emerged from the result of both the first round of MST, in which no binding was recorded, and the second round of SG assay, where all candidates with the exception of one were different, the corrections did not compensate correctly for the pH and the autofluorescence, and the signal did emerge from the background.

Through the second screening round, where both the pH and the autofluorescence had been minimised, six candidates, three per target molecule, were identified. The negative control for UTP was ATP and none of the aptamers responded with the exception of C8. The alignment of the sequence of the C8 candidates and the ATP aptamer showed the sequences shared 17 bases out of the 27 of the Huizenga aptamer, separated by two flanking regions of 7 bases each.

Employing D-glucose as negative control aimed mostly at verifying whether the aptamer was selective for the entirety of the target molecule or also at its parts, just like the ATP aptamer also binds ADP and adenosine. From the results of the SG assay it can be deduced that the candidates showed no response to the presence of D-glucose by itself, but it would be interesting to test whether uridine-diphospate or uridine itself could produce the same result. The same applies to the UTP sequences where the parallel is even more exact.

Optimisation of the aptamer candidates with microscale thermophoresis (MST)) Different combinations of target and aptamer concentrations, buffers and LED and IR power were tested to find the best working condition for each aptamer. On the first attempt at detecting a response to 100 µM target with the new candidates, it was necessary to increase the concentration to 1 mM. That meant that the buffer had to be changed for UTP due to the change in pH. The choice fell on the MST buffer, Tris-

HCl based, with similar concentration of sodium chloride, ten times the amount of magnesium chloride and pH adjusted to 7.4.

On the other hand, no autofluorescence was recorded for UDP-glucose. Additional challenges were posed by the sample contamination originating from the extraction of the DNA sample from the denaturing PAGE gel. The microglass fibre impurity in the sample affected both the DNA quantification with the nanodrop and the MST assay. Spinning of the sample and using only the supernatant did improve the signal-to-noise ratio for the assay enough to record binding for two aptamer candidates, one for each target, in their full-length form using the MST.

E12 binding with UDP-glucose and A8 with UTP had been confirmed by two platforms that exploit completely different physical phenomena to detect the binding event, the next step was to optimise the candidates. The choice of technique fell on MST given its capability to produce quantitative data in a quite short turnaround time. In choosing the optimisation step, the decision fell on truncation since it was the best way to improve the relatively low response amplitudes and of the signal-to-noise ratios. The truncation of the aptamer binding site reduced the aptamer length from 108 bases to 75 bases for one primer removed (FP or RP versions), and to 52 bases in the version without any primer (NP).

Examining further the results recorded for E12, the UDP-glucose candidate: the two version with one primer both showed significant responses whilst the version without any primer did not respond at all to the presence of UDP-glucose. Both one primer versions were characterised for binding affinity and whilst no curve dose response behaviour could be found for E12 RP whilst a K_D of 670 $\pm$ 230 µM was found.

For the UTP counter part A8 showed no response for the FP version and small responses at 1.5 s and 2.5 s MST on-times. However, the removal of both primers resulted in a net improvement in terms of quality of both response amplitude and signal-to-noise ratios, with the first Signal-to-noise exceeding 12.0. The binding affinity characterisation produced a K_D of 628$\pm$ 244 µM.

To put this result into context, I compared the aptamers selected in this work with other published in literature selected for small target molecules, and more specifically for nucleotides. The results are summarised in Table 5.11. From quick overview,

the preferred chemistry for small molecule aptamers is RNA, most likely due to the higher structural complexity that RNA aptamers are known for [308, 183]. At the same time RNA aptamers show lower limits of detection to their DNA counter-parts. That limit of detection is however strongly dependent on the concentration of metal ions and more specifically $MgCl_2$. One example is the ATP aptamer published by Sassanfar and Szostak [220] where a four-fold increase in the metal ion concentration produced a ten-fold improvement in the affinity. In other cases the absence or lower concentration of the metal ions can even result in the loss of affinity [284]. Further, the concentrations of $MgCl_2$ employed with RNA are much higher than those found in celebrospinal fluid, which supports the choice of DNA based chemistry in this project. Affinities recorded for published DNA aptamers are often one or two order of magnitude away from the aptamers selected in this work. However, with further optimisation of the sequence, *e.g.* mutagenesis, sequence engineering and further truncation, better K_D values could be achieved.

To summarise, two aptamers, one for UTP and one for UDP-glucose, were successfully isolated via Stoltenburg, Nikolaus, and Strehlitz [250] Capture-SELEX. The optimisation process to shorten the sequences and mature the affinity to their target molecule was initiated using microscale thermophoresis and it produced so far K_D of 628 µM and 670 µM, for UTP and UDP-glucose respectively. Despite the incomplete maturation process, this result is already significant, especially in the case of UTP for which a selection was previously attempted and failed [181], using a similar Capture-SELEX protocol that employed a library with a shorter random region, 30 nucleotides against the 50 employed here.

Table 5.11. Comparison of aptamers selelected for small molecules and nucleotides

Name	Target	Chemistry	Length	Kd	$MgCl_2$	Publication
E12RP-UDPg	UDP-glucose	DNA	78	670 µM	1 mM	this work
C8NP-UTP	UTP	DNA	52	628 µM	10 mM	this work
ATP-40-1 (ID 97)	ATP	RNA	40	700 nM	20 mM	[220]
				5-8 µM	5 mM	
Adenosine/ATP (ID 98)	ATP/Adenosine	DNA	27	6 µM	5 mM	[95]
ATP (1-1MIN) (ID 99)	ATP	RNA	57	4.8 µM	30 mM	[221]
				11 µM	10 mM	
ADP (ID 262)	ADP	RNA	85	low µM	10 mM	[246]
Adenine 12E4 (ID 96)	Adenine	RNA	91	10 nM	5 mM	[167]
Xanthine XAB (103)	Xanthine/guanine	RNA	32	3.3 nM	5 mM	[110]
cAMP (ID 104)	cAMP/adenosine	RNA	31	10 µM	10 mM	[116]
cAMP	cAMP	DNA	31	1 mM	9 mM	[235]
cNMPs (ID 192, 196, 197)	cAMP, cCMP, cGMP	RNA	90-94	>100 µM	20 mM	[228]
pe35 (ID 113)	L-Tyrosinamide	DNA	49	45 µM	5 mM	[272]
L-Arginine 12-79 (ID 484)	L-arginine	DNA	28	2.5 mM	0 mM	[83]
IL 42-32b (ID 112)	L-isoleucine	RNA	32	200 µM	7.5 mM	[153]

Chapter 6

Future Work

6.1 Electrochemical aptamer-based biosensor for the continuous monitoring of neurochemicals

The electrochemical aptamer-based platform described in this work successfully achieved the concentration range of interest and the recording hypoxia-induced adenosine release. However, especially the experiments conducted in with the tissue have shown some weaknesses in the design that need to be addressed in the future work. Some of these corrections are essential to turn the platform it into a reliable analytical tool.

6.1.1 Range of detection

First item to be addressed is the range of detection. Despite having achieved the detection in the micromolar, the physiological concentration range of neurochemicals starts in the high picomolar concentration range [42]. The range of detection depends on both the transduction and the biorecognition element. For the transduction, exploiting the conductive properties of nanomaterials and nanostructures, could improve the device sensitivity [55]. For example, creating a nanostructured surface, by depositing dendritic structure [216, 143] or metal nanoparticles [35, 255], can be used both for increasing the sensor surface area and improving signal-to-noise ratio [87, 147].

For the aptamer, improving the range means tuning the aptamer affinity window. This result has been achieved in multiple publications by introducing/modulat-

ing a structural switch, by tuning the cooperativity of the aptamer down to promote higher affinity, by introducing an allosteric regulator [288, 5, 20, 48, 184]. The latter however can not be employed in this platform because it does not support continuous monitoring.

6.1.2 Anti-fouling and Calibration-free

Another weakness highlighted by the measurement in complex media is the poor signal stability, that prevented the measurement from being quantitative. One way to improve the fouling resistance,is to passivate the surface by incubating the surface with 30 $\mathrm{mg\,ml^{-1}}$ BSA for 2 h. This treatment efficiently blocks defects sites from reducing oxygen and stabilises the signal. However, it does cause the signal to drop by 40 % [143].

Li et al. [135] have shown a solution that tackles both signal stability and fouling resistance. In this work, the phosphatidylcholine-terminated (PC) MCH backfilling chains not only improved the fouling resistance, losing only 10% of the signal after 12 h in whole blood (65% for the MCH backfilling), and displayed an increased signal stability (over 12 h in flowing blood), but also improved the signal gain upon binding of the target molecule (35 % and 65% signal gain for the MCH and PC sensors respectively).

It would also be beneficial for the sensor characteristics to support calibration free measurements, to ensure the correct quantification of the detected amount and remove batch dependencies variability. This can be achieved by dual frequency measurement technique, which exploit the frequency dependence of the signal gain. By evaluating the ratio between a responsive and a low responsive frequency, one can obtain accurate evaluation of the measured quantity [136]. The drawback of this technique is that the time-resolution of the measurement will lower, further limiting the application spectrum of the device.

6.2 Selecting structure-switching aptamers for UTP and UDP-glucose

Further insight on the selection process and on the enrichment of suitable aptamer candidates could be gathered by performing next generation sequencing of the libraries from each selection round. The data gathered could also provide some new candidates which were lost during the selection process [251]

Regarding the aptamers selected, further work could be conducted to reduce selected aptamers to their minimum-binding sequence to improve the affinity to the target. To achieve that, DNAase foot-printing technique could be employed to determine the minimum binding sequence. The assay employs exonucleases to digest the unbound strands, thus leaving only the functional part of the aptamer [31].

Once a satisfactory binding sequence has been reached, structural information on the aptamer-target complex could be gathered either via nucleic magnetic resonance (NMR) [141] or X/ray crystallography. Additionally circular dichroism spectroscopy (CD) could be used probe the aptamer-target interaction, especially to determine how the aptamer structure changes in presence of the target [27].

Finally, it would be very exciting to integrate the optimised aptamers into an electrochemical aptamer-based platform and record the uracil-nucleotide release (or the lack of it) from brain tissue.

Chapter 7

Summary & Conclusion

At the beginning of my project, I set out to verify whether an aptamer-based electrochemical biosensor could be employed as novel analytical tool to continuously measure the release of small molecules in the brain. A sensor was developed and optimised to detect adenosine, a well characterised neurochemical and a ubiquitous signalling molecule [252, 24]. Its release has been studied in high temporal resolution via existing analytical tools such as fast-scan cyclic voltammetry and amperometric enzymatic biosensors[180, 43]. Additionally, there was an existing 27 base adenosine aptamer that has been fully characterised in terms of structure, binding sites and has been employed on multiple platforms, included an electrochemical one [95, 141, 307, 99, 94, 105]. This prior knowledge from previous studies, grants a variety of options for assays to test my newly developed sensor.

In the first part of the project, I established and optimised the fabrication protocol and tested different device geometries and recording techniques to achieve a sensitivity in the physiological concentration range. Since an electrochemical aptamer-based platform employing the same aptamer and exploiting the same structure-switching design to detect ATP had already been described, the initial effort went into to reproducing the published results [289]. The initial attempt at recording a response was made using cyclic voltammetry. However, due to protocol applied, the contribution of the charging current to the overall signal was greater than the sensor response to the binding, thus reducing the signal-to-noise ratio and the sensitivity [57]. The employ-

ment of square wave voltammetry, solved that issue as the technique applies pulses of potential and samples the current when the charging current contribution is negligible, thus sensibly increasing the signal gain recorded [169]. Following the work by Liu et al. [143], miniaturisation of the device was then employed to improve the sensor's dynamic range. Another fundamentally important step was the change of the sensor design from a gold disk to a gold wire. The change resulted in a four-fold improvement in the signal generated. This result also translated into a low limit of detection (low micromolar), which now covered the physiologically relevant range.

Two engineered versions of the aptamer containing only one binding site and with a destabilised stem, were incorporated for the first time on an electrochemical platform and their response characterised. According to the publication, the two engineered one-binding site versions slightly reduced the K_D from 16 µM to 12µM [307]. However, on the electrochemical platform, only the version with a shorter stem matched, without improving, the performance of the two binding site aptamer, probably due to the enhanced strand displacement. The lack of a significant improvement in the signal supported the findings by Zhang, Oni, and Liu [307], where they found limited cooperativity between the two binding sites.

Finally, the response to some other adenosine-based purines was evaluated to verify the selectivity of the aptamer, especially to the molecules that were more likely to be present in the extracellular environments during recordings from tissue. The aptamer had been characterised for its response to all adenosine nucleotides, down to adenosine, and to all nucleotide triphosphates (NTPs). However, I could not find a previous characterisation of the response to adenosine catabolites: insosine and hypoxanthine. The sensor sensitivity for both catabolites was significantly lower than for adenosine, which was sufficient to conclude that there was selectivity against those metabolites. This constitutes an improvement with respect to the microelectrode enzymatic version in terms of selectivity, which cannot differentiate between adenosine and its metabolites, and that produces an acidic environment due to its catalytic activity over time. The sensor sensitivity to ATP however was significantly higher, with a response four-fold larger than for adenosine. This result is in agreement with previous characterisations.

Overall, the sensor, optimised this far, achieved the objective initially set, as the platform achieved sufficient sensitivity for the detection of adenosine and supported continuous monitoring. To my knowledge, no other published aptamer-based biosensor was capable of detecting adenosine at the low micromolar range whilst supporting continuous monitoring in real time in a continuous flow chamber. The only exception is the work by Liu et al. [143], which obtained detection of ATP on a similar working range after surface passivation, despite a 40% signal loss. As there has not been an electrochemical aptamer based platform showing fast return times (ms resolution) and low LOD for continuous measurements, alternatives detection systems which posses these characteristics are preferred for these applications.

In the second part, control measurements were performed to evaluate the influence of environmental parameters on the aptamer response. Both temperature and pH shifts were found to affect the sensor response. In the case of temperature, it was mainly attributed to the aptamer melting temperature being in the range of the physiological temperature used for the recording. For pH, it was found that the sensor response caused by a pH variation was accompanied by a shift in the peak potential of the sensor, therefore providing a simple way to exclude its contribution to the measurement with a biological sample.

The sensor capability to support analyte detection in tissue and the effect of the tissue on the dynamics of the recording were evaluated with a low density agar block [179]. The sensor was found to be incapable of detecting the target inside the agar and showed clear signs of physical damage upon insertion and removal from the agar block, which resulted in a lower aptamer density on the sensor surface.

Nevertheless, by laying the sensory parallel to the slice surface, the platform was employed to record adenosine release directly from hypoxic slices at room temperature and simultaneously with extracellular recordings to monitor the brain activity. The traces recorded by the sensor presented a strong drift, indicating a poor signal stability and possibly explained by fouling. The sensor still selectively detected adenosine and the signal recorded overlapped with the depression of synaptic activity. However, due to the drift, no quantitative data could be extracted from the recordings.

Despite the lack of quantitative information, the sensor successfully recorded adenosine released from a slice, reproducing the previously published results obtained with the enzyme-based microelectrode sensor. This result is quite novel as it is amongst the first reports of continuous monitoring detection of neurochemicals via electrochemical aptamer-based sensors, joining the work by Nakatsuka et al. [176] and Santos-Cancel et al. [218]. However, it is the first reported sensor to achieve continuous recording of adenosine release from brain slices. This work contributes to the current effort in developing and establishing aptamer-based sensors for continuous detection of neurochemicals [226]. This result provides confirmation that upon further optimisation and with the employment of new aptamers, the sensor described in this work could be employed as a universal platform for the analytical detection of small signalling molecules in the brain.

The extracellular recording from the aptasensor was strongly affected by the chosen measuring technique and could only be taken during the quiet time of the potentiostat. This is due to the significantly larger potentials involved in recording a square wave voltammetry trace. This remains a limiting factor for the sensor as the method will not be employable in recordings that require high temporal resolution. The low temporal resolution (8 s) was mainly attributable to the duty cycle of the potentiostat since the square wave recording only took 3 s. It is possible that using a different potentiostat could halve the total time required for a recording. Additionally employing a different analytical technique could improve the time resolution.

In the third part of this thesis, capture-SELEX was employed to isolate two DNA aptamers for UTP and UDP glucose, two poorly understood and understudied purines which lack analytical tools to quantify their release with sufficient time resolution; With the aim to sand thus to identify exactly their role in the purinergic circuits.

The selection process was challenging, but it was completed after 11 selection rounds. The two libraries emerged from the sequencing were quite heterogeneous. However, some sequence enrichment was identified and used as a parameter to select which aptamer to characterise further. APTANI2 was employed to scan the sequences against a library of known motifs [32]. The software analysis returned a few additional

sequences. Next generation sequencing was used, to gather further insight into the enrichment of the library. However, due to the sudden lost of my research funds, it could not be performed.

SYBRGreen assay was employed for the initial screening of the selected aptamer sub-libraries, to reduce the numbers [163]. Three aptamers for each target molecule showed binding in the SG assay. The binding was confirmed via microscale thermophoresis, which returned reproducible results only for two strands: A8 for UTP an E12 for UDP-glucose. The affinity maturation protocol of the aptamer started with truncation of the constant primer site regions, as a literature review has found that they contribute rarely to the binding [40]. The aim was to reduce the aptamer to its minimum binding sequence. The version of A8 with no primers was found to present the best binding amplitude and signal to noise ratio. For E12 both the versions containing only one primer showed binding. Contrary to the expectation, the version of the aptamer with no primers lacked a response, despite having tested multiple buffer and divalent metal ions conditions. The reduced aptamer candidates were tested to characterise their K_D, which were all in the high micromolar range (< 700 µM).

Two aptamers were successfully selected for UTP and UDP glucose, thus contributing to an expanding library of oligonucleotides aptamers employed in detection of small molecules. The result for the UTP aptamer is made even more significant as previous attempts with a DNA library had failed. The affinities obtained are promising and within the order of magnitude from the K_D of other nucleotide-sensitive aptamers published. With further work towards the reduction to the minimum binding sequence and affinity maturation, similar results might be achieved.

Due to a lack of time, I could complete neither the kinetic characterisation nor the reduction to minimum binding sequence. For the same reason, I could not integrate the final selected aptamers into the sensor platform described in this work and to employ it to record the release of the two uracil-nucleosides. This new analytical tool could significantly contribute to the current understanding of the role of these two signalling molecules and to the effort of characterising their function in the purinergic system, which is involved in the regulation of both the central and peripheral nervous system [61, 129, 128].

Bibliography

[1] Maria P. Abbracchio and Geoffrey Burnstock. "Purinoceptors: are there families of P2X and P2Y purinoceptors?" In: *Pharmacology & Therapeutics* 64.3 (1994), pp. 445–475.

[2] Ralph N. Adams. "Probing brain chemistry with electroanalytical techniques". In: *Analytical Chemistry* 48.14 (Dec. 1, 1976). Publisher: American Chemical Society, 1126A–1138A.

[3] Mariana Alves, Edward Beamer, and Tobias Engel. "The Metabotropic Purinergic P2Y Receptor Family as Novel Drug Target in Epilepsy". In: *Frontiers in Pharmacology* 9 (Mar. 7, 2018), p. 193.

[4] Mariana Alves et al. "Expression and function of the metabotropic purinergic P2Y receptor family in experimental seizure models and patients with drug-refractory epilepsy". In: *Epilepsia* 58.9 (2017), pp. 1603–1614.

[5] Rachel E. Armstrong and Geoffrey F. Strouse. "Rationally Manipulating Aptamer Binding Affinities in a Stem-Loop Molecular Beacon". In: *Bioconjugate Chemistry* 25.10 (Oct. 15, 2014), pp. 1769–1776.

[6] Netzahualcóyotl Arroyo-Currás et al. "High Surface Area Electrodes Generated via Electrochemical Roughening Improve the Signaling of Electrochemical Aptamer-Based Biosensors". In: *Analytical Chemistry* 89.22 (2017), pp. 12185–12191.

[7] Netzahualcóyotl Arroyo-Currás et al. "Real-time measurement of small molecules directly in awake, ambulatory animals". In: *Proceedings of the National Academy of Sciences* 114.4 (Jan. 24, 2017). Publisher: National Academy of Sciences Section: Physical Sciences, pp. 645–650.

[8] Pascal Auffinger, Luigi D'Ascenzo, and Eric Ennifar. "Sodium and Potassium Interactions with Nucleic Acids". In: *The Alkali Metal Ions: Their Role for Life*. Ed. by Astrid Sigel, Helmut Sigel, and Roland K. O. Sigel. Metal Ions in Life Sciences. Cham: Springer International Publishing, 2016, pp. 167–201.

[9] Philipp Baaske et al. "Optical Thermophoresis for Quantifying the Buffer Dependence of Aptamer Binding". In: *Angewandte Chemie International Edition* 49.12 (2010), pp. 2238–2241.

[10] Brian R. Baker et al. "An electronic, aptamer-based small-molecule sensor for the rapid, label-free detection of cocaine in adulterated samples and biological fluids". In: *Journal of the American Chemical Society* 128.10 (2006). ISBN: 0002-7863, pp. 3138–3139.

[11] Saikat Banerjee et al. “Electrochemical Detection of Neurotransmitters”. In: *Biosensors* 10.8 (Aug. 2020). Number: 8 Publisher: Multidisciplinary Digital Publishing Institute, p. 101.

[12] Frank C Barone, Giora Z Feuerstein, and Raymond F White. “Brain Cooling During Transient Focal Ischemia Provides Complete Neuroprotection”. In: *Neuroscience & Biobehavioral Reviews* 21.1 (Jan. 1, 1997), pp. 31–44.

[13] Michael J. Bell et al. “Interstitial Adenosine, Inosine, and Hypoxanthine Are Increased after Experimental Traumatic Brain Injury in the Rat”. In: *Journal of Neurotrauma* 15.3 (Mar. 1998). Publisher: Mary Ann Liebert, Inc., publishers, pp. 163–170.

[14] Maxim Berezovski et al. “Non-SELEX Selection of Aptamers”. In: *Journal of the American Chemical Society* 128.5 (Feb. 2006), pp. 1410–1411.

[15] Candace S. Bever et al. “VHH antibodies: emerging reagents for the analysis of environmental chemicals”. en. In: *Analytical and Bioanalytical Chemistry* 408.22 (Sept. 2016), pp. 5985–6002.

[16] Nikhil Bhalla et al. “Introduction to biosensors”. In: *Essays in Biochemistry* 60.1 (2016), pp. 1–8.

[17] Yonatan Biniuri, Bauke Albada, and Itamar Willner. “Probing ATP/ATP-Aptamer or ATP-Aptamer Mutant Complexes by Microscale Thermophoresis and Molecular Dynamics Simulations: Discovery of an ATP-Aptamer Sequence of Superior Binding Properties”. In: *The Journal of Physical Chemistry B* 122.39 (Oct. 4, 2018). Publisher: American Chemical Society, pp. 9102–9109.

[18] *biosensor - Search Results - PubMed*. URL: `https://pubmed.ncbi.nlm.nih.gov/?term=biosensor` (visited on 08/06/2021).

[19] *Biosensors Market Size & Share — Global Industry Forecasts Report 2027*. Global Market Insights, Inc. URL: `https://www.gminsights.com/industry-analysis/biosensors-market` (visited on 08/06/2021).

[20] Stéphanie Bissonnette et al. “Optimizing the Specificity Window of Biomolecular Receptors Using Structure-Switching and Allostery”. In: *ACS Sensors* 5.7 (July 24, 2020). Publisher: American Chemical Society, pp. 1937–1942.

[21] Dean Brady and Justin Jordaan. “Advances in enzyme immobilisation”. en. In: *Biotechnology Letters* 31.11 (July 2009), p. 1639.

[22] Dennis Breitsprecher et al. “Aptamer Binding Studies Using MicroScale Thermophoresis”. In: *Nucleic Acid Aptamers: Selection, Characterization, and Application*. Ed. by Günter Mayer. Methods in Molecular Biology. New York, NY: Springer, 2016, pp. 99–111.

[23] Thomas Bürgi. “Properties of the gold–sulphur interface: from self-assembled monolayers to clusters”. In: *Nanoscale* 7.38 (2015). Publisher: Royal Society of Chemistry, pp. 15553–15567.

[24] Geoffrey Burnstock. “An introduction to the roles of purinergic signalling in neurodegeneration, neuroprotection and neuroregeneration”. In: *Neuropharmacology* 104 (2016). Publisher: Elsevier Ltd ISBN: 0028-3908, pp. 4–17.

[25] Geoffrey Burnstock. "Purinergic Nerves". In: *Pharmacological Reviews* 24.3 (Sept. 1, 1972). Publisher: American Society for Pharmacology and Experimental Therapeutics, pp. 509–581.

[26] Geoffrey Burnstock. "Purinergic signalling: from discovery to current developments". In: *Experimental Physiology* 99.1 (Jan. 2014), pp. 16–34.

[27] Shundong Cai et al. "Investigations on the interface of nucleic acid aptamers and binding targets". In: *Analyst* 143.22 (Nov. 5, 2018). Publisher: The Royal Society of Chemistry, pp. 5317–5338.

[28] Anaí del Rocío Campos-Contreras et al. "Experimental polycystic ovarian syndrome is associated with reduced expression and function of P2Y2 receptors in rat theca cells: CAMPOS-CONTRERAS ¡span style="font-variant:small-caps;"¿et al.¡/span¿". In: *Molecular Reproduction and Development* 86.3 (Mar. 2019), pp. 308–318.

[29] Susana Campuzano et al. "Antifouling (Bio)materials for Electrochemical (Bio)sensing". In: *International Journal of Molecular Sciences* 20.2 (Jan. 2019). Number: 2 Publisher: Multidisciplinary Digital Publishing Institute, p. 423.

[30] Susana Campuzano et al. "Beyond Sensitive and Selective Electrochemical Biosensors: Towards Continuous, Real-Time, Antibiofouling and Calibration-Free Devices". In: *Sensors* 20.12 (Jan. 2020). Number: 12 Publisher: Multidisciplinary Digital Publishing Institute, p. 3376.

[31] Juan Canoura et al. "Accelerating Post-SELEX Aptamer Engineering Using Exonuclease Digestion". In: *Journal of the American Chemical Society* 143.2 (Jan. 20, 2021), pp. 805–816.

[32] Jimmy Caroli, Mattia Forcato, and Silvio Bicciato. "APTANI2: update of aptamer selection through sequence-structure analysis". In: *Bioinformatics* 36.7 (Apr. 1, 2020), pp. 2266–2268.

[33] Kevin J. Cash and Kevin W. Plaxco. "Signal transduction with a swing". In: *Nature Chemistry* 13.5 (May 2021), pp. 392–393.

[34] Jon K. Chambers et al. "A G Protein-coupled Receptor for UDP-glucose *". In: *Journal of Biological Chemistry* 275.15 (Apr. 14, 2000). Publisher: Elsevier, pp. 10767–10771.

[35] Zhengbo Chen et al. "Electrochemical impedance spectroscopy detection of lysozyme based on electrodeposited gold nanoparticles". en. In: *Talanta* 83.5 (Feb. 2011), pp. 1501–1506.

[36] Alan K. H. Cheng, Bixia Ge, and Hua-Zhong Yu. "Aptamer-Based Biosensors for Label-Free Voltammetric Detection of Lysozyme". In: *Analytical Chemistry* 79.14 (July 1, 2007). Publisher: American Chemical Society, pp. 5158–5164.

[37] Robert S. Clegg and James E. Hutchison. "Fundamental Aspects of Electron Transfer in Substrate-Supported Organized Molecular Assemblies". In: *Electron Transfer in Chemistry*. John Wiley & Sons, Ltd, 2001, pp. 541–577.

[38] J. E. Coelho et al. “Hypoxia-induced desensitization and internalization of adenosine A1 receptors in the rat hippocampus”. en. In: *Neuroscience* 138.4 (Jan. 2006), pp. 1195–1203.

[39] Jon Cooper and A. E. G. Cass, eds. *Biosensors: a practical approach*. 2nd ed. Practical approach series no. 268. Oxford ; New York: Oxford University Press, 2004. 251 pp.

[40] Matthew C. Cowperthwaite and Andrew D. Ellington. “Bioinformatic Analysis of the Contribution of Primer Sequences to Aptamer Structures”. In: *Journal of Molecular Evolution* 67.1 (July 1, 2008), pp. 95–102.

[41] Lin Cui et al. “A reusable ratiometric electrochemical biosensor on the basis of the binding of methylene blue to DNA with alternating AT base sequence for sensitive detection of adenosine”. In: *Biosensors and Bioelectronics* 102 (October 2017 2018). Publisher: Elsevier B.V., pp. 87–93.

[42] Nicholas Dale and Bruno Frenguelli. “Measurement of purine release with microelectrode biosensors”. In: *Neuromethods* 80 (2013). ISBN: 9781627033695, pp. 221–240.

[43] Nicholas Dale, Tim Pearson, and Bruno Frenguelli. “Direct measurement of adenosine release during hypoxia in the CA1 region of the rat hippocampal slice”. In: *The Journal of Physiology* 526.1 (2000), pp. 143–155.

[44] Nicholas Dale et al. “Listening to the brain: microelectrode biosensors for neurochemicals”. In: *Trends in Biotechnology* 23.8 (Aug. 2005), pp. 420–428.

[45] Philippe Dauphin-Ducharme, Netzahualcóyotl Arroyo-Currás, and Kevin W. Plaxco. “High-Precision Electrochemical Measurements of the Guanine-, Mismatch-, and Length-Dependence of Electron Transfer from Electrode-Bound DNA Are Consistent with a Contact-Mediated Mechanism”. In: *Journal of the American Chemical Society* 141.3 (Jan. 23, 2019). Publisher: American Chemical Society, pp. 1304–1311.

[46] Philippe Dauphin-Ducharme et al. “Simulation-Based Approach to Determining Electron Transfer Rates Using Square-Wave Voltammetry”. In: *Langmuir* 33.18 (May 9, 2017). Publisher: American Chemical Society, pp. 4407–4413.

[47] Ulrich K. M. Decking et al. “Hypoxia-Induced Inhibition of Adenosine Kinase Potentiates Cardiac Adenosine Release”. In: *Circulation Research* 81.2 (Aug. 1997). Publisher: American Heart Association, pp. 154–164.

[48] Pietro Delcanale et al. “Aptamers with Tunable Affinity Enable Single-Molecule Tracking and Localization of Membrane Receptors on Living Cancer Cells”. In: *Angewandte Chemie International Edition* 59.42 (2020), pp. 18546–18555.

[49] Poshmaal Dhar, Rasika M. Samarasinghe, and Sarah Shigdar. “Antibodies, Nanobodies, or Aptamers—Which Is Best for Deciphering the Proteomes of Non-Model Species?” en. In: *International Journal of Molecular Sciences* 21.7 (Apr. 2020), p. 2485.

[50] F Di Virgilio and E Adinolfi. “Extracellular purines, purinergic receptors and tumor growth”. In: *Oncogene* 36.3 (Jan. 2017), pp. 293–303.

[51] A. I. Dragan et al. “SYBR Green I: Fluorescence Properties and Interaction with DNA”. In: *Journal of Fluorescence* 22.4 (July 1, 2012), pp. 1189–1199.

[52] T. Gregory Drummond, Michael G. Hill, and Jacqueline K. Barton. “Electron Transfer Rates in DNA Films as a Function of Tether Length”. In: *Journal of the American Chemical Society* 126.46 (Nov. 1, 2004). Publisher: American Chemical Society, pp. 15010–15011.

[53] Yudan Du et al. “A signal on aptamer-based electrochemical sensing platform using a triple-helix molecular switch”. In: *Analytical Methods* 6.16 (2014). Publisher: Royal Society of Chemistry ISBN: 1759-9660, pp. 6294–6300.

[54] Stefan Duhr and Dieter Braun. “Why molecules move along a temperature gradient”. In: *Proceedings of the National Academy of Sciences* 103.52 (Dec. 26, 2006). ISBN: 9780603873102 Publisher: National Academy of Sciences Section: Physical Sciences, pp. 19678–19682.

[55] Sharmila Durairaj et al. “Nanomaterials-Based Electrochemical Sensors for In Vitro and In Vivo Analyses of Neurotransmitters”. In: *Applied Sciences* 8.9 (Sept. 1, 2018), p. 1504.

[56] A. D. Edwards, J. S. Wyatt, and M. Thoresen. “Treatment of hypoxic-ischaemic brain damage by moderate hypothermia”. In: *Archives of Disease in Childhood - Fetal and Neonatal Edition* 78.2 (Mar. 1, 1998). Publisher: BMJ Publishing Group Section: Special review, F85–F88.

[57] Noémie Elgrishi et al. “A Practical Beginner’s Guide to Cyclic Voltammetry”. In: *Journal of Chemical Education* 95.2 (2018). ISBN: 0021-9584, pp. 197–206.

[58] A. D. Ellington and J. W. Szostak. “In vitro selection of RNA molecules that bind specific ligands”. In: *Nature* 346.6287 (Aug. 30, 1990), pp. 818–822.

[59] Clemens Entzian and Thomas Schubert. “Mapping the Binding Site of an Aptamer on ATP Using MicroScale Thermophoresis”. In: *Journal of Visualized Experiments : JoVE* 119 (Jan. 7, 2017), p. 55070.

[60] Clemens Entzian and Thomas Schubert. “Studying small molecule–aptamer interactions using MicroScale Thermophoresis (MST)”. In: *Methods*. Nucleic Acid Aptamers 97 (Mar. 15, 2016), pp. 27–34.

[61] David Erlinge. “Chapter 13 - P2Y Receptors in Health and Disease”. In: *Advances in Pharmacology*. Ed. by Kenneth A. Jacobson and Joel Linden. Vol. 61. Pharmacology of Purine and Pyrimidine Receptors. Academic Press, Jan. 1, 2011, pp. 417–439.

[62] David Erlinge et al. “Uridine triphosphate (UTP) is released during cardiac ischemia”. In: *International Journal of Cardiology* 100.3 (Apr. 28, 2005). Publisher: Elsevier, pp. 427–433.

[63] Larry R. Faulkner. “Understanding electrochemistry: Some distinctive concepts”. In: *Journal of Chemical Education* 60.4 (Apr. 1, 1983). Publisher: American Chemical Society, p. 262.

[64] Leslie A. Fogwe, Vamsi Reddy, and Fassil B. Mesfin. “Neuroanatomy, Hippocampus”. In: *StatPearls*. Treasure Island (FL): StatPearls Publishing, 2021.

[65] J. C. Fowler. "Purine release and inhibition of synaptic transmission during hypoxia and hypoglycemia in rat hippocampal slices". In: *Neuroscience Letters* 157.1 (July 9, 1993), pp. 83–86.

[66] John C. Fowler. "Adenosine antagonists delay hypoxia-induced depression of neuronal activity in hippocampal brain slice". In: *Brain Research* 490.2 (June 26, 1989), pp. 378–384.

[67] Bruno Frenguelli, Enrique. Llaudet, and Nicholas Dale. "High-resolution real-time recording with microelectrode biosensors reveals novel aspects of adenosine release during hypoxia in rat hippocampal slices". In: *Journal of Neurochemistry* 86.6 (2003), pp. 1506–1515.

[68] Bruno Frenguelli and Mark J. Wall. "Combined electrophysiological and biosensor approaches to study purinergic regulation of epileptiform activity in cortical tissue". In: *Journal of Neuroscience Methods*. Methods and Models in Epilepsy Research 260 (Feb. 15, 2016), pp. 202–214.

[69] Bruno Frenguelli et al. "Temporal and mechanistic dissociation of ATP and adenosine release during ischaemia in the mammalian hippocampus". In: *Journal of Neurochemistry* 101.5 (June 2007), pp. 1400–1413.

[70] Shunxiang Gao et al. "Post-SELEX optimization of aptamers". In: *Analytical and Bioanalytical Chemistry* 408.17 (July 2016), pp. 4567–4573.

[71] Annalisa De Girolamo et al. "Immobilization of Aptamers on Substrates". en. In: *Aptamers for Analytical Applications*. Section: 3 _eprint: https://onlinelibrary.wiley.com/doi John Wiley & Sons, Ltd, 2018, pp. 85–126.

[72] Tatsuro Goda and Yuji Miyahara. "Thermo-responsive molecular switches for ATP using hairpin DNA aptamers". In: *Biosensors and Bioelectronics* 26.9 (May 15, 2011), pp. 3949–3952.

[73] Misha V. Golynskiy and Burckhard Seelig. "De novo enzymes: from computational design to mRNA display". en. In: *Trends in Biotechnology* 28.7 (July 2010), pp. 340–345.

[74] Marielle E. Gomez and Angel E. Kaifer. "Voltammetric behavior of a ferrocene derivative: A comparison using surface-confined and diffusion-controlled species". In: *Journal of Chemical Education* 69.6 (June 1992), p. 502.

[75] Alexander V. Gourine, Jackie D. Wood, and Geoffrey Burnstock. "Purinergic signalling in autonomic control". In: *Trends in Neurosciences* 32.5 (May 2009), pp. 241–248.

[76] Sally A. N. Gowers et al. "Development of a Minimally Invasive Microneedle-Based Sensor for Continuous Monitoring of β-Lactam Antibiotic Concentrations in Vivo". In: *ACS Sensors* 4.4 (Apr. 2019). Publisher: American Chemical Society, pp. 1072–1080.

[77] Michael R. Green and Joseph Sambrook. "Isolation of DNA Fragments from Polyacrylamide Gels by the Crush and Soak Method". In: *Cold Spring Harbor Protocols* 2019.2 (Jan. 2, 2019). Publisher: Cold Spring Harbor Laboratory Press, pdb.prot100479.

[78] Man Bock Gu and Hak Sung Kim. *Biosensors based on aptamers and enzymes*. Vol. 140. Publication Title: Advances in Biochemical Engineering/Biotechnology ISSN: 07246145. 2014.

[79] Yuan Guan et al. "Determination of nucleic acids based on the fluorescence quenching of Hoechst 33258 at pH 4.5". In: *Analytica Chimica Acta* 570.1 (June 7, 2006), pp. 21–28.

[80] Kristian Agmund Haanes and Lars Edvinsson. "Characterization of the contractile P2Y14 receptor in mouse coronary and cerebral arteries". In: *FEBS Letters* 588.17 (Aug. 25, 2014), pp. 2936–2943.

[81] H. Hagberg et al. "Extracellular Adenosine, Inosine, Hypoxanthine, and Xanthine in Relation to Tissue Nucleotides and Purines in Rat Striatum During Transient Ischemia". In: *Journal of Neurochemistry* 49.1 (1987), pp. 227–231.

[82] Benjamin L. Hanssen, Shajahan Siraj, and Danny K. Y. Wong. "Recent strategies to minimise fouling in electrochemical detection systems". In: *Reviews in Analytical Chemistry* 35.1 (Apr. 1, 2016). Publisher: De Gruyter Section: Reviews in Analytical Chemistry, pp. 1–28.

[83] K Harada and A. D. Frankel. "Identification of two novel arginine binding DNAs." In: *The EMBO Journal* 14.23 (Dec. 1, 1995). Publisher: John Wiley & Sons, Ltd, pp. 5798–5811.

[84] T. Kendall Harden and Eduardo R. Lazarowski. "Chapter 11 Release of ATP and UTP from astrocytoma cells". In: *Progress in Brain Research*. Vol. 120. Elsevier, 1999, pp. 135–143.

[85] Hijiri Hasegawa et al. "Methods for improving aptamer binding affinity". In: *Molecules* 21.4 (2016).

[86] J. M. Hawryluk et al. "Adenosine inhibits glutamatergic input to basal forebrain cholinergic neurons". en. In: *Journal of Neurophysiology* 107.10 (May 2012), pp. 2769–2781.

[87] Lei He et al. "Current signal amplification strategies in aptamer-based electrochemical biosensor: A review". en. In: *Chinese Chemical Letters* 32.5 (May 2021), pp. 1593–1602.

[88] J. P. Headrick and R. J. Willis. "Adenosine formation and energy metabolism: a 31P-NMR study in isolated rat heart". In: *American Journal of Physiology-Heart and Circulatory Physiology* 258.3 (Mar. 1990). Publisher: American Physiological Society, H617–H624.

[89] Jason Heikenfeld et al. "Accessing analytes in biofluids for peripheral biochemical monitoring". en. In: *Nature Biotechnology* 37.4 (Apr. 2019), pp. 407–419.

[90] Thomas Hermann and Dinshaw J. Patel. "Adaptive Recognition by Nucleic Acid Aptamers". In: *Science* 287.5454 (Feb. 4, 2000). Publisher: American Association for the Advancement of Science Section: Review, pp. 820–825.

[91] Emily Hill et al. “Introduction of Tau Oligomers into Cortical Neurons Alters Action Potential Dynamics and Disrupts Synaptic Transmission and Plasticity”. In: *eNeuro* 6.5 (Sept. 1, 2019). Publisher: Society for Neuroscience Section: New Research.

[92] M A Hofman. “Energy metabolism, brain size and longevity in mammals”. eng. In: *The Quarterly review of biology* 58.4 (Dec. 1983), pp. 495–512.

[93] Jan Hoinka et al. “Identification of sequence–structure RNA binding motifs for SELEX-derived aptamers”. In: *Bioinformatics* 28.12 (June 15, 2012), pp. i215–i223.

[94] Xiang Huang et al. “An efficient signal-on aptamer-based biosensor for adenosine triphosphate detection using graphene oxide both as an electrochemical and electrochemiluminescence signal indicator”. In: *Analyst* 140.17 (Aug. 10, 2015). Publisher: The Royal Society of Chemistry, pp. 6015–6024.

[95] David E. Huizenga and Jack W. Szostak. “A DNA Aptamer That Binds Adenosine and ATP”. In: *Biochemistry* 34.2 (1995). ISBN: 0006-2960, pp. 656–665.

[96] Brad P. Jackson, Susanne M. Dietz, and R. Mark. Wightman. “Fast-scan cyclic voltammetry of 5-hydroxytryptamine”. In: *Analytical Chemistry* 67.6 (Mar. 15, 1995). Publisher: American Chemical Society, pp. 1115–1120.

[97] Sumedha D Jayasena. “Aptamers: An Emerging Class of Molecules That Rival Antibodies in Diagnostics”. In: *Clinical Chemistry* 45.9 (Sept. 1, 1999), pp. 1628–1650.

[98] Hyo Jin Jeong et al. “Adenosine A1 receptor-mediated presynaptic inhibition of GABAergic transmission in immature rat hippocampal CA1 neurons”. en-GB. In: *Journal of Neurophysiology* 89.3 (2003). Number: 3, pp. 1214–1222.

[99] Jing Jia et al. “A simple electrochemical method for the detection of ATP using target-induced conformational change of dual-hairpin DNA structure”. In: *Sensors and Actuators B: Chemical* 222 (Jan. 1, 2016), pp. 1090–1095.

[100] Björn Johansson et al. “Hyperalgesia, anxiety, and decreased hypoxic neuroprotection in mice lacking the adenosine A1 receptor”. In: *Proceedings of the National Academy of Sciences* 98.16 (July 31, 2001). Publisher: National Academy of Sciences Section: Biological Sciences, pp. 9407–9412.

[101] Eric A. Josephs and Tao Ye. “Nanoscale spatial distribution of thiolated DNA on model nucleic acid sensor surfaces”. In: *ACS Nano* 7.4 (2013), pp. 3653–3660.

[102] Di Kang et al. “Expanding the Scope of Protein-Detecting Electrochemical DNA “Scaffold” Sensors”. In: *ACS Sensors* 3.7 (July 2018). Publisher: American Chemical Society, pp. 1271–1275.

[103] Di Kang et al. “Survey of Redox-Active Moieties for Application in Multiplexed Electrochemical Biosensors”. In: *Analytical Chemistry* 88.21 (2016). ISBN: 0003-2700, pp. 10452–10458.

[104] Chandran Karunakaran, Raju Rajkumar, and Kalpana Bhargava. “Introduction to Biosensors”. In: *Biosensors and Bioelectronics*. Elsevier, 2015, pp. 1–68.

[105] Leila Kashefi-Kheyrabadi and Masoud A. Mehrgardi. "Aptamer-based electrochemical biosensor for detection of adenosine triphosphate using a nanoporous gold platform". In: *Bioelectrochemistry* 94 (2013). ISBN: 1878-562X\r1567-5394, pp. 47–52.

[106] Leila Kashefi-Kheyrabadi and Masoud A. Mehrgardi. "Aptamer-conjugated silver nanoparticles for electrochemical detection of adenosine triphosphate". In: *Biosensors and Bioelectronics* 37.1 (Aug. 1, 2012), pp. 94–98.

[107] Shirin Kashfi et al. "A1 Adenosine Receptor Activation Modulates Central Nervous System Development and Repair". In: *Molecular Neurobiology* 54 (2016). Publisher: Molecular Neurobiology, pp. 8128–8139.

[108] Gilles Kauffenstein et al. "NTPDase1 (CD39) controls nucleotide-dependent vasoconstriction in mouse". In: *Cardiovascular Research* 85.1 (Jan. 1, 2010), pp. 204–213.

[109] Masahito Kawamura, David N. Ruskin, and Susan Masino. "Adenosine A1 receptor-mediated protection of mouse hippocampal synaptic transmission against oxygen and/or glucose deprivation: a comparative study". In: *Journal of Neurophysiology* 122.2 (Aug. 1, 2019), pp. 721–728.

[110] D Kiga et al. "An RNA aptamer to the xanthine/guanine base with a distinctive mode of purine recognition." In: *Nucleic Acids Research* 26.7 (Apr. 1, 1998), pp. 1755–1760.

[111] Andrew B. Kinghorn et al. "Aptamer Affinity Maturation by Resampling and Microarray Selection". In: *Analytical Chemistry* 88.14 (July 19, 2016), pp. 6981–6985.

[112] B. P. Klyuch, N. Dale, and M. J. Wall. "Deletion of Ecto-5'-Nucleotidase (CD73) Reveals Direct Action Potential-Dependent Adenosine Release". In: *Journal of Neuroscience* 32.11 (2012). ISBN: 1529-2401 (Electronic)\r0270-6474 (Linking), pp. 3842–3847.

[113] James J. Knierim. "The hippocampus". In: *Current Biology* 25.23 (Dec. 7, 2015). Publisher: Elsevier, R1116–R1121.

[114] Johannes Koch et al. "CAD mutations and uridine-responsive epileptic encephalopathy". In: *Brain* 140.2 (Feb. 1, 2017), pp. 279–286.

[115] Patrick M. Kochanek et al. "The Many Roles of Adenosine in Traumatic Brain Injury". In: *Adenosine: A Key Link between Metabolism and Brain Activity*. Ed. by Susan Masino and Detlev Boison. New York, NY: Springer, 2013, pp. 307–322.

[116] Makoto Koizumi and Ronald R. Breaker. "Molecular Recognition of cAMP by an RNA Aptamer". In: *Biochemistry* 39.30 (Aug. 1, 2000). Publisher: American Chemical Society, pp. 8983–8992.

[117] Schuichi Koizumi et al. "UDP acting at P2Y6 receptors is a mediator of microglial phagocytosis". In: *Nature* 446.7139 (Apr. 2007), pp. 1091–1095.

[118] Natalia Komarova, Daria Barkova, and Alexander Kuznetsov. "Implementation of High-Throughput Sequencing (HTS) in Aptamer Selection Technology". In: *International Journal of Molecular Sciences* 21.22 (Jan. 2020). Number: 22 Publisher: Multidisciplinary Digital Publishing Institute, p. 8774.

[119] Natalia Komarova and Alexander Kuznetsov. "Inside the Black Box: What Makes SELEX Better?" In: *Molecules* 24.19 (Oct. 7, 2019), p. 3598.

[120] Hoon Young Kong and Jonghoe Byun. "Nucleic acid aptamers: New methods for selection, stabilization, and application in biomedical science". In: *Biomolecules and Therapeutics* 21.6 (2013). ISBN: 1976-9148 (Print)\r1976-9148 (Linking), pp. 423–434.

[121] Zsolt Kovács et al. "Uridine modulates neuronal activity and inhibits spike-wave discharges of absence epileptic Long Evans and Wistar Albino Glaxo/Rijswijk rats". In: *Brain Research Bulletin* 97 (Aug. 1, 2013), pp. 16–23.

[122] Matthew S. Krause and Louis. Ramaley. "Analytical application of square wave voltammetry". In: *Analytical Chemistry* 41.11 (Sept. 1, 1969). Publisher: American Chemical Society, pp. 1365–1369.

[123] Mahmoud Labib, Edward H. Sargent, and Shana O. Kelley. "Electrochemical Methods for the Analysis of Clinically Relevant Biomolecules". In: *Chemical Reviews* 116.16 (Aug. 24, 2016). Publisher: American Chemical Society, pp. 9001–9090.

[124] Gideon Lapidoth et al. "Highly active enzymes by automated combinatorial backbone assembly and sequence design". en. In: *Nature Communications* 9.1 (2018), p. 2780.

[125] Serena Latini et al. "Extracellular adenosine concentrations during in vitro ischaemia in rat hippocampal slices". In: *British Journal of Pharmacology* 127.3 (1999), pp. 729–739.

[126] Eduardo Lazarowski. "Regulated release of nucleotides and UDP sugars from astrocytoma cells". In: *Novartis Foundation Symposium* 276 (2006), 73–84, discussion 84–90, 107–112, 275–281.

[127] Eduardo R. Lazarowski. "Vesicular and conductive mechanisms of nucleotide release". In: *Purinergic Signalling* 8.3 (Sept. 1, 2012), pp. 359–373.

[128] Eduardo R. Lazarowski and Richard C. Boucher. "UTP as an extracellular signaling molecule". In: *News in Physiological Sciences: An International Journal of Physiology Produced Jointly by the International Union of Physiological Sciences and the American Physiological Society* 16 (Feb. 2001), pp. 1–5.

[129] Eduardo R. Lazarowski and T. Kendall Harden. "UDP-Sugars as Extracellular Signaling Molecules: Cellular and Physiologic Consequences of P2Y $_{14}$ Receptor Activation". In: *Molecular Pharmacology* 88.1 (July 2015), pp. 151–160.

[130] Eduardo R. Lazarowski et al. "Release of Cellular UDP-Glucose as a Potential Extracellular Signaling Molecule". In: *Molecular Pharmacology* 63.5 (May 1, 2003), pp. 1190–1197.

[131] Huynh-Nhu Le et al. “Label-free fluorescent assay of ATP based on an aptamer-assisted light-up of Hoechst dyes”. In: *Anal. Methods* 6.7 (2014), pp. 2028–2030.

[132] Thao T. Le, Orada Chumphukam, and Anthony E. G. Cass. “Determination of minimal sequence for binding of an aptamer. A comparison of truncation and hybridization inhibition methods”. In: *RSC Adv.* 4.88 (2014), pp. 47227–47233.

[133] Michal Legiewicz et al. “Size, constant sequences, and optimal selection”. en. In: *RNA* 11.11 (Jan. 2005). Company: Cold Spring Harbor Laboratory Press Distributor: Cold Spring Harbor Laboratory Press Institution: Cold Spring Harbor Laboratory Press Label: Cold Spring Harbor Laboratory Press Publisher: Cold Spring Harbor Lab, pp. 1701–1709.

[134] Howard A. Levine and Marit Nilsen-Hamilton. “A mathematical analysis of SELEX”. In: *Computational Biology and Chemistry* 31.1 (Feb. 1, 2007), pp. 11–35.

[135] Hui Li et al. “A Biomimetic Phosphatidylcholine-Terminated Monolayer Greatly Improves the In Vivo Performance of Electrochemical Aptamer-Based Sensors”. In: *Angewandte Chemie International Edition* 56.26 (2017), pp. 7492–7495.

[136] Hui Li et al. “Calibration-Free Electrochemical Biosensors Supporting Accurate Molecular Measurements Directly in Undiluted Whole Blood”. In: *Journal of the American Chemical Society* 139.32 (2017), pp. 11207–11213.

[137] Long Li et al. “Nucleic Acid Aptamers for Molecular Diagnostics and Therapeutics: Advances and Perspectives”. In: *Angewandte Chemie International Edition* 60.5 (2021), pp. 2221–2231.

[138] Yang Li et al. “Adenosine modulates the excitability of layer II stellate neurons in entorhinal cortex through A1 receptors”. en. In: *Hippocampus* 21.3 (2011). _eprint: https://onlinelibrary.wiley.com/doi/pdf/10.1002/hipo.20745, pp. 265–280.

[139] Zhanhong Li et al. “Application of Electrochemical Aptasensors toward Clinical Diagnostics, Food, and Environmental Monitoring: Review”. In: *Sensors (Basel, Switzerland)* 19.24 (Dec. 10, 2019), E5435.

[140] Yuanying Liang et al. “Amplification of aptamer sensor signals by four orders of magnitude via interdigitated organic electrochemical transistors”. In: *Biosensors and Bioelectronics* 144 (Nov. 1, 2019), p. 111668.

[141] C. H. Lin and D. J. Patel. “Structural basis of DNA folding and recognition in an AMP-DNA aptamer complex: distinct architectures but common recognition motifs for DNA and RNA aptamers complexed to AMP”. In: *Chemistry & Biology* 4.11 (Nov. 1997), pp. 817–832.

[142] J. Liu et al. “The Current and Future Role of Aptamers in Electroanalysis”. In: *Journal of the Electrochemical Society* 161.5 (2014). ISBN: 0013-4651, H301–H313.

[143] Juan Liu et al. “Achieving reproducible performance of electrochemical, folding aptamer-based sensors on microelectrodes: Challenges and prospects”. In: *Analytical Chemistry* 86.22 (2014). ISBN: 4104555053, pp. 11417–11424.

[144] Nianzu Liu et al. “Low fouling strategies for electrochemical biosensors targeting disease biomarkers”. In: *Analytical Methods* 11.6 (2019). Publisher: Royal Society of Chemistry, pp. 702–711.

[145] Yixin Liu et al. “Visible light photoelectrochemical aptasensor for adenosine detection based on CdS/PPy/g-C3N4 nanocomposites”. In: *Biosensors and Bioelectronics* 86 (Dec. 15, 2016), pp. 439–445.

[146] Harvey Lodish et al. “The Molecules of Life”. en. In: *Molecular Cell Biology. 4th edition*. Publisher: W. H. Freeman. 2000.

[147] Maren Lönne et al. “Aptamer-Modified Nanoparticles as Biosensors”. In: *Biosensors Based on Aptamers and Enzymes*. Ed. by Man Bock Gu and Hak-Sung Kim. Advances in Biochemical Engineering/Biotechnology. Berlin, Heidelberg: Springer, 2014, pp. 121–154.

[148] Ronny Lorenz et al. “ViennaRNA Package 2.0”. In: *Algorithms for Molecular Biology : AMB* 6 (Nov. 24, 2011), p. 26.

[149] Lihua Lu et al. “Development of a luminescent G-quadruplex-selective iridium(III) complex for the label-free detection of adenosine”. In: *Scientific Reports* 6 (October 2015 2016), pp. 1–9.

[150] Chen Lyu, Imran Mahmood Khan, and Zhouping Wang. “Capture-SELEX for aptamer selection: A short review”. In: *Talanta* 229 (July 1, 2021), p. 122274.

[151] Fábio Madeira et al. “The EMBL-EBI search and sequence analysis tools APIs in 2019”. In: *Nucleic Acids Research* 47 (W1 July 2, 2019), W636–W641.

[152] J. Maher and V. Hachinski. “Hypothermia as a potential treatment for cerebral ischemia”. In: *Cerebrovascular and Brain Metabolism Reviews* 5.4 (1993), pp. 277–300.

[153] I Majerfeld and M Yarus. “Isoleucine:RNA sites with associated coding sequences.” In: *RNA* 4.4 (Apr. 1998), pp. 471–478.

[154] Francesca Malvano, Roberto Pilloton, and Donatella Albanese. “Label-free impedimetric biosensors for the control of food safety – a review”. In: *International Journal of Environmental Analytical Chemistry* 100.4 (Mar. 2020), pp. 468–491.

[155] Citartan Marimuthu et al. “Single-stranded DNA (ssDNA) production in DNA aptamer generation”. In: *Analyst* 137.6 (Feb. 20, 2012). Publisher: The Royal Society of Chemistry, pp. 1307–1315.

[156] Nicholas R. Markham and Michael Zuker. “UNAFold”. In: *Bioinformatics: Structure, Function and Applications*. Ed. by Jonathan M. Keith. Methods in Molecular Biology™. Totowa, NJ: Humana Press, 2008, pp. 3–31.

[157] S. A. Masino et al. “Changes in hippocampal adenosine efflux, ATP levels, and synaptic transmission induced by increased temperature”. In: *Synapse (New York, N.Y.)* 41.1 (July 2001), pp. 58–64.

[158] Elba Mauriz. “Low-Fouling Substrates for Plasmonic Sensing of Circulating Biomarkers in Biological Fluids”. In: *Biosensors* 10.6 (June 2020). Number: 6 Publisher: Multidisciplinary Digital Publishing Institute, p. 63.

[159] Günter Mayer. "The Chemical Biology of Aptamers". In: *Angewandte Chemie International Edition* 48.15 (2009), pp. 2672–2689.

[160] Miles D. Mayer and Rebecca Y. Lai. "Effects of redox label location on the performance of an electrochemical aptamer-based tumor necrosis factor-alpha sensor". In: *Talanta* 189 (Nov. 1, 2018), pp. 585–591.

[161] Maureen McKeague and Maria C. DeRosa. "Challenges and Opportunities for Small Molecule Aptamer Development". In: *Journal of Nucleic Acids* (2012). ISSN: 2090-0201 Library Catalog: www.hindawi.com Pages: e748913 Publisher: Hindawi Volume: 2012.

[162] Maureen McKeague et al. "Analysis of In Vitro Aptamer Selection Parameters". In: *Journal of Molecular Evolution* 81.5 (Dec. 1, 2015), pp. 150–161.

[163] Maureen McKeague et al. "Comprehensive Analytical Comparison of Strategies Used for Small Molecule Aptamer Evaluation". In: *Analytical Chemistry* 87.17 (Sept. 1, 2015). Publisher: American Chemical Society, pp. 8608–8612.

[164] Maureen McKeague et al. "Selection and Characterization of a Novel DNA Aptamer for Label-Free Fluorescence Biosensing of Ochratoxin A". In: *Toxins* 6.8 (Aug. 15, 2014), pp. 2435–2452.

[165] A. D. McNaught and A. Wilkinson. *IUPAC. Compendium of Chemical Terminology, 2nd ed. (the "Gold Book")*. 2nd. Online version (2019-) created by S. J. Chalk. Blackwell Scientific Publications, 1997.

[166] Parikha Mehrotra. "Biosensors and their applications – A review". In: *Journal of Oral Biology and Craniofacial Research* 6.2 (2016), pp. 153–159.

[167] Marc Meli et al. "Adenine-Aptamer Complexes: A BIPARTITE RNA SITE THAT BINDS THE ADENINE NUCLEIC BASE*". In: *Journal of Biological Chemistry* 277.3 (Jan. 18, 2002), pp. 2104–2111.

[168] J. D. Michenfelder and J. H. Milde. "The relationship among canine brain temperature, metabolism, and function during hypothermia". In: *Anesthesiology* 75.1 (July 1991), pp. 130–136.

[169] Valentin Mirčeski, Šebojka Komorsky-Lovrić, and Milivoj Lovrić. *Square-wave voltammetry: theory and application*. Monographs in electrochemistry. OCLC: ocn171563494. Berlin: Springer, 2007. 201 pp.

[170] Harshvardhan Modh et al. "Aptamer-based detection of adenosine triphosphate via qPCR". In: *Talanta* 172 (May 2017). Publisher: Elsevier B.V., pp. 199–205.

[171] G. H. Moser, J. Schrader, and A. Deussen. "Turnover of adenosine in plasma of human and dog blood". In: *American Journal of Physiology-Cell Physiology* 256.4 (Apr. 1, 1989). Publisher: American Physiological Society, pp. C799–C806.

[172] May-Britt Moser and Edvard I. Moser. "Functional differentiation in the hippocampus". In: *Hippocampus* 8.6 (1998), pp. 608–619.

[173] Ahana Mukherjee, Jaydeep Bhattacharya, and Ranjita Ghosh Moulick. "Nanodevices: The Future of Medical Diagnostics". en. In: *NanoBioMedicine*. Ed. by Shailendra K. Saxena and S. M. Paul Khurana. Singapore: Springer, 2020, pp. 371–388.

[174] Souvik Mukherjee et al. "A Graphene and Aptamer Based Liquid Gated FET-Like Electrochemical Biosensor to Detect Adenosine Triphosphate". In: *IEEE Transactions on Nanobioscience* 14.8 (2015), pp. 967–972.

[175] Michael U. Musheev and Sergey N. Krylov. "Selection of aptamers by systematic evolution of ligands by exponential enrichment: Addressing the polymerase chain reaction issue". In: *Analytica Chimica Acta*. Analytical Methods for Proteomics 564.1 (Mar. 30, 2006), pp. 91–96.

[176] Nako Nakatsuka et al. "Aptamer–field-effect transistors overcome Debye length limitations for small-molecule sensing". In: *Science* 362.6412 (Oct. 19, 2018). Publisher: American Association for the Advancement of Science Section: Report, pp. 319–324.

[177] Adela Nano et al. "DNA Electrochemistry: Charge-Transport Pathways through DNA Films on Gold". In: *Journal of the American Chemical Society* 143.30 (Aug. 4, 2021). Publisher: American Chemical Society, pp. 11631–11640.

[178] Maryam Naseri et al. "The Use of Aptamers and Molecularly Imprinted Polymers in Biosensors for Environmental Monitoring: A Tale of Two Receptors". In: *Chemosensors* 8.2 (May 6, 2020), p. 32.

[179] Adam J. H. Newton, Mark J. Wall, and Magnus J. E. Richardson. "Modeling microelectrode biosensors: free-flow calibration can substantially underestimate tissue concentrations". In: *Journal of Neurophysiology* 117.3 (Mar. 1, 2017), pp. 937–949.

[180] Michael D. Nguyen and B. Jill Venton. "Fast-scan Cyclic Voltammetry for the Characterization of Rapid Adenosine Release". In: *Computational and Structural Biotechnology Journal* 13 (Jan. 1, 2015), pp. 47–54.

[181] Razvan Nutiu and Yingfu Li. "In vitro selection of structure-switching signaling aptamers". In: *Angewandte Chemie - International Edition* 44.7 (2005). ISBN: 0002-7863 (Print)\r0002-7863 (Linking), pp. 1061–1065.

[182] Fadwa Odeh et al. "Aptamers Chemistry: Chemical Modifications and Conjugation Strategies". In: *Molecules* 25.1 (Jan. 2020). Number: 1 Publisher: Multidisciplinary Digital Publishing Institute, p. 3.

[183] Erik W. Orava, Nenad Cicmil, and Jean Gariépy. "Delivering cargoes into cancer cells using DNA aptamers targeting internalized surface portals". In: *Biochimica Et Biophysica Acta* 1798.12 (Dec. 2010), pp. 2190–2200.

[184] Gabriel Ortega et al. "Rational design to control the trade-off between receptor affinity and cooperativity". In: *Proceedings of the National Academy of Sciences* 117.32 (Aug. 11, 2020). Publisher: National Academy of Sciences Section: Biological Sciences, pp. 19136–19140.

[185] Patrick Frank Ottensmeyer et al. “Small Molecules Enhance Scaffold-Based Bone Grafts via Purinergic Receptor Signaling in Stem Cells”. In: *International Journal of Molecular Sciences* 19.11 (Nov. 2018). Number: 11 Publisher: Multidisciplinary Digital Publishing Institute, p. 3601.

[186] Abdullah Ozer, John M. Pagano, and John T. Lis. “New technologies provide quantum changes in the scale, speed, and success of SELEX methods and aptamer characterization”. In: *Molecular Therapy - Nucleic Acids* 3 (May 2014). Publisher: American Society of Gene & Cell Therapy ISBN: 2162-2531 (Electronic), e183.

[187] Fariborz Parandeh et al. “Inhibitory effect of UDP-glucose on cAMP generation and insulin secretion”. In: *Journal of Biological Chemistry* 295.45 (Nov. 6, 2020). Publisher: Elsevier, pp. 15245–15252.

[188] Cheonho Park et al. “Fast Cyclic Square-Wave Voltammetry To Enhance Neurotransmitter Selectivity and Sensitivity”. In: *Analytical Chemistry* 90.22 (Nov. 20, 2018). Publisher: American Chemical Society, pp. 13348–13355.

[189] Jaoek Park and Radhey S. Gupta. “Adenosine Metabolism, Adenosine Kinase, and Evolution”. In: *Adenosine: A Key Link between Metabolism and Brain Activity*. Ed. by Susan Masino and Detlev Boison. New York, NY: Springer, 2013, pp. 23–54.

[190] Claudio Parolo et al. “E-DNA scaffold sensors and the reagentless, single-step, measurement of HIV-diagnostic antibodies in human serum”. en. In: *Microsystems & Nanoengineering* 6.1 (Mar. 2020). Bandiera_abtest: a Cc_license_type: cc_by Cg_type: Nature Research Journals Number: 1 Primary_atype: Research Publisher: Nature Publishing Group Subject_term: Biosensors;Chemistry Subject_term_id: biosensors;chemistry, pp. 1–8.

[191] Marçal Pastor-Anglada and Sandra Pérez-Torras. “Who Is Who in Adenosine Transport”. In: *Frontiers in Pharmacology* 9 (June 2018), p. 627.

[192] Bhavik Anil Patel et al. “ATP microelectrode biosensor for stable long-term in vitro monitoring from gastrointestinal tissue”. en. In: *Biosensors and Bioelectronics* 26.6 (Feb. 2011), pp. 2890–2896.

[193] Bhavik Anil Patel et al. “Microelectrode investigation of neuroneal ageing from a single identified neurone”. en. In: *Physical Chemistry Chemical Physics* 12.34 (Aug. 2010). Publisher: The Royal Society of Chemistry, pp. 10065–10072.

[194] Tim Pearson et al. “A Depletable Pool of Adenosine in Area CA1 of the Rat Hippocampus”. In: *The Journal of Neuroscience* 21.7 (Apr. 1, 2001), pp. 2298–2307.

[195] Tim Pearson et al. “Plasticity of purine release during cerebral ischemia: clinical implications?” In: *Journal of Cellular and Molecular Medicine* 7.4 (2003), pp. 362–375.

[196] Felicita Pedata et al. “Adenosine and Stroke”. In: *Adenosine: A Key Link between Metabolism and Brain Activity*. Ed. by Susan Masino and Detlev Boison. New York, NY: Springer, 2013, pp. 273–306.

[197] Felicita Pedata et al. “Investigations into the Adenosine Outflow from Hippocampal Slices Evoked by Ischemia-Like Conditions”. In: *Journal of Neurochemistry* 61.1 (1993), pp. 284–289.

[198] Veeradasan Perumal and Uda Hashim. “Advances in biosensors: Principle, architecture and applications”. In: *Journal of Applied Biomedicine* 12.1 (Jan. 1, 2014), pp. 1–15.

[199] John W. Phillis et al. “Increases in Cerebral Cortical Perfusate Adenosine and Inosine Concentrations during Hypoxia and Ischemia”. In: *Journal of Cerebral Blood Flow & Metabolism* 7.6 (Dec. 1, 1987). Publisher: SAGE Publications Ltd STM, pp. 679–686.

[200] Daniel S. Pilch et al. “Thermodynamics of aminoglycoside–rRNA recognition”. In: *Biopolymers* 70.1 (2003), pp. 58–79.

[201] F. C. Ping and L. C. Jenkins. “Protection of the brain from hypoxia: A review”. In: *Canadian Anaesthetists' Society Journal* 25.6 (Nov. 1978), pp. 468–473.

[202] Piyanut Pinyou, Thierry Noguer, and Vincent Blay. “Enzymes, Aptamers, and Their Use in Sensors”. en. In: *Reference Module in Biomedical Sciences*. Elsevier, Jan. 2021.

[203] Aldyla N. Raditya and Danny O'Hare. “Review—Electrochemical Sensor Biofouling in Environmental Sensor Networks: Characterisation, Remediation and Lessons from Biomedical Devices”. en. In: *Journal of The Electrochemical Society* 167.12 (Aug. 2020). Publisher: The Electrochemical Society, p. 127503.

[204] Sinha Rajeshwari and Shukla Pratyoosh. “Current Trends in Protein Engineering: Updates and Progress”. en. In: *Current Protein & Peptide Science* 20.5 (May 2019), pp. 398–407.

[205] Louis. Ramaley and Matthew S. Krause. “Theory of square wave voltammetry”. In: *Analytical Chemistry* 41.11 (Sept. 1, 1969). Publisher: American Chemical Society, pp. 1362–1365.

[206] T.M. Rawson et al. “Towards a minimally invasive device for continuous monitoring of beta-lactam antibiotics”. en. In: *International Journal of Infectious Diseases* 73 (Aug. 2018), p. 109.

[207] Philipp Reineck, Christoph J. Wienken, and Dieter Braun. “Thermophoresis of single stranded DNA”. In: *ELECTROPHORESIS* 31.2 (2010), pp. 279–286.

[208] Anke Reining et al. “Three-state mechanism couples ligand and temperature sensing in riboswitches”. In: *Nature* 499.7458 (July 2013). Publisher: Nature Publishing Group, pp. 355–359.

[209] Amandine Renaud de la Faverie et al. “Thioflavin T as a fluorescence light-up probe for G4 formation”. In: *Nucleic Acids Research* 42.8 (Apr. 1, 2014), e65–e65.

[210] Francesco Ricci et al. “Effect of Molecular Crowding on the Response of an Electrochemical DNA Sensor”. In: *Langmuir* 23.12 (June 2007). Publisher: American Chemical Society, pp. 6827–6834.

[211] Niina J. Ronkainen, H. Brian Halsall, and William R. Heineman. “Electrochemical biosensors”. In: *Chemical Society Reviews* 39.5 (Apr. 26, 2010), pp. 1747–1763.

[212] Ashley E. Ross and B. Jill Venton. "Sawhorse Waveform Voltammetry for Selective Detection of Adenosine, ATP, and Hydrogen Peroxide". In: *Analytical Chemistry* 86.15 (Aug. 5, 2014). Publisher: American Chemical Society, pp. 7486–7493.

[213] Timothy T. Ruckh and Heather A. Clark. "Implantable Nanosensors: Toward Continuous Physiologic Monitoring". In: *Analytical Chemistry* 86.3 (Feb. 2014). Publisher: American Chemical Society, pp. 1314–1323.

[214] Annamaria Ruscito and Maria C. DeRosa. "Small-Molecule Binding Aptamers: Selection Strategies, Characterization, and Applications". In: *Frontiers in Chemistry* 4 (May 10, 2016).

[215] Juan Sahuquillo and Anna Vilalta. "Cooling the Injured Brain: How Does Moderate Hypothermia Influence the Pathophysiology of Traumatic Brain Injury". In: *Current Pharmaceutical Design* 13.22 (July 31, 2007), pp. 2310–2322.

[216] S. Ehsan Salamifar and Rebecca Y. Lai. "Fabrication of Electrochemical DNA Sensors on Gold-Modified Recessed Platinum Nanoelectrodes". en. In: *Analytical Chemistry* 86.6 (Mar. 2014), pp. 2849–2852.

[217] Bankim J. Sanghavi et al. "Real-Time Electrochemical Monitoring of Adenosine Triphosphate in the Picomolar to Micromolar Range Using Graphene-Modified Electrodes". In: *Analytical Chemistry* 85.17 (Sept. 3, 2013), pp. 8158–8165.

[218] Mirelis Santos-Cancel et al. "Direct, Real-Time Detection of Adenosine Triphosphate Release from Astrocytes in Three-Dimensional Culture Using an Integrated Electrochemical Aptamer-Based Sensor". In: *ACS Chemical Neuroscience* 10.4 (Apr. 17, 2019). Publisher: American Chemical Society, pp. 2070–2079.

[219] Kwabena Sarpong and Bhaskar Datta. "Nucleic-Acid-Binding Chromophores as Efficient Indicators of Aptamer-Target Interactions". In: *Journal of Nucleic Acids* 2012 (Oct. 10, 2012). Publisher: Hindawi, e247280.

[220] Mandana Sassanfar and Jack W. Szostak. "An RNA motif that binds ATP". In: *Nature* 364.6437 (Aug. 1993), pp. 550–553.

[221] Peter L. Sazani, Rosa Larralde, and Jack W. Szostak. "A Small Aptamer with Strong and Specific Recognition of the Triphosphate of ATP". In: *Journal of the American Chemical Society* 126.27 (July 14, 2004). Publisher: American Chemical Society, pp. 8370–8371.

[222] Fritz Scholz et al., eds. *Electroanalytical Methods*. Berlin, Heidelberg: Springer Berlin Heidelberg, 2010.

[223] L.R. Schoukroun-Barnes et al. "Reagentless, Structure-Switching, Electrochemical Aptamer-Based Sensors". In: *Annual Review of Analytical Chemistry* 9.14 (2016).

[224] Peter Schubert et al. "Modulation of nerve and glial function by adenosine—role in the development of ischemic damage". In: *International Journal of Biochemistry* 26.10 (Oct. 1, 1994), pp. 1227–1236.

[225] Tatjana Schütze et al. “Probing the SELEX Process with Next-Generation Sequencing”. In: *PLOS ONE* 6.12 (Dec. 29, 2011). Publisher: Public Library of Science, e29604.

[226] Karen Scida, Kevin W. Plaxco, and Brian G. Jamieson. “High frequency, real-time neurochemical and neuropharmacological measurements in situ in the living body”. In: *Translational Research* 213 (Nov. 1, 2019). Publisher: Elsevier, pp. 50–66.

[227] K. Scott. “2 - Electrochemical principles and characterization of bioelectrochemical systems”. en. In: *Microbial Electrochemical and Fuel Cells*. Ed. by Keith Scott and Eileen Hao Yu. Boston: Woodhead Publishing, Jan. 2016, pp. 29–66.

[228] Sukeerthi Seetharaman et al. “Immobilized RNA switches for the analysis of complex chemical and biological mixtures”. In: *Nature Biotechnology* 19.4 (Apr. 2001), pp. 336–341.

[229] D. Sehnal et al. “Mol*: towards a common library and tools for web molecular graphics”. In: *Proceedings of the Workshop on Molecular Graphics and Visual Analysis of Molecular Data*. MolVA ’18. Goslar, DEU: Eurographics Association, June 4, 2018, pp. 29–33.

[230] David Sehnal et al. “Mol* Viewer: modern web app for 3D visualization and analysis of large biomolecular structures”. In: *Nucleic Acids Research* 49.W1 (July 2021), W431–W437.

[231] Sohyeon Seo and Hyoyoung Lee. “Thermal-Processing-Induced Structural Dynamics of Thiol Self-Assembly in Solution”. In: *The Journal of Physical Chemistry C* 115.31 (Aug. 11, 2011). Publisher: American Chemical Society, pp. 15480–15486.

[232] Yeon-Jung Seo et al. “A Mathematical Analysis of Multiple-Target Selex”. In: *Bulletin of Mathematical Biology* 72.7 (Oct. 1, 2010), pp. 1623–1665.

[233] Samy M. Shaban and Dong-Hwan Kim. “Recent Advances in Aptamer Sensors”. In: *Sensors* 21.3 (Jan. 2021). Number: 3 Publisher: Multidisciplinary Digital Publishing Institute, p. 979.

[234] Keke Shao et al. “Emulsion PCR: a high efficient way of PCR amplification of random DNA libraries in aptamer selection”. In: *PloS one* 6.9 (Jan. 1, 2011), e24910.

[235] Suruchi Sharma, Matthew Zajac, and Yamuna Krishnan. “A DNA aptamer for cyclic adenosine monophosphate that shows adaptive recognition.” In: *Chembiochem : a European journal of chemical biology* 21.1 (Jan. 15, 2020), pp. 157–162.

[236] Sandeep Sheth et al. “Adenosine Receptors: Expression, Function and Regulation”. In: *International Journal of Molecular Sciences* 15.2 (Jan. 2014), pp. 2024–2052.

[237] Hojin Shin et al. “Sensitive and Selective Measurement of Serotonin in Vivo Using Fast Cyclic Square-Wave Voltammetry”. In: *Analytical Chemistry* 92.1 (Jan. 7, 2020). Publisher: American Chemical Society, pp. 774–781.

[238] Aron A. Shoara et al. “Development of a thermal-stable structure-switching cocaine-binding aptamer”. In: *Biochimie*. Aptamer Technology and Applications 145 (Feb. 1, 2018), pp. 137–144.

[239] Bo Si and Edward Song. “Recent Advances in the Detection of Neurotransmitters”. In: *Chemosensors* 6.1 (Mar. 2018). Number: 1 Publisher: Multidisciplinary Digital Publishing Institute, p. 1.

[240] László Simon, Zsófia Bognár, and Róbert E. Gyurcsányi. “Finding the Optimal Surface Density of Aptamer Monolayers by SPR Imaging Detection-based Aptamer Microarrays”. In: *Electroanalysis* 32.4 (2020), pp. 851–858.

[241] Koel Sinha and Chitrangada Das Mukhopadhyay. “Quantitative detection of neurotransmitter using aptamer: From diagnosis to therapeutics”. In: *Journal of Biosciences* 45.1 (Dec. 2020), p. 44.

[242] Rachel K. Smith et al. “Phase Separation within a Binary Self-Assembled Monolayer on Au{111} Driven by an Amide-Containing Alkanethiol”. In: *The Journal of Physical Chemistry B* 105.6 (Feb. 1, 2001). Publisher: American Chemical Society, pp. 1119–1122.

[243] Shiping Song, Hui Xu, and Chunhai Fan. “Potential diagnostic applications of biosensors: current and future directions”. In: *International Journal of Nanomedicine* 1.4 (Dec. 2006), pp. 433–440.

[244] Shiping Song et al. “Aptamer-based biosensors”. In: *TrAC - Trends in Analytical Chemistry* 27.2 (2008). ISBN: 0165-9936, pp. 108–117.

[245] Fabian Spill et al. “Controlling uncertainty in aptamer selection”. In: *Proceedings of the National Academy of Sciences of the United States of America* 113.43 (Oct. 25, 2016), pp. 12076–12081.

[246] Jayaram Srinivasan et al. “ADP-Specific Sensors Enable Universal Assay of Protein Kinase Activity”. In: *Chemistry & Biology* 11.4 (Apr. 1, 2004), pp. 499–508.

[247] Jonathan A. Stamford, Zygmunt L. Kruk, and Julian Millar. “A double-cycle high-speed voltammetric technique allowing direct measurement of irreversibly oxidised species: characterisation and application to the temporal measurement of ascorbate in the rat central nervous system”. In: *Journal of Neuroscience Methods* 10.2 (Feb. 1, 1984), pp. 107–118.

[248] Jonathan A. Stamford, Zygmunt L. Kruk, and Julian Millar. “Regional differences in extracellular ascorbic acid levels in the rat brain determined by high speed cyclic voltammetry”. In: *Brain Research* 299.2 (May 14, 1984), pp. 289–295.

[249] Adam B. Steel, Tonya M. Herne, and Michael J. Tarlov. “Electrochemical Quantitation of DNA Immobilized on Gold”. In: *Analytical Chemistry* 70.22 (Nov. 1, 1998). Publisher: American Chemical Society, pp. 4670–4677.

[250] Regina Stoltenburg, Nadia Nikolaus, and Beate Strehlitz. “Capture-SELEX: Selection of DNA aptamers for aminoglycoside antibiotics”. In: *Journal of Analytical Methods in Chemistry* 1.1 (2012). ISBN: 2090-8873 (Electronic).

[251] Regina Stoltenburg and Beate Strehlitz. “Refining the Results of a Classical SELEX Experiment by Expanding the Sequence Data Set of an Aptamer Pool Selected for Protein A”. In: *International Journal of Molecular Sciences* 19.2 (Feb. 24, 2018).

[252] Trevor W. Stone, Stefania Ceruti, and Mariapia P. Abbracchio. “Adenosine Receptors and Neurological Disease: Neuroprotection and Neurodegeneration”. In: *Adenosine Receptors in Health and Disease*. Ed. by Constance N. Wilson and S. Jamal Mustafa. Handbook of Experimental Pharmacology. Berlin, Heidelberg: Springer, 2009, pp. 535–587.

[253] S. J. Stranick et al. “A New Mechanism for Surface Diffusion: Motion of a Substrate-Adsorbate Complex”. In: *The Journal of Physical Chemistry* 98.43 (Oct. 1, 1994). Publisher: American Chemical Society, pp. 11136–11142.

[254] S. J. Stranick et al. “Phase Separation of Mixed-Composition Self-Assembled Monolayers into Nanometer Scale Molecular Domains”. In: *The Journal of Physical Chemistry* 98.31 (Aug. 1, 1994). Publisher: American Chemical Society, pp. 7636–7646.

[255] Shao Su et al. “Dual-Target Electrochemical Biosensing Based on DNA Structural Switching on Gold Nanoparticle-Decorated MoS2 Nanosheets”. In: *ACS Applied Materials & Interfaces* 8.11 (Mar. 2016). Publisher: American Chemical Society, pp. 6826–6833.

[256] Chenhu Sun et al. “An aptazyme-based electrochemical biosensor for the detection of adenosine”. In: *Analytica Chimica Acta* 669.1 (June 11, 2010), pp. 87–93.

[257] James S. Swensen et al. “Continuous, real-time monitoring of cocaine in undiluted blood serum via a microfluidic, electrochemical aptamer-based sensor”. In: *Journal of the American Chemical Society* 131.12 (2009). ISBN: 0002-7863, pp. 4262–4266.

[258] Zsuzsanna Szeitner et al. “Is less more? Lessons from aptamer selection strategies”. In: *Journal of Pharmaceutical and Biomedical Analysis* 101 (Dec. 2014), pp. 58–65.

[259] T Takahashi et al. “Adenosine and inosine release during hypoxia in the isolated spinal cord of neonatal rats”. In: *British Journal of Pharmacology* 161.8 (Dec. 2010), pp. 1806–1816.

[260] Ying Tan et al. “Label-free fluorescent assays based on aptamer–target recognition”. In: *Analyst* 137.10 (Apr. 23, 2012). Publisher: The Royal Society of Chemistry, pp. 2309–2312.

[261] Zahra Tavakolian-Ardakani et al. “Latest Trends in Electrochemical Sensors for Neurotransmitters: A Review”. In: *Sensors* 19.9 (Jan. 2019). Number: 9 Publisher: Multidisciplinary Digital Publishing Institute, p. 2037.

[262] Ramesh Thevendran et al. “Mathematical approaches in estimating aptamer-target binding affinity”. In: *Analytical Biochemistry* 600 (July 1, 2020), p. 113742.

[263] Daniel R. Thévenot et al. “Electrochemical biosensors: recommended definitions and classification1International Union of Pure and Applied Chemistry: Physical Chemistry Division, Commission I.7 (Biophysical Chemistry); Analytical Chemistry Division, Commission V.5 (Electroanalytical Chemistry).1”. en. In: *Biosensors and Bioelectronics* 16.1 (Jan. 2001), pp. 121–131.

[264] Ian A. P. Thompson et al. “Rational design of aptamer switches with programmable pH response”. In: *Nature Communications* 11.1 (June 10, 2020). Publisher: Nature Publishing Group, p. 2946.

[265] Faming Tian, Enrique Llaudet, and Nicholas Dale. “Ruthenium Purple-Mediated Microelectrode Biosensors Based on Sol-Gel Film”. In: *Analytical Chemistry* 79.17 (Sept. 2007), pp. 6760–6766.

[266] C. Tuerk and L. Gold. “Systematic evolution of ligands by exponential enrichment: RNA ligands to bacteriophage T4 DNA polymerase”. In: *Science* 249.4968 (Aug. 3, 1990). Publisher: American Association for the Advancement of Science Section: Research Articles, pp. 505–510.

[267] Anthony Turner. “Biosensors: then and now”. In: *Trends in Biotechnology* 31.3 (Mar. 1, 2013). Publisher: Elsevier, pp. 119–120.

[268] Hana Vaisocherová, Eduard Brynda, and Jiří Homola. “Functionalizable low-fouling coatings for label-free biosensing in complex biological media: advances and applications”. In: *Analytical and Bioanalytical Chemistry* 407.14 (May 1, 2015), pp. 3927–3953.

[269] Wladir B. Valderrama et al. “Commercially Available Rapid Methods for Detection of Selected Food-borne Pathogens”. In: *Critical Reviews in Food Science and Nutrition* 56.9 (July 2016), pp. 1519–1531.

[270] Barry Vant-Hull et al. “The mathematics of SELEX against complex targets11Edited by F. Cohen”. In: *Journal of Molecular Biology* 278.3 (May 8, 1998), pp. 579–597.

[271] B. Jill Venton and Qun Cao. “Fundamentals of fast-scan cyclic voltammetry for dopamine detection”. In: *Analyst* 145.4 (Feb. 17, 2020). Publisher: The Royal Society of Chemistry, pp. 1158–1168.

[272] Elena Vianini, Manlio Palumbo, and Barbara Gatto. “In vitro selection of DNA aptamers that bind l-tyrosinamide”. In: *Bioorganic & Medicinal Chemistry* 9.10 (Oct. 1, 2001), pp. 2543–2548.

[273] Natalia Vilariño et al. “Biological methods for marine toxin detection”. en. In: *Analytical and Bioanalytical Chemistry* 397.5 (July 2010), pp. 1673–1681.

[274] Emiel W. A. Visser et al. “Continuous biomarker monitoring by particle mobility sensing with single molecule resolution”. en. In: *Nature Communications* 9.1 (June 2018), p. 2541.

[275] Maria A. Vorobyeva et al. “Key Aspects of Nucleic Acid Library Design for in Vitro Selection”. In: *International Journal of Molecular Sciences* 19.2 (Feb. 2018). Number: 2 Publisher: Multidisciplinary Digital Publishing Institute, p. 470.

[276] Mark J. Wall and Nicholas Dale. "Auto-inhibition of rat parallel fibre–Purkinje cell synapses by activity-dependent adenosine release". In: *The Journal of Physiology* 581.2 (2007), pp. 553–565.

[277] Mark J. Wall and Nicholas Dale. "Neuronal transporter and astrocytic ATP exocytosis underlie activity-dependent adenosine release in the hippocampus". In: *The Journal of Physiology* 591.16 (2013), pp. 3853–3871.

[278] Mark J. Wall and Magnus J. E. Richardson. "Localized adenosine signaling provides fine-tuned negative feedback over a wide dynamic range of neocortical network activities". In: *Journal of Neurophysiology* 113.3 (2015), pp. 871–882.

[279] Dongmei Wang et al. "Electrochemical aptamer-based nanosensor fabricated on single Au nanowire electrodes for adenosine triphosphate assay". In: *Biosensors and Bioelectronics* 99 (Jan. 15, 2018), pp. 431–437.

[280] Guixiang Wang et al. "Antifouling aptasensor for the detection of adenosine triphosphate in biological media based on mixed self-assembled aptamer and zwitterionic peptide". In: *Biosensors and Bioelectronics* 101 (October 2017 2018). Publisher: Elsevier B.V., pp. 129–134.

[281] Jinpeng Wang et al. "Influence of Target Concentration and Background Binding on In Vitro Selection of Affinity Reagents". In: *PLOS ONE* 7.8 (Aug. 28, 2012). Publisher: Public Library of Science, e43940.

[282] Po Wang et al. "Construction of a paper-based electrochemical biosensing platform for rapid and accurate detection of adenosine triphosphate (ATP)". In: *Sensors and Actuators, B: Chemical* 256 (2018). Publisher: Elsevier B.V., pp. 931–937.

[283] Xiongjun Wang et al. "UDP-glucose accelerates SNAI1 mRNA decay and impairs lung cancer metastasis". In: *Nature* 571.7763 (July 2019), pp. 127–131.

[284] Becka M. Warfield and Peter C. Anderson. "Molecular simulations and Markov state modeling reveal the structural diversity and dynamics of a theophylline-binding RNA aptamer in its unbound state". In: *PLOS ONE* 12.4 (Apr. 24, 2017). Publisher: Public Library of Science, e0176229.

[285] Andrew M. Waterhouse et al. "Jalview Version 2—a multiple sequence alignment editor and analysis workbench". In: *Bioinformatics* 25.9 (May 1, 2009), pp. 1189–1191.

[286] Herschel M. Watkins et al. "Effects of Crowding on the Stability of a Surface-Tethered Biopolymer: An Experimental Study of Folding in a Highly Crowded Regime". In: *Journal of the American Chemical Society* 136.25 (June 25, 2014). Publisher: American Chemical Society, pp. 8923–8927.

[287] Michelle E. Watts, Roger Pocock, and Charles Claudianos. "Brain Energy and Oxygen Metabolism: Emerging Role in Normal Function and Disease". In: *Frontiers in Molecular Neuroscience* 11 (2018), p. 216.

[288] Ryan J White et al. "Florescent Microparticles for Sensing Cell Microenviorment Oxygen Level within 3D Scaffolds". In: *IFMBE Proceedings* 30.17 (2010). ISBN: 9783642149979, pp. 3068–3074.

[289] Ryan J. White, Aaron A. Rowe, and Kevin W. Plaxco. "Re-engineering aptamers to support reagentless, self-reporting electrochemical sensors". In: *The Analyst* 135.3 (2010), p. 589.

[290] Ryan J. White et al. "Optimization of Electrochemical Aptamer-Based Sensors via Optimization of Probe Packing Density and Surface Chemistry". In: *Langmuir : the ACS journal of surfaces and colloids* 24.18 (Sept. 16, 2008), pp. 10513–10518.

[291] H. R. Winn, R. Rubio, and R. M. Berne. "Brain adenosine concentration during hypoxia in rats". In: *American Journal of Physiology-Heart and Circulatory Physiology* 241.2 (Aug. 1, 1981). Publisher: American Physiological Society, H235–H242.

[292] Yi Xi Wu and Young Jik Kwon. "Aptamers: The "evolution" of SELEX". In: *Methods*. In vitro selection and evolution 106 (Aug. 15, 2016), pp. 21–28.

[293] Zhaofa Wu and Yulong Li. "New frontiers in probing the dynamics of purinergic transmitters in vivo". In: *Neuroscience Research*. Technologies Advancing Neuroscience 152 (Mar. 1, 2020), pp. 35–43.

[294] Yi Xiao et al. "Label-free electronic detection of thrombin in blood serum by using an aptamer-based sensor". In: *Angewandte Chemie - International Edition* 44.34 (2005). ISBN: 1521-3773, pp. 5456–5459.

[295] Ya-chen Xie, Leif A Eriksson, and Ru-bo Zhang. "Molecular dynamics study of the recognition of ATP by nucleic acid aptamers". In: *Nucleic Acids Research* 48.12 (July 9, 2020), pp. 6471–6480.

[296] Fangfang Yan, Fang Wang, and Zilin Chen. "Aptamer-based electrochemical biosensor for label-free voltammetric detection of thrombin and adenosine". In: *Sensors and Actuators, B: Chemical* 160.1 (2011). Publisher: Elsevier B.V. ISBN: 0925-4005, pp. 1380–1385.

[297] Jianhua Yan et al. "Advances in aptamer screening technologies". In: *Talanta* 200 (Aug. 1, 2019), pp. 124–144.

[298] Li Yang et al. "Insertion Approach: Bolstering the Reproducibility of Electrochemical Signal Amplification via DNA Superstructures". In: *Analytical Chemistry* 86.10 (May 20, 2014). Publisher: American Chemical Society, pp. 4657–4662.

[299] Midori A. Yenari and Hyung Soo Han. "Neuroprotective mechanisms of hypothermia in brain ischaemia". In: *Nature Reviews Neuroscience* 13.4 (Apr. 2012), pp. 267–278.

[300] Hua-Zhong Yu et al. "Voltammetric Procedure for Examining DNA-Modified Surfaces: Quantitation, Cationic Binding Activity, and Electron-Transfer Kinetics". In: *Analytical Chemistry* 75.15 (Aug. 1, 2003). Publisher: American Chemical Society, pp. 3902–3907.

[301] Chunze Zhang et al. "An Improved NGS Library Construction Approach Using DNA Isolated from Human Cancer Formalin-Fixed Paraffin-Embedded Samples". In: *The Anatomical Record* 302.6 (2019), pp. 941–946.

[302] Di Zhang et al. “Electrochemical aptamer-based microsensor for real-time monitoring of adenosine in vivo”. In: *Analytica Chimica Acta* 1076 (Oct. 17, 2019), pp. 55–63.

[303] Jingdong Zhang, Jianxun Xia, and Huangui Xiong. “Techniques for Extracellular Recordings”. en. In: *Current Laboratory Methods in Neuroscience Research*. Ed. by Huangui Xiong and Howard E. Gendelman. Springer Protocols Handbooks. New York, NY: Springer, 2014, pp. 325–345.

[304] Shusheng Zhang, Jianping Xia, and Xuemei Li. “Electrochemical biosensor for detection of adenosine based on structure-switching aptamer and amplification with reporter probe DNA modified Au nanoparticles”. In: *Analytical Chemistry* 80.22 (2008). ISBN: 8653284022750, pp. 8382–8388.

[305] Yang Zhang, Bo Shiun Lai, and Mario Juhas. “Recent Advances in Aptamer Discovery and Applications”. In: *Molecules* 24.5 (Jan. 2019). Number: 5 Publisher: Multidisciplinary Digital Publishing Institute, p. 941.

[306] Zijie Zhang and Juewen Liu. “An engineered one-site aptamer with higher sensitivity for label-free detection of adenosine on graphene oxide”. In: *Canadian Journal of Chemistry* 96.11 (Nov. 2018), pp. 957–963.

[307] Zijie Zhang, Olatunji Oni, and Juewen Liu. “New insights into a classic aptamer: binding sites, cooperativity and more sensitive adenosine detection”. In: *Nucleic Acids Research* 45.13 (July 27, 2017), pp. 7593–7601.

[308] Qinchang Zhu, Ge Liu, and Masaaki Kai. “DNA Aptamers in the Diagnosis and Treatment of Human Diseases”. In: *Molecules (Basel, Switzerland)* 20.12 (Nov. 25, 2015), pp. 20979–20997.

[309] Zhenjian Zhuo et al. “Recent Advances in SELEX Technology and Aptamer Applications in Biomedicine”. In: *International Journal of Molecular Sciences* 18.10 (Oct. 2017). Number: 10 Publisher: Multidisciplinary Digital Publishing Institute, p. 2142.